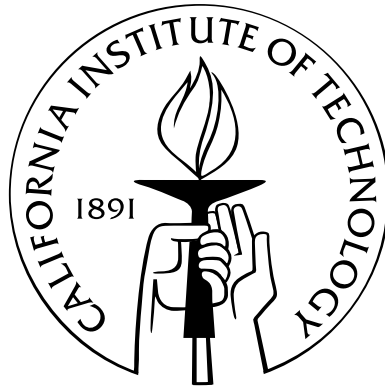


# Three Paths to Particle Dark Matter

Thesis by  
Samuel K. Lee

In Partial Fulfillment of the Requirements  
for the Degree of  
Doctor of Philosophy



California Institute of Technology  
Pasadena, California

2012  
(Defended April 16, 2012)



Some realize the Supreme by meditating, by its aid, on the Self within, others by pure reason, others by right action.

Others again, having no direct knowledge but only hearing from others, nevertheless worship, and they, too, if true to the teachings, cross the sea of death.

— *The Bhagavad Gita (13.25–26)*

---

Forgotten rimes, and college themes,  
Worm-eaten plans, and embryo schemes;—  
A mass of heterogeneous matter,  
A chaos dark, nor land nor water...

— *An Inventory of the Furniture in Dr. Priestley's Study (37–40)*,  
Anna Lætitia Barbauld (1825)

# Acknowledgments

Astronomy now demands bodily abstraction of its devotee... To see into the beyond requires purity... and the securing it makes him perforce a hermit from his kind...

— *Mars and Its Canals*,

Percival Lowell (1906)

I first encountered the above words on my recent cross-country emigration from Caltech to Johns Hopkins; they were engraved as an epitaph on Lowell's mausoleum, which is located on the grounds of the observatory bearing the learn'd astronomer's name. Upon reading them, I felt grateful that I could count myself luckier than Lowell in two respects: first, that we can be reasonably sure that dark matter will not follow the canals of Mars into the forgotten annals of science, and, more importantly, that my experience as a scientist thus far was neither as lonely nor as forsaken as Lowell's profound yet depressing words suggest it should have been. I have no quarrel with Lowell — and perhaps I have not achieved sufficient purity to see into the beyond just yet — but if ever my life's deeds are enough to warrant a mausoleum of my own, I will be sure that my epitaph not imply that those deeds were a solitary effort. In contrast, my pursuits and ambitions have always been supported by a large number of people; I hope they will accept the humble and sincere thanks I offer here.

First and foremost, I am indebted to my adviser, Marc Kamionkowski. The possibility of working with Marc was perhaps the primary reason I decided to attend Caltech for graduate school. Since he has afforded me the opportunity of working on a number of fascinating and intellectually stimulating research topics, it a decision I am very glad to have made. As an adviser, Marc has always been extremely generous with his encouragement and support, as well as with dispensing thoughtful advice that has proved invaluable in matters academic and otherwise. As a scientist, Marc has never failed to impress; many are the times I have been sitting in a colloquium or seminar, usually on a subject far afield from my own interests and expertise, admitting to myself that I have become hopelessly lost and perplexed by the presentation — it is usually at this point that Marc raises his hand and asks some piercing question, physically insightful yet completely clear even to one as confused as me. Although humbling, it is a great source of inspiration to realize that despite the years invested in this thesis, I still have a long way to go before I can hope to match his versatility as a physicist.

Next, I would like to thank those that I collaborated with to produce the work presented in this thesis. To Shin'ichiro Ando, Jonathan Feng, and Annika Peter — I learned many things from the science we did together, for which I am grateful; I am also immensely appreciative of the support you provided during the postdoctoral application process. I would also like to thank Kirill Melnikov and Andrzej Czarnecki for teaching me a thing or ten about thermal field theory. Furthermore, although not presented in this thesis, the work I have completed (or started...) with Savvas Koushiappas, Stefano Profumo, Lorenzo Ubaldi, Michael Dine, and Chris Hirata and the interactions we have had have also been important to my development as a physicist.

I would also like to express gratitude to the students, postdocs, professors, and staff that make Caltech such A Nice Place To Live (And Do A Ph.D.). I am glad to number myself among the Caltech Astronomy graduate students, and am proud of the community we have built during my time in the department. However, were it not for the friendship of my fellow classmates — Mike Anderson, Krzysztof Findeisen, Vera Gluščević, Tucker Jones, Elisabeth Krause, Tim Morton, Drew Newman, and Gwen Rudie — the first year of graduate school would certainly not have been as enjoyable as it was, much less those years subsequent. I am also obliged to Gina Armas and Gita Patel for their diligence and assistance.

Thanks goes to the numerous denizens of TAPIR: my most recent set of office mates Yacine Ali-Haïmoud, Nate Bode, and Anthony Pullen, who deserve credit for not giving me too hard a time about my odd hours; the members of the Tuesday group meetings — especially my elder academic siblings Adrienne Erickcek, Dan Grin, and Tristan Smith, as well as Fabian Schmidt, who have all been welcoming whenever our paths were fortunate enough to cross again, and Donghui Jeong, my fellow Caltech expatriate here at Johns Hopkins; the staff members that kept things running smoothly — JoAnn Boyd, Shirley Hampton, and Chris Mach; and the graduate students that politely put up with my ramblings on particle physics at our Thursday lunch lectures — Esfandiar Alizadeh, Laura Book, Michael Cohen, Jeff Kaplan, Keith Matthews, David Nichols, Evan O'Connor, Chris Wegg, Fan Zhang, Aaron Zimmerman, and others. In particular, I would like to commend Chris Wegg for his excellent taste in music, and thank him for filling the time between the support and the headliner with entertaining conversation. I would also like to generally thank the graduate and undergraduate students of the physics department for many positive experiences, both academic and social.

Some recognition is due to roommates I had through the years spent living in the Caltech Catalina Apartments; thanks to Steven Frankel, Zakary Singer, and Scott Steger for many memories in 201. Many enjoyable trips to the great outdoors — snowboarding, hiking, camping, and so forth — were had with Matt Schenker, who was always rather understanding of my general inexperience with much of the great outdoors. I had many stimulating talks with Think Bui during our frequent runs for Vietnamese food, and spent many equally stimulating hours in front of our CRT television

digesting the great epics of our time with him. Finally, Ryan Trainor has been one of the most dependable, capable, and good-spirited friends I have had the pleasure to know — and his family has always been very good to me, as well.

In the spring of my fourth year, I found myself volunteering to design and build handcrank-powered generators for a public-outreach installation promoting energy conservation and sustainability at the Coachella Valley Music and Arts Festival. I would like to thank Jelena Čulić-Viskota, Toni Lee, Jeff Lehew, Mike Shearn, and Ryan Trainor for entrusting a theoretical astrophysicist with the responsibility of engineering something remotely resembling a functional device (and for letting him use power tools in close proximity to you); the experience was a welcome diversion from my usual pencil-and-paper-and-programming routine.

In my fifth year, I found myself moving across the country to Baltimore. The physicists of Johns Hopkins have been most welcoming, for which I am grateful. However, the chemists also let me occasionally infiltrate their ranks; thanks to Chris Bianco, Tyler Chavez, Mark Hutchinson, and Chris Malbon for times around our kitchen island and elsewhere. In particular, my current housemates Jacob Kravetz and David Wallace deserve special praise for always being scholars (albeit of chemistry) and gentlemen (usually in that order).

As a physicist, I have been fortunate enough to attend a number of schools and conferences; I would like to thank the friends I have made during my travels for opening my eyes to the dedication required to do science in some parts of the world, and for showing me that physics is nevertheless a universal language.

However, I would not be able to speak that language were it not for my experiences during my MIT years. Without my former classmate Duncan Ma, I never would have gotten past 8.012, and it was Scott Hughes's excellent 8.022 lectures that cemented my desire to follow my current career path. Paul Schechter and Harvey Moseley were also great mentors during this formative period. Outside of my physics studies, some of my most challenging and gratifying experiences were had with the MIT Pistol Team, coached by Will Hart.

Even before MIT, several of my friends and teachers played important roles in shaping my growth. Although I have lost touch with some, time has not diminished their contribution; thanks to Anne Barrera (née Nugent), Dwo Chu, Johanna Chu (née Yu), Deborah Crawford, Robert Dennison, Jane Fain, Philip Ho, Jennifer Lee (née Yu), Matt Lee, Kanwar Singh, Chris Vollmer, and innumerable others. Charles Wei has proven to be an invaluable friend through the years.

On a larger scale, I express thanks to those that make my somewhat impractical profession possible. The epigraph that opens this thesis, although a tongue-in-cheek comparison between the three paths leading to particle dark matter and those leading to enlightenment and salvation, may perhaps be more obliquely read as expressing my sentiments on the role of a scientist in a society that values knowledge and the pursuit of deeper truths. Similar sentiments, with which I wholeheartedly

agree, may also be found in the dedication of Misner, Thorne, and Wheeler's well known tome on Gravitation.

At this point, I am running out of synonymous words with which to relate my thanks and gratitude. Fortunately, no words are necessary to express those feelings to my family, who have always loved and supported me unconditionally. To my father and mother — any virtues I may claim to have are merely echoes of yours, and any faults are mine alone. To Elaine and Peter — siblings are among the few people to ever truly know each other from childhood to maturity, and I hope that I have grown into someone you are proud to call your brother.

Finally, I am ever thankful to, and for, Zhitong Zhang. Her love has been a constant through many years of time, and, more often than not, across many miles of space. Despite my years devoted to studying the cosmos — with all its breadth and endless variety — I have yet to come across anything in it more lovely and delightful than she. With her companionship, the Universe seems far less cold, dark, and infinite.

# Abstract

In this thesis, we explore examples of each of the three primary strategies for the detection of particle dark matter: indirect detection, direct detection, and collider production.

We first examine the indirect detection of weakly interacting massive particle (WIMP) dark matter via the gamma-ray photons produced by astrophysical WIMP annihilation. Such photons may be observed by the Fermi Gamma-ray Space Telescope. We propose the gamma-ray-flux probability distribution function (PDF) as a probe of the Galactic halo substructure predicted to exist by N-body simulations. The PDF is calculated for a phenomenological model of halo substructure; it is shown that the PDF may allow a statistical detection of substructure.

Next, we consider the direct detection of WIMPs. We explore the ability of directional nuclear-recoil detectors to constrain the local velocity distribution of WIMP dark matter by performing Bayesian parameter estimation on simulated recoil-event data sets. We discuss in detail how directional information, when combined with measurements of the recoil-energy spectrum, helps break degeneracies in the velocity-distribution parameters. Considering the possibility that velocity structures such as cold tidal streams or a dark disk may also be present in addition to the Galactic halo, we discuss the potential of upcoming experiments to probe such structures.

We then study the collider production of light gravitino dark matter. Light gravitino production results in spectacular signals, including di-photons, delayed photons, kinked charged tracks, and heavy metastable charged particles. We find that observable numbers of light-gravitino events may be found in future collider data sets. Remarkably, this data is also well suited to distinguish between scenarios with light gravitino dark matter, with striking implications for early-Universe cosmology.

Finally, we investigate the related matter of radiative corrections to the decay rate of charged fermions caused by the presence of a thermal bath of photons. The cancellation of finite-temperature infrared divergences in the decay rate is described in detail. Temperature-dependent radiative corrections to the two-body decay of a hypothetical charged fermion and to electroweak decays of a muon are given. We touch upon possible implications of these results for charged particles in the early Universe.



# Contents

<b>Acknowledgments</b>	<b>iv</b>
<b>Abstract</b>	<b>viii</b>
<b>List of Figures</b>	<b>xii</b>
<b>List of Tables</b>	<b>xv</b>
<b>1 Introduction</b>	<b>1</b>
<b>2 Indirect detection: The gamma-ray-flux probability distribution function from Galactic halo substructure</b>	<b>11</b>
2.1 Motivation: Supersymmetric neutralinos as WIMP dark matter . . . . .	11
2.1.1 The WIMP miracle . . . . .	11
2.1.2 Supersymmetry and neutralino dark matter . . . . .	14
2.2 Introduction . . . . .	21
2.3 Substructure/annihilation models and EGRET constraints . . . . .	23
2.3.1 Halo model and microhalo mass function . . . . .	23
2.3.2 Microhalo annihilation models . . . . .	24
2.3.3 EGRET constraints . . . . .	25
2.4 Calculation of the PDF . . . . .	28
2.4.1 Derivation of $P_1(F)$ . . . . .	29
2.4.2 Calculation of the counts distribution . . . . .	29
2.5 Numerical results . . . . .	32
2.6 Detectability . . . . .	33
2.7 Conclusions . . . . .	35
<b>3 Direct detection: Probing the local velocity distribution of WIMP dark matter with directional detectors</b>	<b>38</b>
3.1 Motivation: The directional recoil spectrum from WIMP-nucleus collisions . . . . .	38

3.1.1	Simple estimates for direct detection	38
3.1.2	The directional recoil spectrum	40
3.2	Introduction	43
3.3	The binned likelihood function	44
3.4	Likelihood analyses of simulated data	47
3.4.1	Halo-only model	48
3.4.1.1	$v_{\text{lab}}\text{-}\sigma_{\text{H}}$ analyses	49
3.4.1.2	6-parameter analyses	51
3.4.2	Halo+stream model	52
3.4.3	Halo+disk model	54
3.5	Conclusions	55
<b>4</b>	<b>Collider production: Light gravitinos at colliders and implications for cosmology</b>	<b>70</b>
4.1	Motivation: Supergravity and the gravitino	70
4.1.1	A local $U(1)$ symmetry	70
4.1.2	From local supersymmetry to gravity	72
4.1.3	The super-Higgs mechanism	77
4.1.4	Gravitino interactions	79
4.2	Introduction	82
4.3	Light-gravitino cosmology	84
4.3.1	Canonical scenario	84
4.3.1.1	Relic abundance	84
4.3.1.2	Cosmological constraints	86
4.3.2	Nonstandard early-Universe scenarios	87
4.4	Light gravitinos at colliders	88
4.4.1	Mass and interactions	88
4.4.2	GMSB models	89
4.4.3	Current collider constraints	91
4.5	Tevatron and LHC prospects	92
4.5.1	Gravitino signals	92
4.5.2	GMSB scan and collider simulations	94
4.5.3	Cosmological implications	95
4.6	Conclusions	96
<b>5</b>	<b>A detour: Charged-particle decay at finite temperature</b>	<b>103</b>
5.1	Introduction	103
5.2	Toy model	105

5.2.1	Photon absorption . . . . .	106
5.2.2	Photon emission . . . . .	107
5.2.3	Real-radiation corrections . . . . .	108
5.3	Virtual corrections . . . . .	109
5.3.1	Vertex correction . . . . .	109
5.3.2	Self-energy corrections . . . . .	110
5.4	Total decay rate in the toy model . . . . .	114
5.5	Muon decay $\mu \rightarrow e\nu_\mu\bar{\nu}_e$ . . . . .	115
5.6	Conclusions . . . . .	116
<b>A</b>	<b>Kinetic decoupling</b> . . . . .	<b>118</b>
A.1	Elastic-scattering cross sections . . . . .	120
<b>B</b>	<b>Derivation of <math>P(F)</math></b> . . . . .	<b>125</b>
<b>C</b>	<b>Generation of directional-detection events</b> . . . . .	<b>127</b>
<b>D</b>	<b>Mass singularities and thermal fermionic corrections</b> . . . . .	<b>129</b>
	<b>Bibliography</b> . . . . .	<b>133</b>

# List of Figures

1.1	Three paths to particle dark matter . . . . .	5
2.1	Contributions to the Higgs self-energy from fermion and complex scalar couplings . . .	18
2.2	The intensity $I_h(\psi)$ above 10 GeV from microhalos . . . . .	27
2.3	The flux-density distribution $P_1(F, \psi = 90^\circ)$ for the flux from an individual microhalo	30
2.4	The angular-averaged discrete probability distribution function $P(C)$ for the neutralino model . . . . .	31
2.5	The angular-averaged discrete probability distribution function $P(C)$ , with an arbitrary diffuse background added . . . . .	31
2.6	The angular-averaged discrete probability distribution function $P(C)$ for the line model, with an arbitrary diffuse background added . . . . .	32
2.7	The $K_E$ - $M_{\min}$ parameter space for the line models . . . . .	34
3.1	The elastic scattering of a WIMP off of a nucleus initially at rest . . . . .	40
3.2	Allowed incoming-WIMP velocities $\mathbf{v}$ for an observed nuclear-recoil momentum $\mathbf{q}$ . . .	41
3.3	Left: Simulated recoil spectrum for the halo-only 2-parameter and 3-parameter analyses, with binned signal events. Right: Simulated recoil map for these analyses, in Mollweide projection . . . . .	58
3.4	Top row: Contour plots for the 2D posterior probability distribution in $v_{\text{lab}}$ - $\sigma_H$ space, for the halo-only 2-parameter analyses with fixed $m_\chi$ . Bottom row: The same for the 3-parameter analyses assuming a flat mass prior . . . . .	59
3.5	Recoil spectra showing the energy distribution (normalized to unity) of events in the energy range of 5–50 keV for a halo-only model . . . . .	60
3.6	Recoil maps showing the angular distribution (normalized to unity) of events in the energy range of 5–50 keV for a halo-only model . . . . .	61
3.7	Simulated recoil spectrum for the halo-only 6-parameter analysis . . . . .	62
3.8	Simulated recoil maps for the halo-only 6-parameter analysis . . . . .	62
3.9	Triangle plot showing 1D and 2D posterior probability distributions for the halo-only 6-parameter analysis using only energy information . . . . .	63

3.10	Triangle plot showing 1D and 2D posterior probability distributions over the full prior ranges, for the halo-only 6-parameter analysis using direction+energy information . . .	64
3.11	Simulated recoil spectrum for the halo+stream analysis . . . . .	65
3.12	Simulated recoil maps for the halo+stream analysis . . . . .	65
3.13	Triangle plot for the halo+stream analysis . . . . .	66
3.14	Simulated recoil spectrum for the halo+disk analyses . . . . .	67
3.15	Simulated recoil maps for the halo+disk analyses . . . . .	67
3.16	Triangle plot for the 0–50-keV halo+disk analysis . . . . .	68
3.17	Triangle plot for the 5–50-keV halo+disk analysis . . . . .	69
4.1	Supersymmetrization of the gauge vertex . . . . .	80
4.2	Supersymmetrization of the graviton couplings . . . . .	81
4.3	Plots showing the mapping between the $m_{\tilde{G}}-m_{\text{NLSP}}$ and the $M_{\text{mess}}-\Lambda$ GMSB parameter spaces . . . . .	95
4.4	Contour plots over the $m_{\tilde{G}}-m_{\text{NLSP}}$ parameter space showing the expected number of prompt di-photon events in a model with a neutralino NLSP . . . . .	98
4.5	Contour plots over the $m_{\tilde{G}}-m_{\text{NLSP}}$ parameter space showing the expected number of nonprompt photon events in a model with a neutralino NLSP . . . . .	99
4.6	Contour plots showing the expected number of nonprompt lepton events in a model with a stau NLSP . . . . .	100
4.7	Contour plots showing the expected number of metastable slepton events in a model with a stau NLSP . . . . .	101
4.8	Simulated probability distribution functions for the speed $\beta$ (top panels) and Lorentz factor $\gamma$ (bottom panels) of mother particles decaying to gravitinos . . . . .	102
5.1	The diagram for the decay $\psi \rightarrow \chi\phi$ . . . . .	104
5.2	The two diagrams via which absorption of a photon can lead to induced $\psi$ decay (or $\chi$ and $\phi$ production) . . . . .	105
5.3	The diagrams for radiative $\psi$ -decays . . . . .	107
5.4	The $T$ -dependent part of the photon propagator . . . . .	109
5.5	The diagram contributing to the $T$ -dependent part of the $\mathcal{O}(\alpha)$ correction to the vertex . . . . .	110
5.6	The diagram contributing to the $T$ -dependent part of the fermion self-energy . . . . .	111
A.1	Feynman diagrams for scattering of a fermion $f$ by a neutralino $\chi$ . . . . .	120
D.1	The $T$ -dependent part of the fermion propagator . . . . .	130

D.2	The additional diagrams (appearing at temperatures $m_\chi \ll T \ll m_\psi$ ) that contribute to the $T$ -dependent part of the real corrections, including the thermal corrections to the bare fermion propagator . . . . .	130
D.3	The additional diagrams (appearing at temperatures $m_\chi \ll T \ll m_\psi$ ) that contribute to the $T$ -dependent part of the virtual corrections, including the thermal corrections to the bare fermion propagator . . . . .	131

# List of Tables

2.1	Particle content of the minimal supersymmetric standard model . . . . .	16
3.1	Experimental parameters used to simulate data for likelihood analyses . . . . .	48
3.2	Fiducial parameter values and flat prior ranges used to simulate data and perform likelihood analyses . . . . .	57
4.1	Analogy between the Higgs and super-Higgs mechanisms . . . . .	78

# Chapter 1

## Introduction

The problem of dark matter is surely one of the most exciting open questions in physics. The discovery of dark matter followed in the vein of a historical tradition in astronomy — namely, the revelation of hitherto unknown phenomena via their gravitational effects on visible matter.<sup>1</sup> As early as the 1920s, measurements of the vertical motions of stars near the Galactic plane implied the gravitational influence of an unseen dark component [1]. In 1933, Fritz Zwicky deduced the existence of a non-luminous constituent of the Coma cluster by observing the dynamics of the galaxies contained therein, famously conferring upon it the name of “dark matter” [2].<sup>2</sup>

Evidence for dark matter from astrophysical and cosmological observations now abounds. The astrophysical evidence includes the flattening of galactic rotation curves at radii beyond the visible edges of galaxies, studies of gravitational lensing — both strong and weak — in galaxies and clusters, and so on. Meanwhile, cosmological observations of the cosmic-microwave-background (CMB) anisotropies constrain the dark-matter density (in units of the critical density) of the Universe to be  $\Omega_{dm} = 0.222 \pm 0.026$  [4]. The constraint can be improved when taken in conjunction with measurements of the local Hubble expansion rate calibrated using Cepheid variables [5], the luminosity-distance–redshift relation determined from the light curves of Type Ia supernovae [6], and baryon acoustic oscillations measured from large-scale galaxy surveys [7]. At the same time, these measurements, as well as those of the chemical abundances of the light elements produced during big-bang nucleosynthesis, also determine the density of baryonic matter to be  $\Omega_b = 0.0449 \pm 0.0028$ . Thus, that non-baryonic dark matter composes the majority — roughly 80–85% — of the matter in the Universe, and approximately a quarter of the total matter-energy content, is overwhelmingly suggested by both astrophysical and cosmological evidence (for a more comprehensive overview, see, e.g., Ref. [8]).<sup>3</sup>

---

<sup>1</sup>The respective discoveries of Neptune and general relativity from the observed deviations of the orbits of Uranus and Mercury from the predictions of Newtonian theory followed this pattern.

<sup>2</sup>The dynamics revealed “die Notwendigkeit einer enorm grossen Dichte dunkler Materie”, the need for an enormously large density of dark matter. Interestingly enough, Zwicky also uses the phrase “dunkle (kalte) Materie” in the paper, although the use of “cold” here presumably equates to “non-luminous” (and not the modern interpretation of “nonrelativistic”). A brief overview of the historical development of dark matter is given in Ref. [3].

<sup>3</sup>The other possible explanation — a modification of the laws of gravity — is strongly disfavored, most convincingly



However, despite this abundance of evidence for the *existence* of dark matter, the *nature* of dark matter remains to be understood precisely. Perhaps one reason for this is that the pieces of evidence accumulated so far are derived from the observation of gravitational effects, and do not strongly preclude the possibility that dark matter interacts *solely* via the comparatively feeble force of gravity. Conversely, the exciting possibility that dark matter has “stronger-than-gravitational” interactions with everyday particles of the standard model, potentially allowing for detectable signals, remains viable. Interestingly enough, this latter scenario is realized in numerous theories of particle physics that resolve outstanding issues in the standard model. Many such extensions of the standard model hypothesize the existence of new particles that may naturally be *interesting* dark-matter candidates. That is, these particles are predicted to have properties that not only allow for them to fulfill the astrophysical and cosmological roles that dark matter play gravitationally, but may also allow them to be accessible experimentally. There is no shortage of well-motivated particle candidates; sterile neutrinos, supersymmetric neutralinos and gravitinos, axions, and Kaluza-Klein excitations in theories with extra dimensions number among the more commonly studied (reviews are given in, e.g., Refs. [10–13]).

There are a number of basic criteria related to the fundamental, microphysical particle properties of a dark-matter candidate that must first be satisfied if the particle is to successfully act out its various gravitational roles in a straightforward and non-contrived manner [14]:

- **Relic abundance:** The aforementioned new theories of physics should become relevant at energies greater than those previously explored by particle accelerators. Such energies may have been accessed in the early moments of the Universe, during the hot big bang. It is possible that dark-matter particles were produced then, by either standard thermal production via scattering interactions in the thermal bath or nonthermal mechanisms, in quantities that should be predictable given the new theory and its fundamental parameters. The parameters of the theory — which in turn determine the dark-matter particle properties — and the early-Universe conditions and production mechanisms must then conspire to produce the correct, observed abundance of dark matter.
- **Electromagnetic neutrality:** The dark matter must be truly *dark*. That is, the electromagnetic interactions of dark-matter particles with photons must be much weaker than those of conventionally charged particles. Limits on the strength of the electromagnetic interaction can be expressed in terms of the fractional charge (with respect to the elementary charge) of the dark-matter particle, and can be derived from the non-observation of the variety of astrophysical effects charged dark-matter particles would engender. The strongest constraint comes from the requirement that the dark matter not couple too strongly to photons during the

---

by observations of the Bullet galaxy cluster [9]. In this sense, the discovery of dark matter shares more in common with that of Neptune than that of general relativity.

recombination epoch (avoiding disruption of the CMB acoustic peaks), yielding an upper limit on the fractional charge of  $\sim 10^{-6}$  for GeV-mass particles, rising to  $\sim 10^{-4}$  for 10-TeV-mass particles [15]. Similarly, astrophysical constraints may be placed on the electric or magnetic dipole moments of the dark-matter particle (see, e.g., [16,17]).

- **Interaction strength:** Not only should the dark-matter particle not interact with photons and electrically charged particles, it must also not couple too strongly to electrically neutral standard-model particles. Again, one reason for this is the requirement that the dark matter not couple too strongly to *baryons* during the recombination epoch, as this would also change the CMB acoustic peaks. Significant coupling would also allow the baryon–dark-matter fluid to radiatively cool via the baryons, affecting structure formation. Thus, the link between dark matter and baryons must be relatively “weak” in strength, as a result of either a smallness of the fundamental interaction coupling or by some other mechanism which suppresses the observable consequences of “strong” interactions phenomenologically. Although this interaction between dark matter and baryons need not necessarily be the weak interaction of the standard model, many extensions of the standard model do generically predict the existence of new weakly interacting massive particles (WIMPs) that couple to the weak gauge bosons. As it can be shown that these WIMPs, if produced thermally in the early Universe, naturally have the correct dark-matter relic abundance (a coincidence referred to as the “WIMP miracle”), WIMPs are hence the most well-studied class of dark-matter candidates.
- **Non-baryonic nature:** In the same vein, the dark matter cannot be a non-exotic baryon (here, we actually mean hadron, although the use of the word “baryon” thus far, and conventionally in the literature, is as a misnomer that includes hadronic and leptonic matter). As previously mentioned, this is required in order for the predictions of big-bang nucleosynthesis, which are sensitive to the baryon-to-photon ratio, to be realized. Related to this criterion is the fact that massive compact halo objects (MACHOs), which are dark baryonic objects (including faint neutron stars, brown dwarfs, white dwarfs, planets, etc.) that were once a possible solution to the dark-matter problem, are ruled out [18]. Strong constraints on a possible MACHO population can be deduced from the disagreement of the observed chemical abundances with those expected to be produced by the evolution of stellar MACHOs [19], as well as from searches for microlensing by MACHOs [20,21]. These constraints indicate that the dark matter may indeed be composed of elementary particles.
- **Self-interaction strength:** Furthermore, the self-interaction of the dark-matter particle must be consistent with observations. Interestingly enough, dark matter with some degree of strong scattering self-interactions (but negligible annihilation or dissipation interactions) may alleviate some tensions between observations and collisionless-dark-matter simulations, such

as those arising from the “missing satellite” problem and the issue of the central cusps of dark-matter halos [22]. Several astrophysical constraints may be placed on self-interacting dark matter. For example, observations of the aforementioned Bullet cluster place an upper limit on the ratio of the self-scattering cross section to the dark-matter-particle mass  $\sigma/m \lesssim 1 \text{ cm}^2 \text{ g}^{-1}$ , which must be satisfied if the dark-matter components of the two colliding clusters are to pass through each other as implied by gravitational-lensing maps of the mass distribution.

- **Temperature:** As dark matter must be able to gravitationally collapse to form small-scale structure after it has decoupled from the thermal bath and the Universe becomes matter dominated, the dark-matter particles must have a small or nonrelativistic velocity at that time if they are not to free stream out of density perturbations. The “temperature” of the dark matter must then be fairly cold. At most, the dark matter may be “tepid” or “lukewarm”, with free-streaming lengths on the order of galactic scales, if the correct matter power spectrum is to be realized [23]. Neutrinos, the only standard-model particles that have heretofore satisfied all of the above constraints, are then ruled out, as they decouple when they are relativistic and thus compose hot matter. Mixed dark matter, composed of several distinct particle species with different temperatures, may also be a possibility that can be constrained by such considerations. These considerations then translate into constraints on both the mass of the dark-matter particle and the details of its kinetic decoupling, the latter of which depends on the scattering interactions of the dark-matter particle with particles in the thermal bath.
- **Stability:** The dark matter must be stable on cosmological timescales [24] if it is to be produced in the early Universe, affect the CMB anisotropies formed during recombination, and persist to collapse to form structures present today. The avoidance of significant energy injection from standard-model decay products after the epochs of big-bang nucleosynthesis and recombination is also desirable. Scenarios in which a number of multiple dark-matter species exist and may decay to the lightest among them at late times are also strongly constrained by the requirement that the kicks given to the dark decay products not disrupt dark-matter-halo structure and formation [25, 26]. At the microphysical level, stability is commonly effected by introducing discrete symmetries, such that the dark-matter particle is the lightest of those particles that carry a conserved quantum number not possessed by the particles of the standard model.
- **Equivalence principle:** There is no *a priori* reason that the dark matter should obey the equivalence principle, even though ordinary matter does. For example, a violation of the equivalence principle might arise if light particles mediate an additional long-range force between dark-matter particles. However, observations of the dynamics of tidal tails in the Milky Way strongly constrain such theories [27, 28].

Certainly it is conceivable that some of these basic criteria might be relaxed in the context of a

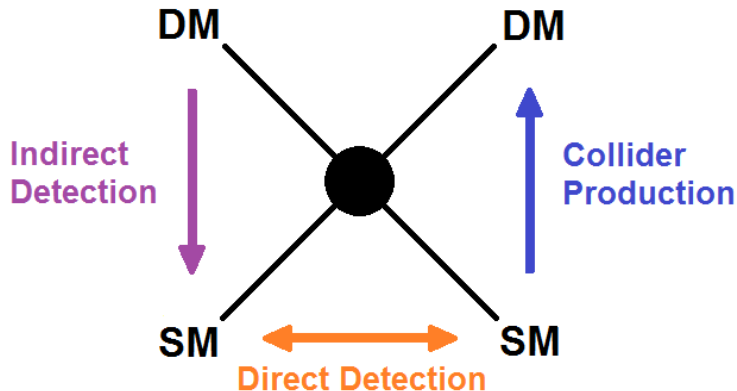


Figure 1.1: Three paths to particle dark matter. This diagram illustrates that stronger-than-gravitational interactions between dark matter and standard-model particles may give rise to interesting experimental signals. Reading the diagram in different directions yields the three primary dark-matter search strategies: indirect detection, direction detection, and collider production.

sufficiently complex dark-matter scenario. Nevertheless, it is clear that there are a bevy of conditions that the large-scale behavior of dark matter must meet — and hence, a number of constraints on the fundamental parameters of the underlying theory — if a given dark-matter candidate is to be consistent with astrophysical and cosmological observations.

It must again be emphasized that although such observations allow the measurement of interesting large-scale quantities, such as the total density of dark matter, they do not allow for the precise determination of the dark-matter particle properties (much less the fundamental theory parameters). This is essentially because such observations are viewed through the non-discerning lens provided by the effects of gravitational-strength interactions on large scales. An allowed dark-matter candidate thus becomes even more interesting if non-gravitational or enhanced-gravitational interactions between dark-matter particles and standard-model particles allow for experimental signals — resulting more directly and essentially from *microphysical* dark-matter interactions — to actually probe the dark-matter particle properties and the fundamental theory. Such interactions are depicted schematically in Figure 1.1, and lead to experimental signals that may be detected through methods generally falling into one of three categories:

- **Indirect detection:** Dark-matter particles may annihilate (or decay, if stability constraints are obeyed) to produce standard-model products — including charged particles, neutrinos, and photons — the detection of which would constitute an *indirect* detection of dark matter. If the mass of the dark-matter particle is relatively large (as is typically the case for WIMPs, which may have weak-scale masses), these products might be energetic. Especially of interest is the possibility that gamma-ray photons might be produced, since the travel of such photons across astrophysical distances is relatively unimpeded and would allow the identification of annihila-

tion sources. Such sources are provided by astrophysical concentrations of dark-matter, such as may be found in the Galactic center, Galactic substructure, dwarf galaxies, extragalactic dark-matter halos, and in clumps of dark matter that may have been captured in the center of baryonic astrophysical objects. A wide array of cosmic-ray and gamma-ray observatories — both in space and on the ground — are currently searching for indirect signals. A complete understanding of the implications of such signals for the microphysical dark-matter properties may inevitably require a parallel understanding of the distribution of dark matter on astrophysical scales. Nevertheless, indirect-detection signals may ultimately yield measurements of the dark-matter mass and the annihilation cross section and spectrum (or the equivalent quantities for decay), providing some insight on the parameters of the underlying theory.

- **Direct detection:** It may also be possible to *directly* detect the local dark-matter particles from our Galactic halo scattering off of ordinary nuclei. A variety of detectors designed to be sensitive to the nuclear recoils induced by collisions with WIMPs are currently collecting data, and have placed bounds on the WIMP-nucleon-cross section—WIMP-mass parameter space. These studies also depend on astrophysical input (in particular, the local phase-space distribution of dark-matter particles), a link that may lead to further insight on the role of dark matter in structure formation.
- **Collider production:** Finally, particle accelerators collide together ordinary, standard-model particles at tremendous energies, in the hopes that heretofore undiscovered particles will emerge from the collisions. Such collisions may then *produce* dark-matter particles, in processes that are the inverse of those that result in annihilation. With detailed studies of the production rates and signals of any other predicted new particles, collider experiments may ultimately result in the most complete picture of the underlying theory, if the relevant energies are accessible. However, there is an epistemological subtlety: we cannot be sure that any given particle observed at colliders is *the* astrophysical dark-matter particle, even if its properties are consistent with the criteria listed above. Thus, the particle properties inferred from collider signals must be cross-checked with those derived from signals arising from astrophysical sources in order to resolve this issue.

Each chapter in this thesis focuses on a study that falls into one of these detection-method categories. The bulk of the presentation of these studies has been adapted from material, previously published or forthcoming, of which I was the first author. However, portions of the pedagogical discussions that preface and motivate each study are original to this thesis, although they are largely adapted from the sources referenced.

We begin Chapter 2 by discussing the indirect detection of WIMP annihilation, examining in

some detail perhaps the best studied WIMP dark-matter candidate: the lightest neutralino of supersymmetry. We then focus on a study concerning gamma-ray photons resulting from WIMP annihilation in a particular class of astrophysical sources — the dense dark-matter microhalos that are thought to compose Galactic substructure, as predicted by N-body simulations. In particular, we present a calculation of the gamma-ray-flux probability distribution function (PDF) for microhalos, as might be observed by the Fermi Gamma-ray Space Telescope [29].

Material in this chapter was adapted from “The gamma-ray-flux PDF from Galactic halo substructure”, by Samuel K. Lee, Shin’ichiro Ando, and Marc Kamionkowski [30]. The basic result of this work can be easily summarized: If dark matter was uniformly distributed in our Galactic halo, then the variation in the number of diffuse-background gamma-ray photons from one Fermi sky pixel to another would arise only from Poisson fluctuations, giving rise to a Poissonian flux PDF. However, if dark matter is indeed clumped into substructure, there will be additional flux variations arising from the discrete nature of the halos, giving a PDF with a power-law tail at high fluxes. This one-point statistic may allow the gamma-ray signal arising from annihilation in microhalos — or other unresolved point-source populations — to be distinguished from the diffuse gamma-ray background.

The idea of exploring the statistical signatures of WIMP annihilation in Galactic substructure to which Fermi might be sensitive, focusing first on the one-point flux PDF for a simple halo-substructure model and the case of monoenergetic annihilation to gamma-ray lines, was proposed by Kamionkowski. After investigating similar and analogous calculations in the literature, I suggested the application of the  $P(D)$  formalism as a means to this end, and worked out the calculation of the PDF, guided by discussions with my coauthors. My coauthors also made some edits to the manuscript. Following the remarks of an anonymous referee, I significantly expanded the work to consider a more complex substructure model, as well as the specific case of neutralino annihilation (which leads to a continuum, rather than monoenergetic, annihilation spectrum).

Also of note is the work “Can proper motions of dark-matter subhalos be detected?”, by Shin’ichiro Ando, Marc Kamionkowski, Samuel K. Lee, and Savvas M. Koushiappas [31], which is not presented in this thesis but was nevertheless completed concurrently with the study of the flux-PDF. In this paper (authored by Ando), we reexamine the idea, originally proposed by Koushiappas in Ref. [32], that microhalos might present as gamma-ray sources exhibiting proper motion. We point out that existing limits on the integrated gamma-ray intensity from the Galactic center severely constrain this possibility. The main argument is that only very nearby and luminous microhalos would be observed as point sources with proper motions, given the point-source sensitivity and angular resolution of Fermi, thus requiring that either the microhalo number density or the microhalo luminosity must be large. Hence, the integrated intensity of such a population of sources would exceed the

aforementioned limits from the Galactic center.

Chapter 3 turns to direct detection, focusing on that of WIMP dark matter. A short primer on the physics of direct detection is given. We then focus on a study of *directional* detection, as may be carried out by experiments sensitive to not only the *energy* of nuclear recoils induced by collisions with WIMPs incoming from the Galactic halo, but also their *direction*. Since the motion of our Sun-Earth system through the galaxy causes a peak in the incoming dark-matter flux in the direction of motion, this directional information may be crucial in distinguishing dark-matter recoil events from background events of terrestrial origin (which should be isotropic).

The directional-detection study presented in Chapter 3 was adapted from “Probing the local velocity distribution of WIMP dark matter with directional detectors”, by Samuel K. Lee and Annika H. G. Peter [33]. In this paper, we use Bayesian likelihood analyses of simulated data to explore the statistical power of directional-detection experiments. Besides allowing for simple background discrimination, these experiments may additionally reveal interesting structures in the local dark-matter velocity distribution, such as those arising from the dark-matter disks, tidal streams, and debris flows predicted by N-body simulations. As such, these directional detectors — essentially, dark-matter telescopes — may allow for the carrying out of “WIMP astronomy”, and may reveal insights about structure formation on galactic scales via observations of the local dark-matter sky. The result of the paper shows that dark-matter velocity structures present at the level indicated by simulations may indeed be detectable with exposures of 30 kg-yr, given the specifications of upcoming directional-detection experiments.

The idea of using Bayesian methods to study the local dark-matter velocity distribution was suggested to me by Peter. Using previous results from the literature, I constructed the necessary theoretical formalism and wrote computer codes to perform the likelihood analyses on simulated recoil events, which were generated for various velocity-distribution models. Peter provided guidance and suggestions, and also assisted in the editing of the manuscript.

Chapter 4 examines the collider production of dark matter. Although collider searches for WIMPs are underway, this thesis shall focus on the production of *gravitinos*, another dark-matter candidate. Light gravitinos arise naturally in theories of supergravity with gauge-mediated supersymmetry breaking (GMSB). Although gravitinos communicate with standard-model particles via interactions that are fundamentally of gravitational strength (i.e., interactions suppressed by the Planck mass), *light* gravitinos have interactions that are enhanced by a factor inversely proportional to the gravitino mass. These “stronger-than-gravitational” interactions thus allow for the intriguing possibility of observable light-gravitino phenomenology. These aspects of light gravitinos will be demonstrated in a heuristic and pedagogical discussion.

We then present a study of light-gravitino collider signals and their ramifications for early-Universe cosmology. This study was originally published as “Light gravitinos at colliders and implications for cosmology”, by Jonathan L. Feng, Marc Kamionkowski, and Samuel K. Lee [34]. In this paper, we simulate the rate of various light-gravitino collider signals at the Tevatron and the Large Hadron Collider (LHC), including relatively spectacular signals such as prompt di-photons, delayed photons, kinked charged tracks, and metastable charged tracks. By examining the rates of these various signals as a function of the gravitino mass, we demonstrate an intriguing coincidence with current astrophysical constraints on the gravitino mass and the possible gravitino-dark-matter scenarios allowed by these constraints. In particular, the observation of a large number of prompt signals would indicate the gravitino is extremely light, implying that it could compose a warm fraction of the dark matter and still be consistent with both small-scale structure constraints (from the CMB anisotropies and observations of the Lyman- $\alpha$  forest) and the canonical cosmological thermal history. However, nonprompt or metastable signals would indicate that the gravitino has an intermediate or a relatively heavy mass, which would require a noncanonical thermal history in order to be consistent with astrophysical observations. Thus, we argue that the observation of gravitino collider signals might have profound implications for the physics of the early Universe.

The idea of exploring the collider phenomenology of gravitino dark matter was suggested jointly by Feng and Kamionkowski. Although I oversaw development of the manuscript, Kamionkowski first developed the argument for the thermalization of light gravitinos in Section 4.3 and Feng contributed material in Section 4.4; both also assisted in the editing of the manuscript. I was responsible for coding the collider simulations, with liberal suggestions and guidance from Feng. I also developed the central arguments pointing out the connection between collider and cosmological scenarios.

Finally, having explored examples from each of the three paths of particle-dark-matter detection methods, we close with a slight detour. Chapter 5 explores a technical curiosity that arose during the writing of the light-gravitino paper. Our paper relied on a previous calculation of the rate at which gravitinos were produced via scattering interactions in the thermal bath of particles that existed after the big bang. Upon examining these calculations, we discovered that some of the scattering rates seemed to possess infrared divergences, curiously implying unphysical *infinite* gravitino production rates!

As it turns out, these infrared divergences are not specific to gravitino production, and are in fact rather generic in processes involving charged particles at finite temperature. Chapter 5 thus presents a study of these processes, originally published as “Charged-particle decay at finite temperature”, by Andrzej Czarnecki, Marc Kamionkowski, Samuel K. Lee, and Kirill Melnikov [35]. In this paper, we demonstrate how the infrared divergences cancel, and discuss the possible implications of mass singularities that may also appear in the finite-temperature rates. Consideration of these divergences



may be important for understanding the production of charged particles in the early Universe, as well as the impact such particles may have on cosmology. For example, these finite-temperature effects may have implications for some proposed models in which charged particles decay or scatter to produce dark matter.

I originally pointed out the problem of finite-temperature infrared divergences in gravitino production to Feng and Kamionkowski during the writing of the light-gravitino paper. However, the problem remained unsolved until Czarnecki and Melnikov brought to our attention their solution to analogous infrared divergences in the process of 3-body muon decay. I then worked out the solution for a more simple process — the 2-body decay of a charged fermion — with some assistance from Melnikov. Although the original muon-decay results are briefly given, the paper mainly focuses on a pedagogical discussion of the simpler 2-body decay.

We close this introduction by noting that a relatively recent collection of reviews on a wide array of topics in particle dark matter may be found in Ref. [36], for example; we do not attempt a comprehensive survey of particle dark matter and the current status of experimental searches in this thesis. That such a survey would necessarily be quite long, and yet would quickly become outdated — due to the rapid and exciting pace of new experimental and theoretical results in recent years — attests to the breadth and profound importance of the problem of dark matter. With a large number of space-based and ground-based observatories conducting indirect dark-matter-annihilation searches, a plethora of direct-detection experiments searching for the elusive signatures of dark-matter-induced nuclear recoils, and the LHC running smoothly and at ever-increasing energies in the hope that production of dark-matter particles will be observed, that an imminent discovery of particle dark matter might be just over the horizon cannot be ignored. Nevertheless, these three paths will certainly require further exploration; whether they will converge at an understanding of the underlying particle physics and cosmology that give rise to the dark matter — or if they will lead us to theoretical landscapes richer and more complex than those previously envisioned — remains to be seen.

## Chapter 2

# Indirect detection: The gamma-ray-flux probability distribution function from Galactic halo substructure

## 2.1 Motivation: Supersymmetric neutralinos as WIMP dark matter

### 2.1.1 The WIMP miracle

Weakly interacting massive particles (WIMPs) are the most favored dark-matter candidate, as they satisfy the astrophysical and cosmological criteria laid out in Section 1 yet still offer the possibility of detectable experimental signals. In particular, the annihilation of WIMPs with weak-scale masses ( $\sim 100$  GeV) should yield energetic standard-model particles, the observation of which would constitute an indirect detection of dark matter.

Perhaps the most intriguing piece of cosmological evidence in favor of WIMP dark matter is that thermally produced WIMPs naturally have a relic abundance close to that observed for dark matter. We shall now show demonstrate this using simple arguments to calculate the WIMP relic abundance. Consider a WIMP  $\chi$  with mass  $m_\chi$ . In the early Universe, such a particle is in equilibrium at temperatures  $T \gg m_\chi$ ; equilibrium is maintained by  $\chi\bar{\chi}$  annihilation processes to standard-model particles and antiparticles — the same processes shown schematically in Figure 1.1 that allow for the possibility of indirect detection — and their inverses.

If it is assumed that the standard-model annihilation products are also in equilibrium, the evo-

---

Material in Sections 2.2–2.7 was first published in “The gamma-ray-flux PDF from Galactic halo substructure,” Samuel K. Lee, Shin’ichiro Ando, and Marc Kamionkowski, *JCAP* **0907**, 007 (2009) [30]. Reproduced here with permission, ©2009 by IOP Publishing Limited.

lution of the WIMP number density  $n_\chi$  is given by the Boltzmann equation

$$\frac{dn_\chi}{dt} + 3Hn_\chi = -\langle\sigma v\rangle [n_\chi^2 - (n_\chi^{\text{EQ}})^2], \quad (2.1)$$

where  $H$  is the Hubble expansion rate,  $\langle\sigma v\rangle$  is the thermally averaged total annihilation cross section, and  $n_\chi^{\text{EQ}}$  is the equilibrium WIMP number density. At temperatures at which  $\Gamma = n_\chi\langle\sigma v\rangle \gtrsim H$  is satisfied, the WIMP annihilation rate  $\Gamma$  is sufficiently high enough to keep the WIMPs in equilibrium; WIMP annihilation is then balanced by the rate of WIMP-creating inverse processes, driving  $n_\chi$  to  $n_\chi^{\text{EQ}}$ . However, as the Universe expands and its temperature falls, the number density of WIMPs decreases, reducing the WIMP annihilation rate until it is smaller than the Hubble expansion rate. The number-changing processes of WIMP annihilation and creation can then no longer maintain chemical equilibrium; the WIMPs chemically decouple from the thermal bath, and the WIMP number density is said to “freeze out”.

The temperature at which freeze-out occurs,  $T_f$ , is then roughly given by

$$\Gamma(T_f) = n_\chi(T_f)\langle\sigma v\rangle(T_f) \sim H(T_f). \quad (2.2)$$

We see that  $T_f$  depends on the annihilation cross section; we shall assume that the cross section is sufficiently large, so that  $T_f < m_\chi$ . That is, WIMPs freeze out when they are nonrelativistic, at a temperature where their equilibrium number density is Boltzmann suppressed and their velocity is small,

$$n_\chi^{\text{EQ}} \sim (m_\chi T_f)^{3/2} \exp^{-m_\chi/T_f} \quad (2.3)$$

$$v \sim (T_f/m_\chi)^{1/2}, \quad (2.4)$$

where we have assumed that the chemical potential of the WIMPs vanishes.

Before continuing the calculation of the relic abundance, let us first show that a simple argument confirms that nonrelativistic freeze-out is indeed realized for WIMPs. Consider a nonrelativistic WIMP-annihilation process that occurs via a weak interaction, resulting in products of energy  $E \sim m_\chi$ . The amplitude for such a process is then  $\mathcal{M} \sim \alpha m_\chi E/M_W^2 \sim \alpha$ , where  $\alpha$  is the fine-structure constant and  $M_W \sim 100$  GeV is the energy scale of the weak interaction. We further assume that the WIMP has a weak-scale mass  $m_\chi \sim M_W$ . This amplitude then gives a weak-scale annihilation cross section on the order of a picobarn,

$$\sigma \sim |\mathcal{M}|^2/m_\chi^2 \sim \alpha^2/m_\chi^2 \quad (2.5)$$

$$\approx 2 \text{ pb} \left( \frac{100 \text{ GeV}}{m_\chi} \right)^2. \quad (2.6)$$

Assuming that freeze-out occurs during the radiation-dominated era, during which

$$H \approx 1.66g_*^{1/2}T^2/M_{\text{pl}} \quad (2.7)$$

depends on the number of relativistic degrees of freedom  $g_*$  and the Planck mass  $M_{\text{pl}}$ , the condition  $\Gamma(T_f) \sim H(T_f)$  then yields

$$\frac{m_\chi}{T_f} \sim \ln \left[ \langle \sigma v \rangle (m_\chi T_f)^{3/2} \frac{M_{\text{pl}}}{T_f^2} \right] \quad (2.8)$$

$$\sim \ln \left( \alpha^2 \frac{M_{\text{pl}}}{m_\chi} \right) \sim 30, \quad (2.9)$$

so the assumption  $T_f < m_\chi$  is indeed self-consistent for WIMPs. Note that at such temperatures, the rate of inverse WIMP-creating processes is also suppressed kinematically, since colliding standard-model particles no longer have sufficient energy to create WIMPs. Thus, it is clear that processes that change the number of WIMPs indeed freeze out at  $T_f \sim m_\chi/30$ .

With the assumption of  $T_f < m_\chi$  and nonrelativistic freeze-out, the present-day WIMP number density  $n_{\chi 0}$  can then be derived. This is accomplished by numerically solving Eq. (2.1), using the nonrelativistic equilibrium number density  $n_\chi^{\text{EQ}}$  as an initial condition at  $T \sim m_\chi$  and evolving until the asymptotic value  $n_{\chi\infty}$  has been found [37]. Assuming  $s$ -wave annihilation (so that  $\langle \sigma v \rangle = \sigma_0(T/m_\chi)^n$  is temperature independent, with  $n = 0$ ), this asymptotic value can be approximated by

$$\frac{n_{\chi\infty}}{s_f} \approx \frac{H_m}{\langle \sigma v \rangle_m s_m} \left( \frac{m_\chi}{T_f} \right), \quad (2.10)$$

where

$$s_x = \frac{2\pi^2}{45} g_{*S,x} T_x^3 \quad (2.11)$$

is the entropy density at temperature  $T_x$ , the values of variables evaluated at  $T = m_\chi$  are denoted by a subscript  $m$ , and

$$g_{*S,x} = \sum_{i=\text{bosons}} g_i \left( \frac{T_i}{T_x} \right)^3 + \frac{7}{8} \sum_{i=\text{fermions}} g_i \left( \frac{T_i}{T_x} \right)^3. \quad (2.12)$$

After the WIMP number density freezes out to this asymptotic value at  $T_f$ , its further evolution is simply dictated by the expansion of the Universe. Hence, it scales as  $a^{-3} \propto s \propto g_{*S} T^3$ , where  $a$  is

the scale factor. The end result is

$$n_{\chi 0} = n_{\chi \infty} \left( \frac{s_0}{s_f} \right) \quad (2.13)$$

$$\approx 10^4 \text{ cm}^{-3} \left( \frac{g_{*,m}^{1/2}}{g_{*S,m}} \right) \left( \frac{m_\chi}{T_f} \right) \left( \frac{1}{M_{\text{pl}} m_\chi \sigma_0} \right). \quad (2.14)$$

Here, the factors of  $g_{*,m}$  and  $g_{*S,m}$  account for the annihilation of particles with mass less than  $m_\chi$  after WIMP freeze-out, which slows the decrease of  $T \propto g_{*S}^{-1/3} a^{-1}$  to be slower than  $a^{-1}$ .<sup>1</sup> Since the majority of the standard-model particles are still relativistic when WIMPs freeze out, typical values are  $g_{*,m} \sim g_{*S,m} \sim 100$ .

The WIMP relic abundance is then given by the present-day WIMP density in terms of the critical density  $\rho_{\text{cr}} = 3H^2/8\pi G \approx 10^{-5} h^2 \text{ GeV/cm}^3$ ,

$$\Omega_\chi h^2 = \frac{m_\chi n_{\chi 0}}{\rho_{\text{cr}}} \approx 0.1 \left( \frac{g_{*,m}^{1/2}/g_{*S,m}}{0.1} \right) \left( \frac{m_\chi/T_f}{30} \right) \left( \frac{\text{pb}}{\sigma_0} \right), \quad (2.15)$$

where  $h = H/(100 \text{ km/sec/Mpc}) \approx 0.7$ . This expression, despite being derived using rough arguments and approximations, is nevertheless mostly correct; a calculation done with greater care gives the more common form

$$\Omega_\chi h^2 \approx 0.1 \left( \frac{3 \times 10^{-26} \text{ cm}^3/\text{sec}}{\langle \sigma v \rangle} \right), \quad (2.16)$$

although this expression likewise assumes values for  $g_{*,m}$  and  $g_{*S,m}$  and also ignores logarithmic corrections arising from the weak dependence of  $T_f$  on  $m_\chi$ .

We see that the final WIMP relic abundance is inversely proportional to the annihilation cross section. This result is intuitively clear; the larger the annihilation cross section, the longer WIMPs remain chemically coupled to the thermal bath and track the equilibrium number density, which is falling as the Universe expands and cools. Most interestingly, a weak-scale annihilation cross section naturally gives a thermally produced WIMP relic abundance that matches the observed dark-matter relic abundance! This striking coincidence is known as the ‘‘WIMP miracle’’, and is the reason that WIMPs are attractive from a cosmological standpoint and are the best studied dark-matter candidates.

### 2.1.2 Supersymmetry and neutralino dark matter

In turn, the lightest supersymmetric neutralino is the best studied WIMP, primarily because supersymmetry not only yields the neutralino as a viable dark-matter candidate but is also independently attractive from a particle-physics standpoint. Since being proposed in the 1970s, supersymmet-

<sup>1</sup>This is analogous to the effect of electron-positron annihilation on the ratio of the CMB-photon and neutrino temperatures; the latter have a lower temperature, since they decouple before this annihilation occurs.

ric theories have been thoroughly explored in the literature; we shall review only those aspects of supersymmetry necessary to introduce the neutralino as a well-motivated dark-matter candidate. <sup>2</sup>

Supersymmetry first arose as a result of investigations of the symmetries of the scattering matrix of quantum field theory. It was shown that the group of the usual symmetries of a nontrivial scattering matrix — which can be expressed as a direct product of the Poincarè group (which gives the symmetries of Minkowski spacetime) and a group of internal symmetries — can be extended by the introduction of anticommuting spinor generators  $Q^A$ ,  $A = 1, \dots, N$ .<sup>3</sup> These generators obey the supersymmetry algebra

$$\{Q^A, Q_B^\dagger\} = -2\sigma_\mu P^\mu \delta_B^A \quad (2.17)$$

$$\{Q^A, Q^B\} = \{Q_A^\dagger, Q_B^\dagger\} = 0 \quad (2.18)$$

$$[Q^A, P^\mu] = [Q_A^\dagger, P^\mu] = 0, \quad (2.19)$$

where  $\sigma^\mu$  are the Pauli matrices (with  $\sigma^0 = I$ ),  $P^\mu$  is the 4-momentum, and the spinor indices on  $Q$  and  $Q^\dagger$  have been suppressed. Just as the generators of the Poincarè and internal groups transform states in spacetime (by Lorentz boosts, translations, or rotations) or internal spaces, respectively, these spinor generators  $Q$  effect the aforementioned transformations between bosonic states  $|B\rangle$  and fermionic states  $|F\rangle$ . Hence, in the same sense that the generators of the internal isospin symmetry “rotate” neutrons and protons into each other, the generators of supersymmetry convert between bosons and fermions; schematically,

$$Q|B\rangle = |F\rangle \quad (2.20)$$

$$Q|F\rangle = |B\rangle. \quad (2.21)$$

The simplest  $N = 1$  supersymmetry is of primary interest, since it admits the existence of chiral fermions. In such a theory, bosonic and fermionic are paired in *supermultiplets*, which are irreducible representations of the supersymmetry algebra. We can further discern between *chiral* supermultiplets, which consist of a spin-1/2 Weyl fermion and a spin-0 complex scalar *sfermion*, and *gauge* or *vector* supermultiplets, which consist of a real spin-1 gauge field and a spin-1/2 Weyl-fermion *gaugino*.<sup>4</sup>

Hence, supersymmetry is a symmetry that relates elementary particles that differ by a half unit of

---

<sup>2</sup>Additional details on supersymmetry may be found in Refs. [38–40], from which some of the material presented here was adapted. The standard review of supersymmetric dark matter is given in Ref. [41]; more recent reviews are given by, e.g., Refs. [42, 43].

<sup>3</sup>This is the Haag-Lopuszanski-Sohnius extension of the Coleman-Mandula no-go theorem.

<sup>4</sup>Specifically, this is true in the two-component spinor representation. Note that an “s-” prefix is added to the name of a fermion to denote the fermion’s scalar superpartner (e.g., squark, slepton, stop, sbottom, selectron, sneutrino, etc.), while an “-ino” suffix replaces the “-on” suffix in the name of a boson to denote the boson’s fermionic superpartner, with some straightforward exceptions (e.g., photino, gravitino, zino, wino, higgsino, etc.).

Name	SM	SUSY
Chiral supermultiplets	spin 1/2	spin 0
quarks & squarks (3 generations)	$(u_L, d_L)$ $u_R, d_R$	$(\tilde{u}_L, \tilde{d}_L)$ $\tilde{u}_R, \tilde{d}_R$
leptons & sleptons (3 generations)	$(e_L, \nu_L)$ $e_R$	$(\tilde{e}_L, \tilde{\nu}_L)$ $\tilde{e}_R$
Higgs & higgsinos	$(H_u^+, H_u^0)$ $(H_d^0, H_d^-)$	$(\tilde{H}_u^+, \tilde{H}_u^0)$ $(\tilde{H}_d^0, \tilde{H}_d^-)$
Gauge supermultiplets	spin 1	spin 1/2
gluons & gluinos	$g$	$\tilde{g}$
W bosons & winos	$W^\pm, W^0$	$\tilde{W}^\pm, \tilde{W}^0$
B boson & bino	$B^0$	$\tilde{B}^0$

Table 2.1: Particle content of the minimal supersymmetric standard model (MSSM). Standard-model (SM) particles and their superpartners predicted by supersymmetry (SUSY) are listed. The neutral higgsinos, wino, and bino mix to give the neutralinos  $\chi_i^0$ ,  $i = 1, \dots, 4$ , while the charged higgsinos and winos mix to give the charginos  $\chi_i^\pm$ ,  $i = 1, 2$ .

spin, which are termed *superpartners*. If supersymmetry is unbroken in a theory, this means that the theory is invariant under transformations that convert between superpartner bosons and fermions; these paired bosons and fermions must additionally have identical quantum numbers. Since the known particles of the standard model cannot be paired as such, the existence of new particles is required if supersymmetry is to be realized. In the minimal supersymmetric standard model (MSSM), the addition of new particles is accomplished by pairing new bosons with the standard-model matter fields in chiral supermultiplets and new fermions with the standard-model gauge fields in gauge supermultiplets; a pair of chiral Higgs supermultiplets is also required if triangle gauge anomalies are to be avoided. The field content of the MSSM is shown in Table 2.1.

Unbroken supersymmetry further requires that the masses of these bosonic and fermionic superpartners are identical. Since particles with such masses are not observed, supersymmetry must be a broken symmetry at the known energy scales — that is, the masses of these new particles must be at scales yet unexplored by colliders. Interestingly enough, if supersymmetric particles have weak-scale ( $\sim$ TeV) masses, several outstanding problems of the standard model may be resolved.

The first problem solved by weak-scale supersymmetry is the so-called “hierarchy problem” involving stabilization of the Higgs potential and the energy scale of electroweak symmetry breaking, which we now describe. The standard model may not be applicable at energies above the  $\sim$ TeV scales explored thus far; it will certainly require modifications near the  $\sim 10^{19}$ -GeV Planck scale of quantum gravity, but new physics may require extensions of the standard model even at some intermediate energy scale  $\Lambda$ . It is then reasonable to impose  $\Lambda$  as an ultraviolet cutoff in momentum

integrals, interpreting it as the scale at which the standard model ceases to be valid.

This cutoff then regularizes divergent loop integrals, such as those that enter in radiative corrections to particle masses. Insensitivity to this cutoff is then a desirable feature in the theory. Interestingly enough, in a theory without elementary scalars, the masses of fermions are protected against large corrections — linear or quadratic in  $\Lambda$  — by chiral symmetry. Only at most logarithmic corrections appear; for example, quantum corrections to fermion masses  $m$  are of the form  $\delta m \propto m \ln(\Lambda/m)$ , so no fine-tuning between the bare fermion masses appearing in the Lagrangian and the physical fermion masses is needed — even if the cutoff scale  $\Lambda$  is large. Similarly, the vanishing mass of the photon is exactly protected by gauge invariance.

However, the mass of the Higgs boson is not afforded any such protection, a feature that is essentially due to the scalar nature of the Higgs. In the standard model, the classical potential of the complex scalar Higgs  $SU(2)_L$  doublet  $\phi = (\phi^+ \ \phi^0)$  is given by

$$V = -\mu^2 |\phi|^2 + \lambda |\phi|^4, \quad (2.22)$$

where vacuum stability requires  $\lambda > 0$ . By further requiring  $\mu^2 > 0$ , the minimum of the potential and the corresponding vacuum state are shifted away from  $\phi = 0$ . Electroweak symmetry breaking is thus achieved via the Higgs mechanism, and the Higgs field is given a vacuum expectation value (VEV)  $\langle \phi \rangle = (0 \ v/\sqrt{2})$ , where  $v = \sqrt{\mu^2/\lambda}$ . Essentially, the  $SU(2)_L$  symmetry between the two components of the doublet, which dictates that  $SU(2)$  “rotations” in the  $\phi^+ - \phi^0$  “space” leave the theory invariant, is now broken by the VEV, which picks out a unique direction in this space. Thus,  $SU(2)_L \times U(1)_Y$  is broken to  $U(1)_{EM}$ .

The tree-level mass of the physical Higgs boson (defined as the real scalar field  $H$ , such that  $\phi^0 = (v + H)/\sqrt{2}$ , with mass term  $-m_H^2 H^2/2$  appearing in the potential  $V$ ) is then

$$m_H^2 = 2v^2\lambda = 2\mu^2, \quad (2.23)$$

and is not fixed by the theory or observations. In contrast, the physical masses of the electroweak gauge bosons that couple to the Higgs *are* fixed by the theory and observations. For example, the tree-level masses of the  $W$  and  $Z$  bosons are given by  $m_W = vg_2/2 \approx 80.4$  GeV and  $m_Z = v\sqrt{g_1^2 + g_2^2}/2 \approx 91.2$  GeV, where  $g_1$  and  $g_2$  are the  $U(1)_Y$  and  $SU(2)_L$  gauge couplings. From the measurement of particle masses it is therefore experimentally known that  $v \approx (\sqrt{2}G_F)^{-1/2} \approx 246$  GeV, where  $G_F$  is the Fermi constant. A weak-scale Higgs mass is then expected at tree level if  $\lambda \sim 1$ .

The discussion thus far has been at tree level. Let us now consider quantum corrections, starting with those arising from the coupling of the Higgs to fermions. A fermion  $f$  coupling to the Higgs



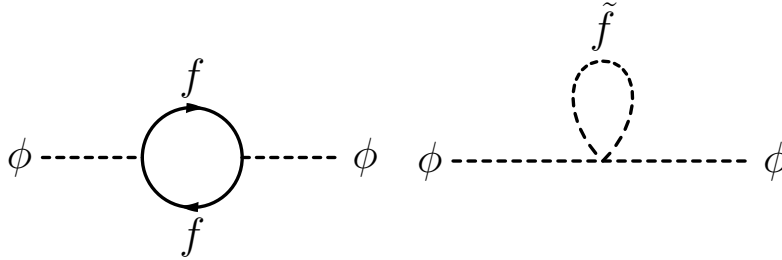


Figure 2.1: Feynman diagrams showing the contributions to the Higgs self-energy from fermion (left) and scalar (right) couplings. Separately, these diagrams yield quantum corrections to the Higgs–mass-squared parameter  $\mu^2$  that depend on the cutoff scale as  $\Lambda^2$ . However, the quadratic divergences cancel in the sum of the diagrams if the fermion and scalar have related couplings and identical masses, yielding only a logarithmic correction  $\ln \Lambda$ . This suggests that paired fermions and scalars may stabilize the weak scale, solving the hierarchy problem.

via the Yukawa-interaction term  $-\lambda_f \phi \bar{f} f$  has a tree-level mass

$$m_f = v \lambda_f / \sqrt{2}, \quad (2.24)$$

since fermion mass terms are of the form  $-m_f \bar{f} f$ .<sup>5</sup> However, this interaction also gives rise to a leading-order quantum 1-loop correction to the  $\mu^2$  parameter via the first diagram shown in Figure 2.1,

$$\delta\mu^2 = -\frac{|\lambda_f|^2}{16\pi^2} \Lambda^2, \quad (2.25)$$

which is *quadratically* sensitive to the cutoff scale  $\Lambda$ . Since the top quark is the heaviest fermion, with a mass  $m_t \approx 173 \text{ GeV} \approx v/\sqrt{2}$ , its Yukawa coupling  $\lambda_t \approx 1$  then provides the largest correction. Now, if the cutoff scale is indeed close to the Planck scale, such that  $\Lambda \sim 10^{19} \text{ GeV}$ , then this implies that the quantum corrections  $\delta\mu^2$  to the Higgs-mass-squared parameter  $\mu^2$  are radically larger than the classical weak-scale value. Put another way, if there is no new physics between the weak scale and the Planck scale, maintaining the weak scales of the *physical*  $\mu^2$  parameter and VEV  $v$  implied by the weak–gauge-boson masses would require a cancellation between the *bare*  $\mu^2$  parameter and these quantum fermion-loop corrections  $\delta\mu^2$  of approximately 1 in  $10^{34}$ ! Similar quadratic corrections also arise from the coupling of the Higgs to gauge bosons and self-coupling of the Higgs. Since the masses of the other particles in the standard model also depend on the VEV  $v$ , they are likewise sensitive to these corrections.

Clearly it is desirable to avoid such drastic fine-tuning. As such, several constructs have been proposed to solve the hierarchy problem — supersymmetry among them. To see how supersymmetry resolves the issue of sensitivity to quadratic corrections, consider now the 1-loop correction to the

<sup>5</sup>We schematically write the interaction as  $-\lambda_f \phi \bar{f} f$ , although more rigorously one should perhaps write  $-\lambda_f \phi \bar{L} f_R + \text{h.c.}$ , where  $L$  is an  $SU(2)_L$  doublet containing  $f_L$  and  $f_R$  is a singlet; here,  $f$  is a Dirac fermion and  $f_L$  and  $f_R$  are Weyl fermions. In the interest of conciseness, the general level of rigor in our arguments here will be only that necessary to motivate the basic ideas of supersymmetry. We shall also not take too much care with factors of order unity, for example.

$\mu^2$  parameter arising from the  $-\lambda_{\tilde{f}}|\phi|^2|\tilde{f}|^2$  coupling of the Higgs to a complex *scalar* particle  $\tilde{f}$ , as shown by the second diagram in Figure 2.1. Such a complex scalar would have a mass term  $-m_{\tilde{f}}^2|\tilde{f}|^2$ , and hence a corresponding mass

$$m_{\tilde{f}} = v\sqrt{\lambda_{\tilde{f}}/2}. \quad (2.26)$$

The sum of the leading-order corrections from both the fermion and scalar couplings is then

$$\delta\mu^2 = \frac{1}{16\pi^2} \left( \lambda_{\tilde{f}} - |\lambda_f|^2 \right) \Lambda^2. \quad (2.27)$$

The relative minus sign between the fermion and scalar contributions arises because of the anticommutation of the fermions in the fermion loop. We then see that the quadratic correction arising from the coupling of the Higgs to a fermion  $f$  can be canceled by the contribution from a scalar  $\tilde{f}$  if the couplings obey

$$\lambda_{\tilde{f}} = |\lambda_f|^2. \quad (2.28)$$

Furthermore, this condition also implies that the masses of the fermion and the scalar should be identical,

$$m_{\tilde{f}} = m_f. \quad (2.29)$$

Our result is then that the introduction of new complex scalars with related couplings and masses identical to those of the standard-model fermions can stabilize the weak scale associated with the Higgs mechanism against quadratic divergences. It can likewise be shown that quadratic corrections arising from the coupling of the Higgs with gauge bosons can be canceled by the introduction of new fermions with related couplings and identical masses. The introduction of superpartners with identical masses in unbroken supersymmetry then realizes this scenario, removing the need for fine-tuning.

Unfortunately, unbroken supersymmetry is not realized in nature. However, recall that it was advertised that *weak-scale* broken supersymmetry — in which the masses of the superpartners are not identical to those of the standard-model particles, but are instead at the weak scale — can still solve the problems of the standard model. In particular, if supersymmetry is broken *softly* by adding supersymmetry-violating mass terms and couplings with positive mass dimension to the Lagrangian, then dimensional arguments show that the additional leading-order quantum corrections to  $\mu^2$  will be of the form

$$\delta\mu^2 \approx m_{\text{soft}}^2 \left[ \frac{g}{16\pi^2} \ln \left( \frac{\Lambda}{m_{\text{soft}}} \right) \right], \quad (2.30)$$

where  $g$  is representative of dimensionless couplings of order unity. Hence, fine-tuning can still be avoided if the mass scale  $m_{\text{soft}}$  of these terms is not too large. In particular, weak-scale values of  $m_{\text{soft}} \sim \text{TeV}$  still avoid fine-tuning even if  $\Lambda \sim M_{\text{pl}}$ . Furthermore, although the relation Eq. (2.28)

between the couplings must still be satisfied to avoid quadratic divergences, soft supersymmetry breaking yields  $m_{\tilde{f}} \neq m_f$ ; the splitting between the standard-model and superpartner masses induced by the soft breaking terms is then roughly  $m_{\text{soft}}$ .

Thus, the key result of our arguments here is that weak-scale broken supersymmetry, which predicts the existence of new particles with weak-scale masses, admits a solution to the hierarchy problem. That weak-scale supersymmetry solves this issue in the standard model is perhaps its greatest strength. However, another attractive feature of supersymmetry is that the inclusion of superpartners in the renormalization-group equations for the evolution of gauge couplings yields unification at high energies, which is not realized if only standard-model particles are accounted for. Furthermore, supersymmetry favors a relatively light Higgs boson (in simple models, the lightest supersymmetric Higgs should be less massive than  $\sim 140$  GeV), which is also preferred by electroweak precision data. Moreover, another fascinating quality of supersymmetry is that theories that are locally supersymmetric necessarily incorporate general relativity; gravity arises classically in theories with local supersymmetry (albeit in a non-renormalizable, effective manner).<sup>6</sup> Such *supergravity* theories hint at the unification of general relativity and quantum field theories, and are generically components of string theories.<sup>7</sup>

All of these features already indicate that weak-scale supersymmetry is extremely well motivated. However, as previously indicated, the most attractive feature of weak-scale supersymmetry from the viewpoint of cosmology is that it predicts the existence of WIMPs, which we have already shown to be natural dark-matter candidates. Be that as it may, there are a few remaining issues to consider before we can have confidence in the ability of supersymmetric WIMPs to play the role of dark matter. The foremost of these is that supersymmetric theories do not generically yield WIMPs that are *stable*.<sup>8</sup> Requiring invariance under supersymmetry restricts the form of terms in the Lagrangian, but nevertheless generally allows for renormalizable interactions that violate baryon and lepton number. Baryon-number and lepton-number processes that are strongly constrained by experiment, e.g., proton decay, would then proceed via these interactions, mediated by superpartners. Such a situation is undesirable, and is typically avoided by further imposing a discrete symmetry called *R-parity*. This symmetry demands the conservation of the quantum number  $R_p \equiv (-1)^{3B+L+2s}$ ,

---

<sup>6</sup>This results because the generators  $Q$  of the supersymmetry transformations are intimately connected to the generators  $P^\mu$  of spacetime translations, as can be seen from the supersymmetry algebra given in Eq. (2.17).

<sup>7</sup>We shall further discuss supergravity in Chapter 4, in which we shall be concerned with the viability of the gravitino — the existence of which is predicted by supergravity theories — as an interesting dark-matter candidate.

<sup>8</sup>Another issue is that the correct dark-matter relic abundance must also be obtained. Although we shall not elaborate this point in detail, we mention that supersymmetric WIMPs are generally overproduced — indeed, detailed calculations show that the predicted supersymmetric-WIMP relic abundances may differ from the observed dark-matter abundance by several orders of magnitude, making the WIMP miracle somewhat less miraculous. Mechanisms that effectively increase the rate of WIMP annihilation, such as coannihilation or resonances, are then necessary. This requirement constrains the regions of supersymmetry parameter space that yield viable WIMP dark matter. However, the dimensionality of this parameter space is quite large — even in the case of the MSSM, where there are 120 free parameters (the majority of which specify the details of soft supersymmetry breaking). In practice, this dimensionality is typically dramatically reduced by making further simplifying assumptions about the parameters. Nevertheless, enough freedom exists to allow regions of parameter space where the correct relic abundance is produced.

where  $B$  is baryon number,  $L$  is lepton number, and  $s$  is spin. All standard-model particles therefore have  $R_p = 1$ , while their superpartners have  $R_p = -1$  (since their spins  $s$  differ by  $1/2$ ).  $R$ -parity conservation then implies that the lightest supersymmetric particle (LSP) is stable against decay to solely standard-model particles (although annihilation of two LSPs to standard-model particles is still allowed).

Depending on the supersymmetric-particle mass spectrum, the LSP may be an electrically neutral WIMP, and hence may be a good dark-matter candidate. WIMPs predicted by supersymmetry include the sneutrinos  $\tilde{\nu}$  (the superpartners of the neutrinos) and the neutralinos  $\chi^0$  (linear combinations of the neutral gauginos  $\tilde{H}_u^0$ ,  $\tilde{H}_d^0$ ,  $\tilde{W}^0$ , and  $\tilde{B}^0$ , which mix to give a total of 4 neutralinos). As sneutrinos should have relatively large scattering cross sections and are thus strongly disfavored by direct-detection experiments, we have finally reached the conclusion advertised at the outset: the lightest neutralino is the most promising supersymmetric WIMP dark-matter candidate, and is well motivated in the context of weak-scale supersymmetry.

As noted previously, the annihilation of WIMPs yields energetic standard-model products, giving rise to the possibility of indirect detection. For example, neutralinos may self-annihilate<sup>9</sup> via weak interactions to produce quarks, leptons, and gauge bosons, which may themselves then further decay. In general, the end result of WIMP annihilation is then the production of cosmic rays and gamma-rays. Gamma-rays are especially of interest — since they are not deflected by magnetic fields, unlike charged cosmic rays, and point back to the astrophysical sources of WIMP annihilation — and may be observed by the Fermi Gamma-ray Space Telescope.

We now turn to the study of a particular topic in indirect detection: the one-point statistics of the gamma-ray flux from WIMP annihilation in Galactic substructure, which may be observed by Fermi. We note that although the aim of the pedagogical introduction here has been to motivate *neutralinos* as WIMP dark-matter candidates that may yield indirect detection signals — and indeed, one of the models in the study focuses on a scenario with neutralino dark matter — the basic results presented below are applicable to WIMPs in general.

## 2.2 Introduction

It has long been a goal of astrophysics and cosmology to determine the distribution and nature of the dark matter that populates our Galactic halo. Only more recently have we begun to focus on the possibility to detect substructures in the Galactic halo [44–55]. In hierarchical structure formation, small gravitationally bound dark-matter systems form first and then merge to form progressively more massive systems. In each stage, some of the earlier generations of structure may

---

<sup>9</sup>Since the neutralino is a Majorana fermion, it is its own antiparticle.

remain intact after merging, and so the Milky Way halo may contain substructures over a wide array of masses. Scaling arguments suggest that substructures may continue all the way down to the smallest mass scales at which there is primordial power [56–62], although the precise details may be uncertain [63–66]. If WIMPs [10, 41, 67] make up the dark matter, the cutoff mass should be in the range  $10^{-4}$ – $10^3 M_{\oplus}$  [68–70], and if axions [71–74] make up the dark matter, it may be as small as  $10^{-12} M_{\oplus}$  [75]. These mass ranges are determined by the temperature at which the dark-matter particle kinetically decouples from the thermal bath; see Appendix A for more details.

If WIMPs make up the dark matter, there may be several avenues toward detecting them. With the launch of the Fermi Gamma-ray Space Telescope (formerly GLAST) [29], however, there is now particular attention being paid to detection of energetic gamma-rays from dark-matter annihilation in the Galactic halo (see, e.g., Ref. [76] and references therein). While the diffuse flux from such annihilation has long been considered [77–95], the possibility to detect substructure, through angular variations in the background, is more recent [96–101]. It is possible that individual substructures may be resolved [102]. Proper motions of the smallest microhalos have also been considered [31, 103].

In this work, we propose the one-point gamma-ray-flux probability distribution function (PDF) as a probe of halo substructure. If dark matter is smoothly distributed, then the variation in the number of diffuse-background photons from one pixel to another should arise only from Poisson fluctuations. If, however, there is substructure, there will be additional flux variations from pixel to pixel. This may provide another route — an alternative to the angular two-point correlation function [96, 97, 100, 101] — to detect substructure statistically, especially for the very smallest microhalo mass scales.<sup>10</sup> It may also allow measurement of the substructure mass function, under certain model assumptions outlined below.

We illustrate with a phenomenological model for Galactic substructure in which a fraction  $f$  of the halo is made of dark-matter microhalos with a power-law mass function (with a lower mass cutoff  $M_{\min}$ ) and a constant mass-to-gamma-ray-luminosity ratio  $\Upsilon = M_{\min}/L_{\min}$ . The next section introduces this model and discusses the constraints from the Energetic Gamma-Ray Experiment Telescope (EGRET) [105] to the parameter space. In Section 2.4, we calculate the flux PDF for this model and discuss the translation to a discrete distribution of counts in each Fermi pixel. We provide in Section 2.5 numerical results for the PDF for an illustrative model. Section 2.6 determines the regions of the parameter space in which the PDF of substructure can be distinguished from that of a smoothly distributed background. In Section 2.7 we summarize and comment on additional steps that must be taken to implement this probe.

---

<sup>10</sup>It has been similarly suggested [104] that background fluctuations may be used to learn about the traditional astrophysical sources contributing to the diffuse background.

## 2.3 Substructure/annihilation models and EGRET constraints

### 2.3.1 Halo model and microhalo mass function

We assume that a fraction  $f$  of the dark matter in the Galactic halo is composed of objects with a power-law mass function  $dn_h/dM_h \propto M_h^{-\alpha}$ , independent of Galactocentric radius  $r$ . We shall take  $\alpha = 2$  in this work when evaluating numerical results, but our approach will hold in general. The mass function obeys the relation

$$f\rho(r) = \int_{M_{\min}}^{M_{\max}} dM_h M_h \frac{dn_h}{dM_h}(r, M_h) \equiv \langle M_h \rangle n_h(r), \quad (2.31)$$

where  $\rho(r)$  is the density profile of the Milky Way halo,  $M_{\min}$  and  $M_{\max}$  are the masses of the smallest and largest subhalos, and in the last equality we define the mean mass  $\langle M_h \rangle$  as well as spatial number density  $n_h(r)$  of subhalos. From Eq. (2.31) and the assumed shape of the mass function, we obtain

$$\frac{dn_h}{dM_h}(r, M_h) = \frac{f\rho(r)}{\ln(M_{\max}/M_{\min})} M_h^{-2}, \quad (2.32)$$

$$n_h(r) = \frac{f\rho(r)}{M_{\min} \ln(M_{\max}/M_{\min})}, \quad (2.33)$$

$$\langle M_h \rangle = M_{\min} \ln(M_{\max}/M_{\min}), \quad (2.34)$$

where in Eq. (2.33), we assumed  $M_{\min} \ll M_{\max}$ . We use the NFW [106] profile,

$$\rho(r) = \frac{\rho_s}{(r/r_s)(1+r/r_s)^2}, \quad (2.35)$$

where  $\rho_s = 5.4 \times 10^{-3} M_{\odot} \text{ pc}^{-3}$  is the characteristic density, and  $r_s = 21.7 \text{ kpc}$  is the scale radius. The density is set to zero beyond a cutoff radius  $r_c = 10 r_s$ , which is approximately the virial radius (i.e., the concentration parameter is  $c \equiv r_{\text{vir}}/r_s \approx 10$ ). This normalizes the virial mass of the Milky Way halo to be  $10^{12} M_{\odot}$ , and gives  $\rho_0 = 7 \times 10^{-3} M_{\odot} \text{ pc}^{-3}$  as the local density at the solar radius ( $r_0 = 8.5 \text{ kpc}$ ).

Following other studies [107], we normalize the mass function by using the results of simulations [108] to fix the fraction of mass contained in high-mass microhalos. Specifically, we choose  $f$  such that 10% of the total mass of the halo is contained in microhalos of mass  $10^7$ – $10^{10} M_{\odot}$ . We then extrapolate the power-law mass function found by the simulations down to a cutoff mass  $M_{\min}$  below the simulation resolution; taking  $M_{\max} = 10^{10} M_{\odot}$ ,  $f$  then becomes a function of  $M_{\min}$ :

$$f(M_{\min}) = 0.10 \log(M_{\max}/M_{\min}) / \log(M_{\max}/10^7 M_{\odot}). \quad (2.36)$$

We shall suppress the argument  $M_{\min}$  when referring to  $f$  below.

For a halo model with  $M_{\min} = M_{\oplus}$ , we find that approximately 52% of the total halo mass is contained in roughly  $4.8 \times 10^{16}$  microhalos in the specified mass range. The number density of microhalos in the solar neighborhood is about  $34 \text{ pc}^{-3}$ . In this work, we will examine a class of halo models in which  $M_{\min}$  is a free parameter, and falls in the range  $10^{-4} - 10^3 M_{\oplus}$  predicted by WIMP kinetic decoupling studies.

### 2.3.2 Microhalo annihilation models

Let us assume that the microhalos have NFW density profiles. The integrated number luminosity  $L_h$  from WIMP annihilation in a microhalo with NFW profile parameters  $r_s$ ,  $c$ , and  $\rho_s$  is given by

$$L_h = \frac{N_\gamma \langle \sigma v \rangle}{m_\chi^2} \int_h dV \rho^2 \equiv a(c) K \rho_s M_h. \quad (2.37)$$

Here,  $N_\gamma$  is the integrated number of photons per annihilating particle,  $\langle \sigma v \rangle$  is the thermally averaged annihilation cross section multiplied by the relative velocity, and  $m_\chi$  is the mass of the WIMP. In the second equality,

$$a(c) \equiv \frac{1 - 1/(1+c)^3}{3[\ln(1+c) - c/(1+c)]} \quad (2.38)$$

is a numerical factor resulting from the volume integral (with a dependence on  $c$ ), and we have defined

$$K \equiv \frac{N_\gamma \langle \sigma v \rangle}{m_\chi^2} = \frac{\langle \sigma v \rangle}{m_\chi^2} \int dE \frac{dN_\gamma}{dE}. \quad (2.39)$$

Here,  $dN_\gamma/dE$  is the photon spectrum per annihilating particle. For the Galactic halo, using the NFW profile parameters defined in the previous section, we find that

$$L_{MW} = 1.2 \times 10^9 K M_\odot^2 \text{pc}^{-3} = 5.1 \times 10^{67} K \text{GeV}^2 \text{cm}^{-3}. \quad (2.40)$$

We now also assume that the integrated gamma-ray number luminosity  $L_h$  of each microhalo is proportional to its mass  $M_h$ , with constant mass-to-light ratio  $\Upsilon \equiv M_h/L_h$ . Then, the luminosity function is  $dn_h/dL_h = \Upsilon(dn_h/dM_h)$ . Note that throughout this study, the luminosity is the *number* (not energy) of photons emitted per unit time; similarly, we deal with number fluxes (fluences) and intensities.

These assumptions are consistent with the results of simulations, which indeed roughly find that  $L_h \propto M_h$ . In particular, Ref. [108] finds that

$$\frac{L_h}{L_{MW}} = \frac{\int_h \rho^2 dV_h}{\int_{MW} \rho^2 dV_{MW}} \approx 3 \times 10^{-12} \left( \frac{M_h}{M_\odot} \right) \quad (2.41)$$

in the range of their simulation, which resolves subhalos down to  $M_h \approx 4 \times 10^6 M_\odot$ . We shall assume this relation holds down to the microhalo masses under discussion in this study. Note that Eq. (2.41) essentially relates the microhalo NFW profile parameters  $r_s$ ,  $c$ , and  $\rho_s$  (which may be complicated functions of mass) to those of the Galactic halo, which were stated previously.

Combining Eqs. (2.37)–(2.41), we can now parameterize the magnitude of the annihilation signal by the parameter  $K$  (or equivalently,  $\Upsilon^{-1} = 3.6 \times 10^{-3} K M_\odot \text{ pc}^{-3} = 0.14 K \text{ GeV cm}^{-3}$  or  $L_{\text{min}} = \Upsilon^{-1} M_{\text{min}}$ , which are both proportional to  $K$ ). Given that our halo model and microhalo mass function were parameterized by  $M_{\text{min}}$ , we see that our overall model has two parameters. We now discuss a constraint on this model, arising from an intensity limit observed by EGRET.

### 2.3.3 EGRET constraints

The gamma-ray intensity  $I_h(\psi)$  (units of photons  $\text{cm}^{-2} \text{ sec}^{-1} \text{ sr}^{-1}$ ) from microhalos along a line of sight at an angular separation  $\psi$  from the Galactic center can be estimated as

$$\begin{aligned} I_h(\psi) &= \frac{1}{4\pi} \int dl \int_{L_{\text{min}}}^{L_{\text{max}}} dL_h L_h \frac{dn_h}{dL_h}(r(l, \psi), L_h) \\ &= \frac{f}{4\pi\Upsilon} \int dl \rho(r(l, \psi)), \end{aligned} \quad (2.42)$$

where  $l$  is the distance along the line of sight; i.e.,  $r^2 = r_0^2 + l^2 - 2r_0l \cos \psi$ . Compare Eq. (2.42) with the intensity  $I_G(\psi)$  from annihilation in the smooth component of the Galactic halo, which contains a fraction  $1 - f$  of the total halo mass:

$$I_G(\psi) = \frac{K(1-f)^2}{4\pi} \int dl \rho^2(r(l, \psi)). \quad (2.43)$$

Note that  $I_h$  and  $I_G$  depend differently on  $\rho(r(l, \psi))$ , causing them to vary differently with  $\psi$ .

Current upper bounds to the diffuse gamma-ray background from EGRET place an upper limit on  $I_h + I_G$ . However, because of the lower energy range of EGRET, these upper limits apply to energies in the range  $0.1 \text{ GeV} \leq E \leq 10 \text{ GeV}$ . Fermi will be more sensitive to photons with energies above 10 GeV (due to larger volume and better angular resolution at higher energies). For any given annihilation model, we are thus interested in the signal of gamma-rays above 10 GeV, but must also check to see that the constraint in the lower energy range is obeyed. We see that we must examine the energy dependence of  $I_h + I_G$ , and hence the annihilation photon spectrum  $dN_\gamma/dE$ , in order to properly apply these constraints. We shall consider the annihilation photon spectrum in two different scenarios.

In the first scenario, we assume that the WIMP is a neutralino, resulting in a photon spectrum



per annihilating particle fit by an analytic approximation given by Ref. [109]:

$$\frac{dN_\gamma}{dE} = \frac{1}{m_\chi} \frac{0.42e^{-8x}}{x^{1.5} + 0.00014}, \quad (2.44)$$

where  $x \equiv E/m_\chi$ . For the neutralino particle properties, we choose typical values used in the literature. We set  $\langle\sigma v\rangle = 3 \times 10^{-26} \text{ cm}^3 \text{ sec}^{-1}$ , which reproduces the observed dark matter density if the WIMP is a thermal relic. We also choose  $m_\chi = 85 \text{ GeV}$ ; this choice maximizes  $K$  for photon energies above 10 GeV, and hence maximizes the annihilation signal.

Along these lines, when discussing annihilation signals in this scenario, we shall redefine the parameter  $K$  in all of the relevant preceding equations by using Eq. (2.44) in Eq. (2.39), and integrating only over the energy range of interest to Fermi ( $E \geq 10 \text{ GeV}$ ). Definitions for  $\Upsilon$ ,  $L_h$ ,  $I_h$ , etc. in this energy range follow. With these values, we find the annihilation parameter for the neutralino model

$$K_N = 4.2 \times 10^{28} \text{ pc}^3 \text{ sec}^{-1} M_\odot^{-2} = 9.9 \times 10^{-31} \text{ cm}^3 \text{ sec}^{-1} \text{ GeV}^{-2}. \quad (2.45)$$

By choosing these properties, we fix the annihilation parameter  $K$ ; our model then depends only on the single parameter  $M_{\min}$ . Hereafter, we shall refer to our overall model in this scenario as the “neutralino model”.

To constrain this model, we rule out values of  $M_{\min}$  that result in intensities exceeding upper limits on the diffuse gamma-ray background found by EGRET (see Ref. [110]). That is, for a given  $M_{\min}$ , we require  $dI_h/dE + dI_G/dE \leq dI_{\text{obs}}/dE$  over the EGRET energy range. Ref. [110] found that the gamma-ray background as observed by EGRET is roughly isotropic (after masking out the Galactic plane and center), and is suitably parameterized by  $dI_{\text{obs}}/dE \approx 2.7 \times 10^{-8} (E/6.5 \text{ GeV})^{-2.1} \text{ cm}^{-2} \text{ sec}^{-1} \text{ sr}^{-1} \text{ GeV}^{-1}$ . For our choice of neutralino properties, the relative shapes of the background and annihilation spectra are such that if the constraint  $dI_h/dE + dI_G/dE \leq dI_{\text{obs}}/dE$  holds at 6.5 GeV, then it is also satisfied over the entire energy range; thus, it suffices to check the constraint at this energy. We find that the constraint is satisfied for all  $M_{\min}$  in the range  $10^{-4}$ – $10^3 M_\oplus$  predicted by kinetic decoupling studies.

We plot in Figure 2.2 the angular dependence of the microhalo intensity  $I_h$  above 10 GeV for a model in this scenario with fiducial cutoff mass  $M_{\min} = M_\oplus$ .<sup>11</sup> We also plot  $I_G$ , the angular dependence of the intensity above 10 GeV from dark-matter annihilation from a smooth component containing  $1 - f$  of the total Galactic halo mass, in order to show that it varies more rapidly with  $\psi$  than the angular dependence of the gamma-ray intensity from substructure. We also show the intensity  $dI_{\text{obs}}/dE$  of the gamma-ray background as measured by EGRET, integrated above 10 GeV.

<sup>11</sup>Note that if  $\rho(r) \propto r^{-1}$  as  $r \rightarrow 0$ , the intensity is formally infinite at  $\psi = 0$ . However, the flux from any finite-size window about the Galactic center involves an integral over the intensity, and the divergence of  $I(\psi)$  at  $\psi = 0$  is such

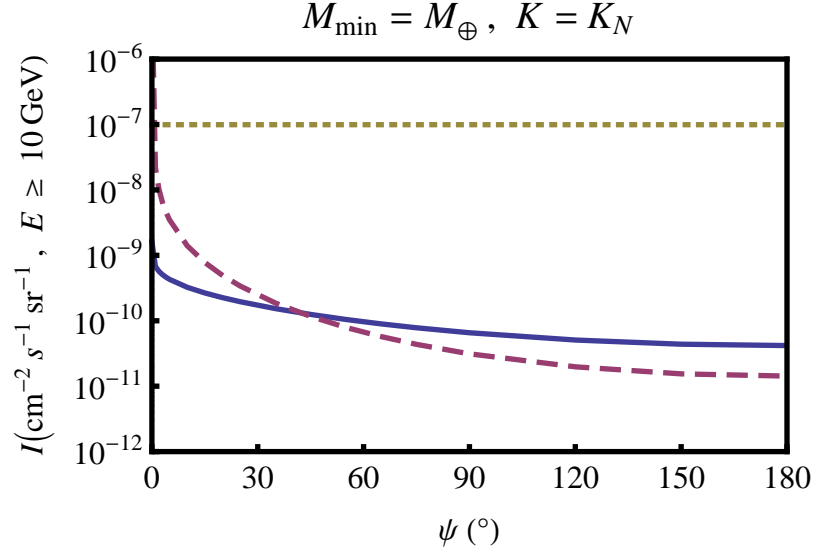


Figure 2.2: The intensity  $I_h(\psi)$  above 10 GeV from microhalos as a function of the angle  $\psi$  the line of sight makes with the Galactic center (solid) for the fiducial photon spectrum given by Eq. (2.44) (the “neutralino model”) and a cutoff mass of  $M_{\min} = M_{\oplus}$ . We also plot (dashed) the angular variation of the intensity  $I_G(\psi)$  above 10 GeV from dark-matter annihilation of a smooth component that contains  $1 - f$  of the total halo mass. Note that the variation with  $\psi$  of the gamma-ray flux from substructure is not as dramatic as that from annihilation in a smooth component. The intensity  $dI_{\text{obs}}/dE$  integrated above 10 GeV of the gamma-ray background as measured by EGRET (dotted) is also indicated.

In the second scenario, we assume that WIMPs annihilate into monoenergetic gamma-rays of energy  $E = 10$  GeV. We leave  $K_E$  as a free parameter. We approximate the upper limit from Ref. [111] to the gamma-ray line intensity, averaged over the  $10^\circ \times 10^\circ$  region around the Galactic center, by  $2 \times 10^{-6} (E/\text{GeV})^{-1/2} \text{cm}^{-2} \text{sec}^{-1} \text{sr}^{-1}$  over the energy range  $0.1 \text{GeV} \leq E \leq 10 \text{GeV}$  (see also Ref. [112]), and we then derive an upper limit,

$$f\Upsilon_E^{-1} \lesssim 10^{29} f_{I,h,l} M_{\odot}^{-1} \text{sec}^{-1} \approx 9 \times 10^{-29} f_{I,h,E} \text{GeV}^{-1} \text{sec}^{-1}. \quad (2.46)$$

Here,  $\Upsilon_E^{-1} = 0.14 K_E \text{GeV cm}^{-3}$  is the light-to-mass ratio under the assumption of monoenergetic annihilation. Also,  $f_{I,h,E} \equiv I_{h,E}/(I_{h,E} + I_{G,E} + I_{d,E}) \leq 1$  is the fraction of the total gamma-ray intensity at 10 GeV from the Galactic center arising from annihilation in microhalos, and depends on the residual intensity  $I_{d,E}$  from any astrophysical backgrounds that may not have been subtracted in Ref. [111].

In the case  $I_{d,E}$  is negligible (i.e., the line intensity limit is saturated, with the observed intensity arising entirely from annihilation in the smooth halo and substructure), then  $f_{I,h,E}$  depends only on the halo model and is a function of  $M_{\min}$ . Using Eqs. (2.42) and (2.43), calculation shows that

---

that the flux is always finite.

a good estimate is given by  $f_{I,h,E} \approx 0.086 (M_{\min}/M_{\oplus})^{-0.081}$ . For a given  $M_{\min}$ , the intensity limit then provides an upper bound on  $K_E$ ; using Eq. (2.46) gives

$$K_E \lesssim 2 \times 10^{-29} \frac{(M_{\min}/M_{\oplus})^{-0.81}}{f(M_{\min})} \text{ cm}^3 \text{ sec}^{-1} \text{ GeV}^{-2}. \quad (2.47)$$

Thus, in this scenario we shall consider models parameterized by  $M_{\min}$  and  $K_E$ , constrained by this limit. We shall refer to models in this scenario as ‘‘line models’’. Comparing Eq. (2.47) to Eq. (2.45), we note that these line models may have much larger fluxes than the neutralino model.

In Sections 2.4-2.5, we shall discuss the neutralino model, using the assumed form of the photon spectrum to predict the PDF for this fiducial model. In Section 2.6, we shall examine how observation of the PDF may place constraints on the  $K_E$ - $M_{\min}$  parameter space for line models.

## 2.4 Calculation of the PDF

The Fermi angular resolution at energies above 10 GeV is roughly  $0.1^\circ$ ; throughout this work we shall assume square pixels of solid angle  $(0.1^\circ)^2$ . This implies that the background flux will be measured in  $\sim 4 \times 10^6$  beams on the sky. One can then make a histogram of the number of counts in each beam. Our goal here is to make predictions for the shape  $P(F)$  for the distribution of these fluxes, under the assumption that these photons come from dark-matter annihilation in a clumpy Galactic halo.

Although  $P(F)$  will in general be a function of the line-of-sight direction  $\psi$ , we shall suppress this dependence in much of the presentation, reinserting it later when required for numerical results. We also refer to all probability distribution functions as  $P(x)$ ; the particular function under discussion should be clear from the argument  $x$ .

If the population of sources has a flux-density distribution  $P_1(F)$ , then the probability  $P(F)$  to see a total flux  $F$  (integrated over all sources in the beam) in a given beam is [113]

$$P(F) = \mathcal{F}^{-1} \left\{ e^{\mu(\mathcal{F}\{P_1(F)\}-1)} \right\}. \quad (2.48)$$

Here  $\mathcal{F}\{x\}$  is the Fourier transform of  $x$  and  $\mathcal{F}^{-1}$  its inverse, and the flux-density distribution  $P_1(F)$  is normalized to  $\int dF P_1(F) = 1$ . The quantity

$$\mu(\psi) = \frac{\Omega_{\text{beam}} f}{\langle M_h \rangle} \int_0^{l_c(\psi)} dl' l'^2 \rho(r(l', \psi)), \quad (2.49)$$

is the mean number of sources in each beam of solid angle  $\Omega_{\text{beam}}$  (in sr). We reproduce in the Appendix the derivation of Eq. (2.48) originally provided by Ref. [113] (see also [114–117]).

### 2.4.1 Derivation of $P_1(F)$

The first step is thus to find the flux-density distribution  $P_1(F)$  for individual sources in the beam. This depends on the luminosity function and on the spatial distribution of microhalos. The luminosity function is  $P(L_h) \propto L_h^{-\alpha}$ , where again we take  $\alpha = 2$ . The probability for an individual microhalo to be at a distance  $l$  along a line of sight  $\psi$  is  $P(l, \psi) \propto l^2 \rho(r(l, \psi))$ . We take a maximum cutoff at  $l_c(\psi)$ , corresponding to a cutoff radius  $r_c = r(l_c(\psi), \psi)$ .

We then find  $P_1(F)$  is given by

$$\begin{aligned} P_1(F, \psi) &= \int dl dL_h P(l, \psi) P(L_h) \delta\left(F - \frac{L_h}{4\pi l^2}\right) \\ &\propto \int_0^{l_c(\psi)} dl l^4 \rho(r(l, \psi)) (l^2 F)^{-\alpha} \theta(4\pi l^2 F - L_{\min}) \theta(L_{\max} - 4\pi l^2 F) \\ &\propto F^{-\alpha} \int_{l(L_{\min}, F)}^{\min[l_c(\psi), l(L_{\max}, F)]} dl l^{4-2\alpha} \rho(r(l, \psi)), \end{aligned} \quad (2.50)$$

where the step functions enforce the cutoffs in  $P(L_h)$ , and  $l(L_i, F) \equiv (L_i/4\pi F)^{1/2}$ . Note also the implicit cutoff in  $P_1(F)$  for  $F < L_{\min}/4\pi l_c^2$ . Eq. (2.50) can be evaluated numerically for a given value of the parameter  $L_{\min} = \Upsilon^{-1} M_{\min}$ . The result is presented in Figure 2.3 for the neutralino model, with the fiducial cutoff mass  $M_{\min} = M_{\oplus}$ .

Note that Eq. (2.50) yields the familiar  $P_1(F) \propto F^{-5/2}$  (conventionally written as  $N(>S) \propto S^{-3/2}$ ) for a homogeneous spatial distribution of sources with a general luminosity function, if the condition  $l_c(\psi) \geq l(L_{\max}, F)$  is satisfied over the range of  $F$  of interest. Under this condition,  $P_1(F)$  will also asymptote to  $F^{-5/2}$  at large  $F$  for a non-pathological spatial distribution. However, if  $l_c(\psi) < l(L_{\max}, F)$  for values of  $F$  within the range of interest, then there will be a break in  $P_1(F)$ ;  $P_1(F)$  will tend to  $F^{-\alpha}$  at  $F$  for which the second condition holds, and will then tend to  $F^{-5/2}$  at higher  $F$ .

For the problem under discussion, values of  $L_{\max}$  in the interesting regions of parameter space are such that  $P_1(F)$  is negligible in the  $F^{-5/2}$  regime. Thus, the essential ‘‘large- $F$ ’’ dependence of  $P_1(F)$  will be  $F^{-\alpha}$ .

### 2.4.2 Calculation of the counts distribution

The function  $P(F)$  gives the probability to observe a flux  $F$  from annihilation in substructure. Unlike the function  $P(F_{\text{BG}})$  giving the probability to observe a flux  $F_{\text{BG}}$  from smoothly distributed background sources (such as annihilation in the smooth component of the Galactic halo or other diffuse backgrounds),  $P(F)$  will not be a Poisson distribution.

We will observe these fluxes in terms of photons beam<sup>-1</sup> year<sup>-1</sup>, or similar units. However, the limits from EGRET require that the mean photon count per beam per year be less than one; thus,

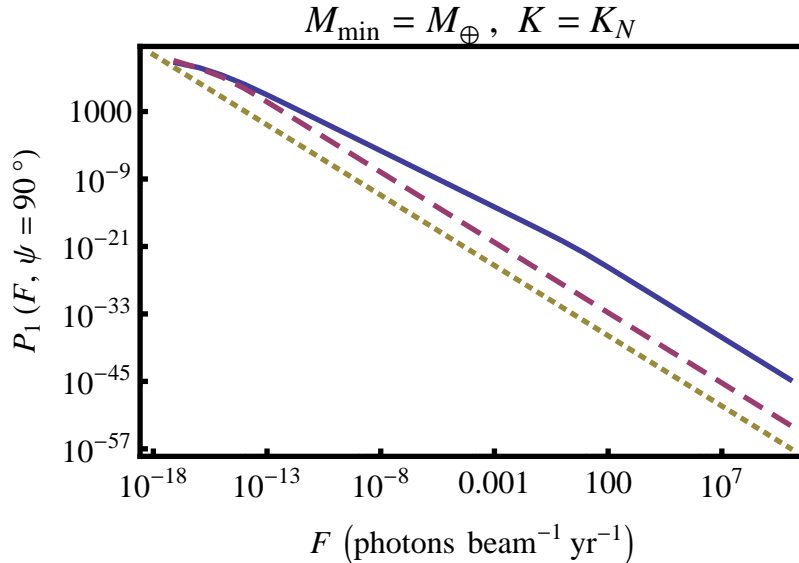


Figure 2.3: The flux-density distribution  $P_1(F, \psi = 90^\circ)$ , normalized to unity, for the flux from an individual microhalo drawn from a population of microhalos with: (1) an NFW spatial distribution and a luminosity function  $\propto L_h^{-2}$ , for a fiducial value of the minimum cutoff luminosity  $L_{\min}$  (solid); (2) an NFW spatial distribution and uniform luminosity  $L_{\min}$  (dashed); and (3) a homogeneous spatial distribution and uniform luminosity  $L_{\min}$  (dotted). Note that the first distribution follows a power-law of  $F^{-2}$  in the probabilistically observable range of  $F$  (following the power-law of the mass function), and then tends to  $F^{-5/2}$  at extremely large  $F$ . The last two distributions also tend to  $F^{-5/2}$ . We have assumed the neutralino model and a cutoff mass  $M_{\min} = M_{\oplus}$ .

even those beams with the highest photon counts will only observe some small integer number of photons per year. It follows that we will need to discretize the continuous variables  $F$  and  $F_{\text{BG}}$ . Furthermore, emission of photons is a Poisson process. Thus, let the total number of photons measured in a given beam over an observation period  $T$  be  $C \approx E(F + F_{\text{BG}}) \in \mathbb{N}$ ; here  $E$  is the exposure in a beam given in units of  $\text{cm}^2 \text{ sec}$ , and is given by  $E \approx AT$ , where  $A \approx 2000 \text{ cm}^2$  is the area of the detector.

The discrete probability distribution  $P(C)$  is then given by the sum of Poisson distributions with mean  $E(F + F_{\text{BG}})$  weighted by  $P(F)$ :

$$P(C) = \int_0^\infty dF P(F) \wp(E(F + F_{\text{BG}}), C), \quad C \in \mathbb{N}. \quad (2.51)$$

The shape of the discrete distribution  $P(C)$  is generally very similar to that of the continuous distribution  $P(EF)$  and is only slightly modified at the low end.

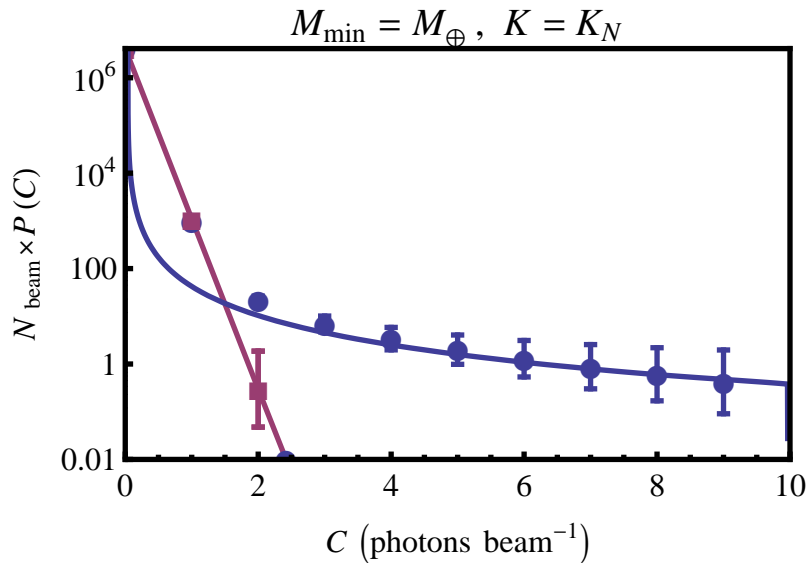


Figure 2.4: The angular-averaged discrete probability distribution function  $P(C)$  for the total photon number  $C$  in a given beam (circles), for the neutralino model with a cutoff mass of  $M_{\min} = M_{\oplus}$ . Angular bins with widths of  $\Delta\psi = 20^\circ$  were used in the averaging. Only counts from annihilation in substructure and the smooth halo component have been included. An observation period of 10 years has been assumed. The angular-averaged continuous  $P(F)$  (solid) and a fitted Poisson distribution (squares) are also plotted for comparison. We have normalized to  $N_{\text{beam}} = 4\pi/(0.1^\circ)^2 \approx 4 \times 10^6$ , the number of beams at the angular resolution limit. Poisson error bars are also shown.

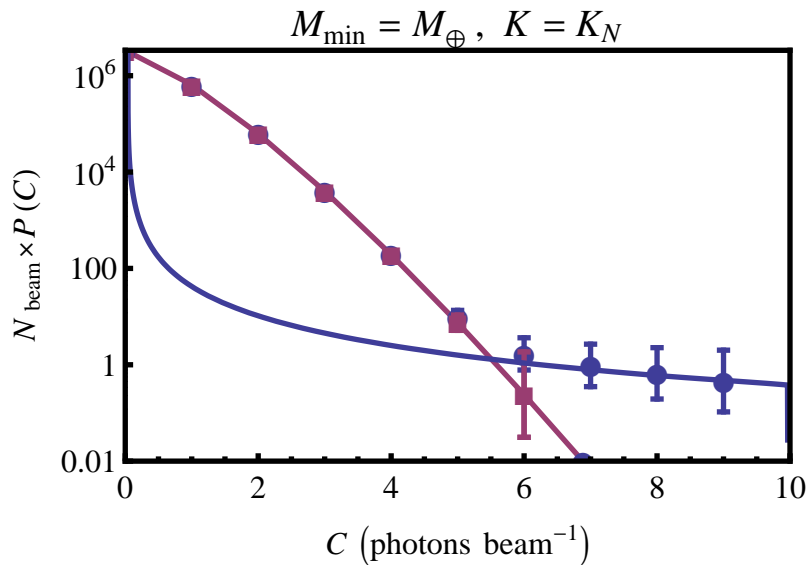


Figure 2.5: The same as in Figure 2.4, but with an arbitrary diffuse background with intensity  $I_d = 10^{-7} \text{ cm}^{-2} \text{ sec}^{-1} \text{ sr}^{-1}$  above 10 GeV added. This additional background adds a large Poisson-like feature to  $P(C)$  at low  $C$ , which obscures the substructure power-law tail. This suggests that the neutralino model may be just outside the range of P(D) analysis, if the diffuse background is indeed this large.

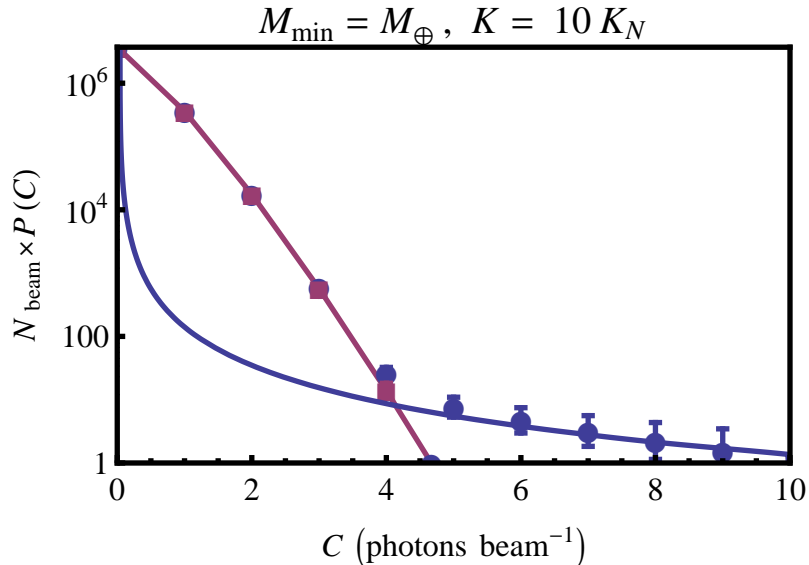


Figure 2.6: The same as in Figure 2.5, but for a line model with  $K_E = 10 K_N$ , an observation period of five years, and a background intensity  $I_{d,E} = 10^{-7} \text{ cm}^{-2} \text{ sec}^{-1} \text{ sr}^{-1}$  at 10 GeV. Note that although the intensity from the diffuse background is still many orders of magnitude above the mean expected intensity from annihilation in substructure, the substructure power-law tail is detectable with high statistical significance. Furthermore, for these model parameters, there will be no detectable individual microhalos. Thus, P(D) analysis may be useful in detecting substructure even when individual point sources are not detected.

## 2.5 Numerical results

Figure 2.4 shows the results of numerical tabulation of the PDF  $P(F)$  for the neutralino model with a fiducial cutoff mass of  $M_{\min} = M_{\oplus}$ . The PDF has a peak at low  $F$  and a power-law tail at high  $F$ . Here, only flux from dark matter annihilation in substructure and the smooth halo are included. Figure 2.5 adds an additional diffuse background with intensity  $I_d = 10^{-7} \text{ cm}^{-2} \text{ sec}^{-1} \text{ sr}^{-1}$  above 10 GeV; in this case, flux from annihilation only comprises a small fraction of the total observed flux, and the substructure PDF may be difficult for Fermi to detect within the mission lifetime.

If the mass-to-light ratio  $\Upsilon$  is increased (equivalently, if  $K$  is decreased), with  $M_{\min}$  held fixed, then the photon flux decreases. The entire distribution is then scaled down along the  $F$ -axis. If  $M_{\min}$  is reduced, with  $\Upsilon$  held fixed, then the relative width of the peak of the PDF decreases. This behavior can be understood by considering the limit  $M_{\min} \rightarrow 0$ ; in this case, we should expect to recover a smooth spatial distribution, resulting in a delta-function  $P(F)$ . Note that this dependence on  $M_{\min}$  implies that the peak of the PDF must be resolved in order to measure  $M_{\min}$ ; if the peak is obscured by an extraneous diffuse background, as in Figure 2.5, then  $M_{\min}$  may be a degenerate parameter.

The distribution  $P(C)$  for discretized counts  $C$  is also plotted in Figures 2.4 and 2.5, for a ten-year Fermi exposure. Also plotted is the Poisson distribution for a smoothly distributed diffuse

background of the same mean flux. As the figures indicate, the large- $F$  power-law tail of the PDF is qualitatively different from the exponential falloff of the Poisson distribution with  $F$ . Thus, detection of substructure amounts to detection of such a power-law tail.

Furthermore, the power-law tail of  $P(F)$  follows the power-law tail of  $P_1(F)$ . This is simply because single bright sources dominate beams with high  $F$ . However, as discussed in Section 2.4.1, the power-law tail of  $P_1(F)$  in turn follows the power-law of the mass function. For example, the power-law tail in Figure 2.4 indeed follows an  $F^{-2}$  dependence. Thus,  $P(F)$  not only provides a method of substructure detection; it can also reveal the substructure mass function.

## 2.6 Detectability

Figures 2.4 and 2.5 are plotted for the neutralino model in which a fiducial value of  $K$  is chosen. This model predicts a mean flux far below the EGRET continuum limit; even Fermi may have to observe for a period of at least ten years in order to detect significant numbers of photons in beams in the substructure power-law tail. However, the constraint on line models given by Eq. (2.46) allows for choices of the parameters  $K_E$  and  $M_{\min}$  that result in mean fluxes much closer to the EGRET line intensity limit. Line models that saturate the limit will produce signals that could be easily detected by Fermi within a year. Figure 2.6 plots the PDF for a fiducial line model.

Of course, Fermi will also be sensitive to a range of line models predicting fluxes below the EGRET bound. However, for line models with mean fluxes below a certain level, the amplitude of the substructure power-law tail will so reduced that it will be impossible to detect, as it was for the neutralino model in Figure 2.5. In this section, we determine the regions of the line model parameter space in which the PDF can be distinguished from the Poisson distribution expected for a completely smooth or diffuse background of the same mean flux, over an observation period of five years. Combined with the EGRET limit, this analysis will show the region of allowed parameter space that can be probed by study of the PDF.

We determine the signal-to-noise with which the PDF  $P(C)$  can be distinguished from the Poisson distribution  $\wp(\langle C \rangle, C)$  with the same mean count rate  $\langle C \rangle$ . The null hypothesis of no substructure can be eliminated at the  $3\sigma$  level if  $S/N > 3$ , where

$$\frac{S}{N} = \sqrt{\sum_{\psi_i} N_{\text{beam,bin}}(\psi_i) \left(\frac{S}{N}\right)_{\psi_i}^2}, \quad (2.52)$$

and

$$\left(\frac{S}{N}\right)_{\psi_i}^2 = \sum_{C=0}^{C_{\max}(\psi_i)} \frac{[P(C, \psi_i) - \wp(\langle C \rangle_{\psi_i}, C)]^2}{\wp(\langle C \rangle_{\psi_i}, C)}. \quad (2.53)$$

Here, we label the angular bins by the central value of the bin  $\psi_i$ . The quantity  $N_{\text{beam,bin}}(\psi_i)$  is



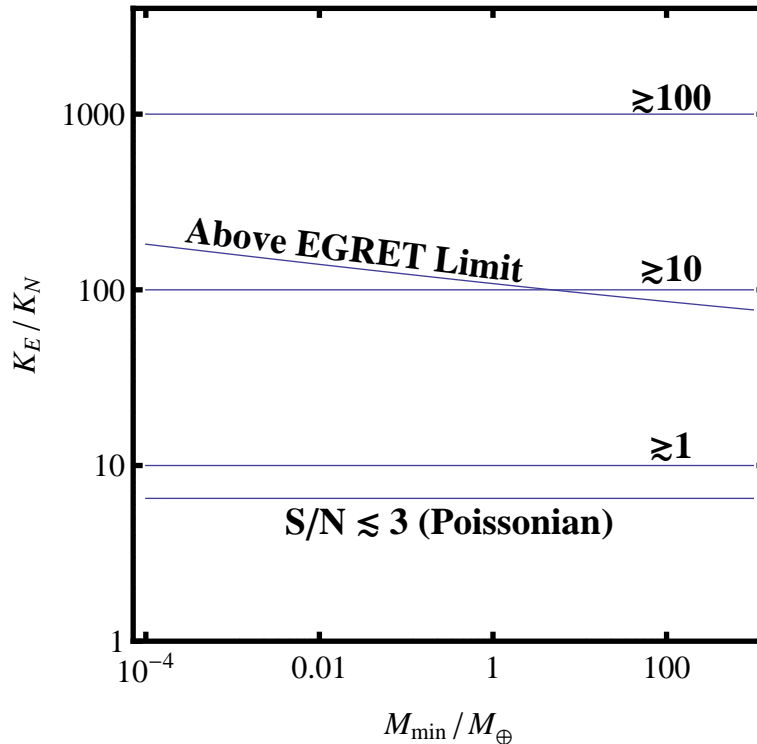


Figure 2.7: The  $K_E$ - $M_{\min}$  parameter space for the line models. On the vertical axis,  $K_E$  is scaled by  $K_N$ , the annihilation parameter for the neutralino model given by Eq. (2.45). We indicate the region that is already ruled out by the EGRET upper limit to the diffuse background; where there will be  $\gtrsim 1$ ,  $\gtrsim 10$ , and  $\gtrsim 100$  detectable point sources with flux greater than the five-year point-source sensitivity of Fermi; and where measurements of the flux PDF cannot be distinguished from a Poisson distribution, for an observation period of five years. Angular bins with widths of  $\Delta\psi = 20^\circ$  were used in the calculation of  $S/N$ , and regions near the Galactic center ( $\psi \leq 30^\circ$ ) were masked.

the number of beams contained in each bin,  $C_{\max}(\psi_i)$  is the highest count observed in each bin, and  $\langle C \rangle_{\psi_i}$  is the mean of the best-fit Poisson distribution in each bin. Eq. (2.52) then quantifies the difference between the discrete probability distributions  $P(C, \psi)$  and  $\wp(\langle C \rangle_{\psi}, C)$ , comparing the substructure PDF with the Poissonian distribution expected from a diffuse background (which may have angular dependence). In Figure 2.7, we plot the regions of the  $K_E$ - $M_{\min}$  parameter space in which the value of  $S/N$  indicates that substructure can be detected. Also plotted are the regions of the parameter space ruled out already by the current EGRET upper limit to the diffuse background.

Note that in Figure 2.7, models fall in the Poissonian regime when the substructure power-law tail at high  $C$  is obscured by the Poisson-like feature at low  $C$ ; in this regime, P(D) analysis cannot be used. Since the Poisson-like feature arises from the flux from extraneous diffuse backgrounds (from sources other than dark matter annihilation in substructure and the smooth halo), the demarcation of the Poissonian regime is ultimately determined by the level of these backgrounds. In determining the Poissonian regime, we have conservatively assumed an arbitrary diffuse background of  $I_{d,E} =$

$10^{-7} \text{ cm}^{-2} \text{ sec}^{-1} \text{ sr}^{-1}$ ; in this case, the EGRET intensity limit is severely unsaturated, and only a small fraction of the observed diffuse background arises from dark matter annihilation in substructure and the smooth halo. In practice, the actual level of these diffuse backgrounds will determine the Poissonian regime, which may then cover a smaller region of parameter space than the conservative estimate presented in Figure 2.7.

Of course, detection of a nontrivial PDF is also intimately related to the criteria for detection of point sources. The number of sources observed with flux greater than  $F$  is given by

$$N(\geq F) = 2\pi \int d\psi \sin \psi \int dL_h \int_0^{l(L_h, F)} dl l^2 \frac{dn_h}{dL_h}(r(l, \psi), L_h). \quad (2.54)$$

Examining this equation shows that  $N(\geq F)$  is only weakly dependent on the cutoff mass  $M_{\text{min}}$ . Furthermore, since the observed microhalos essentially comprise a volume-limited sample, for  $K_E$  in the range of interest  $N(\geq F) \propto K_E$  (at lower  $K_E$ ,  $N(\geq F) \propto K_E^{3/2}$  as expected for a flux-limited sample). Numerical calculation of  $dN(\geq F)/dM$  shows that the observed microhalos will predominantly be those of higher mass  $\gtrsim 10^3 M_\odot$ ; although lower-mass microhalos are far more numerous, Fermi will not be sensitive enough to detect them individually [31].

In certain regions of the parameter space for which Figure 2.7 indicates a nontrivial PDF, substructure will be detectable via detection of individual microhalos, even without a detailed analysis of the PDF. We plot these regions, taking the Fermi five-year  $5\sigma$  point-source sensitivity at 10 GeV of  $F \approx 2 \times 10^{-10} \text{ cm}^{-2} \text{ sec}^{-1}$  [29] (note that this sensitivity assumes the same background level as in our determination of the Poissonian regime). The advantage of the full PDF, however, is that substructure can be detected even in regions of parameter space where individual microhalos elude detection. Measurement of the detailed shape of the PDF can also provide more information on the microhalo mass function and/or spatial distribution in the halo than would be obtained simply by point-source counts; e.g., the slope of the power-law tail in the PDF depends upon the slope of the mass function.

Note that we could have done a similar analysis for a more general WIMP and substructure model in which some of the parameters (e.g., annihilation cross section and spectrum, or subhalo concentration/boost parameters) were allowed to vary. The EGRET continuum constraint allows for a large range of such models. However, for simplicity we have only considered the parameter space of line models and the specific substructure model assumed in Section 2.3.

## 2.7 Conclusions

We have proposed that the distribution of fluxes measured in individual Fermi pixels can be used to probe the existence of substructure in the Galactic halo to very small mass scales. By characterizing

fluctuations in the diffuse gamma-ray background in this way, the existence of Galactic substructure may be inferred statistically even if individual halos cannot be detected. This statistical approach should be viewed as complementary to the use of an angular correlation function [96, 97, 100, 101]. Since the PDF is a convolution of the microhalo mass function and spatial distribution, constraints to the parameters of these distributions may be obtained by measuring the PDF.

The full PDF we have calculated may be useful even in situations where individual microhalos can be detected. For example, the flux in a pixel with a  $3\sigma$  excess which is interpreted as detection of a single point source may actually be due to several point sources; the probability that this is so may be inferred from the PDF.

We have illustrated the PDF that results in a phenomenological model for substructure parameterized a microhalo mass cutoff  $M_{\min}$ , and a mass-to-light ratio  $\Upsilon$ . This is almost certainly an oversimplification. In more realistic models, the mass function may differ from the particular power law we have assumed. The mass-to-light ratio may depend on the microhalo mass, and there may even be a spread of luminosities for each mass. The spatial distribution of microhalos may not trace the Galactic halo. Similarly, contributions to the PDF from astrophysical backgrounds (e.g., from cosmic-ray spallation or extragalactic sources) may need to be considered before a complete comparison of our model predictions with data can be made [118].

In our P(D) analysis, we did not consider the dependence of the angular resolution on the photon energy. Furthermore, we have also assumed here that each microhalo will fall within a single resolution element of Fermi. Taking into account the finite angular size of each microhalo will reduce the length of the power-law tails in the PDF, and will decrease the region of parameter space in which the PDF can probe substructure. However, note that individual extended sources will also be more difficult to detect than point sources. A generalization of Eq. (2.54) will give a smaller number of detectable extended sources; the corresponding lines in Figure 2.7 will also shift upwards. Thus, there will still be an appreciable region of parameter space in which the PDF can be used to detect substructure even if individual sources cannot be detected. Moreover, a conservative rough estimate of the size of these microhalos can be found by approximating the microhalo mass density  $\rho_h$ , assuming a formation redshift of  $z \approx 100$  and a concentration parameter of  $c \approx 1$  [52]. A simple calculation then gives the angular size of the closest and most extended microhalos as  $\theta \approx (f\rho_0/\rho_h)^{1/3} \approx 4^\circ f^{1/3}$ . Thus, if the beam size is increased such that the majority of extended microhalos fall within a single beam, then the point source P(D) formalism presented here is roughly valid. A more careful generalization may be required for comparison to data.

We leave the inclusion of these additional levels of complication to future work. In addition to these future directions, one may also consider going further by combining the angular-correlation and PDF approaches. For example, the full two-point flux probability distribution function can be calculated and may provide additional observables with which to constrain the models or to

distinguish a dark-matter background from other astrophysical backgrounds. Again, this is left for future investigation.

## Chapter 3

# Direct detection: Probing the local velocity distribution of WIMP dark matter with directional detectors

### 3.1 Motivation: The directional recoil spectrum from WIMP-nucleus collisions

WIMPs such as the supersymmetric neutralino investigated in Section 2.1 will have weak-scale interactions with standard-model quarks. As discussed in the previous chapter, these interactions may allow the indirect detection of WIMPs via observation of the decay products of quarks produced in WIMP annihilation; however, as can be seen from Figure 1.1, these interactions also imply the possibility of the scattering of WIMPs off of the quarks contained in the nucleons within nuclei. If the dark-matter Galactic halo of our Milky Way is composed of WIMPs, then the flux of these WIMPs may be detected by experiments sensitive to the recoils induced by WIMP-nucleus collisions, yielding a direct detection of dark matter.<sup>1</sup>

#### 3.1.1 Simple estimates for direct detection

It should be emphasized that the feasibility of direct detection of WIMPs is precisely due to the fact that the interactions and mass of the WIMP are of the *weak scale*. To demonstrate this, let us first

---

Material in this chapter was first published in “Probing the local velocity distribution of WIMP dark matter with directional detectors,” Samuel K. Lee and Annika H. G. Peter, *JCAP* **1204**, 029 (2012) [33]. Reproduced here with permission, ©2012 by IOP Publishing Limited.

<sup>1</sup>Another implication of WIMP-nucleus scattering is that WIMPs should be gravitationally captured in the center of astrophysical bodies, for example the Sun and the Earth. These concentrations of WIMPs may annihilate to neutrinos that then escape, providing sources for indirect-detection studies. Since it can be shown that a steady state — in which the respective capture and annihilation rates are equal — should typically be achieved, limits on the flux of neutrinos also give constraints on the WIMP-nucleus cross section. Again, more details can be found in Ref. [41] or more recent studies.

estimate the energy deposited in a detector by a WIMP-induced nuclear recoil. Since the detector moves (roughly) with our local standard of rest (LSR), which has a velocity  $v_{\text{LSR}} \sim 220$  km/s through the Galactic halo, the momentum of an incoming WIMP is roughly  $p \sim m_\chi v_{\text{LSR}}$ . The energy imparted to a nucleus with atomic mass  $A$  and mass  $m_N \approx Am_p$  is then approximately  $E \sim p^2/2m_N \sim 25$  keV, if  $A \sim 100$ ,  $m_\chi \sim 100$  GeV  $\sim m_N$ , and the scattering is elastic.<sup>2</sup> Energies of this magnitude are accessible to detectors, via the signals that result as the recoiling nucleus distributes its energy to the rest of the detector; such signals include ionization, scintillation, and phonon signatures. Thus, WIMPs with weak-scale masses indeed offer the possibility of direct detection via nuclear recoils.

However, that the energies of such recoils are detectable is moot if the recoils do not occur at an appreciable rate; accordingly, let us now estimate the event rate of WIMP-induced nuclear recoils. Consider the event rate observed in a detector of total mass  $M$ , composed of a total number  $N$  of nuclei with mass  $m_N$ . The WIMP number flux at the Earth is approximately  $\rho_0 v_{\text{LSR}}/m_\chi$ , where  $\rho_0 \approx 0.3$  GeV/cm<sup>3</sup> is the typical value for the local dark-matter density. Defining  $R$  as the total event rate per detector mass  $M = Nm_N$  and  $\sigma_N$  as the WIMP-nucleus scattering cross section, we then have

$$RM \sim \frac{\rho_0 \sigma_N v_{\text{LSR}} N}{m_\chi} \quad (3.1)$$

$$\rightarrow R \sim \frac{\rho_0 \sigma_N v_{\text{LSR}}}{m_\chi m_N} \quad (3.2)$$

$$\sim 10 \text{ kg}^{-1} \text{ yr}^{-1} \left( \frac{\rho_0}{0.3 \text{ GeV/cm}^3} \right) \left( \frac{\sigma_N}{\text{pb}} \right) \left( \frac{100 \text{ GeV}}{m_\chi} \right) \left( \frac{100}{A} \right). \quad (3.3)$$

Thus, we see that the event rate is non-negligible for detectors of reasonable mass if both the WIMP mass and WIMP-nucleon scattering cross section are indeed of the weak scale.<sup>3</sup>

<sup>2</sup>Inelastic dark matter has also been investigated [119], primarily as a possible explanation for the annual-modulation signal (which should occur as a result of the variation in the WIMP flux caused by the orbit of the Earth around the Sun) seen at high significance in the DAMA/LIBRA experiment [120]. However, models with inelastic dark matter seem to be in tension with other experiments [121], although there is still some uncertainty.

<sup>3</sup>However, we note that it is actually the fundamental WIMP-*quark* interactions, which give rise to these cross sections, that should be of weak-scale strength. The relations between the WIMP-nucleon cross sections  $\sigma_{p,n}$ , the WIMP-nucleus cross sections  $\sigma_N$ , and the fundamental WIMP-quark cross sections depend on whether the WIMP-quark interaction is spin-dependent or spin-independent. More importantly, these relations also require some consideration of nuclear physics — essentially, since the WIMP is nonrelativistic, its de Broglie wavelength may be large enough to probe the entire nucleus, leading to coherent-scattering effects. For example, WIMP-nucleus cross sections  $\sigma_N$  scale with  $A^2$  for a spin-independent interaction, and so heavier target nuclei are generally used to increase sensitivity; however, this effect is balanced by the loss of coherence as the nucleus increases in size, which results in form-factor suppression. Since such nuclear effects vary for different target nuclei, results in the literature are typically stated in terms of the WIMP-*nucleon* cross sections  $\sigma_{p,n}$  to ease comparisons. For example, typical WIMP-nucleon spin-independent and spin-dependent cross sections for MSSM neutralinos may be as large as  $\sim 10^{-5}$  pb and  $\sim 10^{-3}$  pb, respectively, although the predictions span several orders of magnitude. Current limits from direct-detection experiments constrain the former to be less than  $\sim 10^{-8}$  pb, although corresponding constraints on the latter are relatively weak; however, as will become clear, these constraints rely on astrophysical inputs. Cross section constraints from WIMP capture in the Sun and colliders are comparatively stringent, but are also accompanied by assumptions.

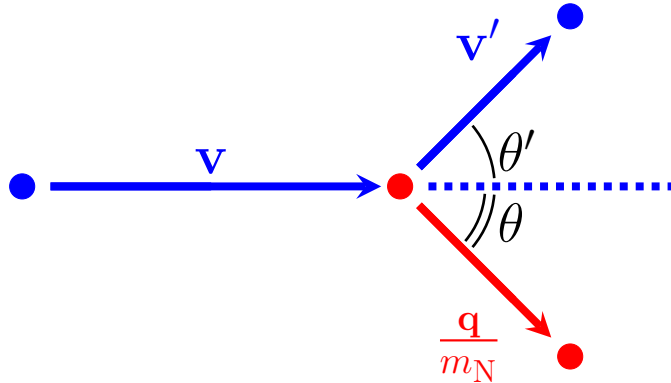


Figure 3.1: The elastic scattering of a WIMP off of a nucleus initially at rest

### 3.1.2 The directional recoil spectrum

These encouraging estimates suggest that the direct detection of WIMPs merits a more rigorous investigation. We thus proceed to more carefully rederive the nuclear-recoil event rate per detector mass  $R$  — and in particular, its dependence on the recoil energy and direction — guided by our arguments in the previous section.<sup>4</sup>

Let us first reexamine the kinematics of the scattering process, which is shown in Figure 3.1. In the lab frame, we assume that the initial velocity of the nonrelativistic WIMP is  $\mathbf{v}$  and that the target nucleus is initially at rest. We then define the final velocity of the WIMP to be  $\mathbf{v}'$  and the final recoil momentum of the nucleus to be  $\mathbf{q}$ . We let the angle between  $\mathbf{v}$  and  $\mathbf{q}$  be  $\theta$  and the angle between  $\mathbf{v}$  and  $\mathbf{v}'$  be  $\theta'$ . Assuming elastic scattering, conservation of energy and momentum then requires that  $\mathbf{v}$ ,  $\mathbf{v}'$ , and  $\mathbf{q}$  lie in a plane, and further, that

$$\frac{1}{2}m_\chi v^2 = \frac{1}{2}m_\chi v'^2 + \frac{q^2}{2m_N} \quad (3.4)$$

$$m_\chi v = m_\chi v' \cos \theta' + q \cos \theta \quad (3.5)$$

$$0 = m_\chi v' \sin \theta' - q \sin \theta. \quad (3.6)$$

Solving these equations gives the condition on the recoil momentum

$$q = 2\mu_N v \cos \theta, \quad 0^\circ \leq \theta \leq 90^\circ, \quad (3.7)$$

where

$$\mu_N \equiv \frac{m_\chi m_N}{m_\chi + m_N} \quad (3.8)$$

<sup>4</sup>The directional dependence of the WIMP signal was first discussed in Ref. [122]. The formalism presented here for the calculation of the event rate induced by WIMPs with a given velocity distribution was worked out in Ref. [123].

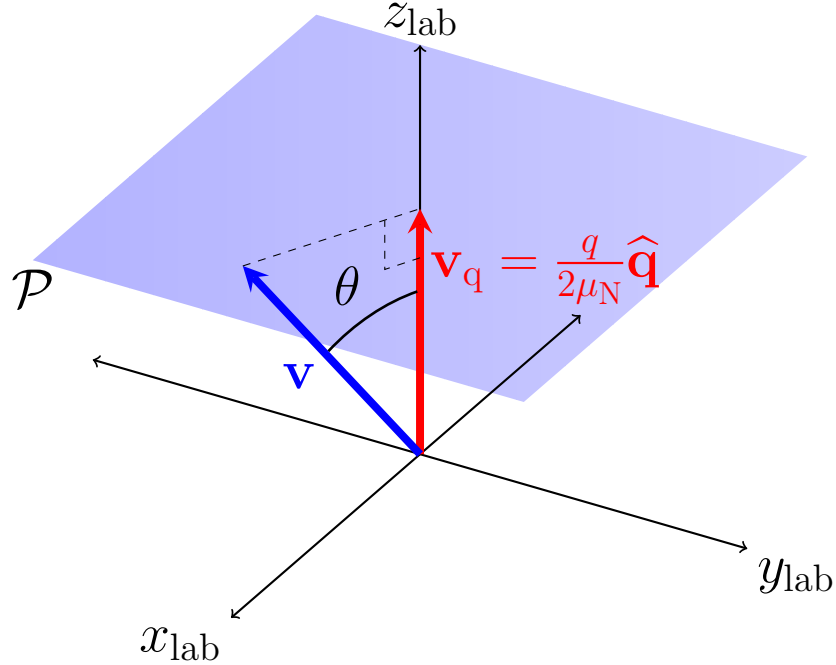


Figure 3.2: Due to the kinematics of elastic WIMP-nucleus scattering, observation of a nuclear-recoil momentum  $\mathbf{q}$  implies that the incoming-WIMP velocity vector  $\mathbf{v}$  must point to a position on the plane  $\mathcal{P}$ , where  $\mathcal{P}$  is perpendicular to  $\mathbf{q}$  and lies at the distance  $v_q = q/2\mu_N$  from the origin;  $v_q$  is then the minimum velocity the incoming WIMP may have had.

is the reduced mass of the WIMP-nucleus system. The recoil energy of the nucleus is then

$$E = \frac{q^2}{2m_N} = \frac{2\mu_N^2 v^2 \cos^2 \theta}{m_N}. \quad (3.9)$$

We thus see that in order to induce a recoil of energy  $E$ , an incoming WIMP must have *at least* a velocity

$$v_q \equiv \frac{q}{2\mu_N} = \sqrt{\frac{Em_N}{2\mu_N^2}}, \quad (3.10)$$

and that this lower bound is saturated in the forward-scattering case  $\theta = 0^\circ$ . This is clear, since an incoming WIMP that scatters a nucleus at more oblique angles needs to be moving with a greater velocity if it is to impart the same energy to the nucleus as in the forward-scattering case.

Equivalently, another way to understand these relations is illustrated in Figure 3.2. This figure shows that given an observed nuclear recoil with energy  $E$  and momentum  $\mathbf{q}$ , it is then known from the kinematics that the incoming WIMP must have had an initial velocity vector  $\mathbf{v}$  that points to a position on the plane  $\mathcal{P}$ , where the plane  $\mathcal{P}$  is perpendicular to  $\mathbf{q}$  and lies a distance  $v_q$  away from the origin. All of this can be succinctly summarized by the condition  $\mathbf{v} \cdot \hat{\mathbf{q}} = v_q$  that defines the plane  $\mathcal{P}$ .

Having reexamined the kinematics, we now turn to a more rigorous derivation of the event rate



as a function of recoil energy and direction. It is clear that the energy and direction dependence will be dictated partially by the kinematics; however, the dependence of the WIMP flux on energy and direction will also be important. In our previous estimate of the WIMP flux, we simply assumed that all of the incoming WIMPs had speeds roughly that of the LSR; we now relax this assumption. Let the distribution of WIMP velocities  $\mathbf{v}_g$  in the Galactic rest frame be given by  $f_g(\mathbf{v}_g)$ . If we neglect the gravitational influence of solar-system bodies, the distribution of WIMP velocities  $\mathbf{v}$  in the lab frame moving with velocity  $\mathbf{v}_{\text{lab}}$  with respect to the Galactic frame is then

$$f(\mathbf{v}) = f_g(\mathbf{v} + \mathbf{v}_{\text{lab}}), \quad (3.11)$$

since the various velocities are related by  $\mathbf{v} = \mathbf{v}_g - \mathbf{v}_{\text{lab}}$ .

We may then rewrite the simple expression in Eq. (3.2) as

$$dR = \frac{\rho_0}{m_\chi m_N} \left( \frac{d\sigma}{dE d\Omega_q}(\mathbf{v}) dE d\Omega_q \right) (v f(\mathbf{v}) d^3v), \quad (3.12)$$

making explicit the energy and direction dependence. We can further write

$$\frac{d\sigma}{dE d\Omega_q}(\mathbf{v}) = \frac{d\sigma}{dE} \frac{1}{2\pi} \delta \left( \cos\theta - \frac{q}{2\mu_N v} \right) \quad (3.13)$$

$$= \frac{d\sigma}{dE} \frac{v}{2\pi} \delta(\mathbf{v} \cdot \hat{\mathbf{q}} - v_q), \quad (3.14)$$

where the delta function fixes the angle  $\theta$  such that it respects the kinematics, and the factor of  $1/2\pi$  is simply from the symmetry in the azimuthal angle. It can then be shown that the directional recoil rate is given by

$$\frac{dR}{dE d\Omega_q} = \frac{\rho_0 \sigma_N S(q)}{4\pi m_\chi \mu_N^2} \hat{f}(v_q, \hat{\mathbf{q}}). \quad (3.15)$$

Again,  $R$  is the number of events per exposure (detector mass multiplied by time),  $\rho_0$  is the local WIMP density,  $\mu_N = m_\chi m_N / (m_\chi + m_N)$  is the reduced mass of the WIMP-nucleus system,  $\mathbf{q} = q\hat{\mathbf{q}}$  is the lab-frame nuclear-recoil momentum,  $E = q^2/2m_N$  is the lab-frame nuclear-recoil energy, and  $v_q = q/2\mu_N$  is the minimum lab-frame WIMP speed required to yield a recoil energy  $E$ . Furthermore, we have written the WIMP-nucleus elastic cross section as  $d\sigma/dq^2 = \sigma_N S(q)/4\mu_N^2 v^2$  (where  $S(q)$  is the nuclear form factor), and

$$\hat{f}(v_q, \hat{\mathbf{q}}) = \int \delta(\mathbf{v} \cdot \hat{\mathbf{q}} - v_q) f(\mathbf{v}) d^3v \quad (3.16)$$

is the Radon transform of the lab-frame WIMP velocity distribution. In practice, it is often easier

to take the Radon transform of the Galactic-frame velocity distribution, and then use the relation

$$\widehat{f}(v_{\mathbf{q}}, \widehat{\mathbf{q}}) = \widehat{f}_{\mathbf{g}}(v_{\mathbf{q}} + \mathbf{v}_{\text{lab}} \cdot \widehat{\mathbf{q}}, \widehat{\mathbf{q}}) \quad (3.17)$$

in Eq. (3.15) to find the directional recoil spectrum. In this work, we shall assume that the velocity of the lab frame is given by that of the LSR; i.e., we take  $\mathbf{v}_{\text{lab}} = (v_{\text{LSR}}, l_{\text{LSR}}, b_{\text{LSR}}) = (220 \text{ km/s}, 90^\circ, 0^\circ)$  in Galactic coordinates [124]. We shall ignore both the motion of the Earth around the Sun and the rotation of the Earth.

Having derived the directional recoil rate, we shall now turn to a investigation of the statistical power of experiments that may be able to measure it.

## 3.2 Introduction

Solid-state and liquid WIMP-dark-matter detectors designed to measure the energy of nuclear recoils from WIMP collisions are entering maturity on both theoretical and experimental fronts. Indeed, a large number of theoretical studies have investigated the statistical power of these experiments to characterize WIMP dark matter [125–132]. Furthermore, a variety of experiments [133–143] are currently running, with a few tantalizing signals already observed [144–146]. In contrast, gas detectors with sensitivity to the nuclear-recoil *direction* via the measurement of ionization tracks are still relatively nascent. Nevertheless, some theoretical studies on directional dark-matter detection have likewise been conducted [147–162], and a small number of directional detectors are currently under development [163–168].

A primary advantage of these directional detectors is that they allow the possibility of easily distinguishing between terrestrial background events (which should be isotropic) and WIMP-induced recoil events (which should be non-isotropic, due to our motion through the Galactic halo, and should additionally have diurnal and annual modulations, due to the rotation of the Earth and the orbit of the Earth around the Sun, respectively). Perhaps even more intriguing is the possibility that directional detectors may allow the details of the local WIMP velocity distribution to be inferred. Theoretical expectations and N-body simulations of the Galactic halo both give us reason to believe that even if the local spatial distribution of dark matter might be expected to be relatively smooth, the *velocity* distribution may possess interesting structure. Possibilities include cold tidal streams passing through the local solar neighborhood, a dark-matter disk aligned with the stellar disk, and warm debris flows [169–184]. Directional-detection experiments may confirm this picture, perhaps shedding light on not only the local velocity distribution but also the process of structure formation on galactic scales. Furthermore, a better understanding of the dark-matter velocity distribution will

yield improved constraints on the particle properties of the dark matter — in particular, the WIMP mass and the WIMP-nucleon cross section.

In this study, we explore the statistical ability of directional detectors to constrain the local WIMP velocity distribution. The organization of the study is as follows. In Section 3.3, we discuss how a binned likelihood analysis of the directional recoil-event data may be used to estimate the parameters of the velocity distribution. In Section 3.4, we perform parameter estimation on simulated data sets to demonstrate the power of these methods. We consider three specific distributions as examples: (1) the standard halo model, (2) a halo model with an additional cold dark-matter stream component, and (3) a halo model with an additional dark-matter disk component. We discuss implications for future directional dark-matter-detection studies and give our conclusions in Section 3.5.

Due to their large sizes, several of the remaining tables and figures in this chapter have been placed at the end of the chapter.

### 3.3 The binned likelihood function

Our ultimate goal will be to investigate the degree to which a binned likelihood analysis of observed recoil events might recover the parameters of the dark-matter velocity distribution. Given a number of observed events, we may construct a sky map of the data by binning both signal and background events into  $N_{\text{pix}}$  pixels (we shall use the pixels of equal angular area given by HEALPIX [185] in this work), as well as binning events in each pixel into  $N_{\text{bins}}$  energy bins (we shall also assume the energy bins are of equal width). That is, the sky map specifies the number of observed signal and background events  $M_{ij}$  in the  $i$ -th pixel of solid angle  $d\Omega_i$  and the  $j$ -th energy bin of width  $\Delta E_j$  for all  $N_{\text{pix}}$  pixels. We use pixels and bins as a proxy for finite angular and energy resolution in the detectors.

We would then like to construct a likelihood function that may be used to compare the observed sky map to the predicted sky map. The predicted sky map can be specified by the total number of events  $N_{\text{tot}}$ , which are observed over the energy-sensitivity range  $[E_{\text{min}}, E_{\text{max}}]$ , as well as the normalized distribution  $P(\hat{\mathbf{q}}, E)$  in angle and energy of these events. These quantities are simply related to the direction recoil spectrum via

$$\lambda N_{\text{tot}} P(\hat{\mathbf{q}}, E) = \mathcal{E} \frac{dR}{dE d\Omega_{\mathbf{q}}}, \quad E \in [E_{\text{min}}, E_{\text{max}}]. \quad (3.18)$$

Here,  $\lambda$  is related to the background-rejection power of the experiment, defined so that the number of signal events is  $N_{\text{sig}} = \lambda N_{\text{tot}}$  and the number of background events is  $N_{\text{bg}} = (1 - \lambda) N_{\text{tot}}$ . The effective exposure  $\mathcal{E}$  gives the fraction of the total exposure  $\mathcal{E}_{\text{tot}}$  arising from the total mass of *target* nuclei; we have implicitly assumed the detector acceptance is not energy dependent.

Note that the predicted angular distribution of signal events is then given by a normalized integral over the energy-sensitivity range

$$\begin{aligned}
P(\hat{\mathbf{q}}) &= \frac{\int_{E_{\min}}^{E_{\max}} dE \frac{dR}{dE d\Omega_{\mathbf{q}}}}{\int d\Omega_{\mathbf{q}} \int_{E_{\min}}^{E_{\max}} dE \frac{dR}{dE d\Omega_{\mathbf{q}}}} \\
&= \frac{\int_{v_{\mathbf{q},\min}}^{v_{\mathbf{q},\max}} dv_{\mathbf{q}} v_{\mathbf{q}} S(2\mu_{\mathbf{N}} v_{\mathbf{q}}) \hat{f}(v_{\mathbf{q}}, \hat{\mathbf{q}})}{\int d\Omega_{\mathbf{q}} \int_{v_{\mathbf{q},\min}}^{v_{\mathbf{q},\max}} dv_{\mathbf{q}} v_{\mathbf{q}} S(2\mu_{\mathbf{N}} v_{\mathbf{q}}) \hat{f}(v_{\mathbf{q}}, \hat{\mathbf{q}})}, \tag{3.19}
\end{aligned}$$

where  $E_{\min} = 2v_{\mathbf{q},\min}^2 \mu_{\mathbf{N}}^2 / m_{\mathbf{N}}$  and  $E_{\max} = 2v_{\mathbf{q},\max}^2 \mu_{\mathbf{N}}^2 / m_{\mathbf{N}}$ . The energy distribution  $P(E)$  of signal events is similarly given by a normalized integral over all angles.

For a given velocity distribution, we see that the predicted mean number of signal and isotropic background events in the  $i$ -th pixel (centered at the direction  $\hat{\mathbf{q}}_i$ ) and  $j$ -th energy bin is then given by

$$\begin{aligned}
\bar{M}_{ij} &= N_{\text{tot}} \int_{d\Omega_i} d\Omega \int_{\Delta E_j} dE [\lambda P(\hat{\mathbf{q}}, E) + (1 - \lambda) \frac{P_B(E)}{4\pi}] \\
&\approx N_{\text{tot}} d\Omega_i \int_{\Delta E_j} dE [\lambda P(\hat{\mathbf{q}}_i, E) + (1 - \lambda) \frac{P_B(E)}{4\pi}], \tag{3.20}
\end{aligned}$$

where  $P_B(E)$  is the energy distribution of the isotropic background events, normalized to unity over the recoil-energy sensitivity range. The approximation in the second line (which approximates the angular integral over each pixel with the value of the integrand at the center of each pixel multiplied by the pixel size) holds in the limit that  $N_{\text{pix}}$  is large. In each energy-binned pixel, the number of events is Poisson distributed, so a suitable likelihood function is given by the product of the distributions in each energy-binned pixel

$$\mathcal{L} = \prod_{i=1}^{N_{\text{pix}}} \prod_{j=1}^{N_{\text{bins}}} \wp(M_{ij} | \bar{M}_{ij}), \tag{3.21}$$

where  $\wp(M_{ij} | \bar{M}_{ij})$  is the Poisson distribution function for the random variable  $M_{ij}$  (the observed number of events) with mean  $\bar{M}_{ij}$  (the predicted number of events, which depends on the velocity distribution  $f_{\mathbf{g}}$  and the experimental conditions).

Let us now assume that the Galactic-frame velocity distribution  $f_{\mathbf{g}}$  depends on the model parameters  $\theta_k$ , the measurement of which is of interest. Then the Radon transform  $\hat{f}(v_{\mathbf{q}}, \hat{\mathbf{q}})$  of the lab-frame velocity distribution also depends on  $\theta_k$ . From Eq. (3.17), we see it further depends on  $\mathbf{v}_{\text{lab}}$ , which may be treated as three additional model parameters  $\{v_{\text{lab}}, l_{\text{lab}}, b_{\text{lab}}\}$  (in Galactic coordinates). Thus, it is clear that  $P(\hat{\mathbf{q}}, E)$  depends on  $\theta_k$  and  $\mathbf{v}_{\text{lab}}$ . Furthermore, examining the form of  $P(\hat{\mathbf{q}}, E)$  in Eq. (3.18), we see from Eq. (3.15) that  $P(\hat{\mathbf{q}}, E)$  additionally depends on  $\mu_{\mathbf{N}}$  (explicitly, as well as implicitly through the dependence on  $v_{\mathbf{q}}$ ). Therefore, it depends on the known target-nucleus

mass  $m_N$  and the unknown WIMP mass  $m_\chi$ , the latter of which may be treated as yet another model parameter we would like to measure. However, the direct dependence of  $P(\hat{\mathbf{q}}, E)$  on  $m_\chi$  weakens at high values of  $m_\chi$ , since the dependence of  $\mu_N$  on  $m_\chi$  is also weak at such values. Finally, the background-rejection power of the detector may not be well known, so we may also treat  $\lambda$  as a model parameter.

The likelihood function  $\mathcal{L}$  can therefore be written in terms of the functions and parameters specifying both the velocity distribution and the experimental conditions as  $\mathcal{L}[m_\chi, \lambda, v_{\text{lab}}, l_{\text{lab}}, b_{\text{lab}}, \theta_k, S(q); m_N, E_{\text{min}}, E_{\text{max}}, N_{\text{pix}}, N_{\text{bins}}, N_{\text{tot}}, P_B(E)]$ . By assuming the forms of  $S(q)$  and  $P_B(E)$ , a likelihood analysis of observed data can then be done to estimate the parameters that are unknown. In this work, we shall take  $S(q) = 1$  and assume that  $P_B(E) = 1/(E_{\text{max}} - E_{\text{min}})$  is a flat spectrum for simplicity.

Note that in this treatment, we have folded all the dependence of the *amplitude* of the signal  $N_{\text{sig}} = \lambda N_{\text{tot}}$  into  $\lambda$ . However, from Eqs. (3.15) and (3.18), it is clear that  $N_{\text{sig}}$  will itself depend not only on the exposure  $\mathcal{E}_{\text{tot}}$ , but also on the additional, totally degenerate parameters  $\rho_0$  and  $\sigma_N$ . If one is more interested in the particle properties of the WIMP, the usual procedure is to fix  $\rho_0 \approx 0.3 \text{ GeV/cm}^3$  (the standard estimate of the local dark-matter density, although various means of measurement yield slightly different values [186–191]) and to treat  $\sigma_N$  as the parameter of interest. In fact, more often the focus is placed on the WIMP-*nucleon* cross section  $\sigma_{\text{p,n}}$ ; for a spin-dependent interaction, this is related to the WIMP-nucleus cross section via

$$\frac{\sigma_N}{\sigma_{\text{p,n}}} = \frac{4}{3} \frac{\mu_N^2}{\mu_{\text{p,n}}^2} \frac{J+1}{J} \frac{(a_{\text{p}} \langle S_{\text{p}} \rangle + a_{\text{n}} \langle S_{\text{n}} \rangle)^2}{a_{\text{p,n}}^2}, \quad (3.22)$$

where  $\mu_{\text{p,n}}$  is the WIMP-nucleon reduced mass,  $J$  is the nuclear spin,  $a_{\text{p,n}}$  are the effective nucleon coupling strengths, and  $\langle S_{\text{p,n}} \rangle$  are the expectation values of the spin content of the nucleon group [41, 192].

However, it can be argued that the typical value of  $\rho_0 \approx 0.3 \text{ GeV/cm}^3$  usually assumed may not even be relevant for direction-detection experiments; it is simply a large-scale average of the dark-matter density at the Galactic radius of the Sun  $r_0 \approx 8.5 \text{ kpc}$ , and does not account for the possible existence of substructure in the immediate neighborhood of the Earth [61, 174]. The assumption of this typical value then strongly colors any conclusions drawn about the estimated value of  $\sigma_{\text{p,n}}$ . Thus, perhaps a more assumption-independent approach would be to ask: if we have observed a given number of events  $N_{\text{tot}}$ , how well can the parameters of an assumed velocity distribution be estimated using only the *distribution*  $P(\hat{\mathbf{q}}, E)$  of these events? In this way, we will sidestep the issues introduced by the degeneracy of  $\rho_0$  and  $\sigma_N$ , which are now subsumed into the single parameter  $\lambda$ .

### 3.4 Likelihood analyses of simulated data

We shall now explicitly demonstrate the feasibility of estimating the parameters of the velocity distribution by performing likelihood analyses on simulated data sets. We shall consider three parameterized velocity distributions: 1) the standard halo model, 2) a halo model with an additional cold stream component, and 3) a halo model with a disk component. The method of analysis is as follows. Assigning fiducial values for the velocity-distribution and experimental parameters, we first randomly generate a number of recoil events using the procedure described in appendix C. We then bin the simulated events in angle (using HEALPIX) and in energy to create a simulated sky map. We then use this to calculate the likelihood function, employing MULTINEST [193,194] to sample the likelihood function within the model parameter space, assuming flat priors. The GETDIST routine from the COSMOMC package [195] is then used to calculate the 1D and 2D marginalized posterior probability distributions. We also calculate the minimum credible intervals (MCIs) (as defined in [196]) of the posterior probability distributions, and examine how well the fiducial parameters have been recovered.

The fiducial values chosen for the velocity-distribution parameters will be discussed below for each of the three cases. However, let us first motivate the choice of the values for the experimental parameters. We shall perform the analyses assuming that the simulated data were collected by a CF<sub>4</sub> MIMAC-like experiment [163, 197–199]. That is, we assume the target nucleus is <sup>19</sup>F, and that the relevant WIMP-nucleus interaction is spin-dependent and can be modeled using  $J = 1/2$ , and assuming a pure proton coupling with  $a_p = 1$ ,  $a_n = 0$ , and  $\langle S_p \rangle = 0.5$ . Furthermore, we take the energy-sensitivity range to be 5–50 keV. This range corresponds to that quoted by the MIMAC collaboration; the 5-keV threshold arises from the ionization threshold (taking into account quenching), while the upper bound is chosen to limit contamination from background events that dominate the signal at higher energies. We shall take a fiducial value of  $m_\chi = 50$  GeV, so we see that the 5-keV recoil-energy threshold corresponds to a sensitivity to WIMP velocities down to  $\sim 150$  km/s.

The experimental parameters also include the angular and energy resolution. In all of the analyses below in which we use directional information, we shall take the number of pixels to be the same, setting  $N_{\text{pix}} = 768$  (i.e., HEALPIX order 8). This roughly corresponds to the  $\sim 10^\circ$  angular resolution expected to be attained by a MIMAC-like experiment.<sup>5</sup> On the other hand, we shall investigate the effect of varying the energy resolution by considering different numbers of energy bins  $N_{\text{bins}}$  for each analysis, which will be given in detail below. For now, we note that the bin widths we shall assume are relatively large and conservative, considering that the energy resolution

<sup>5</sup>This is the expectation in the long term, and will be sufficient to begin to characterize the dark matter. However, such angular resolution is not required for the near-term *exclusion* or *discovery* of dark matter. In that case, angular resolutions of  $\sim 20^\circ$ – $80^\circ$  might be sufficient, even if only axial directional data (without ionization-track head-tail sense discrimination) is available [200].

model	$N_{\text{pix}}$	$N_{\text{bins}}$	$E_{\text{min}}$ (keV)	$E_{\text{max}}$ (keV)	$N_{\text{sig}}$	$N_{\text{bg}}$	$N_{\text{tot}}$	$\mathcal{E}_{\text{tot}}$ (kg-yr)	$R_{\text{bg}}$ ([kg-yr] <sup>-1</sup> )
halo-only ( $m_\chi$ fixed)	768 (or 1)	10 (or 1)	5	50	100	0	100	4.4	0
halo-only ( $m_\chi$ flat prior)	768 (or 1)	10 (or 1)	5	50	100	0	100	4.4	0
halo-only (6 parameters)	768 (or 1)	10	5	50	100	100	200	4.4	23
halo+stream	768	20	5	50	650	300	950	28.9	10.4
halo+disk	768	36	5	50	541	272	813	20	15
halo+disk (zero threshold)	768	40	0	50	900	300	1200	20	15

Table 3.1: Experimental parameters used to simulate data for each analysis. The quoted values of  $\mathcal{E}_{\text{tot}}$  and  $R_{\text{bg}}$  assume a CF<sub>4</sub> detector and the typical values  $\rho_0 \approx 0.3$  GeV/cm<sup>3</sup> and  $\sigma_{\text{p,n}} \approx 10^{-3}$  pb.

of the micromegas detectors used in the MIMAC experiment is expected to be  $\sim 15\%$ . In any case, the exact values assumed for the angular and energy resolutions do not have a large effect on the quality of the parameter estimation, and it can be shown that unbinned likelihood analyses yield similar results.

Finally, there remains the question of the number of signal and background events we should examine for each analysis. We will assume various values of  $N_{\text{sig}}$  and  $N_{\text{bg}}$  for each case, as will be discussed and motivated below.

Values for the experimental parameters used for each analysis are summarized in Table 3.1. Fiducial values for the velocity-distribution parameters and the flat prior ranges are summarized in Table 3.2; we shall proceed to discuss the choice of these fiducial parameters for each velocity distribution in detail.

### 3.4.1 Halo-only model

For simplicity, we shall first consider a Galactic dark-matter halo with a velocity distribution that may be locally approximated as an isotropic Maxwellian with velocity dispersion  $\sigma_{\text{H}}$ , truncated at the Galactic escape speed  $v_{\text{esc}}$ . This truncated-Maxwellian distribution is generally referred to as the standard halo model, and is of the form

$$f_{\text{g}}^{\text{TM}}(\mathbf{v}_{\text{g}}; \sigma_{\text{H}}, v_{\text{esc}}) = \frac{1}{N_{\text{esc}}(2\pi\sigma_{\text{H}}^2)^{3/2}} \exp\left(-\frac{v_{\text{g}}^2}{2\sigma_{\text{H}}^2}\right) \theta(v_{\text{esc}} - v_{\text{g}}), \quad (3.23)$$

where

$$N_{\text{esc}}(\sigma_{\text{H}}, v_{\text{esc}}) = \text{erf}\left(\frac{v_{\text{esc}}}{\sqrt{2}\sigma_{\text{H}}}\right) - \sqrt{\frac{2}{\pi}} \frac{v_{\text{esc}}}{\sigma_{\text{H}}} \exp\left(-\frac{v_{\text{esc}}^2}{2\sigma_{\text{H}}^2}\right). \quad (3.24)$$

The Radon transform of this distribution is given by

$$\widehat{f}_g^{\text{TM}}(w, \widehat{\mathbf{w}}; \sigma_{\text{H}}, v_{\text{esc}}) = \int \delta(\mathbf{v}_g \cdot \widehat{\mathbf{w}} - w) f_g^{\text{TM}}(\mathbf{v}_g; \sigma_{\text{H}}, v_{\text{esc}}) d^3 v_g \quad (3.25)$$

$$= \frac{1}{N_{\text{esc}}(2\pi\sigma_{\text{H}}^2)^{1/2}} \left[ \exp\left(-\frac{w^2}{2\sigma_{\text{H}}^2}\right) - \exp\left(-\frac{v_{\text{esc}}^2}{2\sigma_{\text{H}}^2}\right) \right] \theta(v_{\text{esc}} - w). \quad (3.26)$$

The lab frame moves with respect to this velocity distribution with a velocity  $\mathbf{v}_{\text{lab}}$ , so as in Eq. (3.17) we may find the Radon transform of the velocity distribution in the lab frame

$$\widehat{f}^{\text{H}}(v_{\text{q}}, \widehat{\mathbf{q}}) = \widehat{f}_g^{\text{TM}}(v_{\text{q}} + \mathbf{v}_{\text{lab}} \cdot \widehat{\mathbf{q}}, \widehat{\mathbf{q}}; \sigma_{\text{H}}, v_{\text{esc}}), \quad (3.27)$$

which yields the directional recoil spectrum via Eq. (3.15).

Note that integration of  $\widehat{f}^{\text{H}}(v_{\text{q}}, \widehat{\mathbf{q}})$  over angles gives the recoil spectrum in the usual way; this integral takes the simple analytic form [201]

$$\frac{dR}{dE} \propto \frac{\sqrt{\pi}}{2\sqrt{2}} \frac{\sigma_{\text{H}}}{v_{\text{lab}}} \left\{ \text{erf}\left[\frac{v_{\text{q}}(E) + v_{\text{lab}}}{\sqrt{2}\sigma_{\text{H}}}\right] - \text{erf}\left[\frac{v_{\text{q}}(E) - v_{\text{lab}}}{\sqrt{2}\sigma_{\text{H}}}\right] \right\} - \exp\left(-\frac{v_{\text{esc}}^2}{2\sigma_{\text{H}}^2}\right), \quad (3.28)$$

which approaches a falling exponential in the limit that  $v_{\text{lab}} \rightarrow 0$  and  $v_{\text{esc}} \rightarrow \infty$ .

For the standard halo model, we see that the set of parameters determining the Galactic-frame velocity distribution is simply  $\theta_k = \{\sigma_{\text{H}}, v_{\text{esc}}\}$ . Here and afterwards, we shall assume  $v_{\text{esc}} = 550$  km/s is known independently (and in practice, the energy-sensitivity range is such that the analysis is not sensitive to the exact value of  $v_{\text{esc}}$ ). In total, there are then six parameters  $\{m_{\chi}, \lambda, v_{\text{lab}}, l_{\text{lab}}, b_{\text{lab}}, \sigma_{\text{H}}\}$  that will determine the energy and angular distribution of events. In the following analyses, we shall consider a standard halo model with fiducial parameter values  $\{m_{\chi} = 50$  GeV,  $v_{\text{lab}} = 220$  km/s,  $l_{\text{lab}} = 90^\circ$ ,  $b_{\text{lab}} = 0^\circ$ ,  $\sigma_{\text{H}} = v_{\text{lab}}/\sqrt{2} = 155$  km/s}. Note that the choice of  $\sigma_{\text{H}} = v_{\text{lab}}/\sqrt{2}$  yields a velocity distribution corresponding to a singular isothermal sphere, with halo profile  $\rho(r) \approx \rho_0(r_0/r)^2$ .

#### 3.4.1.1 $v_{\text{lab}}\text{-}\sigma_{\text{H}}$ analyses

To first gain a qualitative and intuitive understanding of the additional power that directional information provides, let us perform a simple illustrative exercise. Using the fiducial parameter values defining the standard halo model above, we generate  $N_{\text{sig}} = 100$  signal and  $N_{\text{bg}} = 0$  background events (i.e., we take  $N_{\text{tot}} = 100$  and  $\lambda = 1$ ). The spectrum and recoil map for these events is shown in Figure 3.3.

We then further assume that the values of the parameters  $\{m_{\chi}, \lambda, l_{\text{lab}}, b_{\text{lab}}\}$  are known exactly, so that only  $\{v_{\text{lab}}, \sigma_{\text{H}}\}$  are unknown and remain to be estimated. Sampling the likelihood function over the 2D  $\{v_{\text{lab}}, \sigma_{\text{H}}\}$  parameter space using MULTINEST (assuming flat priors over the ranges given in Table 3.2), we then perform three separate likelihood analyses of these 100 events. For the first



analysis, we use only the energy information of the recoil events, accomplished by setting  $N_{\text{pix}} = 1$  and  $N_{\text{bins}} = 10$ . For the second analysis, we use only the directional information, setting  $N_{\text{pix}} = 768$  and  $N_{\text{bins}} = 1$ . Finally, we analyze the data using both direction and energy information, setting  $N_{\text{pix}} = 768$  and  $N_{\text{bins}} = 10$ . Doing these three separate analyses allows us to study exactly how the direction and energy information translate into information about  $v_{\text{lab}}$  and  $\sigma_{\text{H}}$ .

The results of the three analyses are presented in the top row of Figure 3.4. We see that the energy-only analysis yields contours for the 2D marginalized posterior probability distribution in  $v_{\text{lab}}\text{-}\sigma_{\text{H}}$  space that indicate that  $v_{\text{lab}}$  and  $\sigma_{\text{H}}$  are anti-correlated. This can be understood simply by noting from Eq. (3.28) that the dependencies of the shape of the energy spectrum on  $v_{\text{lab}}$  and  $\sigma_{\text{H}}$  are similar. Increasing the value of either  $v_{\text{lab}}$  or  $\sigma_{\text{H}}$  results in a larger fraction of recoil events at higher energies, with both actions flattening out the exponentially falling recoil spectrum; this behavior is illustrated in Figure 3.5. Thus, the free parameters  $v_{\text{lab}}$  and  $\sigma_{\text{H}}$  can only vary in a roughly inverse manner with each other if the observed shape of the spectrum is to be maintained.

On the other hand, the direction-only analysis yields contours that indicate  $v_{\text{lab}}$  and  $\sigma_{\text{H}}$  are correlated. Again, this can be easily understood by considering the dependence of the directional recoil map on  $v_{\text{lab}}$  and  $\sigma_{\text{H}}$ , illustrated in Figure 3.6. Note that in the limit that  $v_{\text{lab}}$  vanishes, the recoil map becomes isotropic; conversely, it is clear that increasing the value of  $v_{\text{lab}}$  makes the map more anisotropic and asymmetric by increasing the enhancement in one hemisphere due to forward scattering by incoming particles from the ‘‘WIMP wind’’. In contrast, the recoil map becomes more isotropic as  $\sigma_{\text{H}}$  increases and becomes much larger than  $v_{\text{lab}}$ , since the number of incoming WIMPs arriving in the *opposite* direction from the WIMP wind is then increased. We see that  $v_{\text{lab}}$  and  $\sigma_{\text{H}}$  must vary in a roughly proportional manner with each other if the observed large-scale anisotropy of the recoil map is to be maintained.

Thus, the energy-only and direction-only analyses provide orthogonal sets of information on the velocity and dispersion parameters. It is then easy to see how combining both sets of information in the direction+energy analysis yields contours that demonstrate that  $v_{\text{lab}}$  and  $\sigma_{\text{H}}$  are relatively uncorrelated.

We can repeat this exercise using the same recoil-event data set, this time relaxing the assumption that the WIMP mass  $m_{\chi}$  is known independently. We now allow  $m_{\chi}$  to be an additional free parameter to be estimated, assuming a flat prior as shown in Table 3.2 and sampling over the 3D  $\{m_{\chi}, v_{\text{lab}}, \sigma_{\text{H}}\}$  parameter space. The results of the energy-only, direction-only, and direction+energy analyses are shown in the bottom row of Figure 3.4. Interestingly, we see that the quality of the contours in the energy-only analysis is severely degraded compared to the case where the mass is known exactly, with a long, flat tail in the  $\sigma_{\text{H}}$  direction appearing in the posterior probability distribution. This can be explained in a similar manner as before; allowing for decreased values of  $m_{\chi}$  is only possible if increased values of either  $v_{\text{lab}}$  and  $\sigma_{\text{H}}$  compensate to fix the observed

fraction of events at high energies. However, the slope of the spectrum is slightly more sensitive to changes in  $\sigma_H$  than to changes in  $v_{\text{lab}}$ , as can be shown by examining Eq. (3.28) (in particular, by considering the absolute magnitude of the derivatives of  $dR/dE$  with respect to  $v_{\text{lab}}$  and  $\sigma_H$  in the relevant regions of parameter space). Thus, small values of  $m_\chi$  are more easily compensated for by increasing  $\sigma_H$ , so a long tail appears in the  $\sigma_H$  direction.

It is notable that the analyses incorporating directional information are relatively insensitive to the lack of prior knowledge of the WIMP mass. This again demonstrates the power and robustness of combining directional and energy information to fix parameters of the velocity distribution.

### 3.4.1.2 6-parameter analyses

We now proceed to perform likelihood analyses over the full 6D standard-halo-model parameter space of  $\{m_\chi, \lambda, v_{\text{lab}}, l_{\text{lab}}, b_{\text{lab}}, \sigma_H\}$ . Using the same fiducial values for the velocity-distribution parameters as before, we simulate a total of  $N_{\text{tot}} = 200$  events and take  $\lambda = 0.5$ , corresponding to  $N_{\text{sig}} = 100$  and  $N_{\text{bg}} = 100$ . For a MIMAC-like experiment with 10 kg of target mass, assuming a WIMP mass  $m_\chi = 50$  GeV, a typical local density  $\rho_0 \approx 0.3$  GeV/cm<sup>3</sup>, and a spin-dependent WIMP-nucleon cross section of  $\sigma_{p,n} \approx 10^{-3}$  pb (consistent with current observational limits from both direct-detection and neutrino experiments [202–204]), this number of signal events roughly corresponds to a 5-month observation period. The number of background events then corresponds to the assumption of a relatively high background event rate of  $\sim 23$ /kg/yr (in comparison, it may be reasonable to expect background event rates as low as 10/kg/yr [160]). We again take  $N_{\text{pix}} = 768$ , and bin events into  $N_{\text{bins}} = 10$  energy bins. The recoil spectrum and binned recoil sky maps for the simulated data are shown in Figures 3.7 and 3.8, respectively.

We shall perform both an energy-only ( $N_{\text{pix}} = 1$ ) analysis and a direction+energy analysis. The results of the parameter estimation are shown in the triangle plots of the 1D and 2D marginalized posterior probability distributions in Figures 3.9 and 3.10. Note that the 68% MCIs for each parameter are plotted there, and are also given in Table 3.2 along with the 1D marginal posterior modes.

From the triangle plots, it is clear that the analysis incorporating the directional information is able to recover the parameters with greater fidelity than the energy-only analysis. Not only does this information allow for the direction  $(l_{\text{lab}}, b_{\text{lab}})$  of the lab frame to be recovered quite accurately, it also allows a rough measurement of the background-rejection power  $\lambda$  from the data itself. That is to say, the directional information indeed allows the isotropic background component to be separated from the anisotropic signal component. In contrast, the energy-only analysis is unable to recover  $\lambda$  correctly. As we saw above, flattening of the exponentially falling spectrum may be caused by variations in the other parameters, and cannot be easily separated from the introduction of a truly flat background spectral component using only the energy information (at least, not without

improved statistics from a larger number of events).

Note also that the estimate of  $m_\chi$  is quite poor for both analyses, with a long tail extending to large values of  $m_\chi$ . This partially stems from the fact that we are only using information from the *distribution* of the events, which only has weak dependence on  $m_\chi$  as  $m_\chi$  increases, as discussed previously. Since there is some additional dependence of the amplitude of the signal on  $m_\chi$ , as can be seen from Eq. (3.15), making the aforementioned assumptions about the additional amplitude-fixing parameters  $\rho_0$  and  $\sigma_N$  can greatly improve these estimates of  $m_\chi$ .

Finally, from examination of the plots for  $v_{\text{lab}}$  and  $\sigma_H$  in Figures 3.9 and 3.10, we see that the intuitive results about the ability to constrain these parameters from the simple 2-parameter and 3-parameter analyses are basically borne out even in the full 6-parameter analysis. However, we note that the presence of a flat isotropic background at this level does degrade the ability to pin down  $\sigma_H$ , even with directional information, as is evident from the long tail in the marginalized posterior probability distribution for  $\sigma_H$ . This tail may likewise be reduced by improved statistics or better background rejection.

To summarize, for the standard halo model, the measurement of 100 signal events (which might be observed in a 5-month period, if the cross section is sufficiently large) recovers the direction of the LSR and allows rough constraints to be placed on the velocity and dispersion of the Galactic halo, the presence of a non-negligible background notwithstanding. Of course, the results may be improved simply by lengthening the observation period; a 3-year observation period resulting in a 30-kg-yr exposure might be expected. In such a period, for the fiducial parameter values we have assumed for the standard halo model and WIMP properties, one would expect  $\sim 650$  signal events within the energy-sensitivity range 5–50 keV (and  $\sim 900$  total events down to zero threshold). It is then interesting to ask whether or not any interesting structure in the local dark-matter velocity distribution, such as cold streams or disk components, may be detected with a comparable number of events. We shall proceed to investigate this question in the subsections to follow.

### 3.4.2 Halo+stream model

Motivated by the results of the simulations mentioned in Section 3.2, we next consider a model with a local dark-matter stream in addition to the dark-matter halo. We shall assume that the velocity distribution in the Galactic frame of a stream component is given by

$$f_{\mathbf{g}}^{\text{S}}(\mathbf{v}_{\mathbf{g}}) = f_{\mathbf{g}}^{\text{TM}}(\mathbf{v}_{\mathbf{g}} - \mathbf{v}_{\text{S}}; \sigma_{\text{S}}, v_{\text{esc}}), \quad (3.29)$$

where the velocity vector of the stream in the Galactic frame is  $\mathbf{v}_{\text{S}}$  (and may be indicated by its magnitude  $v_{\text{S}}$  and its direction  $(l_{\text{S}}, b_{\text{S}})$  in Galactic coordinates) and the velocity dispersion  $\sigma_{\text{S}}$  is small for a cold tidal stream. We further assume that the dark-matter particles in the stream consist of a

fraction  $A_S$  of the total particles in both the halo and the stream locally. Using the linearity of the Radon transform and Eq. (3.17), we find

$$\widehat{f^{\text{H+S}}}(v_q, \widehat{\mathbf{q}}) = (1 - A_S) \widehat{f_g^{\text{TM}}}(v_q + \mathbf{v}_{\text{lab}} \cdot \widehat{\mathbf{q}}, \widehat{\mathbf{q}}; \sigma_H, v_{\text{esc}}) + A_S \widehat{f_g^{\text{TM}}}(v_q + (\mathbf{v}_{\text{lab}} - \mathbf{v}_S) \cdot \widehat{\mathbf{q}}, \widehat{\mathbf{q}}; \sigma_S, v_{\text{esc}}), \quad (3.30)$$

which yields the directional recoil spectrum via Eq. (3.15).

We shall assume the fiducial values of the parameters  $\{m_\chi, v_{\text{lab}}, l_{\text{lab}}, b_{\text{lab}}, \sigma_H\}$  determining the halo component of the distribution are identical to those used in the halo-only model above. For simplicity, we shall further assume that the parameter  $v_{\text{lab}} = v_{\text{LSR}} = 220$  km/s is known exactly, so that the halo component is specified by 4 free parameters. This is done simply to differentiate between the two Maxwellian components of the velocity distribution within the likelihood analysis, which would otherwise be arbitrarily assigned. By fixing  $v_{\text{lab}}$ , we can identify the ‘‘halo’’ as the Maxwellian component that moves with mean velocity  $v_{\text{lab}}$  with respect to the lab frame, while the ‘‘stream’’ is identified as the secondary component. For the 5 stream parameters, we shall take the fiducial values  $\{A_S = 0.1, l_S = 65^\circ, b_S = 25^\circ, v_S = 510$  km/s,  $\sigma_S = 10$  km/s}. Including  $\lambda$ , the halo+stream model is specified by 10 parameters in total.

For this halo+stream model, we shall perform only a direction+energy analysis, assuming we have observed an number of events comparable to that expected in the baseline halo-only scenario with a 30 kg-yr total exposure. For the experimental parameters, we adopt  $\{N_{\text{pix}} = 768, N_{\text{bins}} = 20, N_{\text{tot}} = 950, \lambda = 650/950 \approx 0.684\}$ . This yields  $N_{\text{sig}} = 650$  and  $N_{\text{bg}} = 300$ , roughly corresponding to an exposure of 28.9 kg-yr and background rate of 10.4/kg/yr. These values are close to those in the baseline model, since the 10% stream component is merely a small perturbation of the standard halo-only model.

The recoil spectrum and sky maps for the simulated data are shown in Figures 3.11 and 3.12, respectively. The triangle plot of the posterior probability distributions resulting from the direction+energy analysis is shown in Figure 3.13, and the posterior modes and MCIs are given in Table 3.2. The quality of parameter estimation is quite good; with the exception of  $m_\chi$ , all the parameters are recovered accurately without bias and with a low degree of correlation.

This seems to suggest that streams may be detectable with a MIMAC-like experiment. However, let us note that we have adopted a somewhat unrealistically high stream fraction  $A_S$  here (solely for illustrative purposes, e.g., to make visible in the recoil maps in Figure 3.12 the feature arising from the stream). More realistically, simulations suggest that typical stream fractions are more likely at the  $\sim 1\%$  level, and furthermore, that the probability that a tidal stream dominates the local neighborhood of the Sun (averaged on kpc scales) is less than 1% [174, 180]. Nevertheless, our analysis here serves as a proof of principle for the possibility of detecting structure in the velocity distribution beyond the standard halo model and using directional information to constrain

parameters. Furthermore, for a more realistic stream fraction of  $A_S \sim 1\%$ , one might expect only a  $\sim\sqrt{10}$  reduction in statistical power when constraining the stream parameters. Finally, this result suggests that one would expect comparable — or even improved — statistical power when constraining warm debris flows, which may have similarly large mean velocities but are thought to compose a more significant fraction (tens of percent, becoming dominant at large velocities) of the local dark-matter density.

### 3.4.3 Halo+disk model

Finally, we consider a Galactic model with a dark-matter-disk component in addition to the dark-matter halo [173, 205]. We assume that disk rotates such that local particles in the disk move with some average velocity  $\mathbf{v}_D$  with respect to the halo/Galactic frame; this velocity may be specified by its magnitude  $v_D$  and its direction  $(l_D, b_D)$  in Galactic coordinates. We shall take  $\mathbf{v}_D$  to be parallel to  $\mathbf{v}_{\text{LSR}}$ , so that these particles lag the LSR by  $v_{\text{lag}} = v_D - v_{\text{LSR}}$ ; typical values from simulations are  $v_D \approx 170$  km/s and  $v_{\text{lag}} \approx -50$  km/s, such that the dark disk rotates more slowly than the stellar disk. We again assume that the local velocity distribution of the disk component is also a truncated Maxwellian with dispersion  $\sigma_D$  and that particles in the disk compose a fraction  $A_D$  of the local particles, so that the disk velocity distribution is identical to that of halo+stream model for  $\{A_S, v_S, \sigma_S\} \rightarrow \{A_D, v_D, \sigma_D\}$ .

We again use the fiducial values of the halo component parameters, assuming  $v_{\text{lab}} = v_{\text{LSR}} = 220$  km/s is known as before. For the disk parameters, we shall take the fiducial values  $\{A_D = 0.5, l_D = 90^\circ, b_D = 0^\circ, v_D = 170$  km/s,  $\sigma_D = 100$  km/s $\}$ .<sup>6</sup>

It is clear that detecting nuclear recoils from collisions with low-velocity WIMPs in the disk component may be challenging, since the average lab-frame speed  $v_D = 170$  km/s for such WIMPs is close to the  $\sim 150$  km/s velocity threshold (corresponding to the 5-keV energy threshold, with our fiducial values for  $m_N$  and  $m_\chi$ ). Therefore, to investigate the effect of the energy threshold on the parameter estimation, we shall perform two direction+energy analyses: the first with a zero-energy threshold, and the second with a 5-keV threshold as before.

Again, we would like to evaluate the statistical power of our halo+disk analysis, assuming we have observed an number of events comparable to that expected in the baseline halo-only scenario with a 30-kg-yr exposure. As mentioned previously, this baseline scenario would yield  $\sim 900$  signal events in the 0–50-keV range, along with 300 background events (assuming the expected rate of 10/kg/yr). We therefore adopt we adopt  $\{N_{\text{pix}} = 768, N_{\text{bins}} = 40, N_{\text{tot}} = 1200, \lambda = 0.75\}$  for the first zero-threshold analysis. For the second analysis, we then make a cut of all events below the

<sup>6</sup>Disk fractions as high as  $A_D = 0.5$  have indeed been suggested by galactic-scale simulations [173, 205], although recent results find that the disk fraction in the Milky Way should be smaller ( $A_D \lesssim 0.2$ ) [206, 207]. We take the value  $A_D = 0.5$  here in order to investigate the difficulty of detecting a signal even in this optimistic case; as with the stream fraction, a reduction of the disk fraction would likely result in a  $\sqrt{N}$  reduction in statistical power in recovering the disk parameters.

5-keV threshold, resulting in  $\{N_{\text{bins}} = 36, N_{\text{tot}} = 813, \lambda = 541/813 \approx 0.665\}$ . Worth mentioning here is the fact that simulations show that the presence of a disk component *enhances* the local dark-matter density over that from the halo alone, so that  $\rho_0 \rightarrow \rho_0/(1 - A_{\text{D}})$ . This correspondingly decreases the amount of exposure needed to reach the baseline of 900 signal events, and also allows for a larger background rate.

The recoil spectrum and sky maps are shown in Figures 3.14 and 3.15, the triangle plots for the zero-threshold and 5-keV-threshold analyses are shown in Figures 3.16 and 3.17, and the posterior modes and MCIs are again given in Table 3.2. From the triangle plots, it is immediately clear that the finite energy threshold severely restricts the ability to constrain the disk-component parameters, even leading to multimodal posterior probabilities for some of the parameters. Even in the idealized case of zero threshold the parameter estimation is imperfect, as is evidenced by the amount of bias in the estimation of the disk fraction  $A_{\text{D}}$ . Although these results may be improved with better statistics or reduced background, it is clear that measurement of the parameters of a dark-matter disk will be challenging with current energy thresholds, if predictions of the disk parameters from N-body simulations are indeed valid.

### 3.5 Conclusions

Using binned likelihood analyses of simulated WIMP-nucleus recoil events, we have demonstrated how detectors with directional sensitivity may place constraints on the parameters of the local dark-matter velocity distribution. Directional sensitivity allows isotropic background events to be distinguished from signal events, but more interestingly, it also helps to break degeneracies in the velocity-distribution parameters that cannot be broken with spectral information alone. As an illustrative example, we examined the case of a Maxwellian standard-halo-model velocity distribution. By comparing the statistical power of energy-only, direction-only, and direction+energy analyses, we demonstrated how the degeneracy in the standard halo model between the velocity  $v_{\text{lab}}$  of the Earth through the halo and the halo velocity dispersion  $\sigma_{\text{H}}$  is broken with directional information.

If the local dark-matter density is indeed  $\rho_0 \approx 0.3 \text{ GeV/cm}^3$ , for a 50-GeV WIMP and a WIMP-nucleon spin-dependent cross section of  $10^{-3} \text{ pb}$ , a MIMAC-like, 10-kg  $\text{CF}_4$  directional dark-matter detector might observe several hundred WIMP-nucleus recoil events in an observation period of 3 years. With 650 signal events, the presence of a cold stream composing a fraction of the local dark-matter density may be detected, and its properties measured with relatively good accuracy. However, the detection of a dark-disk component requires sensitivity to WIMPs moving at relatively low velocities, and may only be feasible if energy thresholds are improved.

We have focused on an approach that seeks to maximize the amount of information about the velocity distribution, while minimizing the number of assumptions about the particle properties of

the WIMP or the local density of dark matter. The only assumptions of our approach are: 1) the form of the velocity distribution is known and can be parameterized, 2) the background is flat and isotropic. Future work might consider the relaxation of these assumptions. Furthermore, the analyses presented in this work simply provide a proof of principle, showing that the parameter estimation might be feasible in cases of interest. However, a more in-depth study of how the statistics of the parameter estimation improve as the experimental conditions are varied might be warranted, with the goal of finding the best balance between directional sensitivity and the overall event rate. In the event that directional detectors do indeed detect WIMP-induced recoil events, such studies will be crucial in forming a complete picture of the dark-matter particle and the structure of the Galactic halo.

model	$m_\chi$ (GeV)	$\lambda$	$l_{\text{lab}}$ ( $^\circ$ )	$b_{\text{lab}}$ ( $^\circ$ )	$v_{\text{lab}}$ (km/s)	$\sigma_{\text{H}}$ (km/s)	$v_{\text{esc}}$ (km/s)	$A_{\text{C}}$	$l_{\text{C}}$ ( $^\circ$ )	$b_{\text{C}}$ ( $^\circ$ )	$v_{\text{C}}$ (km/s)	$\sigma_{\text{C}}$ (km/s)
halo-only ( $m_\chi$ fixed)	50 [50]	1 [1]	90 [90]	0 [0]	220 [0, 880]	155 [0, 620]	550 [550]	-	-	-	-	-
halo-only ( $m_\chi$ flat prior)	50 [0, 500]	1 [1]	90 [90]	0 [0]	220 [0, 880]	155 [0, 620]	550 [550]	-	-	-	-	-
halo-only	50 [0, 500]	0.5 [0, 1]	90 [0, 180]	0 [-90, 90]	220 [0, 880]	155 [0, 620]	550 [550]	-	-	-	-	-
(6 parameters, energy-only)	62.5 [0, 300]	1.00 [0.68, 1.0]	-81.8 [-130, 110]	-33.7 [-67, 25]	168 [35, 270]	207 [110, 400]	-	-	-	-	-	-
halo-only	50 [0, 500]	0.5 [0, 1]	90 [0, 180]	0 [-90, 90]	220 [0, 880]	155 [0, 620]	550 [550]	-	-	-	-	-
(6 parameters, direction+energy)	24.4 [0, 290]	0.537 [0.45, 0.62]	101 [85, 110]	11.0 [2.5, 20]	215 [160, 280]	136 [98, 180]	-	-	-	-	-	-
halo+stream (direction+energy)	50 [0, 500]	0.684 [0, 1]	90 [0, 180]	0 [-90, 90]	220 [220]	155 [0, 620]	550 [550]	0.1 [0, 1]	65 [0, 180]	25 [-90, 90]	510 [0, 1020]	10 [0, 40]
halo+disk (direction+energy, zero threshold)	78.4 [45, 200]	0.647 [0.61, 0.69]	88.2 [82, 97]	-1.76 [-4.7, 4.2]	-	134 [110, 150]	-	0.118 [0.10, 0.15]	67.1 [59, 74]	22.9 [20, 27]	460 [430, 490]	13.3 [11, 15]
halo+disk (direction+energy, zero threshold)	50 [0, 500]	0.665 [0, 1]	90 [0, 180]	0 [-90, 90]	220 [220]	155 [0, 620]	550 [550]	0.5 [0, 1]	90 [0, 180]	0 [-90, 90]	170 [0, 680]	100 [0, 400]
halo+disk (direction+energy)	29.4 [3.9, 190]	0.745 [0.71, 0.78]	95.3 [85, 100]	5.29 [-2.3, 11]	-	134 [110, 180]	-	0.667 [0.46, 0.75]	95.3 [85, 110]	-0.176 [-13, 12]	173 [140, 200]	94.1 [92, 110]
halo+disk (direction+energy)	50 [0, 500]	0.75 [0, 1]	90 [0, 180]	0 [-90, 90]	220 [220]	155 [0, 620]	550 [550]	0.5 [0, 1]	90 [0, 180]	0 [-90, 90]	170 [0, 680]	100 [0, 400]
halo+disk (direction+energy)	23.8 [0, 59]	0.659 [0.60, 0.70]	92.2 [76, 100]	6.59 [-3.8, 14]	-	177 [110, 240]	-	0.143 [0, 0.38]	111 [-80, -10]	-4.29 [-45, 28]	97.1 [9.4, 170]	114 [65, 250]

Table 3.2: Fiducial parameter values and flat prior ranges used to simulate data and perform likelihood analyses, respectively. Marginalized posterior probability modes and 68% minimum credible intervals are also given in a second set of rows for the halo-only 6-parameter, halo+stream, and halo+disk analyses. Parameters for the stream and disk components (denoted by a subscript C) are both given in the 5 leftmost columns.



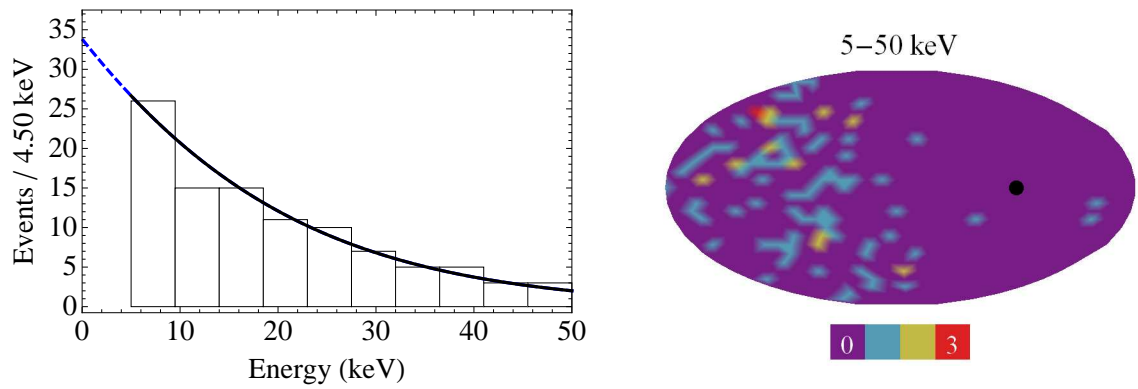


Figure 3.3: Left: Simulated recoil spectrum for the halo-only 2-parameter and 3-parameter analyses in Section 3.4.1.1, with binned signal events. The halo-only spectrum calculated from the fiducial values is also plotted, and is shown in solid black inside the energy sensitivity range. Right: Simulated recoil map for these analyses, in Mollweide projection. The black dot indicates the direction of the LSR, given in Galactic coordinates by  $(l_{\text{LSR}}, b_{\text{LSR}}) = (90^\circ, 0^\circ)$ .

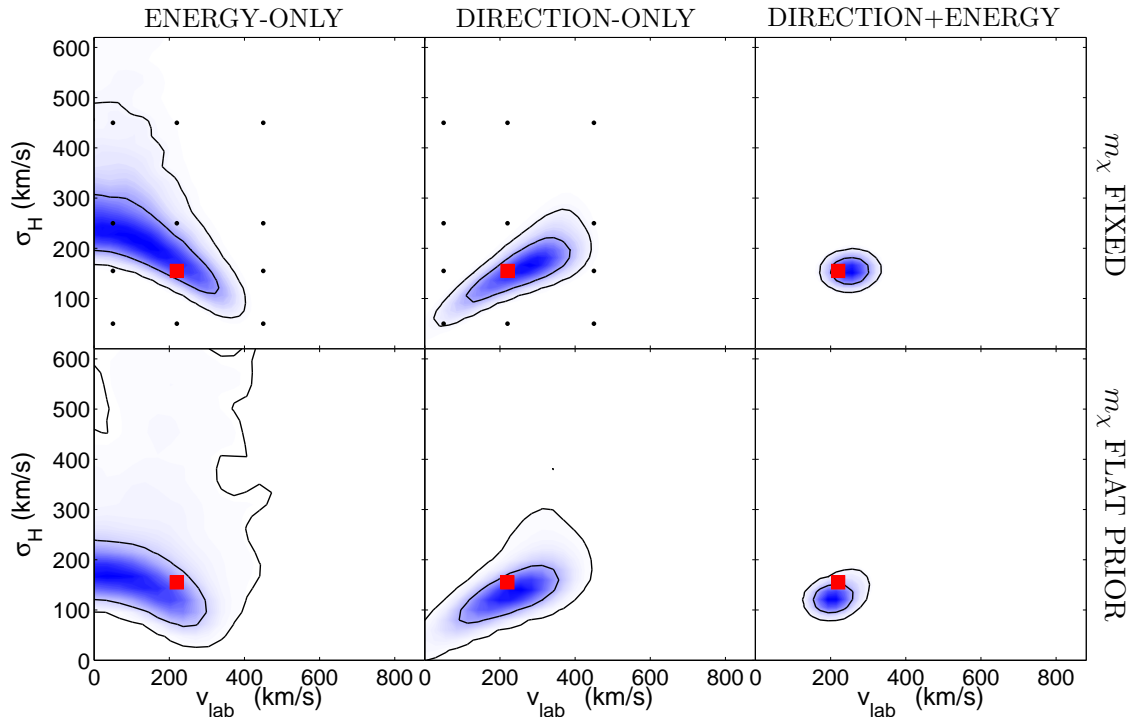


Figure 3.4: Top row: Contour plots for the 2D posterior probability distribution in  $v_{\text{lab}}-\sigma_H$  space, for the halo-only 2-parameter analyses with fixed  $m_\chi$  in Section 3.4.1.1. Analyses using energy-only, direction-only, and direction+energy information are shown. Red square markers indicate the fiducial values used in simulating the data. Black dots indicate the values used to generate the spectra and maps in Figures 3.5 and 3.6. The marginalized posterior probability is shaded blue, with contours indicating 68% and 95% confidence levels. Bottom row: The same for the 3-parameter analyses assuming a flat mass prior. Note that the energy-only contours are larger in the  $\sigma_H$  direction when only a flat prior on  $m_\chi$  is known instead of the exact value; in contrast, the direction+energy contours are relatively insensitive to lack of knowledge about  $m_\chi$ .

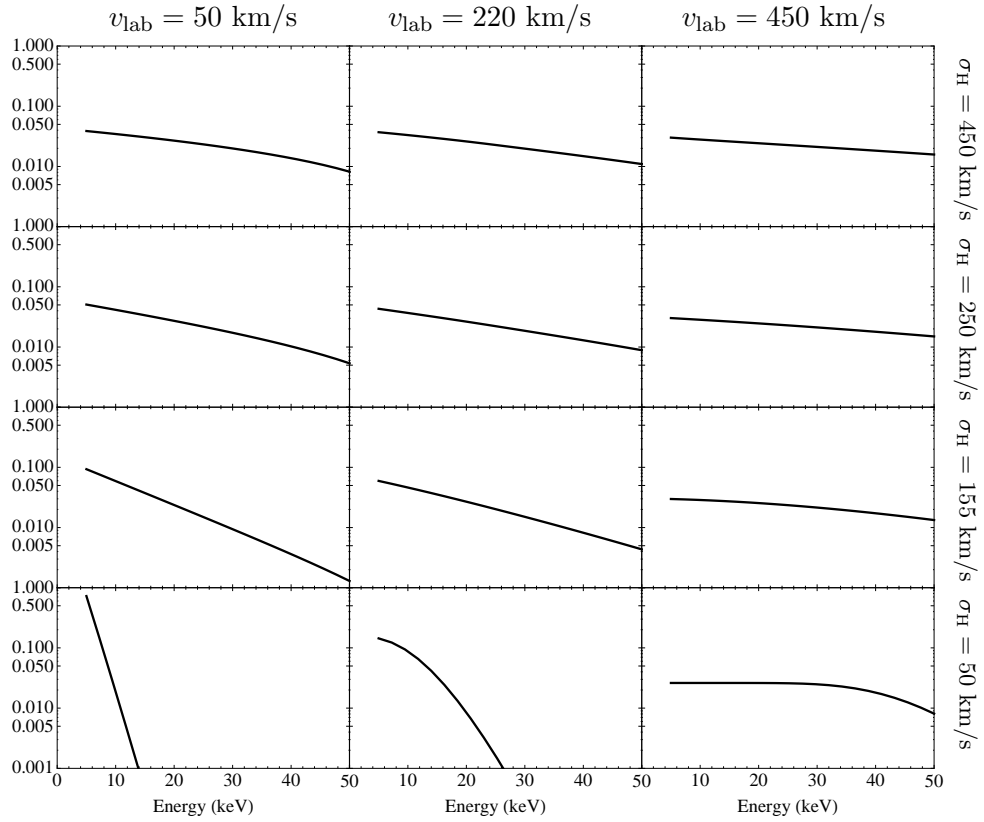


Figure 3.5: Recoil spectra showing the energy distribution (normalized to unity) of events in the energy range of 5–50 keV for a halo-only model, for the values of  $v_{\text{lab}}$  and  $\sigma_{\text{H}}$  indicated by the black dots in Figure 3.4. The similarity of some of the spectra here leads to the parameter degeneracy in the energy-only analysis shown in that figure.

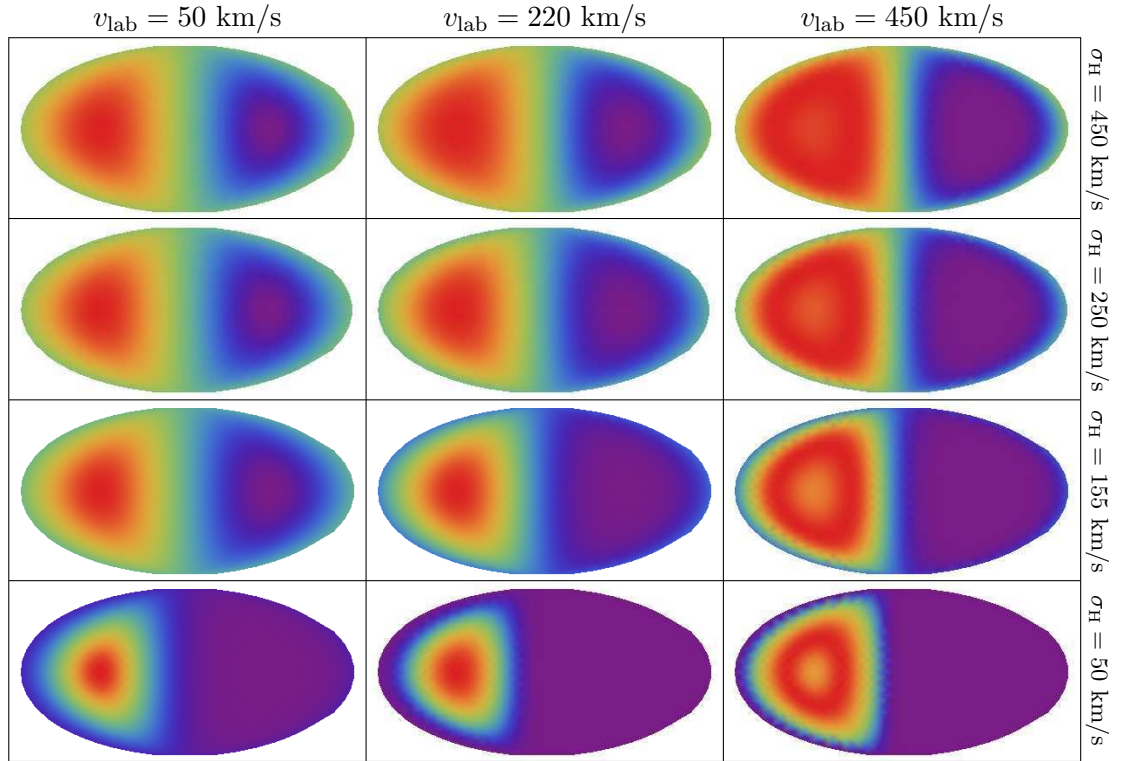


Figure 3.6: Recoil maps showing the angular distribution (normalized to unity) of events in the energy range of 5–50 keV for a halo-only model, for the values of  $v_{\text{lab}}$  and  $\sigma_{\text{H}}$  indicated in Figure 3.4. Note the correspondence between the similarity of some of the maps and the parameter degeneracy in the direction-only analysis. Note also that as  $v_{\text{lab}}$  increases, a *deficit* of events at the usual peak of the distribution appears, since the most energetic forward-scattering events have energies greater than 50 keV at large  $v_{\text{lab}}$ . See also the discussion in Ref. [208].

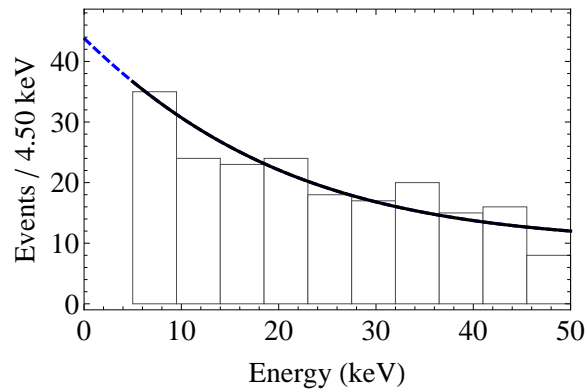


Figure 3.7: Simulated recoil spectrum for the halo-only 6-parameter analysis in Section 3.4.1.2, with binned signal and background events. The fiducial halo-only spectrum with a flat background is also plotted.

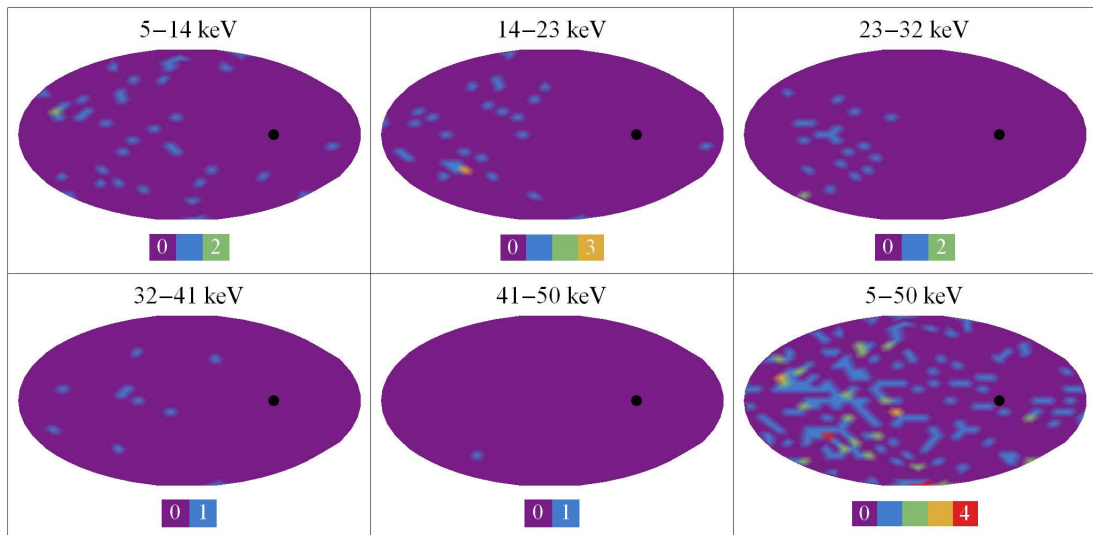


Figure 3.8: Simulated recoil maps for the halo-only 6-parameter analysis in Section 3.4.1.2. Maps of the signal events due to WIMP-induced recoils in 5 different energy bins are shown, along with a map including both signal and background events. Note that the clustering of events tightens as their energy increases because of the kinematics of the scattering process.

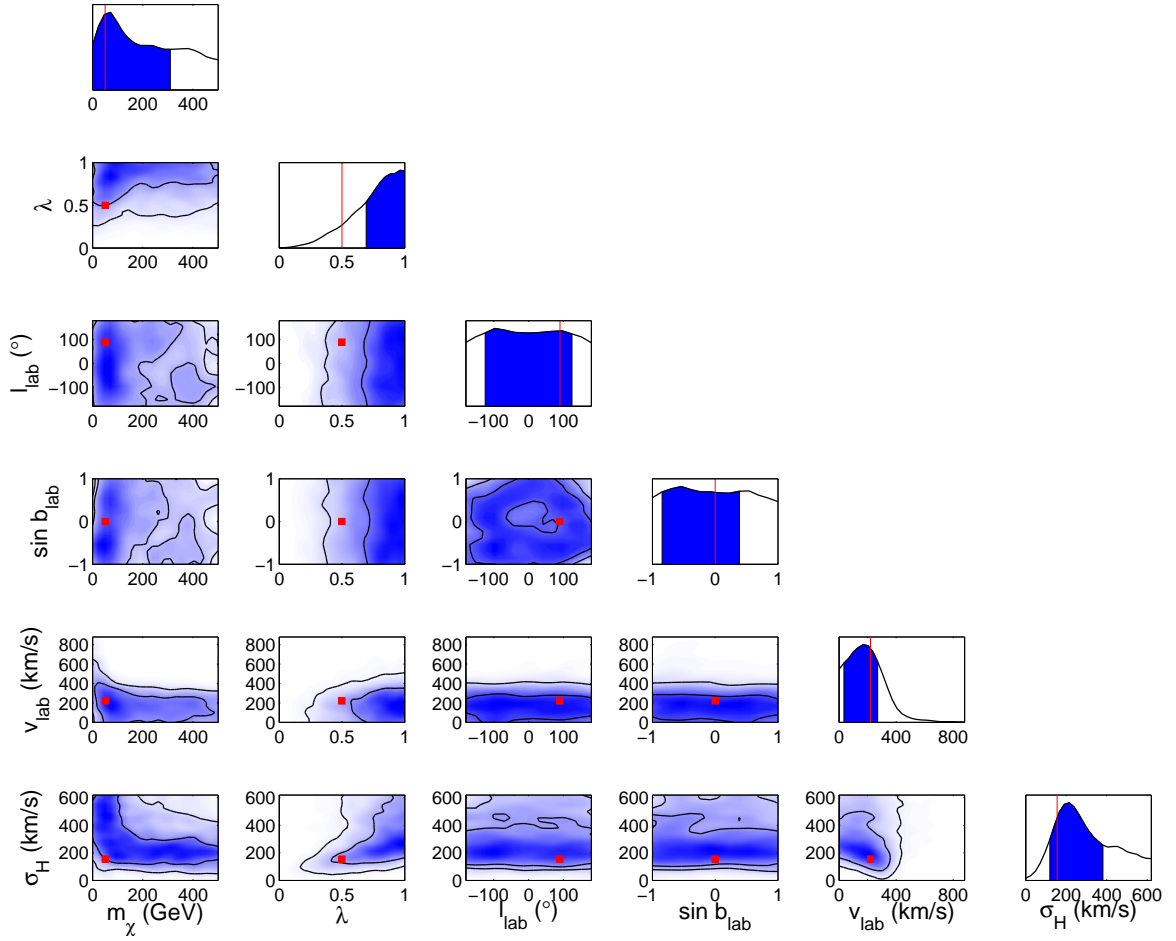


Figure 3.9: Triangle plot showing 1D and 2D posterior probability distributions over the full prior ranges, for the halo-only 6-parameter analysis using only energy information in Section 3.4.1.2. Red lines and square markers indicate the fiducial parameter values used in simulating the data. On the 1D plots, 68% minimum credible intervals are shaded in blue. Parameter estimation is relatively poor.

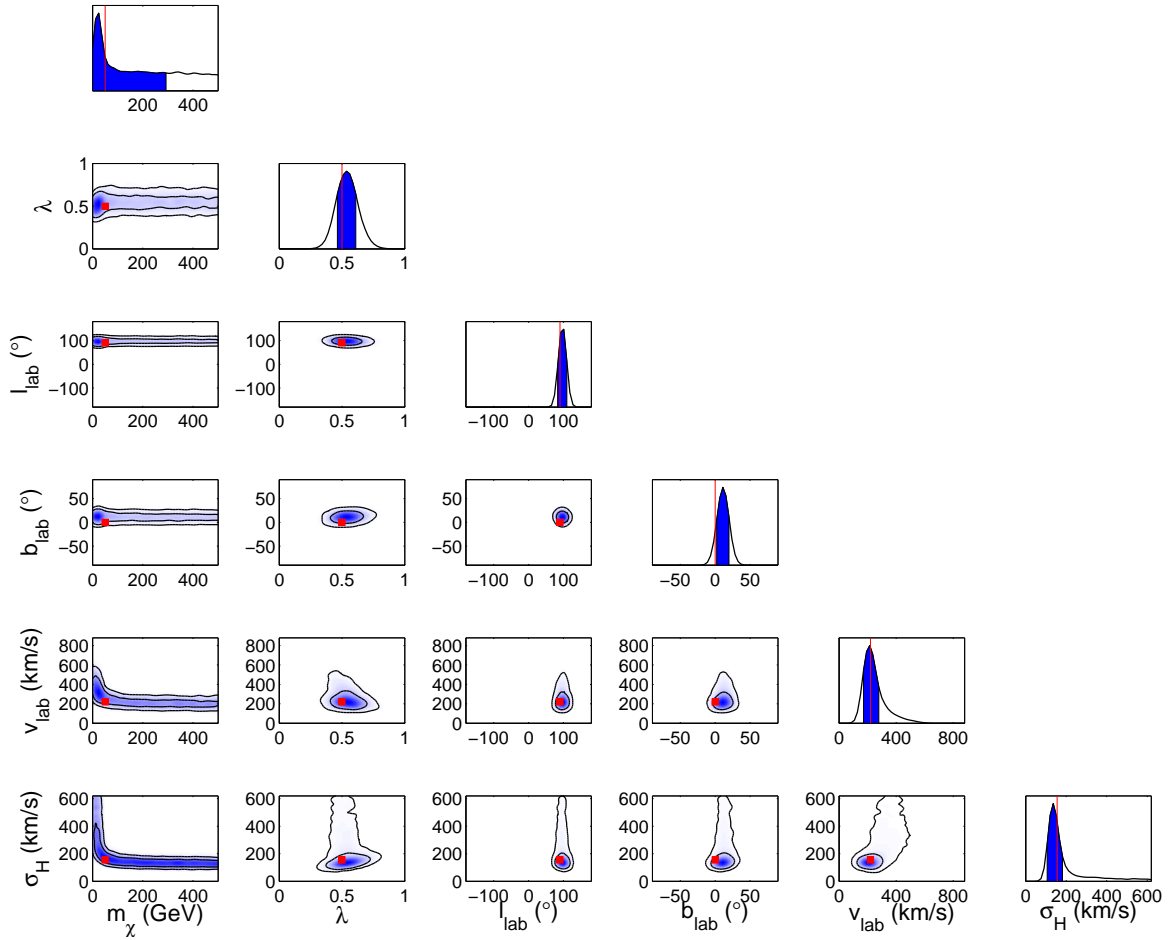


Figure 3.10: The same as Figure 3.9, but for the halo-only 6-parameter analysis using direction+energy information in Section 3.4.1.2. Parameter estimation is much improved over the energy-only analysis.

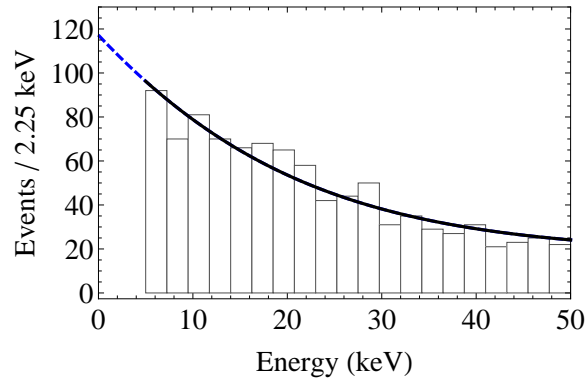


Figure 3.11: Simulated recoil spectrum for the halo+stream analysis in Section 3.4.2. The fiducial halo+stream spectrum with a flat background is also plotted.

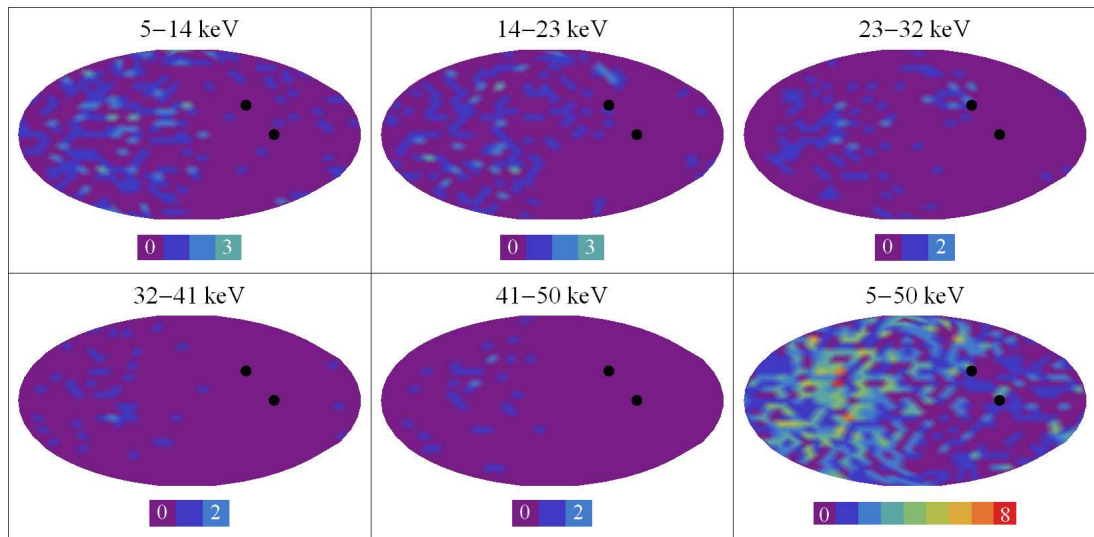


Figure 3.12: Simulated recoil maps for the halo+stream analysis in Section 3.4.2, as in Figure 3.8. Black dots indicate the direction of the LSR and the stream. The cluster of stream events is most easily seen in the top-right panel, although it is slightly visible as a wider ring-like feature at lower energies.



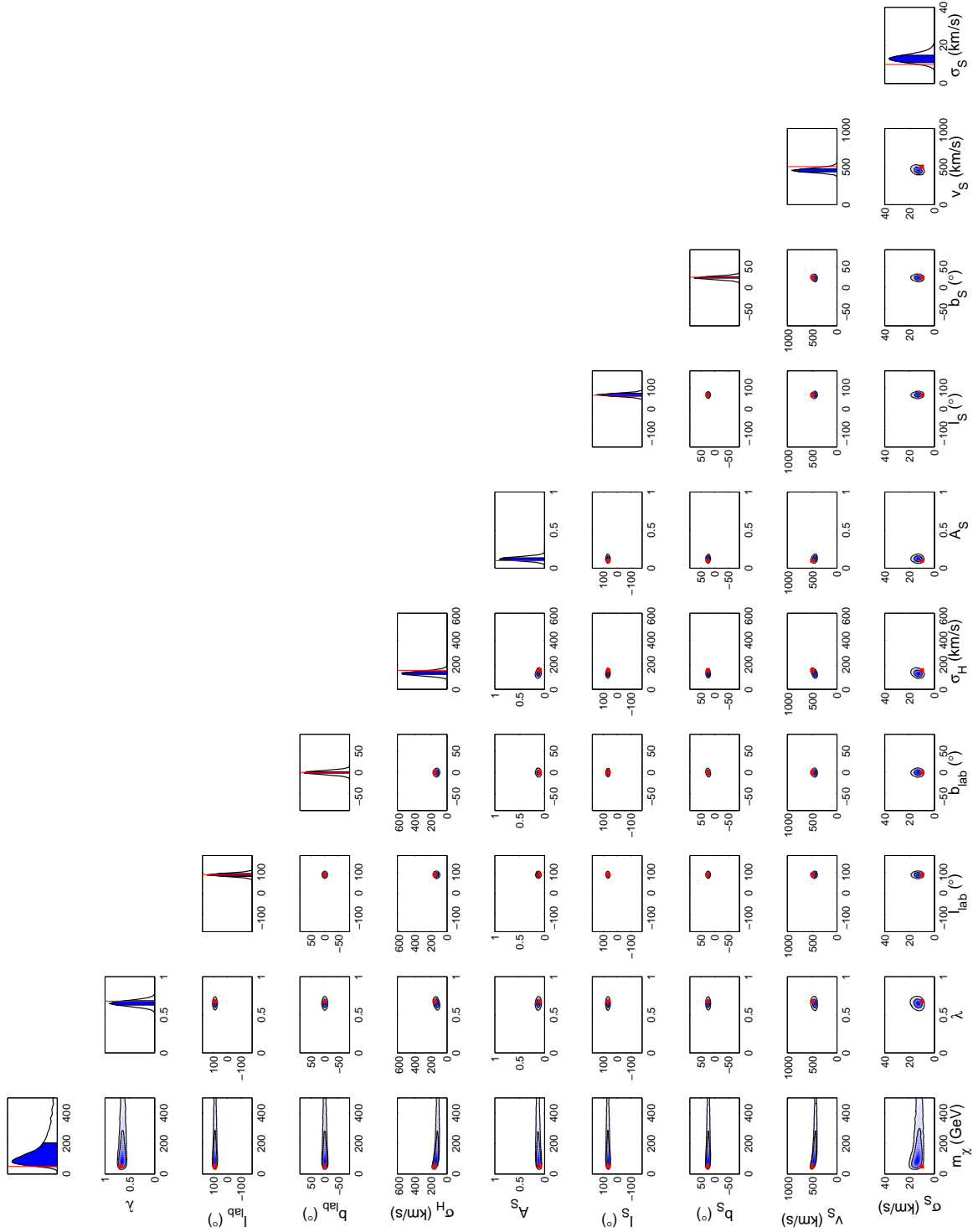


Figure 3.13: Triangle plot for the halo+stream analysis in Section 3.4.2, using direction+energy information. Parameter estimation is relatively good.

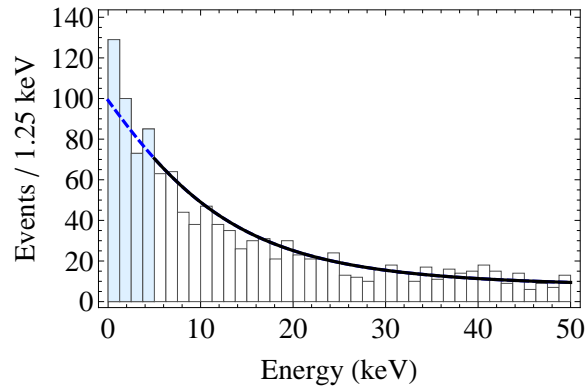


Figure 3.14: Simulated recoil spectrum for the halo+disk analyses in Section 3.4.3. The fiducial halo+disk spectrum with a flat background is also plotted. The shaded light-blue bars indicate the binned events below the 5-keV energy threshold included in the second 0–50-keV analysis.

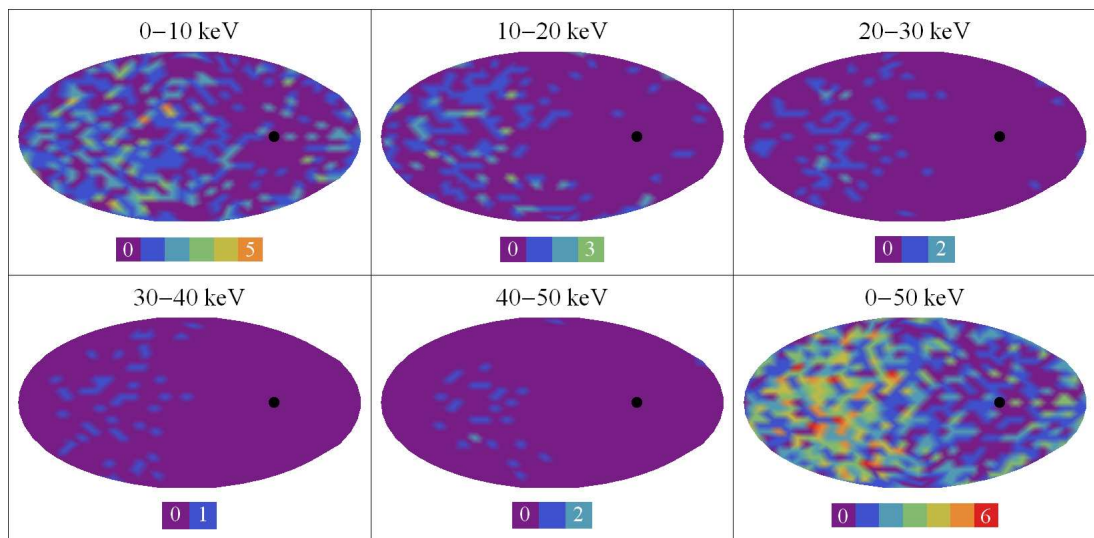


Figure 3.15: Simulated recoil maps for the halo+disk analyses in Section 3.4.3, as in Figure 3.8. Black dots indicate the common direction of the LSR and the disk. Events over the full 0–50-keV energy range are shown.

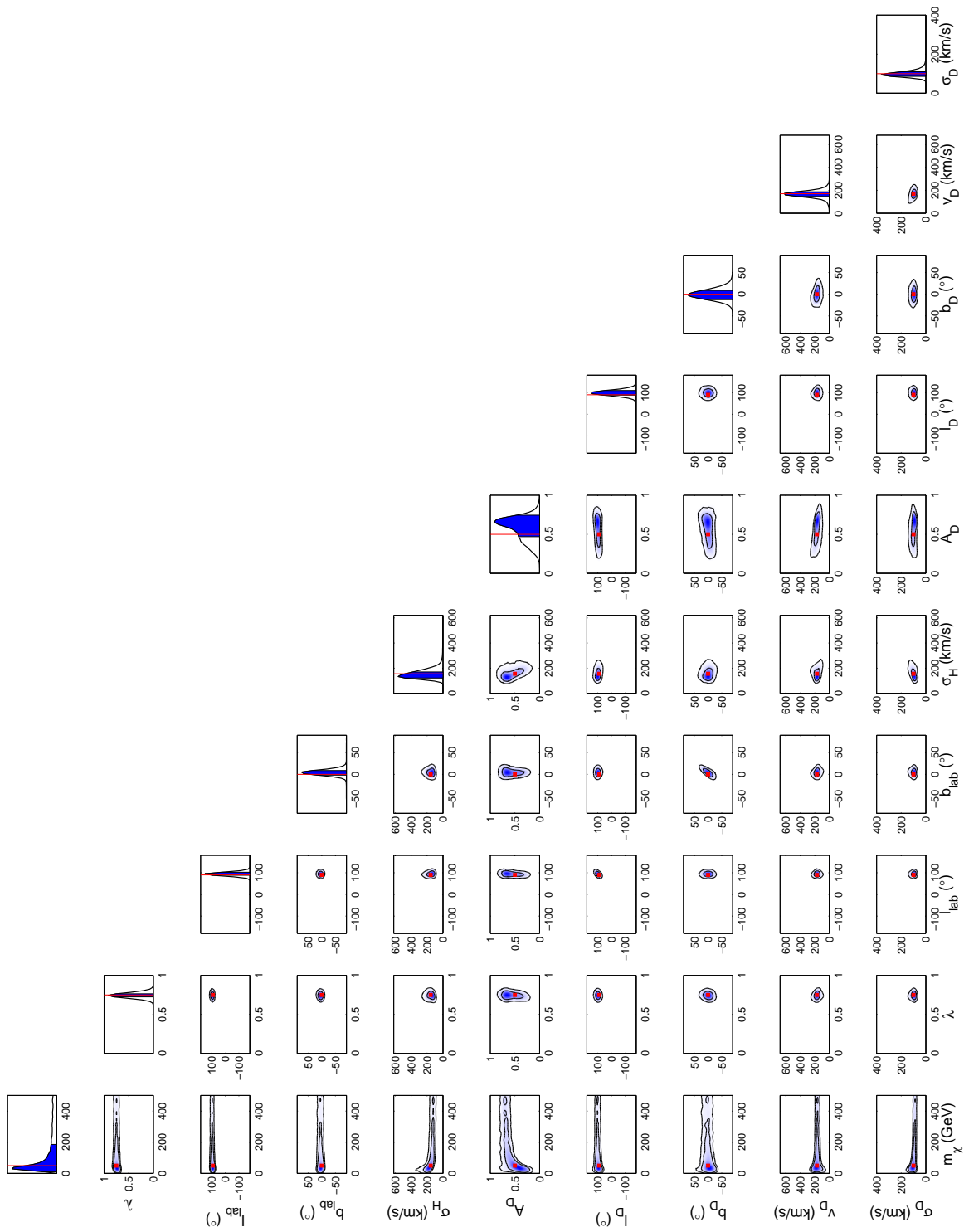


Figure 3.16: Triangle plot for the 0–50-keV halo+disk analysis in Section 3.4.3. Parameter estimation is fair, but some of the disk parameters are recovered with less accuracy.

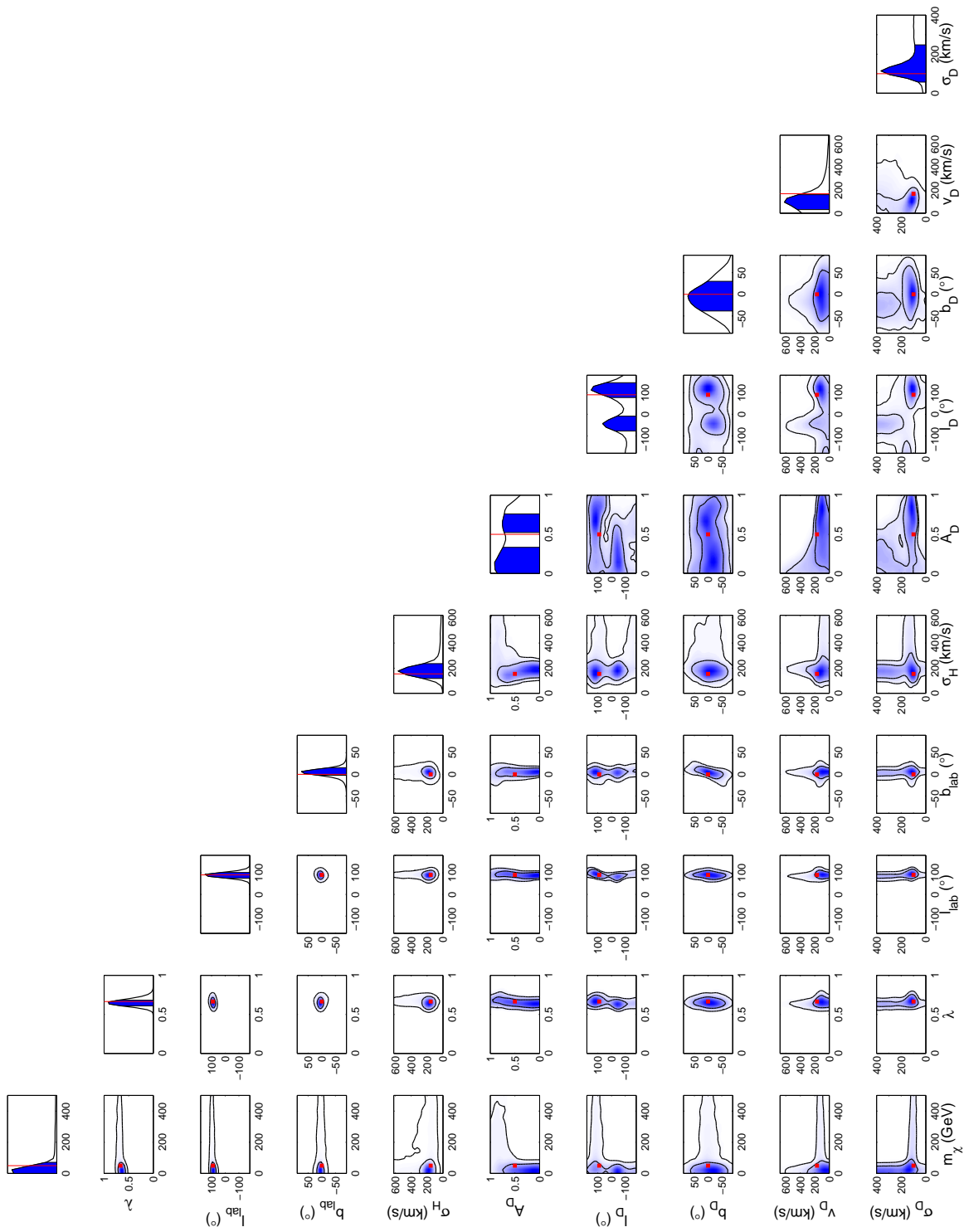


Figure 3.17: Triangle plot for the 5–50-keV halo+disk analysis in Section 3.4.3. The disk parameters are poorly estimated, demonstrating the need for improved energy thresholds.

## Chapter 4

# Collider production: Light gravitinos at colliders and implications for cosmology

### 4.1 Motivation: Supergravity and the gravitino

Stabilization of the weak scale and solving the hierarchy problem were given as the primary motivations for supersymmetry in Section 2.1. However, it was mentioned that another promising aspect of supersymmetry is that gravity naturally arises in the theory when supersymmetry is promoted to a local (or *gauge*) symmetry. We shall now heuristically examine the *super-Higgs* mechanism by which this occurs.<sup>1</sup> Interestingly enough, we shall see that a new dark-matter candidate also arises in some theories of supergravity as the LSP — the gravitino.

#### 4.1.1 A local $U(1)$ symmetry

We first start with a discussion of the promotion of global symmetries to local symmetries. Before examining how this occurs in the case of supersymmetry, let us begin by studying the more simple case of the  $U(1)_{\text{EM}}$  symmetry in electromagnetism. Consider the theory of a free, massless Weyl fermion  $\chi$ , which has the Lagrangian

$$\mathcal{L}_M = i\chi^\dagger \bar{\sigma}^\mu \partial_\mu \chi. \quad (4.1)$$

---

Material in Sections 4.2–4.6 was first published in “Light gravitinos at colliders and implications for cosmology,” Jonathan L. Feng, Marc Kamionkowski, and Samuel K. Lee, *Phys.Rev.* **D82**, 015012 (2010) [34]. Reproduced here with permission, ©2010 by the American Physical Society.

<sup>1</sup>Our presentation will be largely pedagogical, relatively elementary, and rather non-rigorous, and is based in part on Refs. [39] and [209] (and references therein).

This Lagrangian is invariant under a global  $U(1)$  transformation of  $\chi$ ; that is, a transformation that multiplies  $\chi$  by a complex phase, with the form

$$\chi \rightarrow e^{-i\epsilon} \chi \quad (4.2)$$

$$\delta\chi = -i\epsilon\chi, \quad (4.3)$$

leaves the Lagrangian unchanged, with the vanishing variation

$$\delta\mathcal{L}_M = 0. \quad (4.4)$$

Here, the infinitesimal parameter  $\epsilon$  parameterizes the symmetry transformation and is a dimensionless constant.

Let us attempt to promote this  $U(1)$  global symmetry to a  $U(1)$  *local* symmetry, by allowing this parameter to depend on the spacetime position  $x$ ; that is, we promote  $\epsilon \rightarrow \epsilon_x$  in Eqs. (4.2) and (4.3). However, the Lagrangian is not invariant under this local transformation (since the derivative acting upon  $\chi$  in Eq. (4.1) also acts upon  $\epsilon_x$ ), and we now have an additional term in the variation,

$$\delta\mathcal{L}_M = 0 + \partial_\mu \epsilon_x J^\mu, \quad (4.5)$$

where the current  $J^\mu$  multiplying the derivative of the transformation parameter is given by

$$J^\mu \equiv \chi^\dagger \bar{\sigma}^\mu \chi. \quad (4.6)$$

Note that this current is invariant under the transformation of Eqs. (4.2) and (4.3), since the complex phases acting on  $\chi$  and its Hermitian conjugate cancel, so that

$$\delta J^\mu = 0. \quad (4.7)$$

Furthermore, by considering the Euler-Lagrange equations of motion it can also be shown that this current is also conserved, so that  $\partial_\mu J^\mu = 0$ .

Since now  $\delta\mathcal{L}_M \neq 0$ , promoting the global symmetry to a local symmetry has broken the invariance. However, we may restore the invariance by adding to the Lagrangian a real, vector *gauge* field  $A_\mu$  that couples to the current with an interaction strength determined by the dimensionless coupling constant  $g$ ,

$$\mathcal{L}_M = i\chi^\dagger \bar{\sigma}^\mu \partial_\mu \chi - g A_\mu J^\mu. \quad (4.8)$$

Using the product rule, we see that the interaction term  $-g A_\mu J^\mu$  then gives rise to two additional

terms in the variation,

$$\begin{aligned} \delta\mathcal{L}_M &= 0 + \partial_\mu \epsilon_x J^\mu \\ &\quad - g \delta A_\mu J^\mu - g A_\mu \underbrace{\delta J^\mu}_0, \end{aligned} \tag{4.9}$$

where the last term vanishes as in Eq. (4.7). We also note here that the *second-to-last* term may be viewed as arising from the variation of the Lagrangian with respect to the field  $A^\mu$ ,

$$\frac{\partial\mathcal{L}_M}{\partial A^\mu} \delta A_\mu = -g \delta A_\mu J^\mu. \tag{4.10}$$

It is now clear that invariance can be restored in Eq. (4.9), provided the gauge field  $A_\mu$  also transforms as

$$A_\mu \rightarrow A_\mu + \frac{1}{g} \partial_\mu \epsilon_x \tag{4.11}$$

$$\delta A_\mu = \frac{1}{g} \partial_\mu \epsilon_x. \tag{4.12}$$

Indeed, this is just the familiar gauge transformation of the scalar and vector potentials allowed in electromagnetism; the gauge field  $A_\mu$  is simply the photon, and the addition of its usual kinetic term  $-\frac{1}{4}F_{\mu\nu}F^{\mu\nu}$ , which is invariant under the gauge transformation, to the Lagrangian yields Maxwell's equations. However, note that the *mass* term proportional to  $m_A^2 A_\mu A^\mu$  for the photon is *not* invariant; hence, such a mass term is not allowed in the Lagrangian, requiring that  $m_A = 0$  and that the photon is massless. Further note that the presence of the derivative acting on the parameter  $\epsilon_x$  in the above transformation implies that the spin of the gauge field is a unit larger than that of the parameter itself; here, the gauge field is a spin-1 vector, since the parameter is a spin-0 scalar. From this example, we thus glean the basic principle of the ‘‘Noether method’’: in order to maintain invariance under local symmetry transformations, one may add massless gauge fields which couple to currents in the theory so that the variation of the Lagrangian vanishes.

### 4.1.2 From local supersymmetry to gravity

The promotion of global supersymmetry to local supersymmetry follows analogously; we will see that the gauge fields that must be added are the gravitino and the graviton. Let us examine the simplest supersymmetric Lagrangian, the non-interacting Wess-Zumino model of a free, massless complex scalar  $\phi$  (with mass dimension  $[M]^1$ ) and a free, massless Weyl fermion  $\chi$  (with mass dimension  $[M]^{3/2}$ ):

$$\mathcal{L}_M = -\partial_\mu \phi^\dagger \partial^\mu \phi + i\chi^\dagger \bar{\sigma}^\mu \partial_\mu \chi. \tag{4.13}$$

We also note that the mass dimensions of  $\mathcal{L}_M$  and the derivative operator are  $[M]^4$  and  $[M]^1$ , respectively.

This Lagrangian is globally symmetric under a supersymmetric transformation that rotates the bosonic  $\phi$  and fermionic  $\chi$  into each other, which takes the infinitesimal form

$$\delta \begin{pmatrix} \phi \\ \chi \end{pmatrix} = \begin{pmatrix} 0 & \epsilon \\ -i\sigma^\mu \epsilon^\dagger \partial_\mu & 0 \end{pmatrix} \begin{pmatrix} \phi \\ \chi \end{pmatrix}, \quad (4.14)$$

where the infinitesimal parameter  $\epsilon$  is a fermionic (anticommuting) Grassmann constant spinor with mass dimension  $[M]^{-1/2}$  and spin-1/2. The variation of the Lagrangian under this transformation is a total derivative, so the theory is indeed globally supersymmetric. Thus,  $\phi$  and  $\chi$  are members of a chiral supermultiplet.

Let us now promote the supersymmetry to a local symmetry, by again allowing the parameter  $\epsilon$  to be a function of space time and letting  $\epsilon \rightarrow \epsilon_x$  in Eq. (4.14). As before, as a result of the derivatives in the Lagrangian acting on this spacetime dependence, the variation of the Lagrangian then picks up a nonvanishing term that is proportional to the derivative of the transformation parameter,

$$\delta \mathcal{L}_M = \text{tot. der.} + (\partial_\mu \epsilon_x S^\mu + \text{h.c.}), \quad (4.15)$$

where the *supercurrent*  $S^\mu$  is given by

$$S^\mu \equiv \sigma^\nu \bar{\sigma}^\mu \chi \partial_\nu \phi^\dagger. \quad (4.16)$$

Note that the supercurrent has mass dimension  $[M]^{7/2}$ ; furthermore, it is *not* invariant under the supersymmetry transformation, as some algebra shows that

$$\delta S^\mu \neq 0. \quad (4.17)$$

We will shortly see that both of these facts have important consequences for the interpretation of the locally supersymmetric theory as a theory of gravity.

Again, we try to restore invariance by adding a *gravitino* gauge field  $\tilde{\psi}_\mu$  that couples to the supercurrent.<sup>2</sup> As we saw in the  $U(1)$  example, the spin of the gauge field must be a unit larger than that of the transformation parameter  $\epsilon_x$ . As a result, since  $\epsilon_x$  is a spin-1/2 spinor,  $\tilde{\psi}_\mu$  is then a fermionic, spin-3/2 vectorial spinor; furthermore, since we expect  $\tilde{\psi}_\mu$  to be a propagating fermionic field, it should have mass dimension  $[M]^{3/2}$ . Accordingly, we couple the gravitino to the

---

<sup>2</sup>We shall also refer to the gravitino as  $\tilde{G}$  below.



supercurrent by adding a term to the Lagrangian

$$\mathcal{L}_M = -\partial_\mu \phi^\dagger \partial^\mu \phi + i\chi^\dagger \bar{\sigma}^\mu \partial_\mu \chi - \left( \kappa \tilde{\psi}_\mu S^\mu + \text{h.c.} \right), \quad (4.18)$$

where the coupling  $\kappa$  is required to be *dimensionful*, with mass dimension  $[M]^{-1}$ , due to the mass dimensions of  $\tilde{\psi}_\mu$  and  $S^\mu$ . We will see shortly that  $\kappa$  is related to the reduced Planck mass  $M_* = M_{\text{pl}}/\sqrt{8\pi} = (8\pi G)^{-1/2}$ , showing the connection of this theory to gravity. Indeed, gravity is known to be non-renormalizable, as are theories with couplings of negative mass dimension such as we have found here.

However, the similarities to gravity do not end here. We can see this by noting that the variation of the Lagrangian does not completely vanish, even with the addition of the gravitino gauge field. This is precisely because the supercurrent is not invariant under the supersymmetry transformation, as claimed in Eq. (4.17), so the variation of the Lagrangian is

$$\begin{aligned} \delta\mathcal{L}_M = & \text{tot. der.} + \partial_\mu \epsilon_x S^\mu \\ & - \kappa \delta\tilde{\psi}_\mu S^\mu - \kappa \tilde{\psi}_\mu \underbrace{\delta S^\mu}_{\neq 0} + \text{h.c.}, \end{aligned} \quad (4.19)$$

which may be contrasted with the analogous expression for the  $U(1)$  example given by Eq. (4.9). Thus, even when we set the transformation of the gravitino gauge field to cancel the original nonvanishing term in the variation [as we did for the photon field in Eq. (4.12)],

$$\delta\tilde{\psi}_\mu = \frac{1}{\kappa} \partial_\mu \epsilon_x, \quad (4.20)$$

the nonvanishing of the supercurrent variation  $\delta S^\mu$  prevents the restoration of local invariance.

A hint to the resolution of this problem can be found by explicitly working out the form of  $\delta S^\mu$ , starting from Eqs. (4.14) and (4.16). To do so requires some nontrivial algebraic manipulations, but schematically, the basic result is

$$-\kappa \tilde{\psi}_\mu \delta S^\mu \sim \kappa \tilde{\psi}_\mu \sigma_\nu \epsilon_x^\dagger \hat{T}^{\mu\nu} + \dots, \quad (4.21)$$

where we have omitted some terms for brevity. Here,  $\hat{T}^{\mu\nu}$  is a spin-2 field with mass dimension  $[M]^4$ ; further manipulations show that  $\hat{T}^{\mu\nu}$  can in fact be related to the *canonical* energy-momentum tensor  $T^{\mu\nu}$  for the fields  $\phi$  and  $\chi$  arising due to invariance under translations in flat spacetime,

$$\hat{T}^{\mu\nu} \sim T^{\mu\nu} \equiv \frac{\partial\mathcal{L}_M}{\partial(\partial_\mu\phi)} \partial^\nu\phi + \frac{\partial\mathcal{L}_M}{\partial(\partial_\mu\chi)} \partial^\nu\chi - \eta^{\mu\nu}\mathcal{L}_M, \quad (4.22)$$

up to numerical factors and divergenceless terms that may be added to ensure  $\hat{T}^{\mu\nu}$  is symmetric and

invariant (so that  $\delta\widehat{T}^{\mu\nu} = 0$  to leading order).

This suggests that the solution is to add *another* massless gauge field that couples to the energy-momentum tensor  $\widehat{T}^{\mu\nu}$ , with an interaction term whose variation can cancel the contribution from the supercurrent variation. This gauge field will necessarily be a spin-2 field; we shall name it  $g_{\mu\nu}$ , in anticipation that it may play the role of a dynamical metric for a curved spacetime. Adding this metric (by adding a factor of the square root of the metric determinant and promoting derivatives  $\partial_\mu$  to covariant derivatives  $\nabla_\mu$  with respect to the metric) and a term coupling it to the energy-momentum tensor to the Lagrangian, we then have

$$\frac{\mathcal{L}_M}{\sqrt{-g}} \sim -\nabla_\mu \phi^\dagger \nabla^\mu \phi + i\chi^\dagger \bar{\sigma}^\mu \nabla_\mu \chi - \left( \kappa \tilde{\psi}_\mu S^\mu + g_{\mu\nu} \widehat{T}^{\mu\nu} + \text{h.c.} \right). \quad (4.23)$$

The variation of this Lagrangian is then, schematically,

$$\begin{aligned} \frac{\delta\mathcal{L}_M}{\sqrt{-g}} \sim & \text{tot. der.} + \nabla_\mu \epsilon_x S^\mu \\ & - \kappa \delta\tilde{\psi}_\mu S^\mu - \kappa \tilde{\psi}_\mu \underbrace{\delta S^\mu}_{\neq 0} \\ & + \frac{1}{\sqrt{-g}} \frac{\partial\mathcal{L}_M}{\partial g_{\mu\nu}} \delta g_{\mu\nu} - g_{\mu\nu} \underbrace{\delta\widehat{T}^{\mu\nu}}_{=0} + \text{h.c.}, \end{aligned} \quad (4.24)$$

where we have already written the term  $-\delta g_{\mu\nu} \widehat{T}^{\mu\nu}$  (arising from the variation with respect to  $g_{\mu\nu}$ ) as  $\frac{1}{\sqrt{-g}} \frac{\partial\mathcal{L}_M}{\partial g_{\mu\nu}} \delta g_{\mu\nu}$ , analogously to Eq. (4.10). This variation now has sufficient freedom to allow it to vanish at leading order in  $\kappa$ , provided the correct transformation laws are chosen for both gauge fields  $\tilde{\psi}_\mu$  and  $g_{\mu\nu}$ . We can see this by examining Eq. (4.21), and noting that the variation vanishes for

$$-\delta g_{\mu\nu} \widehat{T}^{\mu\nu} = \frac{1}{\sqrt{-g}} \frac{\partial\mathcal{L}_M}{\partial g_{\mu\nu}} \delta g_{\mu\nu} = \kappa \tilde{\psi}_\mu \delta S^\mu \sim -\kappa \tilde{\psi}_\mu \sigma_\nu \epsilon_x^\dagger \widehat{T}^{\mu\nu} + \dots \quad (4.25)$$

We should therefore choose the transformation laws

$$\delta\tilde{\psi}_\mu = \frac{1}{\kappa} \nabla_\mu \epsilon_x \quad (4.26)$$

$$\delta g_{\mu\nu} = \kappa \tilde{\psi}_\mu \sigma_\nu \epsilon_x^\dagger + \dots \quad (4.27)$$

Examining Eq. (4.25), we see that this choice will yield the relation

$$\widehat{T}^{\mu\nu} \sim -\frac{1}{\sqrt{-g}} \frac{\partial\mathcal{L}_M}{\partial g_{\mu\nu}}, \quad (4.28)$$

which we know correctly defines the energy-momentum tensor in general relativity. Since we found that  $\widehat{T}^{\mu\nu}$  was indeed related to the canonical energy-momentum tensor in the special case of a flat spacetime, this again suggests the connection between local supersymmetry and gravity.

Furthermore, note that we can view Eqs. (4.26) and (4.27) as a supersymmetry transformation relating  $\tilde{\psi}_\mu$  and  $g_{\mu\nu}$ , parameterized by  $\epsilon_x$  as before; compare to Eq. (4.14). In particular, we may introduce a propagating spin-2 *graviton* field  $h_{\mu\nu}$  (i.e., one of mass dimension  $[M]$ , as appropriate for propagating bosonic fields), defined perturbatively such that

$$g_{\mu\nu} = \eta_{\mu\nu} + \kappa h_{\mu\nu}. \quad (4.29)$$

In a sense, this graviton field, which should mediate the force of gravity, is then the superpartner of the gravitino field  $\tilde{\psi}_\mu$ ; both fields can be placed in a *supergravity* multiplet.<sup>3</sup>

Let us summarize the progress so far. We have shown that the addition of both a spin-3/2 gravitino and a spin-2 graviton gauge field can maintain invariance under local supersymmetry. We just showed that if the graviton is viewed as a dynamical metric, then the relation between the Lagrangian and the energy-momentum tensor that arises is that expected from general relativity. Earlier, we also showed that the gravitino couples to the supercurrent with an interaction strength determined by the dimensionful coupling  $\kappa$ , noting that this interaction is non-renormalizable — as we know gravitational interactions to be — due to the negative mass dimension  $[M]^{-1}$  of  $\kappa$ . However, we have *not* yet demonstrated that  $\kappa$  is related to the Planck mass that determines the strength of the gravitational interaction.

This final piece of the puzzle falls into place as follows. We recall that we were allowed to add a kinetic term for the photon gauge field to the Lagrangian in the  $U(1)$  example, since such a term was gauge invariant. We may now add similar kinetic terms for the gravitino and the metric. For the metric, the appropriate kinetic term is given by the usual Einstein-Hilbert action of gravity; for the gravitino, which is a spin-3/2 fermion, the appropriate kinetic term is given by the *Rarita-Schwinger* action [210]. This yields the gravitational part of the Lagrangian

$$\mathcal{L}_G = \mathcal{L}_{\text{EH}} + \mathcal{L}_{\text{RS}} = \frac{1}{16\pi G} \sqrt{-g} R + \epsilon^{\mu\nu\rho\sigma} \tilde{\psi}_\mu^\dagger \bar{\sigma}_\nu \nabla_\rho \tilde{\psi}_\sigma, \quad (4.30)$$

where  $R$  is the Ricci scalar for the metric  $g_{\mu\nu}$  and the covariant derivative acting on  $\tilde{\psi}$  includes a spin-connection term. It is precisely the requirement that the variation of this Lagrangian also vanish under the transformations for the gravitino and graviton given in Eqs. (4.26) and (4.27) that sets the coupling constant

$$\kappa = \frac{1}{M_*} = \sqrt{8\pi G}. \quad (4.31)$$

The total Lagrangian including both the gravitational and matter components

$$\mathcal{L} = \mathcal{L}_G + \mathcal{L}_M \quad (4.32)$$

---

<sup>3</sup>More precisely, it is the *vierbein*  $e_\mu^a$ , related to the metric by  $g_{\mu\nu} = \eta_{ab} e_\mu^a e_\nu^b$ , that appear in the supergravity multiplet, along with auxiliary fields.

then gives rise to the celebrated Einstein field equation

$$G_{\mu\nu} = R_{\mu\nu} - \frac{1}{2}g_{\mu\nu}R = 8\pi G\hat{T}_{\mu\nu} \quad (4.33)$$

through the usual procedure, firmly establishing the connection between local supersymmetry and gravity.<sup>4</sup>

### 4.1.3 The super-Higgs mechanism

We have shown how local supersymmetry gives rise to gravity, via the introduction of massless gauge fields — including the spin-3/2 gravitino. However, we have not yet explained how the gravitino acquires its mass, thereby allowing it to be a dark-matter candidate. We may roughly explain the *super-Higgs* mechanism by which this occurs using an analogy to the familiar Higgs mechanism that is responsible for imparting mass to the *weak* gauge fields (as well as the other particles in the standard model).

The matter Lagrangian of the electroweak theory (containing massless fermions) has a global  $SU(2)_L \times U(1)_Y$  symmetry that can be made local by the introduction of massless weak gauge fields, which couple to the matter fields with interaction strengths  $g_{1,2}$ . As we saw in Section 2.1, we may also introduce the Higgs-field doublet and the Higgs potential. Due to the shape of the potential, one component of the Higgs doublet then gets a weak-scale VEV  $v$  that spontaneously breaks the local  $SU(2)_L \times U(1)_Y$  electroweak symmetry down to  $U(1)_{EM}$ . This produces three spin-0 Goldstone bosons, the degrees of freedom of which three of the massless spin-1 weak gauge fields “eat” to acquire masses. This results in the massive  $Z$  and  $W^\pm$  bosons, which thereby gain masses that are proportional to both the interaction strengths and the VEV,

$$M_{Z,W} \sim g_{1,2}v. \quad (4.34)$$

This is the standard Higgs mechanism, by which local electroweak symmetry is spontaneously broken and the electroweak bosons and the other particles of the standard-model acquire mass, despite the fact that gauge-field mass terms are not allowed by the requirement of local invariance.

Analogously, as we saw in the previous section, the matter Lagrangian of a globally supersymmetric theory (containing massless scalars and fermions in chiral supermultiplets) can be made locally invariant by the introduction of a massless gravitino gauge field, which couples to the matter fields with interaction strength suppressed by the reduced Planck mass as  $1/M_*$ . Let us now introduce a chiral supermultiplet of fields, one of which obtains a VEV  $F$  in *superspace* due to the shape of

---

<sup>4</sup>Again, our presentation here has been largely heuristic. To rigorously demonstrate the invariance of the total Lagrangian (including gauge supermultiplets) under local supersymmetry transformations by deriving the correct transformation laws for the fields using the Noether method iteratively — while also maintaining covariance under general coordinate transformations — is a formidable task, well beyond the pedagogical scope of this section.

	Electroweak $SU(2)_L \times U(1)_Y$	Supergravity
Local symmetry transformation	$\delta \begin{pmatrix} \nu_e \\ e^- \end{pmatrix}_L = i (g_1 \epsilon_{1x} + g_2 \epsilon_{2x}^k \sigma_k) \begin{pmatrix} \nu_e \\ e \end{pmatrix}_L$	$\delta \begin{pmatrix} \phi \\ \chi \end{pmatrix} = \begin{pmatrix} 0 & \epsilon_x \\ -i\sigma^\mu \epsilon_x^\dagger \partial_\mu & 0 \end{pmatrix} \begin{pmatrix} \phi \\ \chi \end{pmatrix}$
Massless gauge fields	$B_\mu$ and $W_\mu^k$ (spin-1)	$\tilde{\psi}_\mu$ (spin-3/2) and $g_{\mu\nu}$ (spin-2)
Local SSB	Higgs: vev $v$ 3 spin-0 Goldstone bosons eaten	super-Higgs: vev $F$ spin-1/2 goldstino fermion eaten
Massive gauge fields	$Z_\mu$ and $W_\mu^\pm$ with $M_{Z,W} \sim g_{1,2}v$	$\tilde{\psi}_\mu$ with $m_{\tilde{G}} \sim \frac{1}{M_*}F$

Table 4.1: We may understand the super-Higgs mechanism by an analogy to the familiar Higgs mechanism, since both mechanisms exhibit general characteristics of spontaneous symmetry breaking (SSB).

the potential of these fields; schematically, the VEV picks out a direction in the “boson-fermion” space upon which supersymmetry transformations act.<sup>5</sup> This spontaneous supersymmetry breaking produces a spin-1/2 *goldstino* (a Goldstone fermion) with two degrees of freedom, which the massless spin-3/2 gravitino gauge field eats to acquire mass. In analogy to Eq. (4.34), we may guess that the mass of the gravitino is likewise proportional to the interaction strength and the VEV,

$$m_{\tilde{G}} \sim \frac{F}{M_*}. \quad (4.35)$$

This indeed happens to be the case when worked out in detail. This is therefore known as the super-Higgs mechanism, by which local supersymmetry is broken and the gravitino acquires mass. The analogy is summarized in Table 4.1.

Just as the VEV  $v$  sets the energy scale for electroweak symmetry breaking and the mass scale of the particles in the weak sector, the VEV  $F$  (which has dimensions of  $[M]^2$ ) sets the energy scale  $\sqrt{F}$  for supersymmetry breaking and the mass scale of the superpartners,  $m_{\text{soft}}$ . However, the exact relation between  $F$  and  $m_{\text{soft}}$  depends on how the supersymmetry-breaking field communicates with the superpartners. For various reasons, in the MSSM, this field cannot be one of the MSSM fields; most likely, it should instead be a gauge singlet that does not directly (or strongly) communicate with the fields of the standard model. Many models of supersymmetry breaking thus place the supersymmetry-breaking field in a “hidden” sector; supersymmetry is first broken in this sector, and

<sup>5</sup>This is a rough description of simple “ $F$ -term” breaking. In  $F$ -term breaking, the VEV is actually given to an auxiliary field in the supermultiplet, not the complex scalar or the Weyl fermion. Such auxiliary fields are introduced to close the supersymmetry algebra off-shell (where the Weyl fermion gains two extra degrees of freedom), such that the numbers of bosonic and fermionic degrees of freedom remain equal. Auxiliary fields also appear in the *superfield* and *superspace* formulations of supersymmetric theories. Also note that “ $D$ -term” breaking, where a VEV is given to an auxiliary component of a *gauge* supermultiplet, is also possible, as well as some combination of both  $F$ -term and  $D$ -term breaking.

then this is communicated to the MSSM via interactions common to both the hidden and MSSM sectors.

These interactions must avoid increasing the amount of flavor violation in standard-model processes, since flavor violation is strongly constrained by experiments. The two obvious possibilities are gravitational interactions and the standard-model gauge interactions, since these are both indeed flavor blind. The first possibility is thus called *gravity-mediated* supersymmetry breaking. Since we require  $m_{\text{soft}}$  to vanish in the limits  $F \rightarrow 0$  (where supersymmetry is restored) and  $M_* \rightarrow \infty$  (where gravity is negligible), by dimensional analysis, the superpartner masses in such models must be

$$m_{\text{soft}} \sim \frac{F}{M_*} \sim m_{\tilde{G}}, \quad (4.36)$$

which can be compared to the gravitino mass found in Eq. (4.35). Since the superpartner masses should be at the weak scale, the energy scale of supersymmetry breaking is relatively high in these models,  $\sqrt{F} \sim 10^{10}\text{--}10^{11}$  GeV. Furthermore, the mass of the gravitino would also be at the weak scale and would be comparable to the masses of the superpartners; it is thus possible that the gravitino is not the LSP in such scenarios, possibly ruling it out as a dark-matter candidate.

However, in the second possibility, supersymmetry breaking is communicated by the ordinary standard-model gauge interactions, which also avoids flavor violation [211–216]. In such models, mediating fields that couple the supersymmetry-breaking field in the hidden sector and also have standard-model gauge interactions communicate the supersymmetry breaking radiatively via loop diagrams. These “messenger” fields may have masses  $M_{\text{mess}} \ll M_*$ , leading to superpartner masses

$$m_{\text{soft}} \sim \frac{\alpha_i}{4\pi} \frac{F}{M_{\text{mess}}}, \quad (4.37)$$

where  $\alpha_i/4\pi$  is a loop factor arising from the loop diagrams involving gauge interactions. Again requiring weak-scale superpartner masses, we see that the energy scale of supersymmetry breaking  $\sqrt{F}$  may be low if  $M_{\text{mess}}$  is small; in fact, it may be as low as  $\sqrt{F} \sim 10^4$  GeV, if  $\sqrt{F}$  and  $M_{\text{mess}}$  are comparable. Comparing with the gravitino mass given by Eq. (4.35), we see that gravitino masses as small as an eV are possible! Thus,  $m_{\tilde{G}} \ll m_{\text{soft}}$  may be realized in such *gauge-mediated* supersymmetry breaking (GMSB) scenarios, and the gravitino may indeed be the LSP — and hence, a dark-matter candidate.

#### 4.1.4 Gravitino interactions

Let us now discuss the interactions between gravitinos and other particles in the MSSM. One intuitive way to understand the interactions can be gleaned from a discussion of how supersymmetry relates standard-model interaction vertices to their “supersymmetrized” analogues. An example of this

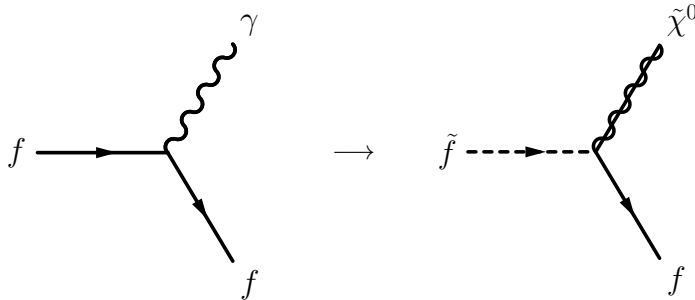


Figure 4.1: Supersymmetrization of the gauge vertex for quantum electrodynamics (on the left) implies a coupling between a neutralino, a charged fermion, and a charged sfermion (on the right). This is achieved by exchanging the photon and one of the fermions in the gauge vertex with their superpartners.

supersymmetrization is shown in Figure 4.1. The basic gauge vertex, which couples the gauge field to the matter current via a gauge-field–fermion–fermion interaction, is shown on the left; specifically, we show the basic vertex of quantum electrodynamics (QED), which couples charged fermions to photons. In general, supersymmetry implies that there are supersymmetrized versions of such gauge vertices, with similar coupling strengths, which may be found by exchanging in the gauge vertex two of the legs with their superpartners. On the right of Figure 4.1, both the gauge boson and one of the fermions have been exchanged, yielding a supersymmetrized vertex that implies a gaugino-fermion-sfermion coupling; in particular, the supersymmetrized QED vertex shown here implies that a coupling between a neutralino, a charged fermion, and a charged sfermion exists.<sup>6</sup>

Thus, to find the gravitino interactions, we may similarly use this supersymmetrization procedure on interactions involving *gravitons*, such as those shown on the left in Figure 4.2. Although the complete quantum field theory involving gravitons is not known, if they are to serve as the gauge fields that mediate the force of gravity between other particles, the effective vertices coupling the graviton to both matter fermions and gauge bosons shown in this figure should exist, with couplings suppressed by the Planck mass. The supersymmetrized versions of these vertices then yield the gravitino interactions; as can be seen, the interactions are of the form gravitino-partner-superpartner, and should also be of gravitational strength.

More rigorously, these properties of the gravitino interactions can be straightforwardly read off from the interaction terms we derived previously. Recall that an interaction term coupling the gravitino to the supercurrent was added to the Lagrangian to partially restore local supersymmetry invariance. Examination of the form of the supercurrent  $S^\mu$ , given in Eq. (4.16), shows that it contains both  $\chi$  and  $\phi$  — i.e., both partner and superpartner; similarly, if gauge supermultiplets are also properly accounted for, the supercurrent will also include terms containing both the gauge-boson

<sup>6</sup>Taking the rule strictly, one might take that the coupling here is to the superpartner of the photon (i.e., the photino), but there are in fact such couplings for neutralinos in general.

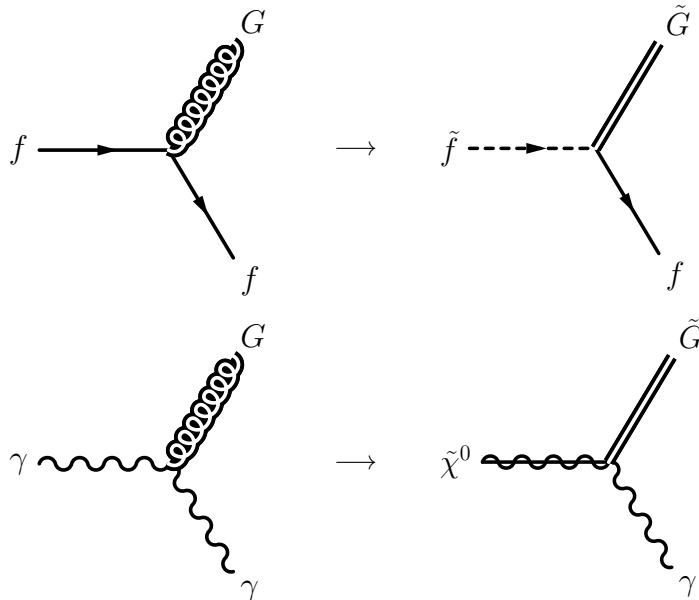


Figure 4.2: Examples of graviton (represented here by  $G$ ) and gravitino ( $\tilde{G}$ ) couplings. Top row: Supersymmetrization of the graviton-fermion coupling implies a gravitino-fermion-sfermion interaction. In GMSB models, this leads to  $\tilde{\tau} \rightarrow \tau\tilde{G}$  decays. Bottom row: Supersymmetrization of the graviton-photon coupling implies a gravitino-photon-neutralino interaction. In GMSB models, this leads to  $\tilde{\chi}^0 \rightarrow \gamma\tilde{G}$  decays.

partners and gaugino superpartners. It is then clear that interactions of the form gravitino-partner-superpartner should indeed arise from the gravitino-supercurrent coupling. Furthermore, since the coupling occurs with strength  $\kappa = 1/M_*$ , we should expect these gravitino interactions to be Planck-suppressed along with the analogous graviton interactions.

One might expect that the suppression of these gravitino interactions by their Planck-mass-scale couplings dims the prospects for interesting gravitino phenomenology. However, a subtlety prevents the complete Planck suppression of the gravitino interactions, giving rise to the possibility of “stronger-than-gravitational” interactions. This subtlety stems from the details of the super-Higgs mechanism. Recall that the gravitino acquires its mass by eating the spin-1/2 goldstino fermion  $\tilde{G}$  that arises when supersymmetry is broken by a field that gains a VEV  $F$  [217–220]. Another consequence of this mechanism is that an effective goldstino interaction term appears in the Lagrangian,

$$\mathcal{L}_{\tilde{G}} = -\frac{1}{F}\tilde{G}\partial_\mu S^\mu + \text{h.c.} \quad (4.38)$$

$$= \frac{1}{F}\partial_\mu\tilde{G}S^\mu + \text{h.c.} + \text{tot. der.}, \quad (4.39)$$

which exhibits a *derivative* coupling between the goldstino and the supercurrent; this implies interactions of the form goldstino-partner-superpartner — similar to that of the gravitino interac-



tions — should exist. Furthermore, we see that although the strength of the coupling given by  $1/F \sim 1/M_* m_{\tilde{G}}$  is Planck-suppressed, it is also enhanced by a factor inversely proportional to the gravitino mass. Thus, when the gravitino eats the two degrees of freedom of the goldstino in order to acquire mass, it inherits the stronger-than-gravitational interactions of the goldstino components. *Light* gravitinos — such as those that arise in GMSB models — may then have phenomenology that is experimentally accessible.

Let us summarize our motivations from particle physics for considering the light gravitino as a dark-matter candidate: Weak-scale supersymmetry is one of the most promising ideas for new physics beyond the standard model. Supersymmetric theories that incorporate local supersymmetry (or supergravity) predict the existence of the gravitino, the spin-3/2 superpartner of the graviton. When supersymmetry is broken, the gravitino acquires a mass through the super-Higgs mechanism, eating the spin-1/2 goldstino, the Goldstone fermion associated with spontaneously broken local supersymmetry. In contrast to other superpartners, the gravitino can have a mass  $m_{\tilde{G}}$  that is not at the weak scale, and viable models exist for gravitino masses as low as the eV scale and as high as 100 TeV. In this work, we specifically consider light gravitinos, with mass in the eV to MeV range. Such gravitinos are highly motivated in particle physics, as they emerge in models with gauge-mediated supersymmetry breaking, in which constraints on flavor violation are naturally satisfied. Furthermore, the interactions of such light gravitinos with other particles in the MSSM are enhanced such that they are stronger-than-gravitational, giving rise to the possibility of interesting phenomenology.

We now turn to a study of the collider phenomenology of light gravitinos and the cosmological implications that observation of gravitino signals might have for the early Universe.

## 4.2 Introduction

Although highly motivated from a particle-physics standpoint alone, light gravitinos with mass in the eV to MeV range also have cosmological motivations. In particular, they are the original supersymmetric dark-matter candidate [221]. Assuming a high reheating temperature, gravitinos are initially in thermal equilibrium and then freeze out while still relativistic. As we discuss in detail below, their resulting relic density is

$$\Omega_{\tilde{G}} h^2 \approx \left[ \frac{m_{\tilde{G}}}{1 \text{ keV}} \right] \left[ \frac{106.75}{g_{*S,f}} \right], \quad (4.40)$$

where  $g_{*S,f}$  is the number of relativistic degrees of freedom at freeze-out, and has been normalized to the total number of degrees of freedom in the standard model. When originally proposed in

the 1980s, uncertainties in  $h$  and the total matter relic density allowed  $m_{\tilde{G}} \sim \text{keV}$ . This led to a simple and attractive gravitino-dark-matter scenario, consistent with standard big bang cosmology, in which the Universe cooled from some high temperature, and keV gravitinos froze out and now form all of the dark matter.

In the intervening years, however, a variety of astrophysical constraints have greatly complicated this picture. First, the dark-matter relic density is now known to be  $\Omega_{\text{DM}} h^2 \approx 0.11$ . Second, constraints on structure formation, as probed by galaxy surveys and Lyman- $\alpha$  forest observations, require that the bulk of dark matter be cold or warm [222]. As we will discuss more fully below, this leads to three scenarios of interest:

1.  $m_{\tilde{G}} \lesssim 15\text{--}30 \text{ eV}$ : Gravitinos are produced by the standard cosmology leading to Eq. (4.40); they are hot dark matter, but their contribution is small enough to be consistent with the observed small-scale structure. Some other dark-matter particle is required.
2.  $15\text{--}30 \text{ eV} \lesssim m_{\tilde{G}} \lesssim \text{few keV}$ : Nonstandard cosmology and a nonstandard gravitino production mechanism are required, both to avoid overclosure and to cool the gravitinos to satisfy small-scale-structure constraints. Some other dark-matter particle may be required.
3.  $m_{\tilde{G}} \gtrsim \text{few keV}$ : Nonstandard cosmology is required to dilute the thermal relic density of Eq. (4.40). Gravitinos produced by thermal freeze-out are cold enough to be all of the dark matter.

Note that the original “keV gravitino” scenario, previously favored, is now the most disfavored, in the sense that it is excluded by both overclosure and small-scale-structure constraints. All of the possibilities are rather complicated, however, as in each case, some additional physics is required, either to provide the rest of the dark matter or to modify the history of the early Universe to allow gravitinos to be all of the dark matter.

In this study, we discuss how collider data may help clarify this picture. Light gravitinos are primarily produced at colliders in the decays of the next-to-lightest supersymmetric particle (NLSP). It is a remarkable coincidence that modern particle detectors, with components placed between 1 cm to 10 m from the beamline, are beautifully suited to distinguish between the NLSP decay lengths predicted in scenarios 1, 2, and 3. For example, the decay length of a bino NLSP decaying to a gravitino is [223]

$$c\tau \approx 23 \text{ cm} \left[ \frac{m_{\tilde{G}}}{100 \text{ eV}} \right]^2 \left[ \frac{100 \text{ GeV}}{m_{\tilde{B}}} \right]^5 . \quad (4.41)$$

This implies that scenarios 1, 2, and 3 make distinct predictions for collider phenomenology, and the identification of the gravitino collider signatures realized in nature may have far-reaching implications for the early Universe.

Of course, this requires that gravitinos can be produced in sufficient numbers and distinguished from standard-model backgrounds. In this work, we determine event rates for a variety of signatures,

including prompt di-photons and delayed and nonpointing photons (relevant for neutralino-NLSP scenarios), as well as kinked charged tracks and heavy metastable charged particles (relevant for stau-NLSP scenarios). We present results for an assumed final Tevatron dataset (20 fb<sup>-1</sup> of 2 TeV  $p\bar{p}$  collisions), an early LHC dataset (1 fb<sup>-1</sup> of 7 TeV  $pp$  collisions), and a future LHC dataset (10 fb<sup>-1</sup> of 14 TeV  $pp$  collisions). We find that the final Tevatron and early LHC data have roughly equivalent sensitivity to these events, with both capable of seeing hundreds of distinctive light-gravitino events. The full LHC data greatly extends the reach in parameter space, and may also allow precision measurements of NLSP lifetimes and gravitino masses.

We begin in Section 4.3 by reviewing the cosmological bounds on light gravitinos and discussing how these bounds are relaxed in early-Universe scenarios that differ from the canonical one. In Section 4.4 we then discuss NLSP decays to gravitinos, GMSB models, and current collider constraints. In Section 4.5 we present our results for the number of light-gravitino events at colliders, based on collider simulations, and discuss the cosmological implications. We summarize our conclusions in Section 4.6.

Due to their large sizes, several of the remaining figures in this chapter have been placed at the end of the chapter.

## 4.3 Light-gravitino cosmology

### 4.3.1 Canonical scenario

#### 4.3.1.1 Relic abundance

In the currently canonical scenario, after inflation, the Universe is reheated to a temperature  $T_R$  that is assumed to be far higher (e.g., 10<sup>12</sup> or 10<sup>15</sup> GeV) than the weak scale. During this phase, inelastic scattering processes and decays can convert standard-model particles in the thermal bath into gravitinos [224–228]. The rate  $C_{\tilde{G}}$  per unit volume for production of light gravitinos (strictly speaking, only the spin-1/2 goldstino components) can be calculated by considering all such processes, which primarily involve strong [229] and electroweak gauge bosons [230, 231], as well as top quarks [232]. The total result, valid in the limit  $T \gg m_{\text{SUSY}}$ , where  $m_{\text{SUSY}}$  is the scale of the superpartner masses, is [232]

$$C_{\tilde{G}} \approx 15 \frac{m_{\tilde{g}}^2}{m_{\tilde{G}}^2} \frac{T^6}{M_{\text{pl}}^2}, \quad (4.42)$$

where  $M_{\text{pl}} \approx 1.2 \times 10^{19}$  GeV is the Planck mass. Here we have assumed that the gaugino masses  $m_{\tilde{g},1}$ ,  $m_{\tilde{g},2}$ , and  $m_{\tilde{g},3}$  and the trilinear scalar coupling  $A_t$  are at a common mass scale. For simplicity, we have set them equal to a universal gaugino mass  $m_{\tilde{g}}$ .

The evolution of the gravitino number density  $n_{\tilde{G}}$  via these production processes, and their

inverses, is governed by the Boltzmann equation

$$\frac{dn_{\tilde{G}}}{dt} + 3Hn_{\tilde{G}} = C_{\tilde{G}} - \Gamma n_{\tilde{G}} , \quad (4.43)$$

where  $H$  is the Hubble expansion rate and  $\Gamma$  is the rate of processes that annihilate gravitinos. The  $3Hn_{\tilde{G}}$  term accounts for dilution of the number density due to cosmological expansion. If  $\Gamma \gg H$ , gravitinos are in thermal equilibrium,  $\Gamma n_{\tilde{G}} = C_{\tilde{G}}$ , and their number density (the solution to the Boltzmann equation) is

$$n_{\tilde{G}}^{\text{eq}} = g \frac{3\zeta(3)}{4\pi^2} T^3 \approx 0.18 T^3 . \quad (4.44)$$

Here we used  $g = 2$ , since it is primarily the spin-1/2 goldstino components that are produced thermally.<sup>7</sup>

The rate  $\Gamma$  at which a given gravitino is destroyed in the plasma is then

$$\Gamma = \frac{C_{\tilde{G}}}{n_{\tilde{G}}^{\text{eq}}} \approx 80 \frac{m_{\tilde{g}}^2 T^3}{m_{\tilde{G}}^2 M_{\text{pl}}^2} . \quad (4.45)$$

Since  $\Gamma \propto T^3$  and  $H \propto T^2$ , the ratio  $\Gamma/H \propto T$  is largest at the highest temperatures. Thus, if  $\Gamma(T_R) \gtrsim H(T_R)$  at reheating, then gravitinos come into thermal equilibrium shortly after reheating. During this era, the expansion rate is given by  $H \approx 1.66 g_*^{1/2} T^2 / M_{\text{pl}}$ ; assuming reheating temperatures  $T_R \gg \text{TeV}$ , at which all particles in the minimal supersymmetric standard model (MSSM) are relativistic, we set the number  $g_*$  of relativistic degrees of freedom to  $g_*(T_R) \approx 228.75$ . Comparing  $\Gamma(T_R)$  and  $H(T_R)$ , we then see that if the reheating temperature satisfies

$$T_R \gtrsim T_f \equiv 4 \text{ GeV} \left[ \frac{m_{\tilde{G}}}{\text{keV}} \right]^2 \left[ \frac{\text{TeV}}{m_{\tilde{g}}} \right]^2 , \quad (4.46)$$

then gravitinos come into thermal equilibrium after reheating. Recalling that the production rate, Eq. (4.42), used here is valid only for  $T \gg m_{\text{NLSP}}$  (i.e.,  $T \gtrsim 10 \text{ TeV}$ ), we conclude that for weak-scale gluino masses, light gravitinos with  $m_{\tilde{G}} \lesssim \text{MeV}$  will come into thermal equilibrium if the reheating temperature is  $T_R \gtrsim 4 \times 10^6 \text{ GeV}$ .

The creation/annihilation rates for gravitinos at temperatures  $T \lesssim 10 \text{ TeV}$  have not yet been calculated, and so the precise temperature at which gravitinos freeze out (which occurs when  $\Gamma \approx H$ ) cannot yet be determined. Still, gravitinos are produced and destroyed individually, requiring (from R-parity conservation) that each creation/destruction is accompanied by creation/destruction of some other supersymmetric particle. Therefore, the freeze-out temperature  $T_f$  cannot be much lower than the mass  $m_{\text{NLSP}}$  of the NLSP, as the equilibrium abundance of SUSY particles then

<sup>7</sup>This expression has been corrected from the published version, where the number density  $n = g\zeta(3)T^3/\pi^2 \approx 0.24T^3$  for relativistic *Bose-Einstein* particles was mistakenly used (and a typo added an extra factor of 2 in the first equality). This also results in minor corrections to the numerical prefactors that follow.

decreases exponentially. We thus conclude that the freeze-out temperature for light gravitinos falls roughly in the range  $10 \text{ GeV} \lesssim T_f \lesssim 10 \text{ TeV}$ .

With this range of freeze-out temperatures,  $T_f \gg m_{\tilde{G}}$ , so gravitinos are relativistic when they freeze out. The relic gravitino density is then [221]

$$\Omega_{\tilde{G}} h^2 \approx 0.1 \left[ \frac{m_{\tilde{G}}}{100 \text{ eV}} \right] \left[ \frac{106.75}{g_{*S,f}} \right], \quad (4.47)$$

the standard result for hot relics with  $g = 2$ , where  $g_{*S,f}$  is the number of relativistic degrees of freedom when the gravitinos freeze out. If gravitinos freeze out when all of the MSSM degrees of freedom are relativistic,  $T_f \gg m_{\text{SUSY}}$ , and  $g_{*S,f} = 228.75$ . However, it is more likely that freeze-out occurs at  $T \sim m_{\text{NLSP}} \sim 100 \text{ GeV}$ , when  $g_{*S,f} \sim 100$  [233].

#### 4.3.1.2 Cosmological constraints

Given that current cosmic-microwave-background and structure-formation measurements constrain the density of dark matter to be  $\Omega_{\text{DM}} h^2 \approx 0.11$ , Eq. (4.47) implies an upper bound  $m_{\tilde{G}} \lesssim 200 \text{ eV}$ . The upper limit  $m_{\tilde{G}} \approx 200 \text{ eV}$  is saturated if the gravitino makes up *all* of the dark matter and freeze-out occurs when  $g_{*S,f} = 228.75$  is the maximum value allowed in the MSSM. However, a gravitino of this mass would be hot dark matter. It would smooth density perturbations on scales probed by galaxy surveys and the Lyman- $\alpha$  forest to a degree that is highly inconsistent with data. As  $m_{\tilde{G}}$  is reduced from this upper limit, the smoothing scale is increased (the gravitinos get “hotter”), but the gravitino abundance is reduced, thus making the magnitude of the smoothing smaller. A combination of data from the cosmic microwave background, galaxy surveys, and the Lyman- $\alpha$  forest constrain the contribution of a hot component of dark matter to be  $\lesssim 15\%$  [222], implying for  $g_{*S,f} \approx 100$  that  $m_{\tilde{G}} \lesssim 15 \text{ eV}$ . This suggests that the most conservative upper bound is given by  $m_{\tilde{G}} \lesssim 30 \text{ eV}$ , in the case that  $g_{*S,f} \approx 200$  approaches the maximal value allowed in the MSSM. Therefore, in this canonical scenario, thermal gravitinos with mass less than 30 eV make up only a fraction of the dark matter, thus requiring some other particle to be the cold dark matter. This is the first cosmological scenario listed in Sec. 4.2.

We conclude by noting that future astrophysical data are likely to improve. And while the current sensitivity is to gravitino masses as small as 15–30 eV, it is forecast that next-generation experiments may be sensitive to gravitino masses as small as 1 eV [234]. A collider detection of a gravitino in the mass range  $m_{\tilde{G}} = 1\text{--}30 \text{ eV}$  would thus lead to testable consequences in forthcoming cosmological data.

### 4.3.2 Nonstandard early-Universe scenarios

There are several ways in which the early-Universe production of relic gravitinos could differ from the canonical scenario outlined above. Thus, there are scenarios in which a gravitino of mass  $m_{\tilde{G}} \gtrsim 30$  eV, ruled out in the canonical model, could be cosmologically consistent or, better yet, completely compose the dark matter.

Let us first consider scenarios in which the gravitinos reach thermal equilibrium in the early Universe, since most observational constraints are strictly valid only under this assumption. As mentioned above, if we only consider particles in the MSSM, then  $g_{*S,f} \leq 228.75$ , and Eq. (4.47) suggests an upper limit of  $m_{\tilde{G}} \lesssim 200$  eV from the relic abundance constraint. One way to evade this limit is to simply consider higher values of  $g_{*S,f}$ ; i.e., gravitinos decouple and freeze out earlier than in the canonical scenario. This may be possible in models with more degrees of freedom than the MSSM. More massive gravitinos that decouple earlier may then be viable, if they have an abundance that obeys the constraint  $\Omega_{\text{DM}} h^2 \lesssim 0.11$ .

It is possible that this constraint is saturated and that these heavier gravitinos entirely compose the dark matter. Of course, we must still require that these heavier gravitinos are not so hot as to erase structure to a degree that contradicts observations. The same combination of cosmic-microwave-background, galaxy-survey, and Lyman- $\alpha$ -forest data that was used to constrain  $m_{\tilde{G}} \lesssim 30$  eV in the canonical scenario can also be used to constrain the gravitino mass in this early-decoupling scenario, assuming that thermal gravitinos make up all of the dark matter. With this assumption, Ref. [222] finds  $m_{\tilde{G}} \gtrsim 550$  eV, using a selection of Lyman- $\alpha$  data. The same authors later find a stronger constraint,  $m_{\tilde{G}} \gtrsim 2$  keV, with SDSS Lyman- $\alpha$  data [235, 236], a result slightly weaker than a bound on warm dark-matter models obtained by Ref. [237]. A number of other small-scale observations also seem to support that  $m_{\tilde{G}} \gtrsim$  few keV under these assumptions [23].

We thus conclude that if  $30$  eV  $\lesssim m_{\tilde{G}} \lesssim$  few keV, then thermal gravitinos are too warm to be the only component of the dark matter, regardless of whether or not they have the correct abundance. Gravitinos in this mass range would only be viable if some other nonstandard early-Universe process cools them, or if there is an additional cold component. This is the second scenario mentioned in Sec. 4.2. However, if  $m_{\tilde{G}} \gtrsim$  few keV, then gravitinos may be sufficiently cold, and may in early-decoupling scenarios have the right abundance, to be the dark matter. This is the third scenario outlined in Sec. 4.2.

Of course, aside from early decoupling, there are other nonstandard mechanisms that can reduce the gravitino abundance. For example, recall that we have no empirical constraints to the early Universe prior to the epoch of big-bang nucleosynthesis (BBN), at which  $T \gtrsim$  few MeV [238]. Thus, some entropy-producing process prior to BBN could also dilute the gravitino abundance. It is possible that there may be some exotic early-Universe physics that conspires to produce the same effect. One relatively simple possibility is that the reheating temperature is low. If the reheating

temperature is smaller than the freeze-out temperature, then gravitinos will never come into thermal equilibrium, and their relic abundance will thus be accordingly smaller [239–245]. The only catch is that for the light gravitinos we consider here, the reheating temperature must be unusually low for this to occur. For example, if  $m_{\tilde{G}} = \text{keV}$  and  $m_{\tilde{g}} = 300 \text{ GeV}$ , then Eq. (4.46) suggests that the reheating temperature must be  $T_R \lesssim 40 \text{ GeV}$ . However, recall that this estimate may not be strictly valid at  $T \lesssim 10 \text{ TeV}$ , as we have already noted. Thus, a more careful calculation of the production rate of light gravitinos at low reheating temperatures may be necessary. Nevertheless, such low reheating temperatures have been considered [246], and Ref. [247] has examined an explicit low-reheat scenario in which a gravitino of mass  $m_{\tilde{G}} = 1\text{--}15 \text{ keV}$  can have the right abundance to be the dark matter.

Finally, we also note that there may be additional mechanisms affecting the generation of gravitinos. For example, in our discussion we have neglected the nonthermal contribution to the gravitino abundance from out-of-equilibrium decays of other supersymmetric particles. There may also be other significant modes of gravitino production or dilution, including processes involving the messenger particles responsible for GMSB [248–253], nonthermal production via oscillations of the inflaton field [254], Q-ball decays [255], and various other mechanisms [256]. There may thus be other reasons why the gravitino abundance or temperature differs from those in the canonical thermal-production scenario; this may be true even if  $m_{\tilde{G}} \lesssim 30 \text{ eV}$ .

To summarize, in the canonical model, gravitinos are required to have mass  $m_{\tilde{G}} \lesssim 30 \text{ eV}$  and form only a fraction of the dark matter. Gravitinos with mass range  $m_{\tilde{G}} \gtrsim 30 \text{ eV}$  would require non-standard physics or cosmology to reduce their abundance or temperature to agree with observations. Below we discuss collider signatures of light gravitinos. We close here by noting that such collider data may, if gravitinos are discovered, thus help discriminate between the diversity of early-Universe scenarios for gravitino production.

## 4.4 Light gravitinos at colliders

### 4.4.1 Mass and interactions

As discussed in Section 4.1, the gravitino mass is determined by the super-Higgs mechanism. In simple models, it is given in terms of the supersymmetry-breaking scale  $F$ , which has mass dimension 2, as

$$m_{\tilde{G}} = \frac{F}{\sqrt{3}M_*} \approx 240 \text{ eV} \left[ \frac{\sqrt{F}}{10^3 \text{ TeV}} \right]^2, \quad (4.48)$$

where  $M_* \equiv M_{\text{pl}}/\sqrt{8\pi} \approx 2.4 \times 10^{18} \text{ GeV}$  is the reduced Planck mass.

The interactions of weak-scale gravitinos are of gravitational strength, as expected since they are the superpartners of gravitons. However, as discussed previously, the couplings of the goldstino

are proportional to  $1/F$  [257, 258]. The interactions of light gravitinos are therefore dominated by their goldstino components, and may be much stronger than gravitational. Decays to gravitinos are faster for light gravitinos.

For reasons to be discussed below, we will focus on cases where the NLSP is either the neutralino or the stau. The interactions of these NLSPs with the gravitino were previously shown in Figure 4.2. For a neutralino NLSP that is dominantly a bino, the decay widths to gravitinos are [223, 259]

$$\Gamma(\tilde{B} \rightarrow \gamma\tilde{G}) = \frac{\cos^2 \theta_W m_{\tilde{B}}^5}{16\pi F^2} \quad (4.49)$$

$$\Gamma(\tilde{B} \rightarrow Z\tilde{G}) = \frac{\sin^2 \theta_W m_{\tilde{B}}^5}{16\pi F^2} \left[ 1 - \frac{m_Z^2}{m_{\tilde{B}}^2} \right]^4, \quad (4.50)$$

where  $\theta_W$  is the weak mixing angle. For  $m_{\tilde{B}} \lesssim m_Z$ , decays to  $Z$  bosons are negligible or kinematically forbidden, and the corresponding decay length is

$$c\tau \approx 23 \text{ cm} \left[ \frac{m_{\tilde{G}}}{100 \text{ eV}} \right]^2 \left[ \frac{100 \text{ GeV}}{m_{\tilde{B}}} \right]^5. \quad (4.51)$$

For heavier neutralinos, the  $Z$  mode may be significant; for very heavy binos, the branching ratio for this mode is  $B(Z) \approx \sin^2 \theta_W \approx 0.23$ . Decays to  $l^+l^-\tilde{G}$ , where  $l = (e, \mu, \text{ or } \tau)$  is a charged lepton, and  $h\tilde{G}$  may also be possible; however, these modes have branching ratios of  $\sim 0.01$  and  $\sim 10^{-6}$ , respectively.

For stau NLSPs, the decay width is [260]

$$\Gamma(\tilde{\tau} \rightarrow \tau\tilde{G}) = \frac{m_{\tilde{\tau}}^5}{16\pi F^2}, \quad (4.52)$$

corresponding to a decay length

$$c\tau \approx 18 \text{ cm} \left[ \frac{m_{\tilde{G}}}{100 \text{ eV}} \right]^2 \left[ \frac{100 \text{ GeV}}{m_{\tilde{\tau}}} \right]^5. \quad (4.53)$$

As anticipated, in both the neutralino-NLSP and stau-NLSP scenarios, the decay lengths for gravitinos in the cosmologically interesting range correspond to distances that bracket the size of collider detectors.

#### 4.4.2 GMSB models

Light gravitinos are expected to be dominantly produced at colliders in the cascade decays of strongly interacting superpartners, such as squarks and gluinos. Collider constraints therefore depend on the full superpartner spectrum, and so are model dependent. Following most of the literature, we will work in the framework of minimal GMSB, and so we briefly review its features here.



Typical GMSB models are characterized by a hidden sector, a messenger sector, and a visible sector, the MSSM. Supersymmetry breaking is triggered by a hidden-sector gauge-singlet superfield  $S$  acquiring the vacuum expectation value  $S = M + \theta^2 F_S$ . This then generates masses for the messenger-sector fields  $M_{\text{mess}} = \lambda M$ , where  $\lambda$  is a coupling in the superpotential. These in turn generate masses for the visible-sector superpartners that are roughly a loop factor times  $\Lambda \equiv F_S/M$ , and so  $\Lambda \sim 100$  TeV. Note that  $M_{\text{mess}} > \Lambda$  is generally assumed.

In the minimal GMSB framework, the entire superpartner spectrum is specified by the parameters

$$\Lambda, M_{\text{mess}}, N_5, \tan \beta, \text{sgn}(\mu), c_{\text{grav}} . \quad (4.54)$$

Here,  $\Lambda$  and  $M_{\text{mess}}$  are as described above; masses and couplings are generated at  $M_{\text{mess}}$  and then evolved to the weak scale via the renormalization group. The number of messenger superfields is given by  $N_5$ , the effective number of  $\mathbf{5} + \bar{\mathbf{5}}$  representations of  $\text{SU}(5)$ . The Higgs sector is specified by the usual parameters  $\tan \beta$  and  $\text{sgn}(\mu)$ . The last parameter is

$$c_{\text{grav}} \equiv \frac{F}{\lambda F_S} , \quad (4.55)$$

where  $F = (F_S^2 + \sum_i F_i^2)^{1/2}$  is the total supersymmetry-breaking vacuum expectation value, which appears in Eq. (4.48). These relations imply

$$m_{\tilde{G}} = c_{\text{grav}} \frac{M_{\text{mess}} \Lambda}{\sqrt{3} M_*} . \quad (4.56)$$

We expect  $c_{\text{grav}} \gtrsim 1$ , since  $F \geq F_S$  and  $\lambda \lesssim 1$ , and in the minimal case that there is only one nonzero  $F$ -term, we expect  $c_{\text{grav}} \sim 1$ .

The superpartner masses are determined by the parameters of Eq. (4.54); for details, see Ref. [40]. Here we note only two things. First, the superpartner masses are determined by gauge couplings. Thus, although, for example, chargino [261] and sneutrino [262] NLSPs have been considered, the canonical NLSP candidates are those with only hypercharge interactions, namely, the bino and right-handed sleptons. Among the right-handed sleptons, the stau is typically the lightest, as renormalization-group evolution and left-right-mixing effects both decrease the stau mass relative to the selectron and smuon, and so we will focus on the bino-NLSP and stau-NLSP scenarios.<sup>8</sup> Second, the bino and stau masses are proportional to  $N_5$  and  $\sqrt{N_5}$ , respectively. For  $N_5 = 1$ , the NLSP is the bino in minimal GMSB, but for  $N_5 > 1$ , the stau may also be the NLSP; see, for example, Figure 1 of Ref. [260].

Thus, to study the bino-like neutralino-NLSP scenario, we will choose  $N_5 = 1$ ; likewise, we choose

---

<sup>8</sup>Note that in the ‘‘slepton co-NLSP’’ scenario, where the three charged sleptons are degenerate to within the mass of the tau, the number of  $\tilde{e} \rightarrow e\tilde{G}$  and  $\tilde{\mu} \rightarrow \mu\tilde{G}$  decays may be comparable to that of the  $\tilde{\tau} \rightarrow \tau\tilde{G}$  decay that usually dominates gravitino production.

$N_5 = 4$  to study the stau-NLSP scenario. For both scenarios, we fix  $\tan \beta = 20$ ,  $\mu > 0$ , and  $c_{\text{grav}} = 1$ . We let  $\Lambda$  and  $M_{\text{mess}}$  be free parameters. Note that the overall mass scale of the supersymmetric partners is roughly proportional to  $\Lambda$ , while the gravitino mass depends on both  $\Lambda$  and  $M_{\text{mess}}$  as in Eq. (4.56). Thus, scanning over the free GMSB parameters will allow us to explore collider signals for a range of masses. We shall now examine the existing collider constraints on the parameter spaces of these two scenarios.

### 4.4.3 Current collider constraints

The high-energy collider signals of GMSB and gravitinos are well studied [259, 260, 263–277]; for a review of current bounds, see Ref. [278]. Here we summarize the most relevant results for the models and signals we consider below.

We shall discuss GMSB signals in more detail below, but we summarize them briefly here. In the neutralino-NLSP scenario, there are several possible signals. For short-lived neutralinos, nearly all supersymmetry events include two prompt high-energy photons. For longer-lived neutralinos that travel a macroscopic distance before decaying to photons in the detector, delayed or nonprompt photons are possible. The stau-NLSP scenario may also lead to a variety of signatures, depending on the stau lifetime, including acoplanar leptons, tracks with large impact parameters, kinked charged tracks, and heavy metastable charged particles.

Several studies have attempted to place constraints on GMSB models by searching for these signals. Given that we will scan over a large range of the GMSB parameter space, we are primarily interested in constraints that are generally valid over this entire range. We shall thus focus on limits from LEP studies, based on an integrated luminosity of  $628 \text{ pb}^{-1}$  at center-of-mass energies of 189–209 GeV, which combined searches for both GMSB and neutral-Higgs signals [279, 280]. The relevant results for our models are the lower limits of  $\Lambda \gtrsim 70 \text{ TeV}$  for our neutralino-NLSP model, and  $\Lambda \gtrsim 20 \text{ TeV}$  for our stau-NLSP model; see Figure 6 of Ref. [279]. These constraints on  $\Lambda$  are valid for all values of  $M_{\text{mess}}$  we include in our scan. Therefore, the allowed region of  $M_{\text{mess}}-\Lambda$  parameter space is constrained by these LEP bounds.

However, there are also a number of studies that focused on constraining specific benchmark models [281], which occupy certain points or lines in the GMSB parameter space. Although these constraints cannot be directly applied to our models, we discuss them to get an idea of the robustness of the LEP bounds on our parameter space.

Of these benchmark-model constraints, the best collider bounds on di-photon events are from the Tevatron, including a D0 search based on an integrated luminosity of  $1.1 \text{ fb}^{-1}$  [282] and a CDF search based on  $2.6 \text{ fb}^{-1}$  [283]. The D0 and CDF bounds, when interpreted assuming the benchmark GMSB model SPS 8 from Ref. [281], lead to lower bounds on the bino mass of 125 GeV and 150 GeV, respectively. For longer-lived neutralinos that travel a macroscopic distance before

decaying to photons in the detector, a CDF search for delayed photons, based on  $570 \text{ pb}^{-1}$  of data, established lower bounds on  $m_{\tilde{B}}$  from 70 to 100 GeV for neutralino decay lengths between 20 cm and 6 m, again when interpreted in the context of SPS 8 [284].

Searches for heavy metastable charged particles have also been performed at D0 [285], assuming the benchmark GMSB model SPS 7 from Ref. [281]. A similar search was performed at CDF [286], but did not interpret results in the context of GMSB models. Based on  $\sim 1 \text{ fb}^{-1}$  of data, and assuming only Drell-Yan slepton production, the constraints resulting from these two searches are not competitive with the LEP bounds stated previously.

Thus, we shall take the more general LEP bounds as constraints on the two models we consider in this work, and shall further take only conservative values of the lower limits. For the neutralino-NLSP model, we shall only scan the parameter space with  $\Lambda \geq 80 \text{ TeV}$ , which should be comfortably allowed by the LEP bounds. However, we acknowledge that it is possible that the Tevatron data may exclude a small range of NLSP masses within this parameter space comparable to that ruled out in the benchmark model (i.e.,  $\lesssim 150 \text{ GeV}$ ), should this data be reanalyzed in the context of our models. For the stau-NLSP model, we shall scan over  $\Lambda \geq 30 \text{ TeV}$ . Given that the current Tevatron constraints are not competitive with the LEP bounds, all of this parameter space should be allowed. As we will see, hadron colliders have bright prospects for probing the parameter spaces of these models.

## 4.5 Tevatron and LHC prospects

### 4.5.1 Gravitino signals

The collider signal of a supersymmetric particle decaying to a gravitino can be classified by (1) the distance from the interaction point at which the decay occurs, and (2) the nature of the accompanying standard-model decay products. The former is determined by the gravitino mass and the masses of the decaying supersymmetric particles, as well as the speed with which the decaying particles are produced. The latter is determined primarily by the nature of the NLSP. We shall define and investigate the following categories of events:

1. Prompt di-photons (in neutralino-NLSP models): Events in which two photons are produced (via a pair of neutralino decays to gravitinos) within  $d_{\text{pr}}$  of the interaction point. We take  $d_{\text{pr}} = 1 \text{ cm}$  as a conservative estimate of the distance to which the origin of any photon can be resolved in detectors at the Tevatron and the LHC. Note that here and below, we cut on the total distance traveled by the NLSP before it decays, not its (transverse) distance from the beamline when it decays.
2. Nonprompt photons (neutralino NLSP): Events in which at least one photon is produced at

a mid-detector distance  $d_{\text{decay}}$  away from the interaction point, where  $d_{\text{pr}} \leq d_{\text{decay}} \leq d_{\text{np}}$ , and  $d_{\text{np}}$  is the maximum distance from the interaction point at which a photon can be observed. We conservatively take  $d_{\text{np}} = 3$  m, roughly the outer radius of the hadronic calorimeters at both the Tevatron and the LHC. (Note that although the calorimeters in the ATLAS detector at the LHC actually extend to  $\sim 4$  m, those in the CMS detector only extend to  $\sim 3$  m; we have thus taken the more conservative 3 m as our cut.) Photons may also convert and be seen in the muon chambers, extending the sensitivity to decays  $\sim 10$  m from the interaction point, but we neglect this possibility here. Here we also take  $d_{\text{pr}} = 1$  cm.

Note that this category of events encompasses both nonpointing photons and delayed photons. A nonpointing photon is simply a photon that does not spatially point back to the interaction point. A delayed photon has the further distinction of being produced only after a significant temporal delay following the time of the initial collision. This may occur when the particle that decays to the photon is produced with a low speed, so that it takes a non-negligible amount of time to travel away from the interaction point before it decays. If this amount of time is comparable to the time between collision events, it may be difficult to properly identify the delayed photon with its originating event.

3. Nonprompt leptons (stau NLSP): Events in which at least one charged lepton is produced (via charged-slepton decays to gravitinos) at a mid-detector distance  $d_{\text{decay}}$ , where  $d_{\text{pr}} \leq d_{\text{decay}} \leq d_{\text{np}}$  as before. We take  $d_{\text{np}} = 5$  m and  $d_{\text{np}} = 7$  m as the outer radii of the muon chambers in the detectors at the Tevatron and the LHC, respectively. (As above, although the muon chambers in the ATLAS detector at the LHC extend to  $\sim 10$  m, those in the CMS detector only extend to  $\sim 7$  m; we take the more conservative 7 m as our cut.) We again take  $d_{\text{pr}} = 1$  cm. Each of these events produces a distinctive charged track with a kink due to the momentum carried away by the gravitino.

As above, both nonpointing and delayed events are included in this category. Furthermore, we include all generations ( $e$ ,  $\mu$ , and  $\tau$ ). As mentioned previously, the stau is generally the lightest slepton, and hence we expect the majority of the decays in the stau-NLSP scenario to be of the form  $\tilde{\tau} \rightarrow \tau \tilde{G}$ . Although the heavier sleptons  $\tilde{l} = (\tilde{e} \text{ or } \tilde{\mu})$  may also decay to  $l \tilde{G}$ , the branching ratio of this decay is generally suppressed compared to the decay to a lepton and a neutralino, i.e.,  $l \tilde{\chi}^0$ . If the latter is kinematically forbidden, then the 3-body decays to  $l \tau^- \tilde{\tau}^+$  or  $l \tau^+ \tilde{\tau}^-$  dominate instead. However, as the mass splitting between the stau NLSP and the heavier sleptons decreases, these 3-body decays become less dominant (becoming kinematically forbidden if the mass splitting becomes less than the tau mass). The decays to  $l \tilde{G}$  may then occur if the heavier sleptons  $\tilde{l}$  are produced at the end of a decay chain.

4. Metastable sleptons (stau NLSP): Events in which at least one charged slepton passes through the entire detector before decaying to a charged lepton and a gravitino. That is, the gravitino

is produced at  $d_{\text{decay}} \geq d_{\text{ms}}$ , where  $d_{\text{ms}}$  is the distance to the outer edge of the detector. We take  $d_{\text{ms}} = 5$  m and  $d_{\text{ms}} = 10$  m as conservative estimates of the sizes of the detectors at the Tevatron and the LHC, respectively. All generations ( $\tilde{e}$ ,  $\tilde{\mu}$ , and  $\tilde{\tau}$ ) are included. These events will produce charged tracks with a relatively large radius of curvature.

For this category, we impose a further cut, requiring that the speeds  $\beta$  of the sleptons satisfy the criteria  $\beta_{\text{lower}} \leq \beta \leq \beta_{\text{upper}}$ . The lower cut removes slower sleptons, which may be identified with the incorrect collision event. The higher cut removes faster sleptons, which may be misidentified as muons. We take typical values  $\beta_{\text{lower}} = 0.6$  and  $\beta_{\text{upper}} = 0.8$ . Note, however, that Ref. [277] suggests a new search strategy that may be sensitive to even higher values of  $\beta$ .

All of these events will also be distinguished by missing energy and momentum carried away by the gravitinos. Note that these categories are chosen to be illustrative of the variety of signals that may be observed, and that they are not comprehensive — we do not investigate prompt dilepton events or neutralino decays to  $Z$  bosons, for example. Furthermore, the categories are not mutually exclusive; for example, one may easily have a single event in which both a nonprompt lepton and a metastable slepton are produced. It is also clear that the relevant detector systematics and backgrounds will also be different for each category. Finally, note that axino-LSP scenarios may have signals that are qualitatively similar to the very long-lived signatures discussed here; however, the gravitino-LSP and axino-LSP scenarios may be distinguished quantitatively by detailed studies of 3-body decay rates [287].

This categorization of events is somewhat oversimplified, as it is based primarily on cuts on the decay length. Certainly, additional cuts will be required in a realistic analysis, possibly reducing the number of detected signals. However, we shall soon see that these simple categories align with the three cosmological scenarios outlined previously.

#### 4.5.2 GMSB scan and collider simulations

We now calculate the event rates for these gravitino signals in a parameterized GMSB model. A large number of programs have been written for the numerical computation of the mass spectra and collider predictions for parameterized supersymmetric models [288, 289]. In this work, we use ISAJET 7.80/ISASUSY [290] to generate mass spectra and decay branching ratio tables. ISASUSY properly includes a number of 3-body decay processes relevant for gravitino phenomenology that are missing in other branching ratio programs.

ISAJET/ISASUSY takes values of the GMSB parameters listed in Eq. (4.54) as input. As discussed previously, here we focus on parameterizations that fix a subset of the GMSB parameters, resulting in either a neutralino or a stau NLSP. We then scan over  $M_{\text{mess}}$  and  $\Lambda$  (requiring that

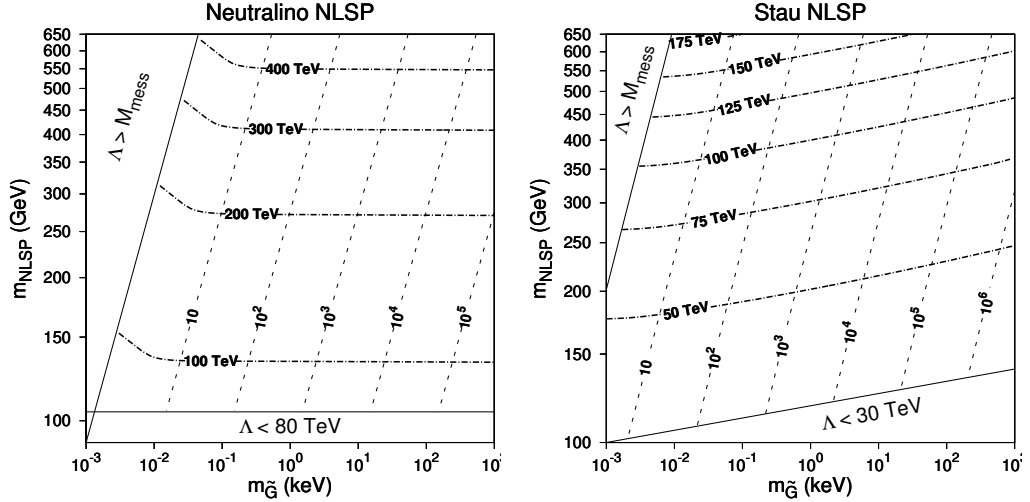


Figure 4.3: Plots showing the mapping between the  $m_{\tilde{G}}-m_{\text{NLSP}}$  and the  $M_{\text{mess}}-\Lambda$  GMSB parameter spaces, for the neutralino-NLSP scenario with  $N_5 = 1$  (left) and stau-NLSP scenario with  $N_5 = 4$  (right), where we fix  $\tan\beta = 20$ ,  $\mu > 0$ , and  $c_{\text{grav}} = 1$  in both cases. Contours of constant  $M_{\text{mess}}/\Lambda$  (dashed black) and  $\Lambda$  (dashed-dotted black) are shown. The region in the upper-left corner is disallowed by theory, while the region at the bottom is excluded by experiment (using the conservative constraints mentioned in the text).

$M_{\text{mess}} > \Lambda$ ), resulting in spectra with a range of gravitino and NLSP masses. The correspondence between the  $M_{\text{mess}}-\Lambda$  scan and the resulting  $m_{\tilde{G}}-m_{\text{NLSP}}$  parameter space is shown in Figure 4.3.

We then take the spectra and decay tables output by ISAJET/ISASUSY and use them as input for the Monte Carlo event generator PYTHIA 6.4.22 [291], including all supersymmetric processes available therein. For a given center-of-mass energy, PYTHIA can simulate a given number of collision events, giving a complete record of the various decay chains and final products generated in each event and an estimation of the various production cross sections. From this record, we can identify the supersymmetric “mother” particles that decay to directly produce gravitino and standard-model “daughter” particles in each individual event. We can also find the decay length  $d_{\text{decay}}$  away from the interaction point that each mother particle travels before decaying to produce a gravitino. Thus, for any number of simulated events, we can find the fraction that fall into each of the above categories. The expected number of signals from each category is then given by the respective fraction multiplied by the total number of supersymmetric events. We can also calculate the average  $\langle d_{\text{decay}} \rangle$  of the decay length, taken over all supersymmetric events.

### 4.5.3 Cosmological implications

The results of the scan are shown in Figures 4.4–4.7. We can see that the simple categorization of collider signals by decay-length cuts corresponds surprisingly well with the categorization of cosmological scenarios outlined previously. For example, Figure 4.4 shows that the observation of

hundreds of prompt events suggests that the first cosmological scenario ( $m_{\tilde{G}} \lesssim 30$  eV) is likely to be valid. Likewise, the second cosmological scenario ( $30 \text{ eV} \lesssim m_{\tilde{G}} \lesssim \text{few keV}$ ) will be implied by the observation of a large number of nonprompt events, as demonstrated by Figures 4.5 and 4.6. Finally, that the observation of a large number of metastable sleptons supports the third cosmological scenario ( $m_{\tilde{G}} \gtrsim \text{few keV}$ ) can be seen in Figure 4.7. We emphasize that this correspondence is not strongly dependent on our specific choice of GMSB models. It is indeed a remarkable coincidence that theoretically motivated supersymmetric and gravitino-mass scales, the physical sizes of collider detectors, and gravitino cosmology all conspire to allow this correspondence.

Note also that we find that the number of gravitino events produced during the initial run of the LHC (center-of-mass energy of 7 TeV and integrated luminosity of  $1 \text{ fb}^{-1}$ ) may be comparable to that produced during an extended run of the Tevatron (center-of-mass energy of 2 TeV and integrated luminosity of  $20 \text{ fb}^{-1}$ ). This is true in regions of parameter space where large numbers of signals are expected. However, the higher center-of-mass energy of the LHC allows it to access regions of parameter space where  $m_{\text{SUSY}}$  is larger; this is especially evident in the neutralino-NLSP scenario, as can be seen by comparing the left and middle panels in both Figures 4.4 and 4.5.

If the distribution of mother-particle decay lengths can be measured with sufficient accuracy along with the total signal rate, then it may be possible to gain some information on the masses of the mother particles and the gravitino. To do so, it will be important to understand the distribution of energies and speeds with which mother particles are produced, since this will directly affect the distribution of decay lengths via dilation of the mother-particle lifetimes. In Figure 4.8, we show some examples of probability distribution functions for the speed  $\beta$  and the Lorentz factor  $\gamma$  of mother particles that decay to gravitinos, for various collider scenarios.

## 4.6 Conclusions

Light gravitinos in the mass range eV to MeV appear in GMSB models that naturally avoid flavor violation. We have examined the decay of supersymmetric particles to light gravitinos at colliders such as the Tevatron and the LHC. These decays will give rise to dramatic signatures, such as prompt di-photons or nonprompt photons, if the NLSP is a neutralino, or kinked charged tracks or heavy metastable charged particles, if the NLSP is a stau (or some other charged particle). We find large regions of the gravitino-mass–NLSP-mass parameter space in which the rate for such events may be appreciable at the Tevatron and LHC and which are consistent with current null supersymmetry searches.

Given that  $m_{\tilde{G}} \ll m_{\text{NLSP}}$  for these events, the decay kinematics of individual events cannot be used to determine the gravitino mass. However, the event rate and the distribution of decay locations may be used to narrow the range of NLSP and gravitino masses. Information about the nature of

the NLSP may also be gleaned from the standard-model decay products.

One of the attractions of supersymmetry has been its ability to provide a natural candidate for the cold dark matter required by a wealth of cosmological observations. Unfortunately, despite being well motivated in GMSB models, the canonical light-gravitino scenario does not provide a natural cold dark-matter candidate. Nevertheless, this canonical scenario does allow gravitinos with masses  $m_{\tilde{G}} \lesssim 30$  eV that compose a fraction of the total dark matter, as determined by current astrophysical constraints on the relic abundance and small-scale structure. Given that upcoming structure-formation observations are expected to probe hot dark-matter masses as low as  $m_{\tilde{G}} \sim$  eV, detection of a gravitino in the mass range  $\text{eV} \lesssim m_{\tilde{G}} \lesssim 30$  eV via prompt signals at colliders would have implications for future small-scale-structure measurements. And although masses  $m_{\tilde{G}} \gtrsim 30$  eV are disfavored, they may still be possible if the pre-BBN history was different than in the canonical scenario. Detection of gravitinos in this mass range via nonprompt and metastable signals at colliders would thus have serious implications for early-Universe cosmology, and may provide some insight into the reheating and inflationary eras. And who knows? There may indeed be new early-Universe physics that results in a gravitino that has the right cosmological abundance and temperature to be the dark matter.



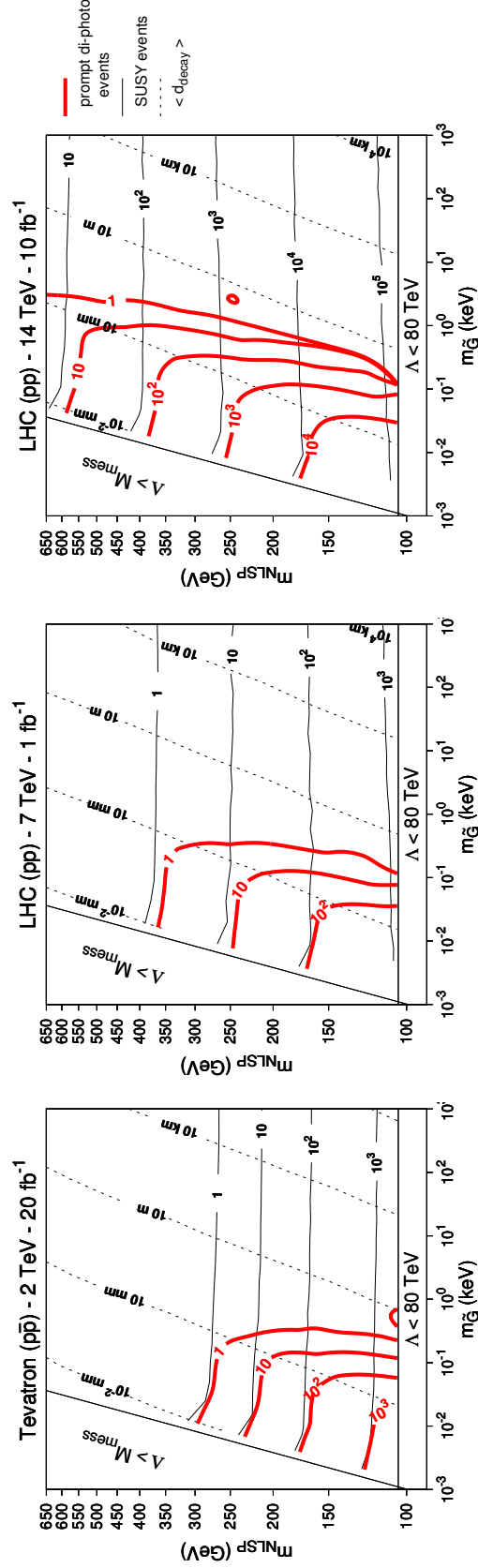


Figure 4.4: Contour plots over the  $m_{\tilde{G}}-m_{\text{NLSP}}$  parameter space showing the expected number of prompt di-photon events (solid red line) in a model with a neutralino NLSP, for the three collider scenarios (indicated at the top of each plot) of interest. The total number of supersymmetric events (dashed-dotted black line) and the average decay length  $\langle d_{\text{decay}} \rangle$  (dashed black line) expected at each point in the parameter space are also indicated by contours. The region in the upper-left corner is disallowed if we require  $\Lambda < M_{\text{mess}}$ , while the region at the bottom is ruled out by LEP (using the conservative constraints discussed in the text). Note that hundreds of signal events may occur at the Tevatron with  $20 \text{ fb}^{-1}$  and at the 7 TeV LHC with  $1 \text{ fb}^{-1}$  if  $m_{\tilde{G}} \lesssim$  tens of eV. Observation of such a number of events would suggest that the canonical thermal-production scenario is correct, and that light gravitinos compose only a fraction of the dark matter. Also, note that a larger fraction of neutralinos instead decay to  $\tilde{Z}\tilde{G}$  as the neutralino mass increases (and that there is some small fraction of decays to  $e^+e^-\tilde{G}$  and  $h\tilde{G}$ ).

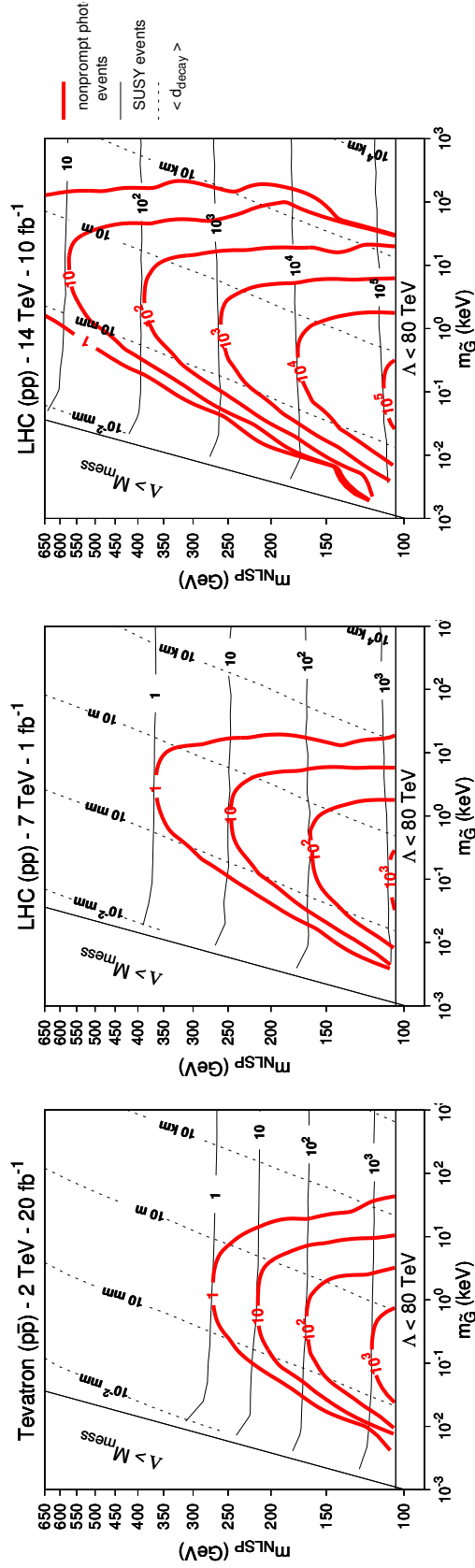


Figure 4.5: The same as Figure 4.4, but for nonprompt photon events. Note that hundreds of signal events may occur at the Tevatron with  $20 \text{ fb}^{-1}$  and at the 7 TeV LHC with  $1 \text{ fb}^{-1}$  if tens of  $eV \lesssim m_{\tilde{G}} \lesssim \text{few keV}$ . Observation of this number of events would suggest that a nonstandard cosmology and gravitino thermal history cooled relic gravitinos, and, for the top part of this mass range, also diluted the relic density.

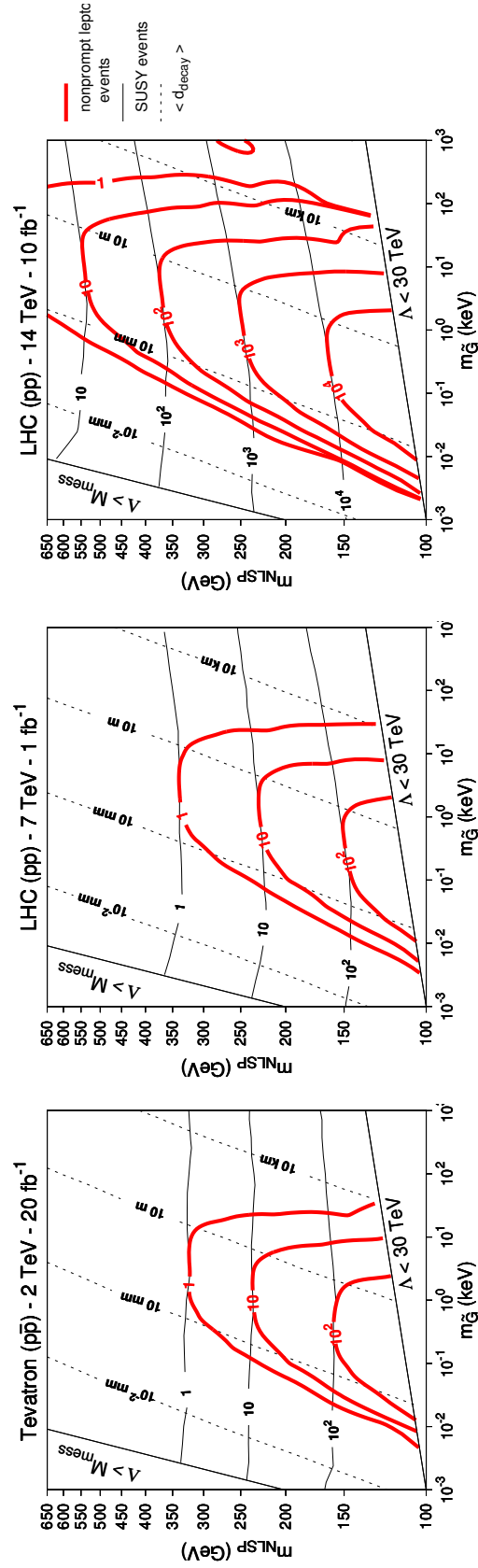


Figure 4.6: Contour plots showing the expected number of nonprompt lepton events in a model with a stau NLSP. Note that hundreds of signal events may occur at the Tevatron with 20  $\text{fb}^{-1}$  and at the 7 TeV LHC with 1  $\text{fb}^{-1}$  if tens of  $eV \lesssim m_{\tilde{g}} \lesssim \text{few keV}$ . Observation of this number of events would suggest that a nonstandard cosmology and gravitino thermal history cooled relic gravitinos, and, for the top part of this mass range, also diluted the relic density.

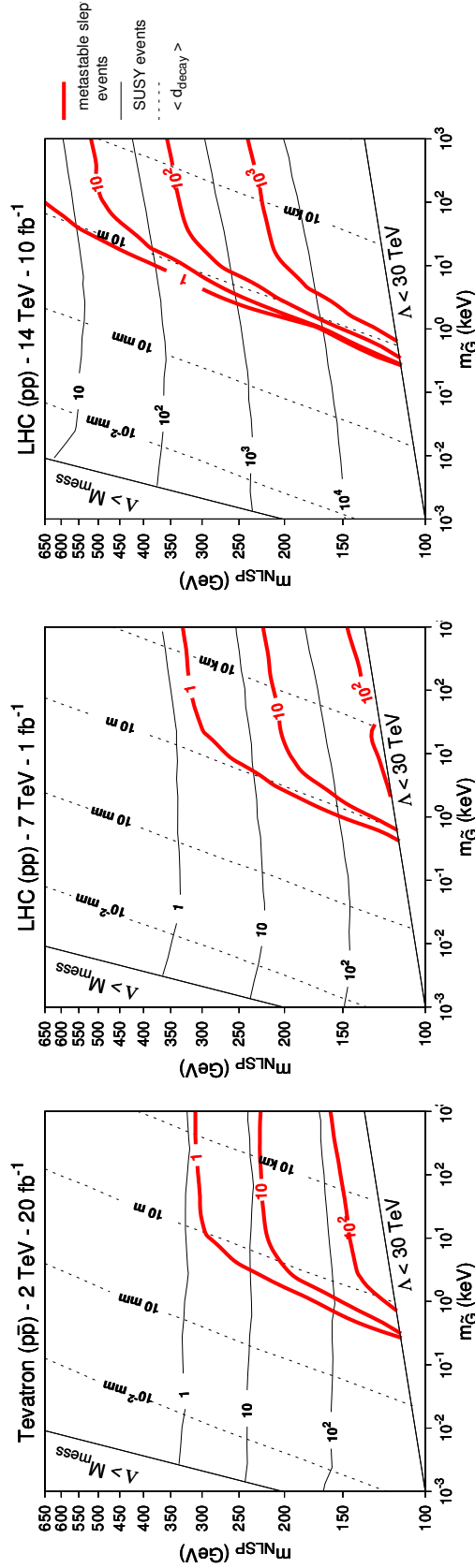


Figure 4.7: The same as Figure 4.6, but for metastable slepton events. Note that hundreds of signal events may occur at the Tevatron with  $20 \text{ fb}^{-1}$  and at the 7 TeV LHC with  $1 \text{ fb}^{-1}$  if  $m_{\tilde{G}} \gtrsim \text{keV}$ . Observation of such a number of events would suggest that gravitinos could entirely compose the dark matter, assuming some nonstandard cosmology diluted relic gravitinos. Also, note that although we only consider  $m_{\tilde{G}} \lesssim \text{MeV}$  here, GMSB models allow larger gravitino masses, up to  $m_{\tilde{G}} \sim \text{GeV}$ . Thus, these plots may be straightforwardly extrapolated to higher gravitino masses if desired. However, note that at higher  $M_{\text{mess}}$ , and hence at higher  $m_{\tilde{G}}$ , the neutralino again becomes the NLSP; see Figure 1 of Ref. [260].

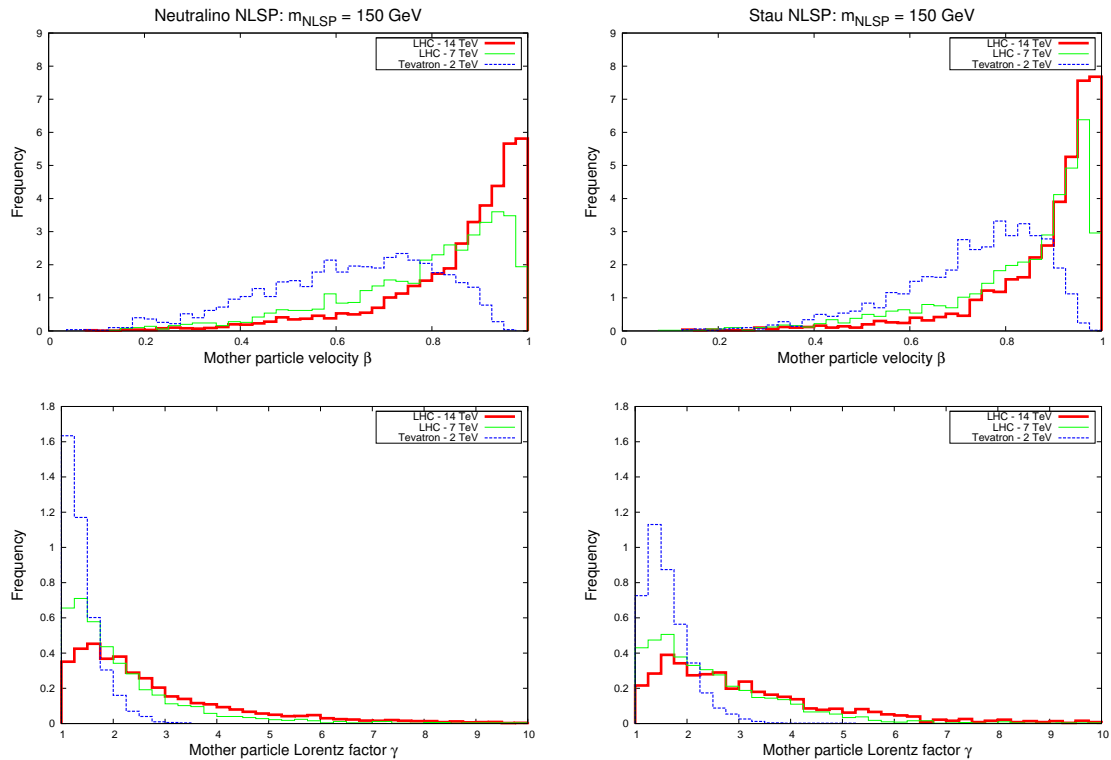


Figure 4.8: Simulated probability distribution functions for the speed  $\beta$  (top panels) and Lorentz factor  $\gamma$  (bottom panels) of mother particles decaying to gravitinos, plotted for the three collider energies of interest, in the neutralino-NLSP (left) and stau-NLSP (right) scenarios. We have chosen models with  $m_{\text{NLSP}} = 150$  GeV for both NLSP scenarios (this was accomplished by choosing  $\Lambda = 115$  TeV in the neutralino-NLSP scenario and  $\Lambda = 40$  TeV in the stau-NLSP scenario, as well as setting  $M_{\text{mess}}/\Lambda = 10^3$  in both scenarios). The area under each curve has been normalized to unity. As expected, increasing the center-of-mass energy results in the production of faster mother particles. Note also that even though  $m_{\text{NLSP}}$  is identical for both of these scenarios, the staus are produced with slightly higher speeds. This is because the squark masses (which increase with increasing  $\Lambda$ ) in the stau-NLSP scenario happen to be slightly lighter than those in the neutralino-NLSP scenario, for these choices of GMSB parameters.

## Chapter 5

# A detour: Charged-particle decay at finite temperature

### 5.1 Introduction

Precise predictions for decay rates of charged particles might be of interest in a variety of cosmological contexts that introduce long-lived particles with electric charge. These include scenarios for modified big-bang nucleosynthesis [292–298] and small-scale-power suppression [299–301] and mechanisms for dark-matter detection wherein a charged quasistable heavier particle is produced [302–310].

In the early Universe, decays of charged particles occur in a thermal bath whose very presence seems to affect decay rates in a peculiar way. Indeed, consider the decay of a hypothetical charged particle  $\psi$  to two lighter particles  $\chi$  and  $\phi$ . The leading-order Feynman diagram is shown in Figure 5.1. In a thermal bath of photons, the process  $\gamma\psi \rightarrow \chi\phi$  also occurs and modifies the vacuum decay rate. Hence, the vacuum decay rate of a particle  $\psi$  must be augmented in the cosmological context by the inclusion of the rate for the “induced” decay wherein the unstable particle absorbs a thermal photon (see Figure 5.2). It is easy to see that a naive computation of the diagrams in Figure 5.2 leads to a divergent result. This divergence is of the infrared type — it appears when the energy of the absorbed photon becomes very small. In this work we discuss in detail how, when all possible processes that modify the vacuum decay rate are taken into account, the infrared divergences cancel out. This is a finite-temperature analog of the celebrated cancellation of infrared divergences in QED pointed out by Bloch and Nordsieck long ago [311].

Although thermal effects have been computed for static thermodynamic quantities such as the effective potential, the free energy, the pressure, and so on [312], sometimes to very high orders in the perturbative expansion in QCD and QED (for recent reviews, see Refs. [313, 314]), less is known about finite-temperature corrections to cross sections and decay rates. Radiative corrections

---

Material in this chapter was first published in “Charged-particle decay at finite temperature,” Andrzej Czarnecki, Marc Kamionkowski, Samuel K. Lee, and Kirill Melnikov, *Phys.Rev.* **D85**, 025018 (2012) [35]. Reproduced here with permission, ©2012 by the American Physical Society.

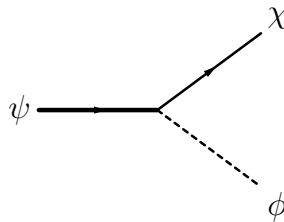


Figure 5.1: The diagram for the decay  $\psi \rightarrow \phi\chi$ . Note that we shall distinguish between the  $\psi$  and  $\chi$  particles in the diagrams below by representing them with thick and thin solid lines, respectively.

to dynamical scattering and decay processes at a finite temperature  $T$  are peculiar for three reasons. First, as pointed out already, if  $T \neq 0$ , new processes involving absorption and emission of particles from the heat bath contribute to cross sections and decay rates. The second complication is that the preferred reference frame defined by the heat bath spoils Lorentz invariance. Third, thermal averages and loop integrals over Bose-Einstein distributions introduce infrared divergences that are powerlike, rather than logarithmic.

Pioneering studies of radiative corrections to neutron  $\beta$ -decays at finite temperature were first described in Refs. [315–318], in the context of big-bang nucleosynthesis. In Ref. [319], the finite-temperature decay rate of a neutral Higgs boson into two charged leptons was first computed. These and subsequent papers [320–333] illustrated the cancellation of infrared divergences and clarified many important features of radiative corrections. They also discussed the issue of radiative corrections that are enhanced by the logarithms of small masses of final-state charged particles. Such terms are known to cancel in total decay rates at zero temperature [334], but the situation at finite temperature is less clear.

Most of the papers just described dealt only with a neutral initial state; in such a case, the problem of an infinite decay rate induced by absorption of very soft photons by the initial state does not occur. Here we discuss the calculation of radiation corrections for a charged initial state, where this issue can not be avoided. For simplicity, we begin by considering a toy model of charged-fermion decay and focus on the low-temperature case. We introduce the toy model in Section 5.2 and calculate the decay rate induced by real-radiation scattering processes in the thermal bath (i.e., absorption and emission of photons), showing how infrared divergences arise. In Section 5.3, we compute the virtual radiative corrections to the decay rate. In Section 5.4, we sum the real and virtual corrections to find the total finite-temperature decay rate, and demonstrate the cancellation of the divergences at first order in perturbation theory. We carry out an analogous analysis for muon decay in Section 5.5.

We conclude and consider the implications for charged particles in the early Universe in Section 5.6.

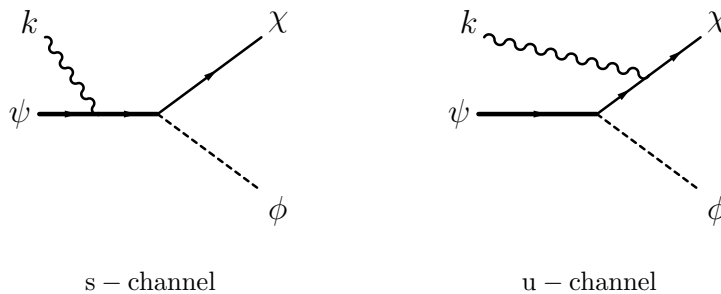


Figure 5.2: The two diagrams via which absorption of a photon can lead to induced  $\psi$  decay (or  $\chi$  and  $\phi$  production)

## 5.2 Toy model

We shall first discuss a simple model to illustrate the nature of the infrared divergences and their cancellation. Consider the process  $\psi \rightarrow \chi\phi$ , the decay of a heavy charged fermion  $\psi$  to a light charged fermion  $\chi$  and a massless neutral scalar  $\phi$  via the interaction

$$\mathcal{L} \supset g\phi\bar{\psi}L\chi + \text{h.c.}, \quad (5.1)$$

depicted in Figure 5.1. Here  $L = (1 - \gamma_5)/2$ . We shall assume that the charge of both fermions is the elementary charge  $e = \sqrt{4\pi\alpha}$ , and that the mass ratio  $\epsilon \equiv m_\chi/m_\psi$  is small.

At  $T = 0$ , the tree-level amplitude for the decay  $\psi \rightarrow \chi\phi$  is given by

$$\mathcal{M}_{\text{tr}} = g\bar{u}_\chi L u_\psi. \quad (5.2)$$

This amplitude gives the  $\mathcal{O}(g^2\alpha^0)$  zero-temperature decay rate,

$$\tilde{\Gamma}_0 = \Gamma_0(1 - \epsilon^4), \quad (5.3)$$

where we have defined  $\Gamma_0 \equiv \frac{g^2}{32\pi}m_\psi$ . We will state our subsequent results for the temperature-dependent decay rate in terms of  $\Gamma_0$ .

On account of radiative corrections and finite-temperature effects, the decay rate can be written as a triple series in  $\tau = T/m_\psi$ ,  $\epsilon = m_\chi/m_\psi$ , and the fine-structure constant  $\alpha$ . Unless explicitly stated otherwise, we work in the low-temperature approximation  $\tau \ll \epsilon \ll 1$ . Our goal is to compute relative corrections to the decay rate that scale as  $\alpha\tau^2$ . In those terms, we shall set  $\epsilon \rightarrow 0$ . Note that terms of the form  $\tau/\epsilon$  do not appear in the total decay rate.



### 5.2.1 Photon absorption

We now consider the process  $\gamma\psi \rightarrow \chi\phi$ , the induced decay of  $\psi$  in a thermal bath of photons. This process can occur via the two diagrams shown in Figure 5.2. For a photon with 4-momentum  $k = (\omega, \mathbf{k})$ , where  $\omega = |\mathbf{k}|$ , the tree-level amplitudes for these channels are

$$\mathcal{M}_{\text{abs,s}} = \frac{eg}{s - m_\psi^2} \bar{u}_\chi L(\not{p}_\psi + \not{k} + m_\psi) \not{\epsilon}_\gamma u_\psi, \quad (5.4)$$

$$\mathcal{M}_{\text{abs,u}} = \frac{eg}{u - m_\chi^2} \bar{u}_\chi \not{\epsilon}_\gamma (\not{p}_\chi - \not{k} + m_\chi) L u_\psi, \quad (5.5)$$

giving the total amplitude  $\mathcal{M}_{\text{abs}} = \mathcal{M}_{\text{abs,s}} + \mathcal{M}_{\text{abs,u}}$ . We use the amplitude to compute the cross section for  $\gamma\psi \rightarrow \chi\phi$  by the standard procedure. We assume that the  $\psi$  particle is at rest with respect to the photon bath and express the result in terms of the energy of the photon  $w \equiv \omega/m_\psi$ .

<sup>1</sup> We find

$$\begin{aligned} \sigma_{\text{abs}}(w) &\equiv \frac{1}{2m_\psi} \frac{1}{2|\omega|} \int d\text{LIPS}_{\chi\phi} (2\pi)^4 \delta^4(p_\psi + k - p_\chi - p_\phi) \langle |\mathcal{M}_{\text{abs}}(k)|^2 \rangle \\ &= \Gamma_0 \frac{\alpha\pi}{m_\psi^3 w^3} \rho(w), \end{aligned} \quad (5.6)$$

where

$$\rho(w) \equiv (1 + 2w + 2w^2) \ln \frac{1 + 2w}{\epsilon^2} - (2 + 4w + 3w^2), \quad (5.7)$$

at leading order in  $\epsilon$ . Note that  $\rho \propto w^0$  and  $\sigma_{\text{abs}} \propto w^{-3}$  as  $w \rightarrow 0$ .

To compute corrections to the decay rate of a particle  $\psi$  due to the absorption of thermal photons from the heat bath, we need to integrate the cross section  $\sigma_{\text{abs}}(w)$  in Eq. (5.6) multiplied with the average occupation number for thermal photons. We find

$$\begin{aligned} \Gamma_{\text{abs}}^T &= \int dw \frac{dn_\gamma}{dw}(w) \sigma_{\text{abs}}(w) \\ &= g_\gamma \int \frac{d^3\mathbf{k}}{(2\pi)^3} f_B(\omega) \sigma_{\text{abs}}(w) \\ &= \frac{\alpha}{\pi} \Gamma_0 \int_0^\infty \frac{dw}{w} f_B(\omega) \rho(w), \end{aligned} \quad (5.8)$$

where  $f_B(\omega) = 1/(e^{\omega/T} - 1) = 1/(e^{w/\tau} - 1)$  is the Bose-Einstein distribution function and  $g_\gamma = 2$  is the number of independent photon polarizations. Since  $f_B \propto w^{-1}$  and  $\rho \propto w^0$  as  $w \rightarrow 0$ , we see that the integrand in Eq. (5.8) is proportional to  $w^{-2}$  as  $w \rightarrow 0$ , and hence  $\Gamma_{\text{abs}}^T$  indeed has a powerlike infrared divergence, implying an infinite decay rate.

<sup>1</sup>We are implicitly considering a cosmological scenario in which the heavy  $\psi$  particle has decoupled from the thermal bath and is out of equilibrium. Furthermore, we assume that the massless  $\phi$  particle is also not thermalized in the bath (which may be the case if the coupling  $g$  is very weak and  $\psi$  decay is the dominant mode of  $\phi$  production, for example). Similar assumptions will also be made in the case of muon decay discussed in Section 5.5.

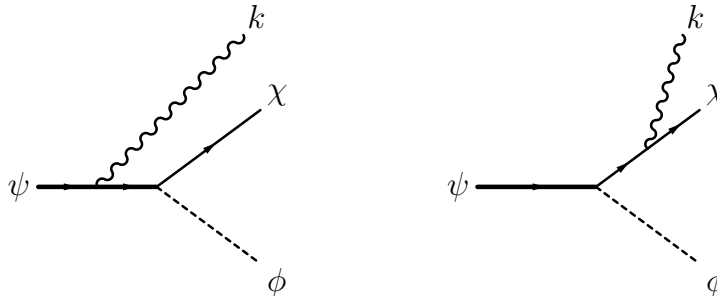


Figure 5.3: The diagrams for radiative  $\psi$ -decays. Note that the topologies of the diagrams are identical to those for absorption in Figure 5.2, with the exception of the photon line placement. This results in the relation given in Eq. (5.9).

As in the case of infrared divergences at zero temperature, the infinite rate is unphysical. We arrived at this unphysical result because we considered only the photon absorption process  $\gamma\psi \rightarrow \chi\phi$  in the calculation of the finite-temperature  $\psi$  decay rate. However, as we shall demonstrate, we cannot consider this absorption process independently of other processes that also result in  $\psi$  decay. In particular, we must also take into account the finite-temperature rates of the radiative decay process  $\psi \rightarrow \gamma\chi\phi$  and the decay process  $\psi \rightarrow \chi\phi$ . At finite temperature, the emission of photons in the first process is stimulated by the presence of photons in the thermal bath. At the same order in  $\alpha$ , the second process is affected by  $T$ -dependent additions to the virtual-photon propagator. When all of these processes are included in the calculation, all  $T$ -dependent infrared divergences cancel to yield a finite rate. The nature of this cancellation is similar to zero-temperature cancellations of infrared divergences in QED, as described in a classic paper by Bloch and Nordsieck [311]. We shall now demonstrate this cancellation to  $\mathcal{O}(g^2\alpha)$ .

### 5.2.2 Photon emission

We begin by considering the photon-emitting radiative decay process  $\psi \rightarrow \gamma\chi\phi$ . The two contributing diagrams are shown in Figure 5.3. Comparing these diagrams to those in Figure 5.2, we see that the amplitudes for emission are formally equivalent to those for absorption given in Eq. (5.4) if we make the substitutions  $k \leftrightarrow -k$  and  $\epsilon_\gamma \leftrightarrow \epsilon_\gamma^*$ . This crossing symmetry gives the photon-emission amplitude from the photon-absorption amplitude,

$$\langle |\mathcal{M}_{\text{em}}(k)|^2 \rangle = g_\gamma \langle |\mathcal{M}_{\text{abs}}(-k)|^2 \rangle, \quad (5.9)$$

where the factor of  $g_\gamma$  arises because we do not average over photon polarizations on the left-hand side. The  $\mathcal{O}(g^2\alpha)$   $T$ -dependent part of the rate for this process is then given by

$$\Gamma_{\text{em}}^T = \frac{1}{2m_\psi} \int d\text{LIPS}_{\gamma\chi\phi} f_B(\omega) (2\pi)^4 \delta^4(p_\psi - k - p_\chi - p_\phi) \langle |\mathcal{M}_{\text{em}}(k)|^2 \rangle, \quad (5.10)$$

where the factor of  $f_B(\omega)$  comes from the  $T$ -dependent part of the  $(1 + f_B)$  Bose-enhancement factor for the final-state photons. Comparing Eq. (5.10) to Eq. (5.8), and using Eqs. (5.6) and (5.9), it can be shown that the expression for the emission rate is very similar to that for the absorption rate given in Eq. (5.8),

$$\Gamma_{\text{em}}^T = \frac{\alpha}{\pi} \Gamma_0 \int_0^{1/2} \frac{dw}{w} f_B(\omega) \rho(-w). \quad (5.11)$$

We see that the only differences are  $\rho(w) \rightarrow \rho(-w)$ , arising from the  $k \rightarrow -k$  substitution used to switch the absorbed photon to an emitted photon, and the limits of integration. The upper limit reflects that the emitted photon is limited by the kinematics to have  $w < 1/2$  in the final state, whereas an absorbed photon is allowed to have any energy in the initial state. Note that this is further reflected in the fact that  $\rho(w)$  is defined only for  $-1/2 < w < \infty$ .

### 5.2.3 Real-radiation corrections

We are now in position to calculate the total rate of  $\psi$  decay due to processes involving either the absorption or emission of real photons,

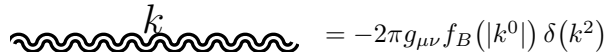
$$\Gamma_{\text{real}}^T = \Gamma_{\text{abs}}^T + \Gamma_{\text{em}}^T = \frac{\alpha}{\pi} \Gamma_0 \int_0^\infty \frac{dw}{w} f_B(\omega) \rho_{\text{real}}(w), \quad (5.12)$$

where  $\rho_{\text{real}}(w) = \rho(w) + \theta(1/2 - w)\rho(-w)$ . Exact integration over  $w$  in the above formula is complicated because of the Bose-Einstein factor. However, if we consider the low-temperature case  $\tau \ll 1$ , then  $f_B(\omega)$  is only non-negligible for  $w \lesssim \tau \ll 1/2$ . We can thus use the approximation  $\theta(1/2 - w) \rightarrow 1$  and integrate Eq. (5.12) by expanding  $\rho_{\text{real}}(w)$  in a Taylor series in  $w$ . This approximation picks up all the terms that are suppressed by powers of  $\tau$ , but it misses the exponentially suppressed terms of  $\mathcal{O}(e^{-1/\tau})$ . The  $\mathcal{O}(g^2\alpha)$  result is then

$$\Gamma_{\text{real}}^T = \frac{\alpha}{\pi} \Gamma_0 \left[ (-4 - 4 \ln \epsilon + \mathcal{O}(\epsilon^2 \ln \epsilon)) J_{-1} + (-2 - 8 \ln \epsilon + \mathcal{O}(\epsilon^2)) J_1 \tau^2 + \mathcal{O}(\tau^4, e^{-1/\tau}) \right], \quad (5.13)$$

where we have defined the integrals

$$J_n \equiv \lim_{x_0 \rightarrow 0} \int_{x_0}^\infty dx x^n f_B(xT) \theta(x - x_0). \quad (5.14)$$



$$\text{wavy line with } k \text{ above it} = -2\pi g_{\mu\nu} f_B(|k^0|) \delta(k^2)$$

Figure 5.4: The  $T$ -dependent part of the photon propagator

Note that for  $n > 0$ ,  $J_n = \text{Li}_{n+1}(1)\Gamma(n+1)$  is finite<sup>2</sup>. The infrared-divergent part of the decay rate due to real-radiation processes is thus given by the  $J_{-1}$  term in Eq. (5.13); we shall now proceed to show that it is canceled by corresponding terms in the virtual corrections to the decay rate.

### 5.3 Virtual corrections

As previously mentioned, the rate of the decay process  $\psi \rightarrow \chi\phi$  is affected by  $T$ -dependent additions to the virtual corrections that enter at  $\mathcal{O}(g^2\alpha)$ . These affect both the vertex correction shown in Figure 5.5 and the charged-fermion self-energies shown in Figure 5.6. At finite temperature, the bare propagator for the virtual photons that appear in these diagrams is modified compared to the zero-temperature case,

$$-\frac{ig_{\mu\nu}}{k^2 + i0} \rightarrow -g_{\mu\nu} \left[ \frac{i}{k^2 + i0} + 2\pi f_B(|k^0|) \delta(k^2) \right]. \quad (5.15)$$

The first term in this equation is the usual  $T = 0$  photon propagator; its effects are accounted for in conventional zero-temperature perturbation theory. The second term in the right-hand side of Eq. (5.15) leads to temperature-dependent corrections to the decay rate (see Figure 5.4). We note that the temperature-dependent contribution to the photon propagator accounts for interactions of real, on-shell photons from the thermal bath with the charged fermions in the initial and final states. In particular, it represents processes in which a photon from the thermal bath is absorbed by either of the fermions, while simultaneously another photon is emitted by either of the fermions with the exact same momentum and polarization as the initial photon.<sup>3</sup>

#### 5.3.1 Vertex correction

We first consider the  $T$ -dependent part of the  $\mathcal{O}(\alpha)$  correction to the vertex, shown in Figure 5.5. The  $T$ -dependent part of the relevant amplitude is given by

$$\mathcal{M}_{\text{vert}}^T = -e^2 g \int \frac{d^4 k}{(2\pi)^3} F(k^0, \mathbf{k}) f_B(|k^0|) \delta(k^2), \quad (5.16)$$

<sup>2</sup>A few terms read  $J_1 = \frac{\pi^2}{6}$ ,  $J_3 = \frac{\pi^4}{15}$ ,  $J_5 = \frac{8\pi^6}{63}$ ,  $J_7 = \frac{8\pi^8}{15}$ .

<sup>3</sup>We can see how the term arises by expanding the photon field in terms of creation and annihilation operators in the usual manner. At  $T = 0$ ,  $aa^\dagger$  terms generate the usual propagator, but the  $a^\dagger a$  terms proportional to the particle number vanish. At finite temperature, the latter terms are instead proportional to the occupation number  $f_B$  and hence are nonvanishing.

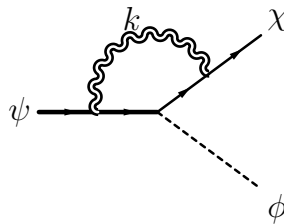


Figure 5.5: The diagram contributing to the  $T$ -dependent part of the  $\mathcal{O}(\alpha)$  correction to the vertex

where

$$F(k^0, \mathbf{k}) \equiv \frac{\bar{u}_\chi \gamma^\mu (\not{p}_\chi - \not{k} + m_\chi) L (\not{p}_\psi - \not{k} + m_\psi) \gamma_\mu u_\psi}{[(p_\chi - k)^2 - m_\chi^2] [(p_\psi - k)^2 - m_\psi^2]} . \quad (5.17)$$

We may use the properties of the gamma matrices to simplify this expression. Integration over  $k^0$  removes  $\delta(k^2)$ ,

$$\mathcal{M}_{\text{vert}}^T = -e^2 g \int \frac{d^3 \mathbf{k}}{(2\pi)^3 2\omega} [F(\omega, \mathbf{k}) + F(-\omega, \mathbf{k})] f_B(\omega) , \quad (5.18)$$

where  $\omega = |\mathbf{k}|$ . Now, by changing the variable of integration from  $\mathbf{k} \rightarrow -\mathbf{k}$  in the second term in the sum enclosed in brackets, the sum becomes  $[F(k) + F(-k)]$ . Examining Eq. (5.17), we see that the numerator of this sum is then independent of  $k$ , since  $k^2 = 0$  and terms that are linear in  $k$  cancel. However, the denominator of the sum retains its quadratic dependence on  $k$ , since it is proportional to  $(p_\chi \cdot k)(p_\psi \cdot k)$ . By counting powers of  $\omega$  and recalling that  $f_B \propto \omega^{-1}$  at small values of  $\omega$ , we observe that the integral in Eq. (5.18) indeed has a powerlike divergence.

We can then take the interference of this amplitude with the tree-level amplitude given in Eq. (5.2). The  $T$ -dependent part of the vertex correction to the decay rate then follows by taking the usual spin-sum average and evaluating the resulting integral over  $\mathbf{k}$ , using the appropriate kinematics of the 2-body decay in the rest frame of the  $\psi$  particle. Writing the result in terms of the integrals  $J_n$  as before, we find at  $\mathcal{O}(g^2 \alpha)$

$$\Gamma_{\text{vert}}^T = \frac{\alpha}{\pi} \Gamma_0 [(4 \ln \epsilon + \mathcal{O}(\epsilon^2 \ln \epsilon)) J_{-1}] . \quad (5.19)$$

Comparing to the decay rate due to real-radiation processes in Eq. (5.13), we see that part of the divergent  $J_{-1}$  term is indeed canceled.

### 5.3.2 Self-energy corrections

The remaining part of the infrared divergence is canceled by the  $T$ -dependent corrections to the fermion self-energy  $\Sigma^T(p)$ , which enter via the virtual photon propagator in Figure 5.6 and lead to  $T$ -dependent contributions to the full (dressed) fermion propagator  $S_F^T(p)$ . At  $T = 0$ , these

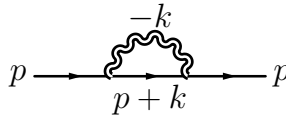


Figure 5.6: The diagram contributing to the  $T$ -dependent part of the fermion self-energy

self-energy contributions are conveniently treated through the mass shift  $\delta m$ , and the wave-function renormalization factor  $Z_2$ . The wave function renormalization factors are usually obtained as derivatives of the self-energy  $\Sigma$  with respect to  $p$ , evaluated on the mass shell  $p^2 = m^2$ . This treatment relies on the fact that at  $T = 0$ ,  $\Sigma$  depends only on the momentum of the particle  $p$ . Unfortunately, this feature is violated at finite temperature because the thermal bath introduces a preferred reference frame. As a result, the self-energy of a particle at rest and the self-energy of a particle in motion are not related in an obvious way.

We will need expressions for the self-energy of both the  $\psi$  and  $\chi$  fermions. We can consider more generally the  $T$ -dependent part of the self-energy  $\Sigma^T(p)$  of a fermion with electric charge  $e$  and  $T = 0$  physical mass  $m$ . This calculation has been discussed extensively in the literature; below, we loosely follow the formalism laid out in Ref. [335]. Our ultimate goal will be to use the expression for  $\Sigma^T$  to show that, in the limit  $p^2 \rightarrow m_T^2$ , the full finite-temperature fermion propagator takes the form

$$S_F^T(p) = Z_2^T \frac{i \sum_s u_s^T(p) \bar{u}_s^T(p)}{p^2 - m_T^2}. \quad (5.20)$$

That is, the pole of the propagator is shifted to the finite-temperature physical mass  $m_T$ , and the fermion wave functions are given by  $\Psi_s(p) = \sqrt{Z_2^T/2p^0} u_s^T(p) e^{-ip \cdot x}$ , where  $Z_2^T$  and  $u_s^T(p)$  are the finite-temperature wave-function renormalization factor and the finite-temperature spinor, respectively.<sup>4</sup> This form implies that self-energy corrections to the decay rate will follow from three distinct sources: (1) matrix elements will be multiplied by a factor of  $Z_2^T$  for each external fermion line, (2) the shift in the physical mass, which will effectively modify the fermion phase-space, and (3) the spinor completeness relation will be modified, affecting the evaluation of spin sums.

To this end, we start by finding the self-energy  $\Sigma^T$  at  $\mathcal{O}(\alpha)$ . We take  $p$  to be the off-shell fermion momentum and  $-k$  to be the momentum of the photon in the loop, as shown in Figure 5.6. The self-energy reads

$$\Sigma^T(p) = 2e^2 \int \frac{d^4 k}{(2\pi)^3} \frac{\not{p} + \not{k} - 2m}{(p+k)^2 - m^2} f_B(|k^0|) \delta(k^2). \quad (5.21)$$

<sup>4</sup>Note that we assume that renormalization has already been carried out at  $T = 0$ .

It is convenient to decompose  $\Sigma^T(p)$  as

$$\Sigma^T(p) = \not{p}c_B(p) - 2mc_B(p) + \not{K}(p), \quad (5.22)$$

where

$$c_B(p) \equiv 2e^2 \int \frac{d^4k}{(2\pi)^3} \frac{f_B(|k^0|)\delta(k^2)}{(p+k)^2 - m^2}, \quad (5.23)$$

$$\begin{aligned} K^\mu(p) &\equiv 2e^2 \int \frac{d^4k}{(2\pi)^3} k^\mu \frac{f_B(|k^0|)\delta(k^2)}{(p+k)^2 - m^2} \\ &\xrightarrow{p^2=m^2} \frac{\alpha}{\pi} J_1 \frac{T^2}{|\mathbf{p}|} \left( L_p, \frac{\mathbf{p}}{|\mathbf{p}|} \left[ \frac{p^0}{|\mathbf{p}|} L_p - 2 \right] \right), \end{aligned} \quad (5.24)$$

and  $L_p = \ln \frac{p^0 + |\mathbf{p}|}{p^0 - |\mathbf{p}|}$ . We can now use these results for  $\Sigma^T$  to find the full (dressed) finite-temperature fermion propagator  $S_F^T(p)$  at  $\mathcal{O}(\alpha)$  in the usual way,

$$\begin{aligned} S_F^T(p) &= \frac{i}{\not{p} - m - \Sigma^T} \\ &= \frac{i[\not{p}(1 - c_B) + m(1 - 2c_B) - \not{K}]}{p^2(1 - 2c_B) - m^2(1 - 4c_B) - 2p \cdot K + \mathcal{O}(\alpha^2)}. \end{aligned} \quad (5.25)$$

Examining the denominator of Eq. (5.25), we see that it can be simplified by defining

$$\begin{aligned} \delta m_T^2 &\equiv 2e^2 \int \frac{d^4k}{(2\pi)^3} f_B(|k^0|)\delta(k^2) \\ &= \frac{2\pi}{3} \alpha T^2. \end{aligned} \quad (5.26)$$

Also, since  $-2p \cdot k = -[(p+k)^2 - m^2] + (p^2 - m^2) + k^2$ , we can write

$$-2p \cdot K = -\delta m_T^2 + (p^2 - m^2)c_B. \quad (5.27)$$

Finally, we can expand in  $(p^2 - m^2)$  around the on-shell momentum  $\widehat{p}$  (which satisfies  $\widehat{p}^2 = m^2$ ) by writing

$$c_B(p) = \widehat{c}_B + (p^2 - m^2)\widehat{c}_B' + \mathcal{O}((p^2 - m^2)^2), \quad (5.28)$$

where  $\widehat{c}_B \equiv c_B(\widehat{p}) = 0$  and

$$\begin{aligned} \widehat{c}_B' &\equiv \frac{dc_B}{dp^2}(\widehat{p}) \\ &= -2e^2 \int \frac{d^4k}{(2\pi)^3} \frac{f_B(|k^0|)\delta(k^2)}{((\widehat{p}+k)^2 - m^2)^2} \left( 1 + \frac{d(2p \cdot k)}{dp^2}(\widehat{p}) \right) \\ &= -\frac{\alpha}{\pi} \frac{J_{-1}}{m^2}. \end{aligned} \quad (5.29)$$

We note that the vanishing of the  $\widehat{c}_B$  coefficient follows from the antisymmetry of the integrand for  $c_B$  in Eq. (5.23) at  $p = \hat{p}$  w.r.t.  $k \rightarrow -k$ ; for the same reason, the derivative term in the integrand in Eq. (5.29) vanishes as well.

We are now in position to recover the form of the propagator advertised in Eq. (5.20), by using Eqs. (5.27) and (5.28) in Eq. (5.25), and keeping only  $\mathcal{O}(\alpha)$  terms there. We find the result

$$S_F^T(p) = (1 - 2m^2\widehat{c}_B') \frac{i(\not{p} + m - \not{K})}{p^2 - m^2 - \delta m_T^2}. \quad (5.30)$$

Comparing this expression with Eq. (5.20) and using Eqs. (5.26) and (5.29), we obtain

$$\begin{aligned} Z_2^T &= 1 - 2m^2\widehat{c}_B' \\ &= 1 + 2\frac{\alpha}{\pi}J_{-1}, \end{aligned} \quad (5.31)$$

$$\begin{aligned} m_T^2 &= m^2 + \delta m_T^2 \\ &= m^2 + \frac{2\pi}{3}\alpha T^2, \end{aligned} \quad (5.32)$$

$$\sum_s u_s^T(p)\bar{u}_s^T(p) = \not{p} + m - \not{K}(p), \quad (5.33)$$

where in the last expression the momentum-dependent results of Eq. (5.23) are to be used in evaluating spin sums. These finite-temperature relations affect the decay rate in the three aforementioned ways; we shall now calculate each of their contributions separately.

First, the finite-temperature wave-function renormalization factor  $Z_2^T$  simply affects the tree-level decay rate  $\widetilde{\Gamma}_0$  of Eq. (5.3) as an overall multiplicative factor; one factor enters for each external fermion line. This yields the  $\mathcal{O}(g^2\alpha)$  temperature-dependent contribution

$$\Gamma_{Z_2}^T = \frac{\alpha}{\pi}\Gamma_0 [(4 + \mathcal{O}(\epsilon^4))J_{-1}]. \quad (5.34)$$

Combining this with Eqs. (5.13) and (5.19), we see that this contribution cancels the remaining infrared-divergent  $J_{-1}$  part of the total decay rate.

Second, Eq. (5.32) results in a shift of the pole of the fermion propagator to  $p^2 = m_T^2$ . Since the pole masses of the fermions define the leading-order rate, the mass shifts  $\Delta m_i \equiv m_{T,i} - m_i \approx \delta m_{T,i}^2/2m_i$  lead to the following  $\mathcal{O}(g^2\alpha)$  “phase-space” correction

$$\begin{aligned} \Gamma_{\text{ph}}^T &= \frac{\partial\widetilde{\Gamma}_0}{\partial m_\psi}\Delta m_\psi + \frac{\partial\widetilde{\Gamma}_0}{\partial m_\chi}\Delta m_\chi \\ &= \frac{\alpha}{\pi}\Gamma_0 [(2 + \mathcal{O}(\epsilon^2))J_1\tau^2]. \end{aligned} \quad (5.35)$$

Finally, the finite-temperature spin-sum relation found in Eq. (5.33) modifies the calculation of



matrix elements. Note from Eq. (5.23) that the relation is actually momentum-dependent, and must be computed for both the  $\psi$  particle (at rest) and the  $\chi$  particle (with energy  $p^0 = m_\psi(1+\epsilon^2)/2$ ). The leading-order contribution to the decay rate is then found by using the finite-temperature spin-sum relation in the tree-level calculation, giving the  $\mathcal{O}(g^2\alpha)$  temperature-dependent part,

$$\Gamma_K^T = \frac{\alpha}{\pi}\Gamma_0 [(-2 + 8 \ln \epsilon + \mathcal{O}(\epsilon^4)) J_1 \tau^2] . \quad (5.36)$$

The total  $\mathcal{O}(g^2\alpha)$  self-energy correction is then given by the sum of these three effects [Eqs. (5.34)–(5.36)],

$$\begin{aligned} \Gamma_\Sigma^T &= \Gamma_{Z_2}^T + \Gamma_{\text{ph}}^T + \Gamma_K^T \\ &= \frac{\alpha}{\pi}\Gamma_0 [(4 + \mathcal{O}(\epsilon^4)) J_{-1} + (8 \ln \epsilon + \mathcal{O}(\epsilon^2)) J_1 \tau^2] . \end{aligned} \quad (5.37)$$

## 5.4 Total decay rate in the toy model

We are now in position to present the final formula for the decay rate of the hypothetical fermion  $\psi$  in a thermal bath. We consider the low-temperature limit  $T \ll m_\psi, m_\chi$  and include contributions from processes involving both real photons and virtual photons; the latter category includes the vertex correction and corrections arising from the self-energy of charged fermions. The total decay rate is the sum of these contributions given in Eqs. (5.13), (5.19), and (5.37). We remind the reader that our calculation is performed in the approximation  $\tau \ll \epsilon \ll 1$  and that we are interested in the leading  $\mathcal{O}(\alpha\tau^2)$  temperature-dependent correction to the rate. We find

$$\begin{aligned} \Gamma_{\text{tot}}^T &= \Gamma_{\text{real}}^T + \Gamma_{\text{vert}}^T + \Gamma_\Sigma^T \\ &= -\alpha \frac{\pi}{3} \tau^2 \Gamma_0 + \mathcal{O}(\tau^2 \epsilon^4, \tau^4, e^{-1/\tau}) . \end{aligned} \quad (5.38)$$

We see that all the infrared-divergent terms proportional to the integrals  $J_{-1}$  cancel out in the total rate. We note that this statement remains valid if exact  $\epsilon$ -dependence of the rate is restored. Furthermore, we find in Eq. (5.38) that all the terms that contains logarithms of the mass ratio  $\ln \epsilon$  cancel in the correction to the total rate, in contrast to individual contributions in Eqs. (5.13) and (5.36). Cancellation of such terms in the zero-temperature case follows from the Kinoshita-Lee-Nauenberg theorem [334, 336]. We are not aware of a general proof of a similar cancellation at a *finite* temperature, so it is important to watch for such terms in explicit  $T \neq 0$  computations.

## 5.5 Muon decay $\mu \rightarrow e\nu_\mu\bar{\nu}_e$

In this section, we present the temperature-dependent correction to the muon decay rate at low temperature. The details of the calculation are similar to the preceding discussion of the toy model. The main difference is that the muon decay is a three-body process, so that integration over the phase-space of final-state particles is more complex.

The muon decay to electron and neutrinos is described by an effective Lagrangian

$$\mathcal{L} \supset \frac{4G_F}{\sqrt{2}} \bar{e}\gamma^\rho L\nu_e \bar{\nu}_\mu\gamma_\rho L\mu, \quad (5.39)$$

where  $G_F$  is the Fermi constant. The leading-order, zero-temperature decay rate reads

$$\tilde{\Gamma}_0 = \Gamma_0 (1 - 8\epsilon^2 - 24\epsilon^4 \ln \epsilon + 8\epsilon^6 - \epsilon^8), \quad (5.40)$$

where now  $\Gamma_0 \equiv \frac{G_F^2 m_\mu^5}{192\pi^3}$  and  $\epsilon \equiv m_e/m_\mu$ . Similar to the toy-model case, the radiative corrections to the rate are given by the sum of real photon emission/absorption corrections, the vertex corrections and the self-energy corrections. For future reference, we show those corrections separately.

The contribution to the decay rate from real photon emission/absorption reads

$$\Gamma_{\text{real}}^T = \frac{\alpha}{\pi}\Gamma_0 \left[ \left( -\frac{17}{3} - 4 \ln \epsilon \right) J_{-1} + \left( -\frac{70}{3} - 32 \ln \epsilon \right) J_1 \tau^2 \right]. \quad (5.41)$$

Note that here and below we keep only the leading term in  $\epsilon$  for each power of  $\tau \equiv T/m_\mu$ , and consistently neglect all powers of  $\tau$  beyond  $\tau^2$ . The result for the vertex correction reads

$$\Gamma_{\text{vert}}^T = \frac{\alpha}{\pi}\Gamma_0 \left[ \left( \frac{5}{3} + 4 \ln \epsilon \right) J_{-1} \right]. \quad (5.42)$$

We note that the temperature dependence in Eq. (5.42) is exact and that higher-order terms in  $\tau$  do not appear there.

The self-energy correction to the fermion propagator was discussed in the previous section and much of that discussion remains valid. For this reason, we just summarize the result. The total self-energy correction is given by

$$\Gamma_{\Sigma}^T = \frac{\alpha}{\pi}\Gamma_0 \left[ 4J_{-1} + \left( \frac{64}{3} + 32 \ln \epsilon \right) J_1 \tau^2 \right]. \quad (5.43)$$

The final result for temperature-dependent radiative corrections to the muon decay is given by the sum of the three contributions of Eqs. (5.41)–(5.43). Including also the  $T = 0$  radiative

corrections [337, 338], we find the final  $\mathcal{O}(\alpha, \tau^2, \epsilon^0)$  result

$$\Gamma_{\mu \rightarrow e\nu\bar{\nu}} = \Gamma_0 \left\{ 1 + \frac{\alpha}{\pi} \left[ \left( \frac{25}{8} - \frac{\pi^2}{2} \right) - \frac{\pi^2}{3} \tau^2 \right] \right\}. \quad (5.44)$$

We note that  $\mathcal{O}(\alpha\tau^2)$  correction to the rate for the muon decay is identical to the analogous correction to the two-body fermion decay rate in the toy model, suggesting the possibility of deriving and understanding this result in a simpler fashion. We also note that our result Eq. (5.44) disagrees with the one given in Ref. [339].

Part of the discrepancy can be traced to the issue of mass singularities. Indeed, in Ref. [339], the  $\ln \epsilon$  terms are present even at  $\mathcal{O}(\alpha\tau^2)$  contributions to the rate but, as follows from our analysis, such terms cancel when all contributions are taken into account. Nevertheless, as pointed out already, whether mass singularities cancel in the rate if higher-order terms in  $\tau$  are accounted for is an open question. When we extend the calculation of the muon decay rate to include  $\mathcal{O}(\alpha\tau^4)$  terms, we find that Eq. (5.44) is modified by

$$\Delta\Gamma_{\mu \rightarrow e\nu\bar{\nu}} = -\frac{\alpha}{\pi} \Gamma_0 \frac{64\pi^4 \tau^4}{45} \left( 2 \ln \epsilon + \frac{1}{3} \right), \quad (5.45)$$

which shows the logarithmic sensitivity to the electron-to-muon mass ratio. In the low-temperature regime  $\tau \ll \epsilon \ll 1$  that we consider in this work, there exist more important corrections to Eq. (5.44) than the ones displayed in Eq. (5.45). However, most of the “more relevant” corrections involve powers of the mass ratio  $\epsilon$ , while Eq. (5.45) shows logarithmic sensitivity to  $\epsilon$ , a unique feature in the low-temperature regime. It is interesting to point out that by relaxing the relationship between the temperature  $T$  and the mass of the charged particle in the final state (the electron), we obtain new sources of mass logarithms related to the thermal Fermi-Dirac distribution of *fermions* in the heat bath. Complete analysis of the corrections to the muon decay rate for the *intermediate-temperature regime*  $m_e \ll T \ll m_\mu$  — where proper interplay of bosonic and fermionic temperature-dependent corrections becomes important — is beyond the scope of the present discussion, but some details of the calculation are given in Appendix D.

## 5.6 Conclusions

Long-lived charged particles appear in a variety of scenarios for early-Universe physics and dark matter. In all cases, these long-lived particles are bathed for a long time in a gas of photons, giving rise to the possibility of induced decays through processes such as those shown in Figure 5.2. If the rate of this induced process is large, then the cosmological effects of these long-lived charged particles may be substantially modified.

A naive evaluation of the rate for these induced decays leads to a result which diverges as

the frequency of the photon in the heat bath that induces the decay vanishes. As with infrared divergences at zero temperature, a proper calculation of the decay rate requires accounting for all degenerate processes. Once this is done, the infrared divergences cancel, leading to small correction to the decay rate. By considering a simple toy model with a two-body final state and a realistic process — muon decay — with a three-body final state, we found a universal leading finite-temperature correction  $\delta\Gamma/\Gamma_0 = -\frac{\alpha}{\pi} \frac{\pi^2 T^2}{3m^2}$ , where  $m$  is the mass of the decaying particle.

In this study, we focused on discussing infrared divergences in decays of charged particles in the thermal bath. This issue can be sharply defined by considering temperatures that are small compared to masses of decaying particles and their decay products. An interesting set of questions arises if we depart from the low-temperature regime and consider the “intermediate”-temperature scenario, where the mass of the decaying particle is large and masses of decay products are small, compared to the heat-bath temperature. In such a case, radiative corrections enhanced by the logarithms of the mass ratios can become numerically important in the context of a variety of scenarios that occur in the early Universe. For example, light gravitinos that arise in theories of supergravity with gauge-mediated supersymmetry breaking may be produced by the decay of short-lived charged staus to taus [211–216]. Temperatures greater than the tau mass will then fall into the “intermediate”-temperature scenario. If mass-enhanced corrections are indeed present, large modifications of the stau decay rate and the production rate of light gravitino dark matter become conceivable. Such modifications may affect the early-Universe thermal history and have implications for collider phenomenology [34].

Furthermore, in some regions of the supersymmetric parameter space, the process of coannihilation is important in the determination of the dark-matter relic abundance after freeze-out [340,341]. Freeze-out occurs roughly at temperatures  $T \sim m_{\text{SUSY}}/20$  that may be greater than the masses of some of the products of supersymmetric particle decay, so this indeed presents another intermediate-temperature scenario. Finite-temperature effects and mass singularities may then become important in determining the individual scattering and decay rates for charged particles, which would be important if one is interested in the detailed thermal history of these particles. However, note that the final dark-matter relic abundance is most likely not strongly affected by finite-temperature effects, since only the coannihilation rates (and not other scattering or decay rates) enter the calculation [342]. For example, in Ref. [343] it was found that finite-temperature corrections to coannihilation occur only at the  $10^{-4}$  level. Finite-temperature effects may also affect neutrino decoupling [344]. It has also been suggested that the original calculations of temperature-dependent corrections to neutron decay are incomplete [345]. Clearly, there remains much work to be done concerning finite-temperature effects in the early Universe.

# Appendix A

## Kinetic decoupling

The kinetic-decoupling temperature  $T_{\text{kd}}$  at which the dark matter WIMPs  $\chi$  decouple from the radiation in the early Universe sets the small-scale cutoff in the power spectrum and determines the mass of the first collapsed structures. An estimate in Ref. [49], which considers effects of free-streaming and acoustic oscillations, gives the relation between the  $T_{\text{kd}}$  and the mass of the first collapsed structures as

$$M_c \approx 33.3 (T_{\text{kd}}/10\text{MeV})^{-3} M_{\oplus}. \quad (\text{A.1})$$

The kinetic decoupling process thus links the microscopic scales of particle physics to the macroscopic scales of astrophysics.

Before deriving the kinetic-decoupling temperature, let us first reexamine the process of chemical decoupling. Recall that the number of dark matter WIMPs in the early Universe is regulated by self-annihilation. As we saw in Section 2.1, we can define the chemical-decoupling temperature at freeze-out by

$$H(T_{\text{cd}}) = \Gamma_{\text{an}}(T_{\text{cd}}). \quad (\text{A.2})$$

Using the expression for the Hubble expansion rate during the radiation-dominated era, we can write

$$g_*^{1/2} T_{\text{cd}}^2 / M_{\text{pl}} \sim n_{\chi} \langle \sigma_{\text{an}} v_{\chi} \rangle. \quad (\text{A.3})$$

Assuming that the WIMPs are nonrelativistic, we can use the thermal equilibrium relations

$$n_{\chi} \sim (m_{\chi} T)^{3/2} e^{-m_{\chi}/T} \quad (\text{A.4})$$

$$v_{\chi} \sim (T/m_{\chi})^{1/2}. \quad (\text{A.5})$$

With a weak-scale annihilation cross section  $\sigma_{\text{an}} \sim |\mathcal{M}|^2 / m_{\chi}^2 \sim \alpha^2 / m_{\chi}^2$ , using these relations in

---

This chapter contains previously unpublished work, which was completed in collaboration with Marc Kamionkowski and Stefano Profumo.

Eq. (A.3) gives the approximation

$$\frac{m_\chi}{T_{\text{cd}}} \sim 30. \quad (\text{A.6})$$

Let us now examine the process of kinetic decoupling of the WIMPs. After the WIMPs fall out of chemical equilibrium, they can nevertheless remain in *kinetic* equilibrium via elastic collisions with the lighter relativistic particles that compose the radiation. That is, although Eq. (A.4) does not hold as the temperature of the Universe decreases, Eq. (A.5) may still hold, provided that the rate of elastic collisions is sufficiently high. When the collision rate falls below that required to maintain kinetic equilibrium, then the WIMPs are said to be kinetically decoupled from the radiation. We see from Eq. (A.6) that this happens at a temperature that is at most a few GeV.

To first approximation, we can define the kinetic-decoupling temperature  $T_{\text{kd}}$  via an analogue of Eq. (A.2). However, there is a crucial difference: elastic collisions, unlike annihilations, do not destroy the particles involved. Thus, a WIMP may collide with multiple relativistic particles in order to maintain Eq. (A.5). The relevant rate to compare to the Hubble expansion rate is then the relaxation rate, i.e., the inverse of the timescale for  $N_{\text{col}}$  collisions, the number required to maintain kinetic equilibrium, to occur. That is,  $T_{\text{kd}}$  satisfies

$$H(T_{\text{kd}}) = \Gamma_{\text{rlx}}(T_{\text{kd}}) = N_{\text{col}}^{-1} \sum_f n_f \langle \sigma_{f\chi} \rangle, \quad (\text{A.7})$$

where  $n_f \sim T_{\text{kd}}^3$  is the thermal equilibrium comoving number density of the relativistic species  $f$ ,  $\sigma_{f\chi}$  is the cross section for elastic scattering of  $f$  particles from the WIMP, and the sum is taken over all species of light particles that are relativistic at  $T_{\text{kd}}$ . Again, all of the variables in this expression are functions of temperature.

We can estimate  $N_{\text{col}}$  by assuming that a WIMP undergoes a random walk as it scatters off multiple light particles [60]. The relaxation timescale is then the amount of time needed for the WIMP to undergo a total momentum change  $\Delta p_\chi$  on the order of its own momentum  $p_\chi \sim (m_\chi T)^{1/2}$  [given by Eq. (A.5)], thus maintaining kinetic equilibrium. Since the momentum imparted by each collision is on the order of the momentum of the light particle,  $\Delta p \sim p_f \sim T$  for each collision. Then the total momentum change of the WIMP after  $N_{\text{col}}$  collisions is  $\Delta p_\chi \sim N_{\text{col}}^{1/2} \Delta p \sim N_{\text{col}}^{1/2} T$ . Kinetic equilibrium is thus established when  $\Delta p_\chi \sim p_\chi$ , or after  $N_{\text{col}} \sim m_\chi/T$  collisions.

Using these results, we arrive at an analogue to Eq. (A.3) that serves to define the kinetic-decoupling temperature  $T_{\text{kd}}$ :

$$1.66 g_*^{1/2} T_{\text{kd}}^2 / M_{\text{pl}} = (T_{\text{kd}} / m_\chi) \sum_f n_f \langle \sigma_{f\chi} \rangle. \quad (\text{A.8})$$

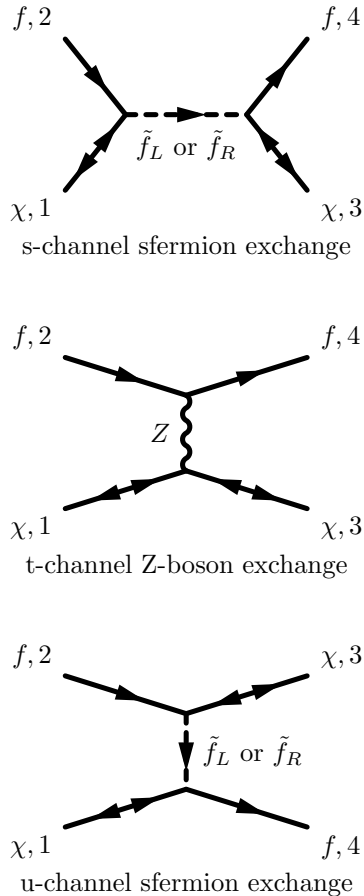


Figure A.1: Feynman diagrams for scattering of a fermion  $f$  by a neutralino  $\chi$ . Double arrows indicate that the neutralinos are Majorana spinors.

Here, we include a degeneracy factor in the comoving number density  $n_f$  to account for the multiplicity of particle, antiparticle, and spin states. Accordingly, we take  $\sigma_{f\chi}$  to be the spin-averaged cross section. Since  $\sigma_{f\chi}$  will be a function of the energy of the light particles,  $E \sim T$ , the quantity of interest is  $\langle \sigma_{f\chi} \rangle$ , the average of the cross section over the thermal distribution of the light particles.

Note that more exact definitions of  $T_{\text{kd}}$  have been formalized; these treatments utilize the Boltzmann equation to define more rigorously the conditions at which kinetic decoupling can be said to occur. Solving Eq. (A.8) nevertheless gives an approximation for  $T_{\text{kd}}$ . However, in order to do this we must first find  $\langle \sigma_{f\chi} \rangle$  as a function of  $T_{\text{kd}}$ ; i.e., we must calculate cross sections for elastic scattering of various light particles from WIMPs.

## A.1 Elastic-scattering cross sections

We wish to calculate the cross section for elastic scattering between the light relativistic particles comprising the radiation and the WIMPs, which we take to be the neutralino of the minimally su-

persymmetric standard model (MSSM). Since the neutralino is weakly interacting, we are primarily interested in scattering of light fermions (e.g., quarks and leptons); scattering of photons is suppressed. Since the neutralinos are nonrelativistic and much more massive than these light fermions, we can also evaluate the cross sections in the fixed-target limit. This approximation should suffice for the simplified model of kinetic decoupling implied by Eq. (A.8); however, note that the more rigorous treatments mentioned above can accommodate more sophisticated calculations of the cross sections.

Let us examine the various ways in which scattering of fermions by neutralinos can occur. The relevant interaction Lagrangian terms are

$$\begin{aligned}\mathcal{L}_{\tilde{f}f\chi} &= \tilde{f}_L\bar{f}(g_{\tilde{f}_L f\chi}^L P_L + g_{\tilde{f}_L f\chi}^R P_R)\chi \\ &\quad + \tilde{f}_R\bar{f}(g_{\tilde{f}_R f\chi}^L P_L + g_{\tilde{f}_R f\chi}^R P_R)\chi + h.c. \\ &\equiv \tilde{f}_L\bar{f}\mathbf{K}_L\chi + \tilde{f}_R\bar{f}\mathbf{K}_R\chi + h.c.\end{aligned}\tag{A.9}$$

$$\begin{aligned}\mathcal{L}_{Z\tilde{f}f} &= Z_\mu\bar{f}\gamma^\mu(g_{Z\tilde{f}f}^L P_L + g_{Z\tilde{f}f}^R P_R)f + h.c. \\ &\equiv Z_\mu\bar{f}\mathbf{L}^\mu f + h.c.\end{aligned}\tag{A.10}$$

$$\begin{aligned}\mathcal{L}_{Z\chi\chi} &= \frac{1}{2}Z_\mu\bar{\chi}\gamma^\mu(g_{Z\chi\chi}^L P_L + g_{Z\chi\chi}^R P_R)\chi + h.c. \\ &\equiv Z_\mu\bar{\chi}\mathbf{M}^\mu\chi + h.c.\end{aligned}\tag{A.11}$$

Here,  $\gamma^\mu$  are the Dirac matrices and  $P_L$  and  $P_R$  are the projection matrices; we have also defined the matrices  $\mathbf{K}_L$ ,  $\mathbf{K}_R$ ,  $\mathbf{L}^\mu$  and  $\mathbf{M}^\mu$ . The Lorentz indices on  $\mathbf{M}^\mu$  and  $\mathbf{L}^\mu$  follow the Einstein summation convention, treating the set of Dirac matrices  $\gamma^\mu$  as a 4-vector. The metric is given by  $\eta = \text{diag}(1, -1, -1, -1)$  in this section.

These interactions allow scattering of a fermion  $f$  by a neutralino  $\chi$  by either Z-boson exchange or sfermion exchange ( $\tilde{f}_L$  or  $\tilde{f}_R$ ). The corresponding tree-level Feynman diagrams are shown in Figure A.1.

These diagrams represent the amplitudes

$$\begin{aligned}\mathcal{M}_s &= \frac{1}{s - m_{\tilde{f}_L}^2 + i\Gamma_{\tilde{f}_L} m_{\tilde{f}_L}}(\bar{u}_4\mathbf{K}_L v_3)(\bar{v}_1\bar{\mathbf{K}}_L u_2) \\ &\quad + (L \rightarrow R)\end{aligned}\tag{A.12}$$

$$\mathcal{M}_t = -\frac{1}{t - m_Z^2}(\bar{u}_4\mathbf{L}^\mu u_2)(\bar{u}_3\mathbf{M}_\mu u_1)\tag{A.13}$$

$$\begin{aligned}\mathcal{M}_u &= \frac{1}{u - m_{\tilde{f}_L}^2}(\bar{u}_4\mathbf{K}_L u_1)(\bar{u}_3\bar{\mathbf{K}}_L u_2) \\ &\quad + (L \rightarrow R).\end{aligned}\tag{A.14}$$



Here,  $s$ ,  $t$ , and  $u$  are the Mandelstam variables,  $C$  is the charge conjugation matrix, and the  $u$ -spinors and  $v$ -spinors are the free-particle and free-antiparticle spinor wave functions. We have also used the standard Breit-Wigner prescription for  $s$ -channel resonances, i.e.,  $\Gamma_{\tilde{f}}$  is the decay rate of the sfermion  $\tilde{f}$ . Furthermore, we take the low-energy limit of the Z-boson propagator. The total amplitude  $\mathcal{M}$  for scattering is given by the sum of these amplitudes; note that

$$|\mathcal{M}|^2 = |\mathcal{M}_s|^2 + |\mathcal{M}_t|^2 + |\mathcal{M}_u|^2 + 2\Re(\mathcal{M}_s\mathcal{M}_t^* + \mathcal{M}_s\mathcal{M}_u^* + \mathcal{M}_t\mathcal{M}_u^*). \quad (\text{A.15})$$

From Eqs. (A.12)–(A.14), we can compute and average the spin sums of each term of Eq. (A.15) (using the completeness relations of Majorana free-particle spinor wave functions). The averaged spin sums of the individual terms in Eq. (A.15) are given by:

$$\begin{aligned} \langle |\mathcal{M}_s|^2 \rangle &= \frac{S}{(s - m_{\tilde{f}_L}^2 + i\Gamma_{\tilde{f}_L} m_{\tilde{f}_L})(s - m_{\tilde{f}_R}^2 - i\Gamma_{\tilde{f}_R} m_{\tilde{f}_R})} \\ &\quad \times \text{Tr}\left((\not{p}_4 + m_4)\mathbf{K}_L(\not{p}_3 - m_3)\bar{\mathbf{K}}_R\right) \text{Tr}\left((\not{p}_2 + m_2)\mathbf{K}_R(\not{p}_1 - m_1)\bar{\mathbf{K}}_L\right) \\ &\quad + (L \leftrightarrow R) + (L \rightarrow R) + (R \rightarrow L) \end{aligned} \quad (\text{A.16})$$

$$\langle |\mathcal{M}_t|^2 \rangle = \frac{S}{(t - m_Z^2)^2} \times \text{Tr}\left((\not{p}_4 + m_4)\mathbf{L}^\mu(\not{p}_2 + m_2)\bar{\mathbf{L}}^\nu\right) \text{Tr}\left((\not{p}_3 + m_3)\mathbf{M}_\mu(\not{p}_1 + m_1)\bar{\mathbf{M}}_\nu\right) \quad (\text{A.17})$$

$$\begin{aligned} \langle |\mathcal{M}_u|^2 \rangle &= \frac{S}{(u - m_{\tilde{f}_L}^2)(u - m_{\tilde{f}_R}^2)} \\ &\quad \times \text{Tr}\left((\not{p}_4 + m_4)\mathbf{K}_L(\not{p}_1 + m_1)\bar{\mathbf{K}}_R\right) \text{Tr}\left((\not{p}_3 + m_3)\bar{\mathbf{K}}_L(\not{p}_2 + m_2)\mathbf{K}_R\right) \\ &\quad + (L \leftrightarrow R) + (L \rightarrow R) + (R \rightarrow L) \end{aligned} \quad (\text{A.18})$$

$$\begin{aligned} \langle \mathcal{M}_s\mathcal{M}_t^* \rangle &= \frac{S}{(s - m_{\tilde{f}_L}^2 + i\Gamma_{\tilde{f}_L} m_{\tilde{f}_L})(t - m_Z^2)} \\ &\quad \times \text{Tr}\left((\not{p}_4 + m_4)\mathbf{K}_L(\not{p}_3 - m_3)(C\bar{\mathbf{M}}^{\mu\text{T}}C^{-1})(\not{p}_1 - m_1)\bar{\mathbf{K}}_L(\not{p}_2 + m_2)\bar{\mathbf{L}}_\mu\right) \\ &\quad + (L \rightarrow R) \end{aligned} \quad (\text{A.19})$$

$$\begin{aligned} \langle \mathcal{M}_s\mathcal{M}_u^* \rangle &= \frac{S}{(s - m_{\tilde{f}_L}^2 + i\Gamma_{\tilde{f}_L} m_{\tilde{f}_L})(u - m_{\tilde{f}_R}^2)} \\ &\quad \times \text{Tr}\left((\not{p}_4 + m_4)\mathbf{K}_L(\not{p}_3 - m_3)\mathbf{K}_R(\not{p}_2 - m_2)\bar{\mathbf{K}}_L(\not{p}_1 + m_1)\bar{\mathbf{K}}_R\right) \\ &\quad + (L \leftrightarrow R) + (L \rightarrow R) + (R \rightarrow L) \end{aligned} \quad (\text{A.20})$$

$$\begin{aligned} \langle \mathcal{M}_t\mathcal{M}_u^* \rangle &= -\frac{S}{(t - m_Z^2)(u - m_{\tilde{f}_L}^2)} \\ &\quad \times \text{Tr}\left((\not{p}_4 + m_4)\mathbf{L}^\mu(\not{p}_2 + m_2)\mathbf{K}_L(\not{p}_3 + m_3)\mathbf{M}_\mu(\not{p}_1 + m_1)\bar{\mathbf{K}}_L\right) \\ &\quad + (L \rightarrow R) \end{aligned} \quad (\text{A.21})$$

Here,  $(L \leftrightarrow R)$  indicates an exchange of indices in the original term, while  $(L \rightarrow R)$  and  $(R \rightarrow L)$  indicate a replacement of indices in the original term. We also use the standard Feynman slash notation  $\not{a} \equiv a^\mu \gamma_\mu$ . The Lorentz indices on  $\mathbf{M}^\mu$  and  $\mathbf{L}^\mu$  follow the Einstein summation convention, treating the set of Dirac matrices  $\gamma^\mu$  as a 4-vector. The metric is given by  $\eta = \text{diag}(1, -1, -1, -1)$ . One can also note that  $C\bar{\mathbf{M}}^{\mu\text{T}}C^{-1} = -\eta_{\mu\nu}\mathbf{M}^{\nu\dagger}$  in Eq. (A.19); the placement of indices here is intended, since  $\gamma^\mu$  is not a true 4-vector. The factor  $S$  accounts for the average over the final spin states, and is given by the reciprocal of the multiplicity of the final spin states; e.g.,  $S = 1/4$  for electron-neutralino scattering, and  $S = 1/2$  for neutrino-neutralino scattering.

We can now find the spin-averaged cross sections for elastic fermion-neutralino scattering. Since the neutralino is relatively massive, we can approximate the elastic cross sections in the frame of the neutralino in the limit that the fermions are massless and that the recoil of the neutralino is negligible. That is, we use the expression

$$\frac{d\sigma_{f\chi}}{d\Omega} = \frac{|\mathcal{M}|_f^2}{(8\pi m_\chi)^2}. \quad (\text{A.22})$$

We can also assume that the particles have the following four-momenta before and after the collision:

$$p_1 = (m_\chi, 0, 0, 0) \quad (\text{A.23})$$

$$p_2 = E_f(1, 0, 0, 1) \quad (\text{A.24})$$

$$p_3 = (m_\chi, 0, 0, 0) \quad (\text{A.25})$$

$$p_4 = E_f(1, \cos\theta, 0, \sin\theta). \quad (\text{A.26})$$

Note that this implies that the Mandelstam variables are given by

$$s = (p_1 + p_2)^2 \approx m_\chi^2 + 2m_\chi E_f \quad (\text{A.27})$$

$$t = (p_1 - p_3)^2 \approx 0 \quad (\text{A.28})$$

$$u = (p_1 - p_4)^2 \approx m_\chi^2 - 2m_\chi E_f. \quad (\text{A.29})$$

Using these momenta in the expressions given by Eq. (A.16)-A.21 in the Appendix, we can explicitly compute the traces. Thus, we have all the components needed to evaluate Eq. (A.22), and can find the spin-averaged cross section for each fermion species.

Finally, we need to compute the thermal average  $\langle\sigma_{f\chi}\rangle$ . Since we find that  $\sigma_{f\chi} \propto E_f^2$  (ignoring corrections of order  $E_f/m_\chi$ ), we make the approximation

$$\langle\sigma_{f\chi}(E_f)\rangle \approx \sigma_{f\chi}(\sqrt{\langle E_f^2 \rangle}). \quad (\text{A.30})$$

For a distribution of relativistic fermions at temperature  $T$ , we have

$$\sqrt{\langle E_f^2 \rangle} \approx 3.60T. \quad (\text{A.31})$$

Using this in Eq. (A.30), we find the thermally averaged spin-averaged cross section for fermion-neutralino elastic scattering as a function of temperature. We can now solve Eq. (A.8) to find the kinetic-decoupling temperature for a given parameterization of the MSSM.

We have merely outlined the calculation of the kinetic-decoupling temperature and the microhalo cutoff mass here; a more rigorous presentation and complete results are presented in Ref. [70]. For the MSSM, typical values are  $T_{\text{kd}} \sim \text{MeV-GeV}$  and  $M_{\text{min}} \sim 10^{-11}\text{-}10^{-3} M_{\odot}$ .

## Appendix B

# Derivation of $P(F)$

Here we derive the relation between the flux-density distribution  $P_1(F)$  and the flux PDF  $P(F)$ . Such a calculation is termed “ $P(D)$  analysis” in the literature, as it was first performed for observations of faint radio sources that produced “deflections” of the measuring apparatus. This  $P(D)$  analysis is useful in determining if an observed diffuse background is actually composed of numerous faint point sources. If this is the case, then there will be fluctuations in the diffuse signal from the random Poisson clustering of point sources in each beam. The shape of  $P(F)$  thus depends not only on  $P_1(F)$ , but also the mean number  $\mu$  of sources [Eq. (2.49)] in each beam.

We wish to find the probability distribution for a total flux  $F$  in a beam, given that it is the sum  $F = \sum_i^k F_i$  of the fluxes  $F_i$  from individual microhalos. Each of the  $F_i$  is a random variable with probability distribution  $P_1(F_i)$ . Furthermore, the number  $k$  of fluxes  $F_i$  entering into the sum is itself a random variable given by a Poisson distribution with mean  $\mu$ . Let us call  $P_k(F)$  the probability that  $k$  random variables  $F_i$  sum to  $F$ ; i.e., the probability that  $k$  microhalos emit a total flux  $F$ . Then

$$P(F) = \sum_{k=0}^{\infty} \varphi(\mu, k) P_k(F), \quad (\text{B.1})$$

where  $\varphi(\mu, k)$  is a Poisson probability distribution for  $k$  with mean  $\mu$ .

It now remains to determine  $P_k(F)$ . For  $k = 0$ , it is clear that  $P_0(F) = \delta(F)$ ;  $P_1(F)$  is given. For  $k > 1$ ,  $P_k(F)$  is given by

$$P_k(F) = \int_0^{\infty} dF_1 \dots \int_0^{\infty} dF_k \left( \prod_{i=1}^k P_1(F_i) \right) \delta\left(F - \sum_{i=1}^k F_i\right). \quad (\text{B.2})$$

The easiest way to compute Eq. (B.2) is to note that the Dirac delta function transforms the

---

Material in this chapter was first published in “The gamma-ray-flux PDF from Galactic halo substructure,” Samuel K. Lee, Shin’ichiro Ando, and Marc Kamionkowski, *JCAP* **0907**, 007 (2009) [30]. Reproduced here with permission, ©2009 by IOP Publishing Limited.

integral into a convolution [104, 113]. To see this, let us examine the integral for  $k = 2$ :

$$\begin{aligned}
P_2(F) &= \int_0^\infty dF_1 \int_0^\infty dF_2 P_1(F_1) P_1(F_2) \delta(F - (F_1 + F_2)) \\
&= \int_0^\infty dF_1 P_1(F_1) P_1(F - F_1) \\
&= (P_1 * P_1)(F).
\end{aligned} \tag{B.3}$$

It follows that  $P_k(F) = (P_{k-1} * P_1)(F)$ ; then by induction,  $P_k(F)$  is given by  $P_1(F)$  convolved (or autocorrelated) with itself  $k$  times. Using the convolution theorem, it then follows that

$$P_k(F) = \mathcal{F}^{-1} \left\{ \mathcal{F} \{ P_1(F) \}^k \right\}, \tag{B.4}$$

where  $\mathcal{F}$  denotes a Fourier transform. Note that Eq. (B.4) also holds for  $k = 0$  (and trivially for  $k = 1$ ).

Inserting Eq. (B.4) into Eq. (B.1) and using the linearity of the inverse Fourier transform, we find

$$\begin{aligned}
P(F) &= \sum_{k=0}^{\infty} \frac{e^{-\mu} \mu^k}{k!} \mathcal{F}^{-1} \left\{ \mathcal{F} \{ P_1(F) \}^k \right\} \\
&= e^{-\mu} \mathcal{F}^{-1} \left\{ \sum_{k=0}^{\infty} \frac{(\mu \mathcal{F} \{ P_1(F) \})^k}{k!} \right\} \\
&= \mathcal{F}^{-1} \left\{ e^{\mu (\mathcal{F} \{ P_1(F) \} - 1)} \right\}.
\end{aligned} \tag{B.5}$$

Eq. (B.5) gives the desired relation for  $P(F)$  in terms of  $P_1(F)$  and  $\mu$ . Although the presence of the inverse Fourier transform prevents further analytic simplification in general, this expression can be computed numerically using fast Fourier transforms on a discretized  $P_1(F)$ .

## Appendix C

# Generation of directional-detection events

For simple velocity distributions, Eq. (3.15) may be used to generate random scattering events and their corresponding nuclear-recoil momentum vectors directly from the analytic form of the recoil spectrum. However, for more general velocity distributions, an analytic form for the Radon transform may not be easily found. In such a case, it is then easier to use the velocity distribution to generate random incoming-WIMP velocity vectors, and then to randomly generate the corresponding nuclear-recoil momentum distribution by noting that the elastic scattering is isotropic in the center-of-mass frame of the WIMP-nucleus system.

We first note that the rate for scattering by a WIMP with velocity  $v$  is proportional to  $vf(v)$ , as can be shown from Eqs. (3.15) and (3.16). We thus draw randomly generated incoming-WIMP velocity vectors from the distribution proportional to  $vf(\mathbf{v})$ . This is done using the method given in Section 7.3 of Ref. [346]. That is, we uniformly sample points in the 4-dimensional space  $(\mathbf{v}, g)$ , where the range of sampled velocity vectors  $\mathbf{v}$  is determined by the truncation by the escape speed, and  $g \in [0, \max(vf)]$  is at most the maximum value of  $vf(\mathbf{v})$ . If a sampled point fails to satisfy the criteria  $vf(\mathbf{v}) \geq g$ , then the sampled velocity vector  $\mathbf{v}$  is discarded; otherwise, it is retained. The retained velocity vectors will then be distributed according to  $vf(\mathbf{v})$ , as was desired.

We then use these generated incoming-WIMP velocities to generate the corresponding nuclear recoil momenta. We first note that the recoil direction angular distribution is isotropic in the center-of-mass frame for nonrelativistic elastic scattering events; however, this clearly implies that the lab-frame recoil direction distribution is anisotropic, and will be a function of the incoming velocity  $\mathbf{v}$ . To be specific, it is the distribution of the angle between  $\mathbf{v}$  and  $\hat{\mathbf{q}}$  that is anisotropic in the lab frame. Thus, we could determine the appropriate distribution for each generated  $\mathbf{v}$ , and then draw the recoil directions from these anisotropic distributions. However, it is easier to simply randomly

---

Material in this chapter was first published in “Probing the local velocity distribution of WIMP dark matter with directional detectors,” Samuel K. Lee and Annika H. G. Peter, *JCAP* **1204**, 029 (2012) [33]. Reproduced here with permission, ©2012 by IOP Publishing Limited.

draw the recoil direction from the isotropic center-of-mass frame distribution, and then transform it to the lab frame appropriately.

Let the direction  $\hat{\mathbf{v}}$  of the incoming-WIMP lab-frame velocity vector be given by the spherical coordinates  $(\theta_v, \phi_v)$ . Furthermore, let the angle between  $\hat{\mathbf{v}}$  and the nuclear recoil direction  $\hat{\mathbf{q}}$  be  $\theta$  in the lab frame, and  $\theta_{\text{CM}}$  in the center-of-mass frame; these angles are related by

$$\cos \theta = \frac{1}{\sqrt{2}}(1 + \cos \theta_{\text{CM}})^{1/2}. \quad (\text{C.1})$$

Isotropic scattering in the center-of-mass frame implies that  $\cos \theta_{\text{CM}}$  is uniformly distributed in the range  $[-1, 1]$ ; the distribution for  $\cos \theta$  then follows. However, it also implies that the angle  $\phi$  between the plane defined by the lab-frame  $z$ -axis and  $\hat{\mathbf{v}}$  and the scattering plane (defined by  $\hat{\mathbf{q}}$  and  $\hat{\mathbf{v}}$ ) is uniformly distributed in the range  $[0, 2\pi]$ .

Thus, we determine  $\hat{\mathbf{q}}$  by first randomly generating the vector  $\hat{\mathbf{q}}_0$  with spherical coordinates given by  $(\theta_v + \theta(\theta_{\text{CM}}), \phi_v)$ , which lies in the  $\hat{\mathbf{z}} - \hat{\mathbf{v}}$  plane and forms an angle  $\theta$  with  $\hat{\mathbf{v}}$ . Rotating  $\hat{\mathbf{q}}_0$  by the randomly generated angle  $\phi$  around the  $\hat{\mathbf{v}}$  axis then gives  $\hat{\mathbf{q}}$  with a distribution that is kinematically consistent with the incoming-WIMP velocity  $\mathbf{v}$ . That is,  $\hat{\mathbf{q}} = \mathbf{R}(\phi, \hat{\mathbf{v}})\hat{\mathbf{q}}_0$ , where in Cartesian coordinates

$$\mathbf{R}(\phi, \hat{\mathbf{v}}) = \begin{pmatrix} \cos \phi + \hat{v}_x^2(1 - \cos \phi) & \hat{v}_x \hat{v}_y(1 - \cos \phi) - \hat{v}_z \sin \phi & \hat{v}_x \hat{v}_z(1 - \cos \phi) + \hat{v}_y \sin \phi \\ \hat{v}_x \hat{v}_y(1 - \cos \phi) + \hat{v}_z \sin \phi & \cos \phi + \hat{v}_y^2(1 - \cos \phi) & \hat{v}_y \hat{v}_z(1 - \cos \phi) - \hat{v}_x \sin \phi \\ \hat{v}_x \hat{v}_z(1 - \cos \phi) - \hat{v}_y \sin \phi & \hat{v}_y \hat{v}_z(1 - \cos \phi) + \hat{v}_x \sin \phi & \cos \phi + \hat{v}_z^2(1 - \cos \phi) \end{pmatrix}. \quad (\text{C.2})$$

Finally, the nuclear-recoil momentum  $q = 2\mu \cos \theta$  is given by the kinematics. Thus, we have shown how to randomly generate the recoil momentum vectors  $\mathbf{q} = q\hat{\mathbf{q}}$  corresponding to randomly generated incoming-WIMP velocity vectors  $\mathbf{v}$  drawn from a given velocity distribution  $f(\mathbf{v})$ .

## Appendix D

# Mass singularities and thermal fermionic corrections

At zero temperature, mass singularities from real-radiation, vertex, and self-energy diagrams all cancel [337]. Whether the same is true at finite temperature is still an interesting open question.

As mentioned above, we find in Eq. (5.38) no mass singularities.<sup>1</sup> However, we have not yet proven that the decay rate remains finite in the  $\epsilon \rightarrow 0$  limit of a massless  $\chi$  particle. This is because we assumed  $T \ll m_\chi \ll m_\psi$ , so that only the photons had a non-negligible thermal distribution  $f_B$ . Again, factors of  $f_B$  entered into the calculation of the decay rate in two places: (1) in the calculation of the real-radiation corrections, via the thermal average for absorbed photons and the Bose-enhancement factor for emitted photons, and (2) the modification of the bare photon propagator given in Eq. (5.15).

However, at higher temperatures the thermal fermion populations may also be non-negligible. To illustrate their effect, we return to discussion of the toy model. Let us assume that the temperature satisfies  $m_\chi \ll T \ll m_\psi$ , as will be the case in the massless limit under discussion.<sup>2</sup> At these “intermediate” temperatures, we must then consider the Fermi-Dirac distribution for the  $\chi$  particles,

$$f_F(E_\chi) = \frac{1}{e^{E_\chi/T} + 1}. \quad (\text{D.1})$$

Factors of  $f_F$  for the  $\chi$  particle will then enter the calculation of the decay rate similarly in two places.

First, a  $(1 - f_F)$  Pauli-blocking term for the final-state  $\chi$  particles will be present, since the

---

This chapter contains previously unpublished work, which was completed in collaboration with Marc Kamionkowski and Kirill Melnikov.

<sup>1</sup>Note that at this order in perturbation theory, the virtual corrections can only contribute at up to  $\mathcal{O}(\tau^2)$ , and therefore can only cancel out infrared divergences and mass singularities from the real corrections that appear at this order in the temperature. We do not explicitly give the real corrections at  $\mathcal{O}(\tau^4)$  and higher, but they appear to be free of infrared divergences and mass singularities for the toy model under consideration. However, preliminary calculations show that this does not appear to be the case for muon decay.

<sup>2</sup>At even higher temperatures satisfying  $T \gg m_\psi$ , the Fermi-Dirac distribution of the  $\psi$  particles would also be non-negligible. In this case, the  $\mathcal{O}(\alpha^0\tau)$  correction to the decay rate due to time dilation caused by the thermal motion of the  $\psi$  particles would dominate over the thermal corrections under discussion [347].



$$\text{---} \overline{\text{---}} \overline{\text{---}} \xrightarrow{p} \text{---} = -2\pi(\not{p} + m)f_F(|p^0|)\delta(p^2 - m^2)$$

Figure D.1: The  $T$ -dependent part of the fermion propagator

emission of  $\chi$  particles will be reduced by the presence of the  $\chi$  particles in the thermal bath. For our toy model, the effect of this additional term will be exponentially suppressed for the decay and absorption rates (since there, the  $\chi$  energy is fixed by the kinematics to be  $E_\chi \approx m_\chi/2 \gg T$ , so that  $1 - f_F(E_\chi) \approx 1$ ). However, for the emission rate, the  $(1 - f_F)$  Pauli-blocking term will multiply the  $(1 + f_B)$  Bose-enhancement term for the final-state photons, leading to two new temperature-dependent pieces. The cross-term piece that goes as  $f_B(\omega)f_F(E_\chi)$  will be suppressed, which again follows from the kinematics (since  $\omega/T$  will be relatively large whenever  $E_\chi/T$  is small). However, the term that goes as  $f_F(E_\chi)$  will introduce contributions to the real radiation rate that depend on integrals of the Fermi-Dirac distribution.

Second, the bare fermion propagator will be modified by the addition of a temperature-dependent part,

$$\frac{i(\not{p} + m)}{p^2 - m^2} \rightarrow \frac{i(\not{p} + m)}{p^2 - m^2} - 2\pi(\not{p} + m)f_F(|p^0|)\delta(p^2 - m^2), \quad (\text{D.2})$$

which we will represent by the fermion line shown in Figure D.1. This propagator will enter the real corrections via the diagrams shown in Figure D.2. By similar kinematical arguments, we see that the contribution from the absorption process is again exponentially suppressed, and that only the emission contribution is non-negligible.

The modified fermion propagator will also enter via the vertex and self-energy corrections as shown in the diagrams in Figure D.3. These diagrams will then introduce additional virtual corrections that depend on Fermi-Dirac integrals. Notably, the relations given in Eqs. (5.31)–(5.33) for

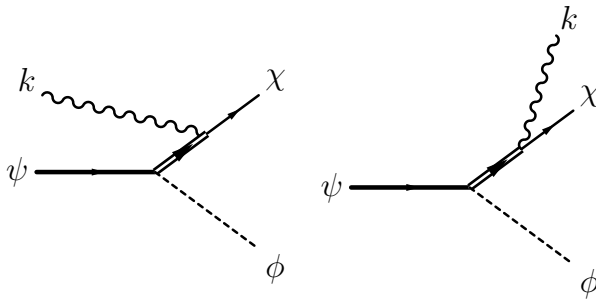


Figure D.2: The additional diagrams (appearing at temperatures  $m_\chi \ll T \ll m_\psi$ ) that contribute to the  $T$ -dependent part of the real corrections, including the thermal corrections to the bare fermion propagator. The absorption contribution is exponentially suppressed.

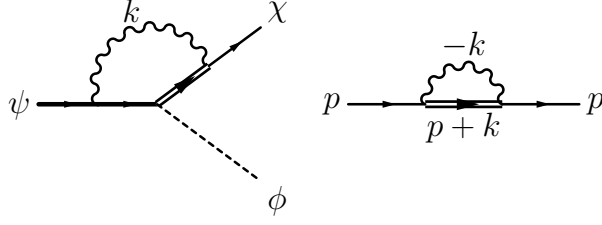


Figure D.3: The additional diagrams (appearing at temperatures  $m_\chi \ll T \ll m_\psi$ ) that contribute to the  $T$ -dependent part of the virtual corrections, including the thermal corrections to the bare fermion propagator.

the fermion self-energy corrections will now have additional terms,

$$Z_2^T = 1 - \widehat{c}_F - 2m^2(\widehat{c}_B' - \widehat{c}_F'), \quad (\text{D.3})$$

$$m_T^2 = m^2(1 + 2\widehat{c}_F) + \delta m_T^2, \quad (\text{D.4})$$

$$\sum_s u_s^T(p) \bar{u}_s^T(p) = \not{p} + m - \widehat{K}(p), \quad (\text{D.5})$$

where now

$$\delta m_T^2 \equiv 2e^2 \int \frac{d^4 k}{(2\pi)^3} [f_B(|k^0|)\delta(k^2) + f_F(|k^0|)\delta(k^2 - m^2)], \quad (\text{D.6})$$

$$K(p) \equiv 2e^2 \int \frac{d^4 k}{(2\pi)^3} k \left[ \frac{f_B(|k^0|)\delta(k^2)}{(p+k)^2 - m^2} - \frac{f_F(|k^0|)\delta(k^2 - m^2)}{(p-k)^2} \right], \quad (\text{D.7})$$

$$\widehat{c}_F \equiv 2e^2 \int \frac{d^4 k}{(2\pi)^3} \frac{f_F(|k^0|)\delta(k^2 - m^2)}{(\widehat{p} - k)^2}, \quad (\text{D.8})$$

$$\widehat{c}_F'(p) \equiv -2e^2 \int \frac{d^4 k}{(2\pi)^3} \frac{f_F(|k^0|)\delta(k^2 - m^2)}{((\widehat{p} - k)^2)^2} \left( 1 - \frac{d(2p \cdot k)}{dp^2}(\widehat{p}) \right). \quad (\text{D.9})$$

Hence, to find the corrections to the  $\chi$  propagator in the diagrams in Figure D.3, we take  $m = m_\chi$  in the above, and the kinematics of the decay give the derivatives of the off-shell  $\chi$  momentum  $p$ ,

$$\frac{dp^0}{dp^2}(\widehat{p}) = -\frac{d|\mathbf{p}|}{dp^2}(\widehat{p}) = \frac{1}{2m_\psi}, \quad (\text{D.10})$$

to be used in the evaluation of  $\widehat{c}_F'(p)$  in Eq. (D.9).<sup>3</sup>

Since these Fermi-Dirac integrals are relatively nontrivial, we leave their evaluation (and hence, the determination of the finite-temperature decay rate at intermediate temperatures obeying  $m_\chi \ll T \ll m_\psi$ ) to future work. However, we note that similar calculations have been carried out in the literature for neutral initial-state particles. For example, the thermal fermionic corrections to the  $H^0 \rightarrow e^+e^-$  decay rate have been found. Furthermore, Ref. [323] found that mass singularities

<sup>3</sup>In our case,  $\widehat{c}_F'(p)$  is independent of the momentum since  $m_\phi = 0$ , but this is not true in general.

from the fermionic contributions do not completely cancel out at these intermediate temperatures, leading to corrections to the decay rate as large as  $\mathcal{O}(10\%)$  when  $m_e/T \approx 5\%$ . Still, a considerable body of subsequent work has found that mass singularities cancel, even at finite temperature, in a variety of processes, and it suggests — though by no means proves — that they may always cancel. If this speculation is correct, then the result of Ref. [323] would need to be revisited.

For the case of muon decay, we find that mass singularities cancel at  $\mathcal{O}(\alpha\tau^2)$ . This disagrees with Ref. [339], which found mass singularities at this order from the low-temperature thermal photonic corrections alone, and claimed that these were cancelled by thermal fermionic corrections at high temperature. Again, the cancellation of mass singularities in this process needs further investigation.

# Bibliography

- [1] J. H. Jeans, *Mon.Not.Roy.Astron.Soc.* **82**, 122–132 (1922).
- [2] F. Zwicky, *Helv.Phys.Acta* **6**, 110–127 (1933).
- [3] J. Einasto, [arXiv:0901.0632](#).
- [4] N. Jarosik, C. Bennett, J. Dunkley, B. Gold, M. Greason, et al., *Astrophys.J.Suppl.* **192**, 14 (2011), [[arXiv:1001.4744](#)].
- [5] A. G. Riess, L. Macri, S. Casertano, M. Sosey, H. Lampeitl, et al., *Astrophys.J.* **699**, 539–563 (2009), [[arXiv:0905.0695](#)].
- [6] R. Kessler, A. Becker, D. Cinabro, J. Vanderplas, J. A. Frieman, et al., *Astrophys.J.Suppl.* **185**, 32–84 (2009), [[arXiv:0908.4274](#)].
- [7] SDSS Collaboration: W. J. Percival et al., *Mon.Not.Roy.Astron.Soc.* **401**, 2148–2168 (2010), [[arXiv:0907.1660](#)].
- [8] M. Roos, [arXiv:1001.0316](#).
- [9] D. Clowe, M. Bradac, A. H. Gonzalez, M. Markevitch, S. W. Randall, et al., *Astrophys.J.* **648**, L109–L113 (2006), [[astro-ph/0608407](#)].
- [10] G. Bertone, D. Hooper, and J. Silk, *Phys.Rept.* **405**, 279–390 (2005), [[hep-ph/0404175](#)].
- [11] F. D. Steffen, *Eur.Phys.J.* **C59**, 557–588 (2009), [[arXiv:0811.3347](#)].
- [12] L. Bergstrom, *New J.Phys.* **11**, 105006 (2009), [[arXiv:0903.4849](#)].
- [13] J. L. Feng, *Ann.Rev.Astron.Astrophys.* **48**, 495 (2010), [[arXiv:1003.0904](#)].
- [14] M. Taoso, G. Bertone, and A. Masiero, *JCAP* **0803**, 022 (2008), [[arXiv:0711.4996](#)].
- [15] S. D. McDermott, H.-B. Yu, and K. M. Zurek, *Phys.Rev.* **D83**, 063509 (2011), [[arXiv:1011.2907](#)].

- [16] K. Sigurdson, M. Doran, A. Kurylov, R. R. Caldwell, and M. Kamionkowski, *Phys.Rev.* **D70**, 083501 (2004), [[astro-ph/0406355](#)].
- [17] S. Profumo and K. Sigurdson, *Phys.Rev.* **D75**, 023521 (2007), [[astro-ph/0611129](#)].
- [18] K. Freese, B. Fields, and D. Graff, [astro-ph/9904401](#).
- [19] B. D. Fields, K. Freese, and D. S. Graff, *Astrophys.J.* **534**, 265–276 (2000), [[astro-ph/9904291](#)].
- [20] **MACHO** Collaboration: C. Alcock et al., *Astrophys.J.* **542**, 281–307 (2000), [[astro-ph/0001272](#)].
- [21] **EROS-2** Collaboration: P. Tisserand et al., *Astron.Astrophys.* **469**, 387–404 (2007), [[astro-ph/0607207](#)].
- [22] D. N. Spergel and P. J. Steinhardt, *Phys.Rev.Lett.* **84**, 3760–3763 (2000), [[astro-ph/9909386](#)].
- [23] J. R. Primack, [arXiv:0909.2247](#).
- [24] S. De Lope Amigo, W. M.-Y. Cheung, Z. Huang, and S.-P. Ng, *JCAP* **0906**, 005 (2009), [[arXiv:0812.4016](#)].
- [25] A. H. Peter and A. J. Benson, *Phys.Rev.* **D82**, 123521 (2010), [[arXiv:1009.1912](#)].
- [26] A. H. Peter, C. E. Moody, A. J. Benson, and M. Kamionkowski, *PoS IDM2010*, 084 (2011), [[arXiv:1011.4970](#)].
- [27] M. Kesden and M. Kamionkowski, *Phys.Rev.Lett.* **97**, 131303 (2006), [[astro-ph/0606566](#)].
- [28] M. Kesden and M. Kamionkowski, *Phys.Rev.* **D74**, 083007 (2006), [[astro-ph/0608095](#)].
- [29] <http://fermi.gsfc.nasa.gov/>.
- [30] S. K. Lee, S. Ando, and M. Kamionkowski, *JCAP* **0907**, 007 (2009), [[arXiv:0810.1284](#)].
- [31] S. Ando, M. Kamionkowski, S. K. Lee, and S. M. Koushiappas, *Phys.Rev.* **D78**, 101301 (2008), [[arXiv:0809.0886](#)].
- [32] S. M. Koushiappas, *AIP Conf.Proc.* **921**, 142–146 (2007), [[astro-ph/0703778](#)].
- [33] S. K. Lee and A. H. Peter, *JCAP* **1204**, 029 (2012), [[arXiv:1202.5035](#)].
- [34] J. L. Feng, M. Kamionkowski, and S. K. Lee, *Phys.Rev.* **D82**, 015012 (2010), [[arXiv:1004.4213](#)].

- [35] A. Czarnecki, M. Kamionkowski, S. K. Lee, and K. Melnikov, *Phys.Rev.* **D85**, 025018 (2012), [[arXiv:1110.2171](#)].
- [36] G. Bertone, *Particle Dark Matter: Observations, Models and Searches*. Cambridge University Press, Cambridge, UK, 2010.
- [37] E. W. Kolb and M. S. Turner, *Front.Phys.* **69**, 1–547 (1990).
- [38] J. Wess and J. Bagger.
- [39] S. P. Martin, [hep-ph/9709356](#).
- [40] H. Baer and X. Tata, *Weak scale supersymmetry: from superfields to scattering events*. Cambridge University Press, Cambridge, UK, 2006.
- [41] G. Jungman, M. Kamionkowski, and K. Griest, *Phys.Rept.* **267**, 195–373 (1996), [[hep-ph/9506380](#)].
- [42] J. L. Feng, *Annals Phys.* **315**, 2–51 (2005).
- [43] J. Ellis and K. A. Olive, [arXiv:1001.3651](#).
- [44] S. Ghigna et al., *Mon.Not.Roy.Astron.Soc.* **300**, 146–162 (1998), [[astro-ph/9801192](#)].
- [45] A. A. Klypin, S. Gottlöber, A. V. Kravtsov, and A. M. Khokhlov, *Astrophys.J.* **516**, 530–551 (1999), [[astro-ph/9708191](#)].
- [46] A. A. Klypin, A. V. Kravtsov, O. Valenzuela, and F. Prada, *Astrophys.J.* **522**, 82–92 (1999), [[astro-ph/9901240](#)].
- [47] B. Moore et al., *Astrophys.J.* **524**, L19–L22 (1999), [[astro-ph/9907411](#)].
- [48] A. Helmi, S. D. M. White, and V. Springel, *Phys.Rev.* **D66**, 063502 (2002), [[astro-ph/0201289](#)].
- [49] A. Loeb and M. Zaldarriaga, *Phys.Rev.* **D71**, 103520 (2005), [[astro-ph/0504112](#)].
- [50] D. Reed et al., *Mon.Not.Roy.Astron.Soc.* **359**, 1537–1548 (2005), [[astro-ph/0406034](#)].
- [51] E. Bertschinger, *Phys.Rev.* **D74**, 063509 (2006), [[astro-ph/0607319](#)].
- [52] J. Diemand, M. Kuhlen, and P. Madau, *Astrophys.J.* **667**, 859–877 (2007), [[astro-ph/0703337](#)].
- [53] C. Giocoli, L. Pieri, and G. Tormen, [arXiv:0712.1476](#).

- [54] V. Berezhinsky, V. Dokuchaev, and Y. Eroshenko, *Phys.Rev.* **D77**, 083519 (2008), [[arXiv:0712.3499](#)].
- [55] V. Springel et al., *Mon.Not.Roy.Astron.Soc.* **391**, 1685–1711 (2008), [[arXiv:0809.0898](#)].
- [56] A. M. Green, S. Hofmann, and D. J. Schwarz, *Mon.Not.Roy.Astron.Soc.* **353**, L23 (2004), [[astro-ph/0309621](#)].
- [57] A. M. Green, S. Hofmann, and D. J. Schwarz, *JCAP* **0508**, 003 (2005), [[astro-ph/0503387](#)].
- [58] A. M. Green, S. Hofmann, and D. J. Schwarz, *AIP Conf.Proc.* **805**, 431–434 (2006), [[astro-ph/0508553](#)].
- [59] J. Diemand, M. Kuhlen, and P. Madau, *Astrophys.J.* **649**, 1–13 (2006), [[astro-ph/0603250](#)].
- [60] T. Bringmann and S. Hofmann, *JCAP* **0407**, 016 (2007), [[hep-ph/0612238](#)].
- [61] M. Kamionkowski and S. M. Koushiappas, *Phys.Rev.* **D77**, 103509 (2008), [[arXiv:0801.3269](#)].
- [62] J. Diemand, B. Moore, and J. Stadel, *Nature* **433**, 389–391 (2005), [[astro-ph/0501589](#)].
- [63] H.-S. Zhao, J. Taylor, J. Silk, and D. Hooper, [astro-ph/0502049](#).
- [64] H. Zhao, J. E. Taylor, J. Silk, and D. Hooper, *Astrophys.J.* **654**, 697–701 (2007), [[astro-ph/0508215](#)].
- [65] V. Berezhinsky, V. Dokuchaev, and Y. Eroshenko, *Phys.Rev.* **D73**, 063504 (2006), [[astro-ph/0511494](#)].
- [66] T. Goerdt, O. Y. Gnedin, B. Moore, J. Diemand, and J. Stadel, *Mon.Not.Roy.Astron.Soc.* **375**, 191–198 (2007), [[astro-ph/0608495](#)].
- [67] D. Hooper and S. Profumo, *Phys.Rept.* **453**, 29–115 (2007), [[hep-ph/0701197](#)].
- [68] X.-l. Chen, M. Kamionkowski, and X.-m. Zhang, *Phys.Rev.* **D64**, 021302 (2001), [[astro-ph/0103452](#)].
- [69] S. Profumo, K. Sigurdson, and M. Kamionkowski, *Phys.Rev.Lett.* **97**, 031301 (2006), [[astro-ph/0603373](#)].
- [70] T. Bringmann, *New J.Phys.* **11**, 105027 (2009), [[arXiv:0903.0189](#)].
- [71] M. S. Turner, *Phys.Rept.* **197**, 67–97 (1990).
- [72] G. G. Raffelt, *Phys.Rept.* **198**, 1–113 (1990).

- [73] L. J. Rosenberg and K. A. van Bibber, *Phys.Rept.* **325**, 1–39 (2000).
- [74] S. J. Asztalos, L. J. Rosenberg, K. van Bibber, P. Sikivie, and K. Zioutas, *Ann.Rev.Nucl.Part.Sci.* **56**, 293–326 (2006).
- [75] M. C. Johnson and M. Kamionkowski, *Phys.Rev.* **D78**, 063010 (2008), [[arXiv:0805.1748](#)].
- [76] E. A. Baltz et al., *JCAP* **0807**, 013 (2008), [[arXiv:0806.2911](#)].
- [77] L. Bergstrom, J. Edsjo, and P. Ullio, *Phys.Rev.* **D58**, 083507 (1998), [[astro-ph/9804050](#)].
- [78] L. Bergstrom, J. Edsjo, P. Gondolo, and P. Ullio, *Phys.Rev.* **D59**, 043506 (1999), [[astro-ph/9806072](#)].
- [79] C. Calcano-Roldan and B. Moore, *Phys.Rev.* **D62**, 123005 (2000), [[astro-ph/0010056](#)].
- [80] B. Moore et al., *Phys.Rev.* **D64**, 063508 (2001), [[astro-ph/0106271](#)].
- [81] A. Tasitsiomi and A. V. Olinto, *Phys.Rev.* **D66**, 083006 (2002), [[astro-ph/0206040](#)].
- [82] V. Berezhinsky, V. Dokuchaev, and Y. Eroshenko, *Phys.Rev.* **D68**, 103003 (2003), [[astro-ph/0301551](#)].
- [83] A. Tasitsiomi, J. M. Siegal-Gaskins, and A. V. Olinto, *New Astron.Rev.* **48**, 473–475 (2004), [[astro-ph/0306561](#)].
- [84] F. Stoehr, S. D. M. White, V. Springel, G. Tormen, and N. Yoshida, *Mon.Not.Roy.Astron.Soc.* **345**, 1313 (2003), [[astro-ph/0307026](#)].
- [85] S. M. Koushiappas, A. R. Zentner, and T. P. Walker, *Phys.Rev.* **D69**, 043501 (2004), [[astro-ph/0309464](#)].
- [86] T. Oda, T. Totani, and M. Nagashima, *Astrophys.J.* **633**, L65–L68 (2005), [[astro-ph/0504096](#)].
- [87] S. Ando, *Phys.Rev.Lett.* **94**, 171303 (2005), [[astro-ph/0503006](#)].
- [88] L. Pieri, E. Branchini, and S. Hofmann, *Phys.Rev.Lett.* **95**, 211301 (2005), [[astro-ph/0505356](#)].
- [89] E. A. Baltz, J. E. Taylor, and L. L. Wai, *Astrophys.J.Lett.* **659**, L125–L128 (2007), [[astro-ph/0610731](#)].
- [90] J. M. Siegal-Gaskins, V. Pavlidou, A. V. Olinto, C. Brown, and B. D. Fields, *J.Phys.Conf.Ser.* **60**, 312–314 (2007), [[astro-ph/0611273](#)].



- [91] L. E. Strigari, S. M. Koushiappas, J. S. Bullock, and M. Kaplinghat, *Phys.Rev.* **D75**, 083526 (2007), [[astro-ph/0611925](#)].
- [92] V. Berezhinsky, V. Dokuchaev, and Y. Eroshenko, *JCAP* **0707**, 011 (2007), [[astro-ph/0612733](#)].
- [93] L. Pieri, G. Bertone, and E. Branchini, *Mon.Not.Roy.Astron.Soc.* **384**, 1627 (2008), [[arXiv:0706.2101](#)].
- [94] M. Kuhlen, J. Diemand, and P. Madau, [arXiv:0805.4416](#).
- [95] V. Springel et al., [arXiv:0809.0894](#).
- [96] S. Ando and E. Komatsu, *Phys.Rev.* **D73**, 023521 (2006), [[astro-ph/0512217](#)].
- [97] S. Ando, E. Komatsu, T. Narumoto, and T. Totani, *Phys.Rev.* **D75**, 063519 (2007), [[astro-ph/0612467](#)].
- [98] A. Cuoco et al., *JCAP* **0704**, 013 (2007), [[astro-ph/0612559](#)].
- [99] A. Cuoco, J. Brandbyge, S. Hannestad, T. Haugboelle, and G. Miele, *Phys.Rev.* **D77**, 123518 (2008), [[arXiv:0710.4136](#)].
- [100] J. M. Siegal-Gaskins, *JCAP* **0810**, 040 (2008), [[arXiv:0807.1328](#)].
- [101] S. Ando, *Phys.Rev.* **D80**, 023520 (2009), [[arXiv:0903.4685](#)].
- [102] D. Hooper and P. D. Serpico, *JCAP* **0706**, 013 (2007), [[astro-ph/0702328](#)].
- [103] S. M. Koushiappas, *Phys.Rev.Lett.* **97**, 191301 (2006), [[astro-ph/0606208](#)].
- [104] T. D. Willis, [astro-ph/0201515](#).
- [105] <http://heasarc.gsfc.nasa.gov/docs/cgro/cossc/egret/>.
- [106] J. F. Navarro, C. S. Frenk, and S. D. M. White, *Astrophys.J.* **490**, 493–508 (1997), [[astro-ph/9611107](#)].
- [107] M. Fornasa, L. Pieri, G. Bertone, and E. Branchini, *Phys.Rev.* **D80**, 023518 (2009), [[arXiv:0901.2921](#)].
- [108] J. Diemand, M. Kuhlen, and P. Madau, *Astrophys.J.* **657**, 262–270 (2007), [[astro-ph/0611370](#)].
- [109] L. Bergstrom, J. Edsjo, and P. Ullio, *Phys.Rev.Lett.* **87**, 251301 (2001), [[astro-ph/0105048](#)].

- [110] **EGRET** Collaboration: P. Sreekumar et al., *Astrophys.J.* **494**, 523–534 (1998), [[astro-ph/9709257](#)].
- [111] A. R. Pullen, R.-R. Chary, and M. Kamionkowski, *Phys.Rev.* **D76**, 063006 (2007), [[astro-ph/0610295](#)].
- [112] G. D. Mack, T. D. Jacques, J. F. Beacom, N. F. Bell, and H. Yuksel, *Phys.Rev.* **D78**, 063542 (2008), [[arXiv:0803.0157](#)].
- [113] P. A. G. Scheuer, *Proc.Cambridge Phil.Soc.* **53**, 764–773 (1957).
- [114] X. Barcons, *Astrophys.J.* **396**, 460–468 (1992).
- [115] X. Barcons and A. C. Fabian, *Mon.Not.Roy.Astron.Soc.* **243**, 366–371 (1990).
- [116] A. Franceschini, *Astrophys.Space Sci.* **86**, 3–11 (1982).
- [117] D. Windridge and S. Phillipps, *Mon.Not.Roy.Astron.Soc.* **319**, 591–605 (2000).
- [118] S. Dodelson, A. V. Belikov, D. Hooper, and P. Serpico, *Phys.Rev.* **D80**, 083504 (2009), [[arXiv:0903.2829](#)].
- [119] D. Tucker-Smith and N. Weiner, *Phys.Rev.* **D64**, 043502 (2001), [[hep-ph/0101138](#)].
- [120] S. Chang, G. D. Kribs, D. Tucker-Smith, and N. Weiner, *Phys.Rev.* **D79**, 043513 (2009), [[arXiv:0807.2250](#)].
- [121] **XENON100** Collaboration: E. Aprile et al., *Phys.Rev.* **D84**, 061101 (2011), [[arXiv:1104.3121](#)].
- [122] D. N. Spergel, *Phys.Rev.* 1353–1355 (1988).
- [123] P. Gondolo, *Phys.Rev.* **D66**, 103513 (2002), [[hep-ph/0209110](#)].
- [124] F. J. Kerr and D. Lynden-Bell, *Mon.Not.Roy.Astron.Soc.* **221**, 1023–1038 (1986).
- [125] A. M. Green, *JCAP* **1010**, 034 (2010), [[arXiv:1009.0916](#)].
- [126] C.-L. Shan, [[arXiv:1103.0481](#)].
- [127] Y. Akrami, C. Savage, P. Scott, J. Conrad, and J. Edsjo, *JCAP* **1104**, 012 (2011), [[arXiv:1011.4318](#)].
- [128] M. Pato et al., *Phys.Rev.* **D83**, 083505 (2011), [[arXiv:1012.3458](#)].
- [129] A. H. G. Peter, *Phys.Rev.* **D83**, 125029 (2011), [[arXiv:1103.5145](#)].
- [130] C. Arina, J. Hamann, and Y. Y. Y. Wong, *JCAP* **1109**, 022 (2011), [[arXiv:1105.5121](#)].

- [131] M. T. Frandsen, F. Kahlhoefer, C. McCabe, S. Sarkar, and K. Schmidt-Hoberg, *JCAP* **1201**, 024 (2012), [[arXiv:1111.0292](#)].
- [132] C. Streve, R. Trotta, G. Bertone, A. H. G. Peter, and P. Scott, [arXiv:1201.3631](#).
- [133] **DEAP-CLEAN** Collaboration: F. Giuliani, *AIP Conf.Proc.* **1200**, 985–988 (2010).
- [134] **CDMS-II** Collaboration: Z. Ahmed et al., *Science* **327**, 1619–1621 (2010), [[arXiv:0912.3592](#)].
- [135] E. Behnke et al., *Phys.Rev.Lett.* **106**, 021303 (2011), [[arXiv:1008.3518](#)].
- [136] M. Felizardo et al., [arXiv:1106.3014](#).
- [137] H. Sekiya, *J.Phys.Conf.Ser.* **308**, 012011 (2011), [[arXiv:1006.1473](#)].
- [138] **ArDM** Collaboration: A. Marchionni et al., *J.Phys.Conf.Ser.* **308**, 012006 (2011), [[arXiv:1012.5967](#)].
- [139] **CDMS** Collaboration: Z. Ahmed et al., *Phys.Rev.* **D84**, 011102 (2011), [[arXiv:1105.3377](#)].
- [140] **XENON100** Collaboration: E. Aprile et al., *Phys.Rev.* **D84**, 052003 (2011), [[arXiv:1103.0303](#)].
- [141] **XENON100** Collaboration: E. Aprile et al., *Phys.Rev.Lett.* **107**, 131302 (2011), [[arXiv:1104.2549](#)].
- [142] D. C. Malling et al., [arXiv:1110.0103](#).
- [143] **DARWIN** Consortium: L. Baudis, [arXiv:1201.2402](#).
- [144] R. Bernabei et al., *Eur.Phys.J.* **C67**, 39–49 (2010), [[arXiv:1002.1028](#)].
- [145] C. E. Aalseth et al., *Phys.Rev.Lett.* **107**, 141301 (2011), [[arXiv:1106.0650](#)].
- [146] G. Angloher et al., [arXiv:1109.0702](#).
- [147] C. J. Copi, J. Heo, and L. M. Krauss, *Phys.Lett.* **B461**, 43–48 (1999), [[hep-ph/9904499](#)].
- [148] C. J. Copi and L. M. Krauss, *Phys.Rev.* **D63**, 043507 (2001), [[astro-ph/0009467](#)].
- [149] B. Morgan, A. M. Green, and N. J. C. Spooner, *Phys.Rev.* **D71**, 103507 (2005), [[astro-ph/0408047](#)].
- [150] B. Morgan and A. M. Green, *Phys.Rev.* **D72**, 123501 (2005), [[astro-ph/0508134](#)].
- [151] C. J. Copi, L. M. Krauss, D. Simmons-Duffin, and S. R. Stroiney, *Phys.Rev.* **D75**, 023514 (2007), [[astro-ph/0508649](#)].

- [152] A. M. Green and B. Morgan, *Phys.Rev.* **D77**, 027303 (2008), [[arXiv:0711.2234](#)].
- [153] M. S. Alenazi and P. Gondolo, *Phys.Rev.* **D77**, 043532 (2008), [[arXiv:0712.0053](#)].
- [154] D. P. Finkbeiner, T. Lin, and N. Weiner, *Phys.Rev.* **D80**, 115008 (2009), [[arXiv:0906.0002](#)].
- [155] S. Ahlen et al., *Int.J.Mod.Phys.* **A25**, 1–51 (2010), [[arXiv:0911.0323](#)].
- [156] A. M. Green and B. Morgan, *Phys.Rev.* **D81**, 061301 (2010), [[arXiv:1002.2717](#)].
- [157] M. Lisanti and J. G. Wacker, *Phys.Rev.* **D81**, 096005 (2010), [[arXiv:0911.1997](#)].
- [158] J. Billard, F. Mayet, J. F. Macias-Perez, and D. Santos, *Phys.Lett.* **B691**, 156–162 (2010), [[arXiv:0911.4086](#)].
- [159] J. Billard, F. Mayet, and D. Santos, *Phys.Rev.* **D82**, 055011 (2010), [[arXiv:1006.3513](#)].
- [160] J. Billard, F. Mayet, and D. Santos, *Phys.Rev.* **D83**, 075002 (2011), [[arXiv:1012.3960](#)].
- [161] J. Billard, F. Mayet, and D. Santos, *Phys.Rev.* **D85**, 035006 (2012), [[arXiv:1110.6079](#)].
- [162] C.-T. Chiang, M. Kamionkowski, and G. Z. Krnjaic, [arXiv:1202.1807](#).
- [163] C. Grignon et al., *JINST* **4**, P11003 (2009), [[arXiv:0909.0654](#)].
- [164] **DRIFT** Collaboration: M. Pipe, *J.Phys.Conf.Ser.* **203**, 012031 (2010).
- [165] K. Miuchi et al., *Phys.Lett.* **B686**, 11–17 (2010), [[arXiv:1002.1794](#)].
- [166] S. Ahlen et al., *Phys.Lett.* **B695**, 124–129 (2011), [[arXiv:1006.2928](#)].
- [167] T. Naka et al., [arXiv:1109.4485](#).
- [168] S. E. Vahsen et al., [arXiv:1110.3401](#).
- [169] G. Lake, *Astron.J.* **98**, 1554–1556 (1989).
- [170] G. Gelmini and P. Gondolo, [hep-ph/0405278](#).
- [171] K. Freese, P. Gondolo, and H. J. Newberg, *Phys.Rev.* **D71**, 043516 (2005), [[astro-ph/0309279](#)].
- [172] C. Savage, K. Freese, and P. Gondolo, *Phys.Rev.* **D74**, 043531 (2006), [[astro-ph/0607121](#)].
- [173] J. I. Read, G. Lake, O. Agertz, and V. P. Debattista, [arXiv:0803.2714](#).
- [174] M. Vogelsberger, A. Helmi, V. Springel, S. D. White, J. Wang, et al., *Mon.Not.Roy.Astron.Soc.* **395**, 797–811 (2009), [[arXiv:0812.0362](#)].

- [175] J. I. Read, L. Mayer, A. M. Brooks, F. Governato, and G. Lake, [arXiv:0902.0009](#).
- [176] M. Kuhlen et al., *JCAP* **1002**, 030 (2010), [[arXiv:0912.2358](#)].
- [177] R. F. Lang and N. Weiner, *JCAP* **1006**, 032 (2010), [[arXiv:1003.3664](#)].
- [178] D. S. M. Alves, M. Lisanti, and J. G. Wacker, *Phys.Rev.* **D82**, 031901 (2010), [[arXiv:1005.5421](#)].
- [179] M. Lisanti and D. N. Spergel, [arXiv:1105.4166](#).
- [180] M. Maciejewski, M. Vogelsberger, S. D. White, and V. Springel, *Mon.Not.Roy.Astron.Soc.* **415**, 2475 (2011), [[arXiv:1010.2491](#)].
- [181] A. Natarajan, C. Savage, and K. Freese, *Phys.Rev.* **D84**, 103005 (2011), [[arXiv:1109.0014](#)].
- [182] D. S. M. Fantin, A. M. Green, and M. R. Merrifield, *Mon.Not.Roy.Astron.Soc.* **418**, 2648–2655 (2011), [[arXiv:1108.4411](#)].
- [183] M. Kuhlen, M. Lisanti, and D. N. Spergel, [arXiv:1202.0007](#).
- [184] J. D. Vergados, [arXiv:1202.3105](#).
- [185] K. M. Gorski et al., *Astrophys.J.* **622**, 759–771 (2005), [[astro-ph/0409513](#)].
- [186] K. Kuijken and G. Gilmore, *Mon.Not.Roy.Astron.Soc.* **239**, 651–664 (1989).
- [187] L. Bergstrom, P. Ullio, and J. H. Buckley, *Astropart. Phys.* **9**, 137–162 (1998), [[astro-ph/9712318](#)].
- [188] J. Holmberg and C. Flynn, *Mon.Not.Roy.Astron.Soc.* **313**, 209–216 (2000), [[astro-ph/9812404](#)].
- [189] R. Catena and P. Ullio, *JCAP* **1008**, 004 (2010), [[arXiv:0907.0018](#)].
- [190] P. Salucci, F. Nesti, G. Gentile, and C. Frigerio Martins, *Astron.Astrophys.*
- [191] F. Iocco, M. Pato, G. Bertone, and P. Jetzer, *JCAP* **1111**, 029 (2011), [[arXiv:1107.5810](#)].
- [192] F. Giuliani, *Phys.Rev.Lett.* **93**, 161301 (2004), [[hep-ph/0404010](#)].
- [193] F. Feroz and M. P. Hobson, *Mon.Not.Roy.Astron.Soc.* **384**, 449 (2008), [[arXiv:0704.3704](#)].
- [194] F. Feroz, M. P. Hobson, and M. Bridges, *Mon.Not.Roy.Astron.Soc.* **398**, 1601–1614 (2009), [[arXiv:0809.3437](#)].
- [195] A. Lewis and S. Bridle, *Phys.Rev.* **D66**, 103511 (2002), [[astro-ph/0205436](#)].

- [196] J. Hamann, S. Hannestad, G. G. Raffelt, and Y. Y. Y. Wong, *JCAP* **0708**, 021 (2007), [[arXiv:0705.0440](#)].
- [197] D. Santos, O. Guillaudin, T. Lamy, F. Mayet, and E. Moulin, *J.Phys.Conf.Ser.* **65**, 012012 (2007), [[astro-ph/0703310](#)].
- [198] F. Mayet, O. Guillaudin, D. Santos, and A. Trichet, *EAS Publ.Ser.* **36**, 263 (2009), [[arXiv:0905.4697](#)].
- [199] D. Santos et al., *J.Phys.Conf.Ser.* **309**, 012014 (2011), [[arXiv:1102.3265](#)].
- [200] J. Billard, F. Mayet, and D. Santos, [arXiv:1202.3372](#).
- [201] J. Lewin and P. Smith, *Astropart.Phys.* **6**, 87–112 (1996).
- [202] **Super-Kamiokande** Collaboration: T. Tanaka et al., *Astrophys.J.* **742**, 78 (2011), [[arXiv:1108.3384](#)].
- [203] **IceCube** Collaboration: R. Abbasi et al., *Phys.Rev.* **D85**, 042002 (2012), [[arXiv:1112.1840](#)].
- [204] **PICASSO** Collaboration: S. Archambault et al., [arXiv:1202.1240](#).
- [205] J. I. Read, L. Mayer, A. M. Brooks, F. Governato, and G. Lake, *Mon.Not.Roy.Astron.Soc.* **397**, 44–51 (2009), [[arXiv:0902.0009](#)].
- [206] C. W. Purcell, J. S. Bullock, and M. Kaplinghat, *Astrophys.J.* **703**, 2275–2284 (2009), [[arXiv:0906.5348](#)].
- [207] C. Bidin, G. Carraro, R. Mendez, and W. van Altena, *Astrophys.J.* **724**, L122–L126 (2010), [[arXiv:1011.1289](#)].
- [208] N. Bozorgnia, G. B. Gelmini, and P. Gondolo, [arXiv:1111.6361](#).
- [209] T. Moroi, [hep-ph/9503210](#).
- [210] W. Rarita and J. Schwinger, *Phys.Rev.* **60**, 61 (1941).
- [211] M. Dine, W. Fischler, and M. Srednicki, *Nucl.Phys.* **B189**, 575–593 (1981).
- [212] S. Dimopoulos and S. Raby, *Nucl.Phys.* **B192**, 353 (1981).
- [213] C. R. Nappi and B. A. Ovrut, *Phys.Lett.* **B113**, 175 (1982).
- [214] L. Alvarez-Gaume, M. Claudson, and M. B. Wise, *Nucl.Phys.* **B207**, 96 (1982).

- [215] M. Dine, A. E. Nelson, and Y. Shirman, *Phys.Rev.* **D51**, 1362–1370 (1995), [[hep-ph/9408384](#)].
- [216] M. Dine, A. E. Nelson, Y. Nir, and Y. Shirman, *Phys.Rev.* **D53**, 2658–2669 (1996), [[hep-ph/9507378](#)].
- [217] D. Volkov and V. Soroka, *JETP Lett.* **18**, 312–314 (1973).
- [218] P. Fayet and J. Iliopoulos, *Phys.Lett.* **B51**, 461–464 (1974).
- [219] B. de Wit and D. Z. Freedman, *Phys.Rev.Lett.* **35**, 827 (1975).
- [220] S. Deser and B. Zumino, *Phys.Rev.Lett.* **38**, 1433 (1977).
- [221] H. Pagels and J. R. Primack, *Phys.Rev.Lett.* **48**, 223 (1982).
- [222] M. Viel, J. Lesgourgues, M. G. Haehnelt, S. Matarrese, and A. Riotto, *Phys.Rev.* **D71**, 063534 (2005), [[astro-ph/0501562](#)].
- [223] N. Cabibbo, G. R. Farrar, and L. Maiani, *Phys.Lett.* **B105**, 155 (1981).
- [224] S. Weinberg, *Phys.Rev.Lett.* **48**, 1303 (1982).
- [225] J. R. Ellis, J. E. Kim, and D. V. Nanopoulos, *Phys.Lett.* **B145**, 181 (1984).
- [226] T. Moroi, H. Murayama, and M. Yamaguchi, *Phys.Lett.* **B303**, 289–294 (1993).
- [227] M. Kawasaki and T. Moroi, *Prog.Theor.Phys.* **93**, 879–900 (1995), [[hep-ph/9403364](#)].
- [228] S. Borgani, A. Masiero, and M. Yamaguchi, *Phys.Lett.* **B386**, 189–197 (1996), [[hep-ph/9605222](#)].
- [229] M. Bolz, A. Brandenburg, and W. Buchmuller, *Nucl.Phys.* **B606**, 518–544 (2001), [[hep-ph/0012052](#)].
- [230] J. Pradler and F. D. Steffen, *Phys.Rev.* **D75**, 023509 (2007), [[hep-ph/0608344](#)].
- [231] J. Pradler, [arXiv:0708.2786](#).
- [232] V. S. Rychkov and A. Strumia, *Phys.Rev.* **D75**, 075011 (2007), [[hep-ph/0701104](#)].
- [233] E. Pierpaoli, S. Borgani, A. Masiero, and M. Yamaguchi, *Phys.Rev.* **D57**, 2089–2100 (1998), [[astro-ph/9709047](#)].
- [234] K. Ichikawa, M. Kawasaki, K. Nakayama, T. Sekiguchi, and T. Takahashi, *JCAP* **0908**, 013 (2009), [[arXiv:0905.2237](#)].

- [235] M. Viel, J. Lesgourgues, M. G. Haehnelt, S. Matarrese, and A. Riotto, *Phys.Rev.Lett.* **97**, 071301 (2006), [[astro-ph/0605706](#)].
- [236] A. Boyarsky, J. Lesgourgues, O. Ruchayskiy, and M. Viel, *JCAP* **0905**, 012 (2009), [[arXiv:0812.0010](#)].
- [237] U. Seljak, A. Makarov, P. McDonald, and H. Trac, *Phys.Rev.Lett.* **97**, 191303 (2006), [[astro-ph/0602430](#)].
- [238] S. Hannestad, *Phys.Rev.* **D70**, 043506 (2004), [[astro-ph/0403291](#)].
- [239] T. Asaka, K. Hamaguchi, and K. Suzuki, *Phys.Lett.* **B490**, 136–146 (2000), [[hep-ph/0005136](#)].
- [240] R. Allahverdi, A. Jokinen, and A. Mazumdar, *Phys.Rev.* **D71**, 043505 (2005), [[hep-ph/0410169](#)].
- [241] E. J. Copeland and O. Seto, *Phys.Rev.* **D72**, 023506 (2005), [[hep-ph/0505149](#)].
- [242] K. Kohri, T. Moroi, and A. Yotsuyanagi, *Phys.Rev.* **D73**, 123511 (2006), [[hep-ph/0507245](#)].
- [243] F. D. Steffen, *JCAP* **0609**, 001 (2006), [[hep-ph/0605306](#)].
- [244] J. Pradler and F. D. Steffen, *Phys.Lett.* **B648**, 224–235 (2007), [[hep-ph/0612291](#)].
- [245] K.-Y. Choi, L. Roszkowski, and R. Ruiz de Austri, *JHEP* **04**, 016 (2008), [[arXiv:0710.3349](#)].
- [246] K. Kohri, A. Mazumdar, and N. Sahu, *Phys.Rev.* **D80**, 103504 (2009), [[arXiv:0905.1625](#)].
- [247] D. Gorbunov, A. Khmelnitsky, and V. Rubakov, *JHEP* **12**, 055 (2008), [[arXiv:0805.2836](#)].
- [248] S. Dimopoulos, G. F. Giudice, and A. Pomarol, *Phys.Lett.* **B389**, 37–42 (1996), [[hep-ph/9607225](#)].
- [249] K. Choi, K. Hwang, H. B. Kim, and T. Lee, *Phys.Lett.* **B467**, 211–217 (1999), [[hep-ph/9902291](#)].
- [250] E. A. Baltz and H. Murayama, *JHEP* **05**, 067 (2003), [[astro-ph/0108172](#)].
- [251] M. Fujii and T. Yanagida, *Phys.Lett.* **B549**, 273–283 (2002), [[hep-ph/0208191](#)].
- [252] K. Jedamzik, M. Lemoine, and G. Moultaqa, *Phys.Rev.* **D73**, 043514 (2006), [[hep-ph/0506129](#)].
- [253] F. Staub, W. Porod, and J. Niemeyer, *JHEP* **01**, 058 (2010), [[arXiv:0907.0530](#)].



- [254] R. Kallosh, L. Kofman, A. D. Linde, and A. Van Proeyen, *Phys.Rev.* **D61**, 103503 (2000), [[hep-th/9907124](#)].
- [255] I. M. Shoemaker and A. Kusenko, *Phys.Rev.* **D80**, 075021 (2009), [[arXiv:0909.3334](#)].
- [256] A. de Gouvea, T. Moroi, and H. Murayama, *Phys.Rev.* **D56**, 1281–1299 (1997), [[hep-ph/9701244](#)].
- [257] R. Casalbuoni, S. De Curtis, D. Dominici, F. Feruglio, and R. Gatto, *Phys.Lett.* **B215**, 313 (1988).
- [258] T. Lee and G.-H. Wu, *Phys.Lett.* **B447**, 83–88 (1999), [[hep-ph/9805512](#)].
- [259] S. Ambrosanio, G. L. Kane, G. D. Kribs, S. P. Martin, and S. Mrenna, *Phys.Rev.* **D54**, 5395–5411 (1996), [[hep-ph/9605398](#)].
- [260] J. L. Feng and T. Moroi, *Phys.Rev.* **D58**, 035001 (1998), [[hep-ph/9712499](#)].
- [261] G. D. Kribs, A. Martin, and T. S. Roy, *JHEP* **01**, 023 (2009), [[arXiv:0807.4936](#)].
- [262] Y. Santoso, *AIP Conf.Proc.* **1200**, 494–497 (2010), [[arXiv:0909.4742](#)].
- [263] D. R. Stump, M. Wiest, and C. P. Yuan, *Phys.Rev.* **D54**, 1936–1943 (1996), [[hep-ph/9601362](#)].
- [264] S. Dimopoulos, M. Dine, S. Raby, and S. D. Thomas, *Phys.Rev.Lett.* **76**, 3494–3497 (1996), [[hep-ph/9601367](#)].
- [265] S. Dimopoulos, S. D. Thomas, and J. D. Wells, *Phys.Rev.* **D54**, 3283–3288 (1996), [[hep-ph/9604452](#)].
- [266] **DELPHI** Collaboration: P. Abreu et al., *Eur.Phys.J.* **C16**, 211–228 (2000), [[hep-ex/0103026](#)].
- [267] H. Baer, P. G. Mercadante, X. Tata, and Y.-l. Wang, *Phys.Rev.* **D62**, 095007 (2000), [[hep-ph/0004001](#)].
- [268] S. Ambrosanio, B. Mele, S. Petrarca, G. Polesello, and A. Rimoldi, *JHEP* **01**, 014 (2001), [[hep-ph/0010081](#)].
- [269] **CDF and D0** Collaborations: C. Pagliarone, [hep-ex/0312005](#).
- [270] K. Hamaguchi, Y. Kuno, T. Nakaya, and M. M. Nojiri, *Phys.Rev.* **D70**, 115007 (2004), [[hep-ph/0409248](#)].
- [271] J. L. Feng and B. T. Smith, *Phys.Rev.* **D71**, 015004 (2005), [[hep-ph/0409278](#)].

- [272] P. Wagner and D. A. Toback, *Int.J.Mod.Phys.* **A20**, 3267–3269 (2005), [[hep-ph/0410267](#)].
- [273] H. U. Martyn, *Eur.Phys.J.* **C48**, 15–24 (2006), [[hep-ph/0605257](#)].
- [274] M. Klasen and G. Pignol, *Phys.Rev.* **D75**, 115003 (2007), [[hep-ph/0610160](#)].
- [275] K. Hamaguchi, S. Shirai, and T. T. Yanagida, *Phys.Lett.* **B663**, 86–94 (2008), [[arXiv:0712.2462](#)].
- [276] S. Tarem, S. Bressler, H. Nomoto, and A. Di Mattia, *Eur.Phys.J.* **C62**, 281–292 (2009).
- [277] J. Chen and T. Adams, *Eur.Phys.J.* **C67**, 335–342 (2010), [[arXiv:0909.3157](#)].
- [278] J. L. Feng, J.-F. Grivaz, and J. Nachtman, *Rev.Mod.Phys.* **82**, 699–727 (2010), [[arXiv:0903.0046](#)].
- [279] **ALEPH** Collaboration: A. Heister et al., *Eur.Phys.J.* **C25**, 339–351 (2002), [[hep-ex/0203024](#)].
- [280] **ALEPH, DELPHI, L3, and OPAL** Collaborations: LEP SUSY working group et al., *Note LEPSUSYWG/02-09.2*, <http://lepsusy.web.cern.ch/lepsusy/Welcome.html/> (2001).
- [281] B. C. Allanach et al., *Eur.Phys.J.* **C25**, 113–123 (2002), [[hep-ph/0202233](#)].
- [282] **D0** Collaboration: V. M. Abazov et al., *Phys.Lett.* **B659**, 856–863 (2008), [[arXiv:0710.3946](#)].
- [283] **CDF** Collaboration: T. Aaltonen et al., *Phys.Rev.Lett.* **104**, 011801 (2010), [[arXiv:0910.3606](#)].
- [284] **CDF** Collaboration: A. Abulencia et al., *Phys.Rev.Lett.* **99**, 121801 (2007), [[arXiv:0704.0760](#)].
- [285] **D0** Collaboration: V. M. Abazov et al., *Phys.Rev.Lett.* **102**, 161802 (2009), [[arXiv:0809.4472](#)].
- [286] **CDF** Collaboration: T. Aaltonen et al., *Phys.Rev.Lett.* **103**, 021802 (2009), [[arXiv:0902.1266](#)].
- [287] A. Brandenburg, L. Covi, K. Hamaguchi, L. Roszkowski, and F. D. Steffen, *Phys.Lett.* **B617**, 99–111 (2005), [[hep-ph/0501287](#)].
- [288] P. Z. Skands et al., *JHEP* **07**, 036 (2004), [[hep-ph/0311123](#)].
- [289] B. C. Allanach et al., *Comp.Phys.Commun.* **180**, 8–25 (2009), [[arXiv:0801.0045](#)].

- [290] F. E. Paige, S. D. Protopopescu, H. Baer, and X. Tata, [hep-ph/0312045](#).
- [291] T. Sjostrand, S. Mrenna, and P. Z. Skands, *JHEP* **05**, 026 (2006), [[hep-ph/0603175](#)].
- [292] M. Kaplinghat and A. Rajaraman, *Phys.Rev.* **D74**, 103004 (2006), [[astro-ph/0606209](#)].
- [293] K. Kohri and F. Takayama, *Phys.Rev.* **D76**, 063507 (2007), [[hep-ph/0605243](#)].
- [294] M. Kawasaki, K. Kohri, and T. Moroi, *Phys.Lett.* **B649**, 436–439 (2007), [[hep-ph/0703122](#)].
- [295] M. Kusakabe, T. Kajino, R. N. Boyd, T. Yoshida, and G. J. Mathews, *Phys.Rev.* **D76**, 121302 (2007), [[arXiv:0711.3854](#)].
- [296] K. Jedamzik, *Phys.Rev.* **D77**, 063524 (2008), [[arXiv:0707.2070](#)].
- [297] F. Takayama, *Phys.Rev.* **D77**, 116003 (2008), [[arXiv:0704.2785](#)].
- [298] T. Jittoh et al., *Phys.Rev.* **D84**, 035008 (2011), [[arXiv:1105.1431](#)].
- [299] K. Sigurdson and M. Kamionkowski, *Phys.Rev.Lett.* **92**, 171302 (2004), [[astro-ph/0311486](#)].
- [300] S. Profumo, K. Sigurdson, P. Ullio, and M. Kamionkowski, *Phys.Rev.* **D71**, 023518 (2005), [[astro-ph/0410714](#)].
- [301] K. Kohri and T. Takahashi, *Phys.Lett.* **B682**, 337–341 (2010), [[arXiv:0909.4610](#)].
- [302] I. Albuquerque, G. Burdman, and Z. Chacko, *Phys.Rev.Lett.* **92**, 221802 (2004), [[hep-ph/0312197](#)].
- [303] X.-J. Bi, J.-X. Wang, C. Zhang, and X.-m. Zhang, *Phys.Rev.* **D70**, 123512 (2004), [[hep-ph/0404263](#)].
- [304] M. Ahlers, J. Kersten, and A. Ringwald, *JCAP* **0607**, 005 (2006), [[hep-ph/0604188](#)].
- [305] I. F. M. Albuquerque, G. Burdman, and Z. Chacko, *Phys.Rev.* **D75**, 035006 (2007), [[hep-ph/0605120](#)].
- [306] M. Ahlers, J. I. Illana, M. Masip, and D. Meloni, *JCAP* **0708**, 008 (2007), [[arXiv:0705.3782](#)].
- [307] M. H. Reno, I. Sarcevic, and J. Uscinski, *Phys.Rev.* **D76**, 125030 (2007), [[arXiv:0710.4954](#)].
- [308] S. Ando, J. F. Beacom, S. Profumo, and D. Rainwater, *JCAP* **0804**, 029 (2008), [[arXiv:0711.2908](#)].
- [309] B. Canadas, D. G. Cerdeno, C. Munoz, and S. Panda, *JCAP* **0904**, 028 (2009), [[arXiv:0812.1067](#)].

- [310] I. F. M. Albuquerque, G. Burdman, C. A. Krenke, and B. Nosratpour, *Phys.Rev.* **D78**, 015010 (2008), [[arXiv:0803.3479](#)].
- [311] F. Bloch and A. Nordsieck, *Phys.Rev.* **52**, 54–59 (1937).
- [312] M. Le Bellac, *Thermal field theory*. Cambridge University Press, Cambridge, UK, 2000.
- [313] U. Kraemmer and A. Rebhan, *Rept.Prog.Phys.* **67**, 351 (2004), [[hep-ph/0310337](#)].
- [314] J. Moller and Y. Schroder, *Nucl.Phys.Proc.Suppl.* **205-206**, 218–223 (2010), [[arXiv:1007.1223](#)].
- [315] D. A. Dicus et al., *Phys.Rev.* **D26**, 2694 (1982).
- [316] J.-L. Cambier, J. R. Primack, and M. Sher, *Nucl.Phys.* **B209**, 372 (1982).
- [317] R. Baier, B. Pire, and D. Schiff, *Phys.Rev.* **D38**, 2814 (1988).
- [318] R. Baier, E. Pilon, B. Pire, and D. Schiff, *Nucl.Phys.* **B336**, 157 (1990).
- [319] J. F. Donoghue and B. R. Holstein, *Phys.Rev.* **D28**, 340 (1983) [Erratum: **D29**, 3004 (1984)].
- [320] J. F. Donoghue, B. R. Holstein, and R. W. Robinett, *Ann.Phys.* **164**, 233 (1985) [Erratum: **172**, 483 (1986)].
- [321] R. L. Kobes, G. W. Semenoff, and N. Weiss, *Z.Phys.* **C29**, 371 (1985).
- [322] A. E. I. Johansson, G. Peressutti, and B. S. Skagerstam, *Nucl.Phys.* **B278**, 324 (1986).
- [323] K. Ahmed and S. S. Masood, *Phys.Rev.* **D35**, 1861–1871 (1987).
- [324] S. S. Masood, *Phys.Rev.* **D36**, 2602–2605 (1987).
- [325] T. Grandou, M. Le Bellac, and J. L. Meunier, *Z.Phys.* **C43**, 575 (1989).
- [326] W. Keil, *Phys.Rev.* **D40**, 1176 (1989).
- [327] W. Keil and R. Kobes, *Physica* **A158**, 47–57 (1989).
- [328] T. Grandou, M. Le Bellac, and D. Poizat, *Phys.Lett.* **B249**, 478–484 (1990).
- [329] T. Altherr, *Phys.Lett.* **B262**, 314–319 (1991).
- [330] H. A. Weldon, *Phys.Rev.* **D44**, 3955–3963 (1991).
- [331] A. Niegawa and K. Takashiba, *Nucl.Phys.* **B370**, 335–364 (1992).
- [332] A. Niegawa, *Phys.Rev.Lett.* **71**, 3055–3058 (1993).

- [333] D. Indumathi, *Annals Phys.* **263**, 310–339 (1998), [[hep-ph/9607206](#)].
- [334] T. Kinoshita, *J.Math.Phys.* **3**, 650–677 (1962).
- [335] T. Altherr and P. Aurenche, *Phys.Rev.* **D40**, 4171 (1989).
- [336] T. D. Lee and M. Nauenberg, *Phys.Rev.* **133**, B1549–B1562 (1964).
- [337] R. E. Behrends, R. J. Finkelstein, and A. Sirlin, *Phys.Rev.* **101**, 866–873 (1956).
- [338] S. M. Berman, *Phys.Rev.* **112**, 267–270 (1958).
- [339] K. Jagannathan, *Phys.Rev.* **D41**, 1667–1671 (1990).
- [340] P. Binetruy, G. Girardi, and P. Salati, *Nucl.Phys.* **B237**, 285 (1984).
- [341] K. Griest and D. Seckel, *Phys.Rev.* **D43**, 3191–3203 (1991).
- [342] J. Edsjo and P. Gondolo, *Phys.Rev.* **D56**, 1879–1894 (1997), [[hep-ph/9704361](#)].
- [343] T. Wizansky, *Phys.Rev.* **D74**, 065007 (2006), [[hep-ph/0605179](#)].
- [344] N. Fornengo, C. W. Kim, and J. Song, *Phys.Rev.* **D56**, 5123–5134 (1997), [[hep-ph/9702324](#)].
- [345] L. S. Brown and R. F. Sawyer, *Phys.Rev.* **D63**, 083503 (2001), [[astro-ph/0006370](#)].
- [346] W. H. Press, S. A. Teukolsky, W. T. Vetterling, and B. P. Flannery, *Numerical Recipes 3rd Edition: The Art of Scientific Computing*. Cambridge University Press, New York, NY, USA, 2007.
- [347] A. Czarnecki, G. P. Lepage, and W. J. Marciano, *Phys.Rev.* **D61**, 073001 (2000), [[hep-ph/9908439](#)].